

**TOWARDS A PERFORMANCE
EVALUATION METHOD
FOR DURABLE AND SUSTAINABLE
THIN SURFACINGS**

Yue XIAO

The background of the cover is a photo of antiskid runway surface in Gilze-Rijen Airfield.

Towards a Performance Evaluation Method for Durable and Sustainable Thin Surfacing

Proefschrift

ter verkrijging van de graad van doctor
aan de Technische Universiteit Delft,
op gezag van de Rector Magnificus prof. ir. K.C.A.M. Luyben,
voorzitter van het College voor Promoties,
in het openbaar te verdedigen op Donderdag 29 August 2013 om 10:00 uur

door

Yue XIAO

Master of Science in Materials Science and Engineering
Wuhan University of Technology, P.R. China
geboren te Ji'an, Jiangxi, P.R. China

Dit proefschrift is goedgekeurd door de promotoren:

Prof.dr.ir. A.A.A. Molenaar

Prof. S.P. Wu, BSc., MSc., PhD.

Copromotor Ir. M.F.C. van de Ven

Samenstelling promotiecommissie:

Rector Magnificus,	Technische Universiteit Delft, voorzitter
Prof.dr.ir. A.A.A. Molenaar	Technische Universiteit Delft, promotor
Prof. S.P. Wu, BSc., MSc., PhD.	Wuhan University of Technology, promotor
Ir. M.F.C. van de Ven	Technische Universiteit Delft, copromotor
Prof. dr. ir. S.M.J.G. Erkens	Technische Universiteit Delft
Prof. dr. ir. H.E.J.G. Schlangen	Technische Universiteit Delft
Dr. ir. Z. Su	Icopal Group R&D
Dr. ir. C.A.P.M. van Gulp	KOAC-NPC
Prof.ir. A.Q.C. van der Horst	Technische Universiteit Delft, reservelid

Published and distributed by:

Yue Xiao
Road and Railway Engineering Section
Faculty of Civil Engineering and Geosciences
Delft University of Technology
P.O. Box 5048, 2600 GA Delft, the Netherlands
Email: yuedelft@gmail.com, xiaoy@whut.edu.cn

ISBN 978-94-6186-186-3

Key Words: Antiskid Surfacing, Pavement Design, Epoxy Modified Bitumen, Adhesion

Printing: Wohrman Print Service, Zutphen (the Netherlands)

©2013 by Yue Xiao

All rights reserved. No part of this publication may be reproduced, stored in a retrieval system or transmitted in any form or by any means, electronic, mechanical, photocopying, recording, or otherwise without the prior permission of the proprietor.

I dedicate this dissertation to my dear families.

Acknowledgements

Doing a PhD is like running a Golden Tenloop (a traditional long distance running event in Delft). It is a long journey, as much guidance, understanding and support are required in the process, so I would like to express my deepest thanks to those who helped me in this long journey of my research and my life.

This research was carried out at the section of Road and Railway Engineering of Delft University of Technology (TU Delft), under the financial support of China Scholarship Council (CSC). Thanks should first go to the CSC for its four years support and TU Delft for offering me this opportunity.

My study story in TU Delft stemmed from the successful cooperation between TU Delft and WHUT (Wuhan University of Technology, China). Life is full of coincidences. Without this remarkable cooperation, I would not be here for my PhD research. So many thanks go to those who contributed a lot to the cooperation and I wish a shining future for both sections and their cooperation.

First and foremost, I would like to express my deep hearted thanks to my promotor, Prof.dr.ir. A.A.A. Molenaar. He proposed this research position to me, and has given careful reviews and invaluable guidance and comments on my test results and reports during my PhD study. This dissertation could not have been completed without his overall support. I also wish to extend my appreciation to my promotor, Prof.dr. Shaopeng Wu, who was also my supervisor during my master study. He encouraged me to study abroad and shared with me his extensive experience both in the academic and industrial world, which is also important for my future career.

The help and support of my daily supervisor, associate professor Martin van de Ven, is greatly appreciated. I am so grateful that he was always there and I could just walk in his office when I needed any help. His daily supervision, extensive comments on my research and writing was extremely valuable.

This research is based on projects that were supported by CROW, Amsterdam Schiphol Airport and the Dutch Ministry of Defense. So, I would like to express my thanks to the project committee members for their support and guidance. Special thanks go to J.P. Verbeek's contribution to my work. I also would like to acknowledge Dr. Zhao Su for his kind help and suggestions on my research. He provided me a lot of significant insights into the antiskid research.

I am very grateful to the staff in the Road and Railway Engineering group, associate professor Lambert Houben, Marco Poot, Jan Moraal, Jan-Willem Bientjes and Dirk Doedens, who made my lab life easier. Great thanks to Jacqueline Barnhoorn, who helped me so much with administrative issues. I would like to express my sincere thanks to my officemates, Milliyon Woldekidan and Mingliang Li. Sitting with a smiling guy and another "noise-reducing" guy made every day in the office memorable. I appreciate for the lunch, coffee, break, colloquium and discussion times with my dear talented colleagues, Gang, Jian, Dongxing, Sadegh, Mairder, Mohamad, Diederik, Ning, Punkgy, Nico, Jingang,

Mauricio, Yuan, Dongya, Xiangyun, Shaoguang, Chang and Pengpeng. PhD life with you guys and ladies was very nice and surely I will miss you all. Meanwhile, I also would like to take this opportunity to express my thanks to my former colleagues (Sonja van den Bos, Abdol, Liantong, Oscar, Xin and Quantao) and all the new PhD students at the Road and Railway Engineering Section for their support.

I am so grateful to those friends that I met in the Netherlands. Because of you, I know many other interesting topics besides black asphalt.

I would like say thanks to my dear parents for their understanding and support during all these years when I was far away from home pursuing my study. Many thanks to my elder brother and sister-in-law, who always backed me up and stayed with our parents.

My special thanks go to my dear darling Huanhuan Mao, who gave up every opportunity in China to come here to accompany me. She does not know what asphalt is, but give me many helpful suggestions on my writing. Every time you were the first reader to check my grammar and left the first valuable comments. I am very grateful for all the love, understanding, encouragement and happiness that you gave to me.

Yuè Xiāo

月 肖

August, 2013, Delft

Summary

Thin surfacings are widely used as surface layers to provide additional functions and to extend the service life of existing pavements. They can protect the treated road surfaces from external aggressive substances, the degeneration process of weather and the ageing caused by Ultraviolet light and oxygen.

Antiskid surfacing is one type of thin surfacings. It refers to road surface treatment which includes high-friction aggregates and an adhesive binder to bond the aggregates to the road surface. Antiskid surfacing is designed to provide skid resistance, which means excellent adhesion property is then necessary for binding the aggregates together on the surface. So binders with high adhesion strength with aggregates are strongly required.

In the Netherlands, most of the airfield runways used tar-containing binders for the antiskid surfacings. Unlike bitumen based materials, tar-containing surface layers, because of the unique chemical and molecular structure of refined tar, are inherently resistant to chemicals and can provide better adhesive property. However, tar-containing binder is toxic and carcinogenic because of its high Polycyclic Aromatic Hydrocarbons (PAHs) content. It cannot meet the Dutch environmental standards and hence will not be allowed for antiskid surfacing on the runways. Therefore, alternatives to tar-containing binders are urgently required. Research on this topic has been being under investigation for a number of years.

This research mainly focuses on the definition of requirements for the alternatives, together with a design approach on thin surfacings. Firstly, specimens with tar-containing antiskid layers on the surface were collected from six airfields' runways. Fourier Transform Infrared, surface characteristics, tensile adhesion and shear adhesion at the interface were investigated. The tar-containing antiskid layers have a minimum 1.26 mm of texture depth and can keep this texture depth for a long service life. The improved pull test and shear test methods are suitable for evaluating the adhesive properties between thin antiskid surface layer and underlying asphalt mixture layer. The shear strength at the interface between tar-containing antiskid layer and underlying asphalt mixture layer is higher than the value at the interface between asphalt mixture layers. The conclusions from these test results are used as benchmarks for alternative antiskid surfacings.

Secondly, newly designed binders, which are considered as potential binders for antiskid surfacings, were researched. Copolymer modified bitumen emulsion (MBE), 2-component Modified Epoxy Resin (MER) and 2-component Epoxy Modified Bitumen (EMB) were included. The curing behavior, direct tensile strength, high temperature resistance, weather resistance and low temperature relaxation properties were studied by means of Direct Tensile Test, oven ageing and weatherometer ageing, Dynamic Shear Rheometer test, Dynamic Mechanic Thermal Analysis and Relaxation test. Test results indicate that the investigated 2-component epoxy modified bitumen can be designed as a

suitable binder for antiskid surfacing, with good high temperature resistance, qualified relaxation behavior, sufficient tensile strength and enough failure strain.

Thirdly, one of the researched 2-component epoxy modified bitumen was then used to design antiskid surfacing in the lab. The surface characteristics, resistance to tensile stress and shear stress were then investigated. Noise-reducing thin surface layers were also included in this research. The results show that EMB based antiskid layer can provide better adhesion at the interface than tar-containing antiskid layer and polymer modified bitumen based antiskid layers.

Fourthly, the Finite Element Models of antiskid surfacing were developed to simulate the loading condition in the antiskid surface layers. The viscoelastic properties of EMB and MBE were used as input. The calculation shows that the antiskid structure has huge influence on the resulting binder behaviors. The stresses generated in the EMB binder are slightly higher than in the MBE binder, while the MBE is subjected to much higher maximum principal strain and shear strain levels. Furthermore, the EMB binder has better ability to recover after loading. The aggregate skeleton has a higher influence on the stresses and strains in the soft MBE binder than on the stresses and strains in the EMB binder.

At the end, some recommendations are given for further research. Trial sections in the field and fuel resistance are suggested. Fatigue property and failure mechanics are also recommended to investigate the damage mechanisms with FEM model.

Samenvatting

Dunne bekledingen worden veel gebruikt als oppervlaktelagen om extra functies te verschaffen en de levensduur van bestaande verhardingen te verlengen. Zij kunnen het behandelde wegdek beschermen tegen externe agressieve stoffen, het degenererende proces van het weer en de veroudering veroorzaakt door ultraviolet licht en zuurstof.

Een antiskidlaag is een type van dunne toplagen. Het omvat wegdekbehandeling met aggregaten met hoge wrijving en een bindmiddel die de aggregaten aan het wegdek hecht. Antiskidverhardingen worden ontworpen op stroefheid, wat inhoudt dat uitstekende hechting eigenschappen noodzakelijk zijn voor het samen hechten van aggregaten aan het oppervlak. Dus bindmiddelen met hoge kleefkracht met aggregaten zijn vereist.

In Nederland werden voor het grootste deel van de start- en landingsbanen teerhoudende bindmiddelen gebruikt als antiskidwegdekken. Vergeleken met bitumineuze materialen, zijn teerhoudende oppervlaktelagen intrinsiek resistent tegen chemicaliën en kunnen ze betere hechting verschaffen, vanwege de unieke chemische en moleculaire structuur van geraffineerde teer. Echter, teerhoudend bindmiddel is giftig en kankerverwekkend vanwege het hoge polycyclische aromatische koolwaterstoffen (PAK) gehalte. Het kan niet voldoen aan de Nederlandse milieunormen en zullen daarom niet worden toegestaan voor antiskidverharding op start- en landingsbanen. Daarom zijn alternatieven voor teerhoudende bindmiddelen dringend noodzakelijk. Onderzoek betreffende dit onderwerp is al voor een aantal jaren aan de gang.

Dit onderzoek richt zich vooral op de definitie van eisen voor de alternatieven, samen met een ontwerpaanpak voor dunne toplagen. Ten eerste werden er monsters met teerhoudende antiskidlagen aan het oppervlak verzameld van startbanen van zes vliegvelden. Fourier Transform Infrared, oppervlaktekenmerken, treksterkte en afschuifsterkte aan het grensvlak zijn onderzocht. De teerhoudende antiskidlagen hebben minimaal 1,26 mm aan textuur diepte en kunnen deze textuur diepte behouden gedurende een lange levensduur. De verbeterde trekproef en afschuiftestmethoden zijn geschikt voor het evalueren van de hechting tussen dunne antiskidtoplagen en de onderliggende laag van het asfaltmengsel. De afschuifsterkte aan het grensvlak tussen de teerhoudende antiskidlaag en de onderliggende asfaltlaag is hoger dan de waarde aan het grensvlak tussen verschillende lagen van asfaltmengsels. De conclusies uit deze testresultaten worden als referentie gebruikt voor alternatieve antiskidwegdekken.

Ten tweede, nieuw ontworpen bindmiddelen, die worden beschouwd als mogelijke bindmiddelen voor antiskidbekledingen werden onderzocht. Copolymeer bitumenemulsie (MBE), 2-component gemodificeerde epoxyhars (MER) en 2-componenten epoxy bitumen (EMB) werden in beschouwing genomen. Het uithardingsgedrag, de directe treksterkte, de bestendigheid tegen hoge temperaturen, de weersbestendigheid en de relaxatie-eigenschappen bij lage

temperaturen werden onderzocht door middel van Directe Trekproeven, ovenveroudering en veroudering d.m.v. weatherometer, Dynamic Shear Rheometer test, Dynamisch Mechanische Thermische Analyse en relaxatieproeven. De testresultaten geven aan dat de onderzochte 2-component epoxy gemodificeerd bitumen als een geschikt bindmiddel kan dienen voor antiskiddekragen, met goede hoge temperatuurbestendigheid, voldoende relaxatiegedrag, voldoende treksterkte en voldoende vervormingsrek bij falen.

Ten derde, een van de onderzochte 2-componenten epoxy gemodificeerde bitumen werd vervolgens gebruikt voor het ontwerpen van antiskidlagen in het lab. De oppervlakte-eigenschappen, weerstand tegen treksterkte en afschuifsterkte werden vervolgens onderzocht. Geluidsreducerende dunne dekragen werden ook opgenomen in dit onderzoek. De resultaten tonen aan dat op EMB gebaseerde antiskidlagen betere hechting kunnen bieden aan het grensvlak dan teerhoudende antiskidlagen en op polymeer gemodificeerd bitumen gebaseerde antiskidlagen.

Ten vierde werden er Eindige Elementen Modellen van antislip verhardingen ontwikkeld voor de simulatie van de belastingstoestand voor stoeve oppervlaktelagen. De visco-elastische eigenschappen van EMB en MBE werden als input gebruikt. Uit de berekening blijkt dat de antiskidstructuur grote invloed heeft op het resulterende gedrag van het bindmiddel. De ontstane spanningen in het EMB bindmiddel zijn iets hoger dan in het MBE bindmiddel, terwijl de MBE is blootgesteld aan veel hogere maximale waarden voor 'principal strain' en afschuifspanning. Verder heeft het EMB bindmiddel een groter vermogen om te herstellen na belasting. Het steenskelet heeft een grotere invloed op de spanningen en vervormingen in het zachte MBE bindmiddel dan op de spanningen en vervormingen in het EMB bindmiddel.

Aan het einde worden enkele aanbevelingen gegeven voor verder onderzoek. Proefsecties in het veld en onderzoek naar de weerstand tegen brandstoffen worden voorgesteld. Vermoeiingseigenschappen en mechanica van het bezwijken worden ook aanbevolen om de schademechanismen te onderzoeken met EEM modellen.

ABBREVIATIONS

AC	Asphalt Concrete
AI	Ageing Index
BST	Black Surface Temperature
CROW	A Dutch technology platform for transport, infrastructure and public space
CRS	Cationic Rapid Setting bitumen emulsion
CT	Computerized Tomography
DMA	Dynamic Mechanic Analysis
DSR	Dynamic Shear Rheometer
DSS	Direct Shear Strength
DTS	Direct Tensile Strength
DTT	Direct Tensile Test
EMA	Ethylene Methacrylate
EMB	2-component Epoxy Modified Bitumen
EVA	Ethylene Vinyl Acetate
FOD	Foreign Object Damage
FAA	Federal Aviation Administration
FEM	Finite Element Model
FTIR	Fourier Transform Infrared
HMA	Hot Mix Asphalt, Hot Asphalt Mixture
HPTO	High Performance Thin Overlays
LDPE	Low Density Polyethylenes
LOT	Lifetime Optimization Tool
LVE	Linear Viscoelastic
LWT	Loaded Wheel Test
MB	Modified Bitumen
MBE	Modified Bitumen Emulsion
MER	Modified Epoxy Resin
MPD	Mean Profile Depth
NRTSL	Noise Reducing Thin Surface Layer
OGFC	Open Grade Friction Courses
OMMT	Organo-montmorillonite
PA	Porous Asphalt
PAHs	Polycyclic Aromatic Hydrocarbons
PFC	Porous Friction Coating
PSV	Polished Stone Value
RT	Relaxation Test
SBR	Styrene Butadiene Rubber
SBS	Styrene-Butadiene-Styrene
SHRP	Strategic Highway Research Program
SMA	Stone Mastic Asphalt
SPT	Sand Patch Test

TD	Texture Depth
TSL	Thin Surface Layers
TU Delft	Delft University of Technology
UTFC	Ultra-thin friction courses
UV light	Ultraviolet light
VOC	Volatile Organic Compound
WHUT	Wuhan University of Technology
WLF	Williams-Landel-Ferry equation

Table of Contents

1. Introduction	- 1 -
1.1 Background	- 1 -
1.2 Research Questions	- 2 -
1.3 Objectives of This Research	- 3 -
1.4 Organization of This Thesis	- 6 -
REFERENCES	- 7 -
2. Literature Review	- 9 -
2.1 Overview of TSLs	- 9 -
2.1.1 Surface Dressing.....	- 9 -
2.1.1.1 Advantages	- 10 -
2.1.1.2 Applications.....	- 11 -
2.1.1.3 Antiskid Surfacing.....	- 12 -
2.1.2 Slurry Seals	- 13 -
2.1.2.1 Advantages	- 14 -
2.1.2.2 Micro-surfacing	- 15 -
2.1.3 Thin Hot Mix Overlays.....	- 15 -
2.1.3.1 Novachip.....	- 15 -
2.1.3.2 Ultra-Thin Friction Courses	- 16 -
2.2 Thin Surfacing for Airfields	- 17 -
2.2.1 Research on Tar-containing Antiskid	- 17 -
2.2.1.1 Bonding Test	- 18 -
2.2.1.2 Raveling Test.....	- 19 -
2.2.2 POSSEHL ANTISKID	- 20 -
2.2.3 Super AirMat	- 21 -
2.3 Aggregates for Surfacing	- 21 -
2.3.1 Aggregate Shape	- 21 -
2.3.2 Aggregate Gradation	- 22 -
2.4 Binders for Surfacing	- 23 -
2.4.1 Bitumen Emulsion	- 24 -
2.4.2 Modified Bitumen Emulsion	- 28 -
2.4.3 Epoxy Modified Bitumen.....	- 33 -
2.4.4 Other Binders	- 36 -
2.4.4.1 Polyurethane Resins	- 36 -
2.4.4.2 Epoxy Resins	- 38 -

2.5 Modeling of Thin Surfacing	- 40 -
2.5.1 Different Modeling Levels.....	- 40 -
2.5.1.1 Macro-level.....	- 40 -
2.5.1.2 Meso-level.....	- 41 -
2.5.1.3 Micro-level.....	- 41 -
2.5.2 Macro-level Models.....	- 41 -
2.5.3 Meso-level Models.....	- 41 -
2.5.3.1 Idealized Models.....	- 42 -
2.5.3.2 Scan/photo Models.....	- 43 -
2.6 Summary	- 44 -
REFERENCES	- 45 -
3. Materials and Test Methods	- 49 -
3.1 Materials	- 50 -
3.1.1 Tar-Containing Antiskid Surface Layers.....	- 50 -
3.1.2 New Potential Binders.....	- 54 -
3.1.2.1 Two-Component Epoxy Modified Bitumen.....	- 54 -
3.1.2.2 Modified Epoxy Resin.....	- 58 -
3.1.2.3 Polymer Modified Bitumen Emulsion.....	- 59 -
3.1.3 Potential Antiskid Layers.....	- 60 -
3.1.4 Noise Reducing Thin Surface Layers.....	- 65 -
3.2 Tests on Binders	- 66 -
3.2.1 Ageing Evaluations.....	- 66 -
3.2.1.1 Oven Ageing.....	- 66 -
3.2.1.2 Weatherometer Ageing.....	- 66 -
3.2.2 Direct Tensile Test.....	- 68 -
3.2.3 Relaxation Test.....	- 70 -
3.2.4 Dynamic Shear Rheometer.....	- 71 -
3.2.4.1 Standard DSR Test.....	- 73 -
3.2.4.2 Column Shear Test.....	- 75 -
3.2.4.3 Master Curves.....	- 76 -
3.2.5 Dynamic Mechanical Thermal Analysis.....	- 77 -
3.3 Adhesion Tests	- 79 -
3.3.1 Pull Adhesion Test.....	- 80 -
3.3.2 Leutner Shear Adhesion Test.....	- 83 -
3.3.3 Failure Modes.....	- 85 -
3.4 Surface Characteristics	- 86 -
3.4.1 Texture Depth.....	- 87 -
3.4.2 Sand Patch Test.....	- 88 -
3.4.3 Microscope.....	- 89 -
3.4.4 CT Scan.....	- 90 -

REFERENCES	- 92 -
4. Set Benchmark by Evaluating the Properties of Tar-containing Antiskid Layers	- 95 -
4.1 Tar-Containing Antiskid Layers.....	- 95 -
4.1.1 Tar Detector	- 96 -
4.1.2 High Temperature Resistance	- 99 -
4.2 Surface Characteristics	- 101 -
4.2.1 CT Scans.....	- 101 -
4.2.2 Microscopy	- 105 -
4.2.3 Sand Patch Test	- 110 -
4.3 Aging Resistance	- 112 -
4.4 Modulus and Phase Angle	- 118 -
4.4.1 Sample Preparation.....	- 118 -
4.4.2 Frequency Sweep Test	- 119 -
4.4.3 Test Results	- 120 -
4.5 Adhesion Properties	- 123 -
4.5.1 Failure Modes.....	- 123 -
4.5.2 Leutner Shear Test Results.....	- 125 -
4.5.3 Pull Test Results	- 128 -
4.6 Tests from CROW	- 132 -
4.7 Benchmark Development.....	- 133 -
4.7.1 Benchmarks.....	- 133 -
4.7.2 Reliability and Number of Tests.....	- 134 -
4.8 Conclusions.....	- 136 -
REFERENCES	- 137 -
5. Rheological and Ageing Properties of Alternative Binders	- 139 -
5.1 Modified Epoxy Resin (MER)	- 140 -
5.1.1 Dynamic Mechanical Analysis	- 140 -
5.1.2 Direct Tensile Test	- 141 -
5.1.2.1 Curing Behavior	- 143 -
5.1.2.2 Direct Tensile Strength.....	- 145 -
5.1.3 Relaxation Test.....	- 147 -
5.2 Modified Bitumen Emulsion (MBE)	- 148 -
5.2.1 Curing Behavior	- 149 -
5.2.2 Dynamic Shear Rheometer	- 150 -
5.3 Epoxy Modified Bitumen (EMB)	- 155 -
5.3.1 Preliminary Tests.....	- 155 -

5.3.1.1 Curing Behavior	- 155 -
5.3.1.2 Dynamic Shear Rheometer Results	- 160 -
5.3.1.3 Direct Tensile Strength.....	- 164 -
5.3.1.4 Relaxation.....	- 166 -
5.3.1.5 Ageing Resistance	- 167 -
5.3.2 A3-UV Binder	- 170 -
5.3.2.1 Weatherometer Ageing.....	- 171 -
5.3.2.2 Dynamic Shear Rheometer.....	- 171 -
5.3.2.3 Dynamic Mechanic Analysis.....	- 174 -
5.3.2.4 Relaxation.....	- 176 -
5.4 Conclusions.....	- 178 -
REFERENCES	- 179 -
6. Tests on Newly Designed Antiskid Surfaces and Thin Surfaces	- 181 -
6.1 Test results on EMB-based Antiskid	- 181 -
6.1.1 Texture Depth.....	- 183 -
6.1.2 Tensile Strength	- 185 -
6.1.3 Shear Strength	- 187 -
6.2 Test Results on Schiphol Antiskid	- 188 -
6.2.1 Texture Depth.....	- 188 -
6.2.2 Tensile Strength	- 189 -
6.2.3 Shear Strength	- 192 -
6.3 Failure Energy	- 193 -
6.4 Thin Surface Layer.....	- 195 -
6.4.1 Tensile Strength	- 196 -
6.4.2 Shear Strength	- 197 -
6.5 CT Scan Results	- 199 -
6.6 Conclusions.....	- 201 -
REFERENCES	- 202 -
7. Finite Element Modeling of Surface Layers	- 203 -
7.1 FEM Methodology	- 203 -
7.1.1 2D Images for FEM Model.....	- 204 -
7.1.2 Antiskid Models.....	- 206 -
7.2 Loading Signals	- 207 -
7.3 Material Inputs	- 212 -
7.3.1 Binder inputs	- 212 -
7.3.1.1 Generalized Maxwell Model.....	- 213 -
7.3.1.2 Model Parameter Determination	- 214 -

7.3.2 Other Inputs.....	- 216 -
7.4 Results and Analyses.....	- 216 -
7.4.1 Influence of the Antiskid Structures	- 218 -
7.4.2 Influence of the Binders	- 220 -
7.4.3 Principal Stresses and Strains	- 223 -
7.5 Conclusions.....	- 225 -
REFERENCES	- 225 -
8. Conclusions and Recommendations.....	- 227 -
8.1 Conclusions.....	- 227 -
8.1.1 Benchmark Development.....	- 227 -
8.1.2 Research into Alternative Binders	- 228 -
8.1.3 Properties of Newly Designed Antiskid Layers.....	- 230 -
8.1.4 FEM Analysis.....	- 230 -
8.1.5 Noise Reducing Thin Surface Layers	- 231 -
8.2 Recommendations	- 231 -
Appendix	- 233 -

1. Introduction

1.1 Background

The (treatment of a) pavement surface is very important from a user's point of view. In many situations, the load bearing capacity of the pavement can be entirely met by the structural layers under the surface layers, while the surfacing layer can be optimally designed to meet specific road-user requirements, such as noise reduction, high friction also in wet condition, ride quality and durability.

In addition, surface layers can protect pavements against external aggressive substances such as spilled oil, gasoline, hydraulic fluid, organic solvents and compounds, deicing chemicals, etc. They can furthermore protect bituminous pavements against negative effects due to weather and ageing caused by ultraviolet (UV) light and oxygen.

An antiskid surfacing is one type of such a specially designed surface layer. It refers to a road surface treatment in which high-friction aggregates with a high Polished Stone Value (PSV) are used, together with binder to bind the aggregates to the road surface. Usually it is an expensive material, but it is particularly used in areas like crossings, roundabouts and access slopes of parking garages where a high friction is required and is more durable than regular surface layers. In antiskid surfacings for road pavements mostly bitumen based binders are used.

In the Netherlands, antiskid surfaces are mainly used for airport runways. Airport runways can get slippery because of snow, ice, water and rubber deposits and these conditions should be avoided at all costs to enhance safe aircraft operations [1]. Therefore, the macrotexture of an antiskid layer should be high enough and the aggregates should have a high microtexture. Good friction is useful for safe landing at a runway particularly when the runway is moist or wet. Excellent adhesion properties are necessary for binding the aggregates together and to the surface. All in all, binders with a high adhesion to aggregates are required.

Besides a high adhesion, the antiskid surface on runways also requires a good fuel resistance, because on runways, fuel spillage happens quite frequently. Unfortunately, most bitumen based materials do not have such a good resistance. Bitumen based materials can easily be affected by gasoline and oil drippings, salt and chemicals. Furthermore, bitumen based materials can be gradually damaged and eventually aged due to thermal, UV and oxygen induced oxidation.

Tar based materials have several advantages over bitumen based materials. Tar-containing surface layers, unlike bitumen based materials, are inherently resistant to chemicals from outside and have better adhesion properties, due to

the unique chemical and molecular structure of refined tar. Regular application of coal tar emulsion pavement sealers did protect the pavement surface and extended the service life of pavements. The better fuel resistance and adhesion were the main reasons for the extensive use of tar-containing antiskid surface layers on runways in the Netherlands.

Tar-containing materials are toxic and carcinogenic because of their high Polycyclic Aromatic Hydrocarbons (PAHs) content. In the Netherlands and many other European countries, the use of tar in pavement applications is not allowed anymore because of environmental concerns. The only temporary exception for the use of tar was on antiskid runway surfaces for airport applications (See Figure 1-1). However, also this application is not allowed anymore since 2010. Therefore, alternatives to replace tar-containing antiskid runways were urgently required. Research on this topic has been done previously [2, 3], and this thesis is building on these earlier research findings.



Figure 1-1 Construction of an antiskid runway surface in the airfield

1.2 Research Questions

In 2004, a CROW¹ working committee was founded in the Netherlands with the task to determine if there were any existing surface layers or coatings available that were qualitatively comparable to tar-containing antiskid surfaces. Six existing materials for surface layers and coatings were selected, and compared with tar-containing antiskid surface layers. The result was that none of those possible alternative surface layers achieved the same results on all properties as the tar-containing antiskid layer.

It was concluded that, instead of using these existing thin surface treatment technologies, new materials were needed to replace tar-containing materials for antiskid layers on runways. By considering this goal, one of the major questions

¹ CROW: The Dutch technology platform to provide professional technical and specialized knowledge about infrastructure, traffic, transport and public space, <http://www.crow.nl>.

for this research was formulated, namely how to determine which material can be used to replace the tar-containing material in antiskid thin surfaces for airfield runways.

In order to answer this question, it is necessary to consider first the following sub questions:

- Q1: What are the properties of the tar-containing binder that is currently used for antiskid layers on airfield runways?
- Q2: What are the most important properties to be determined for new potential binders? What are the requirements for these important properties? Are all requirements equally important?
- Q3: How can we measure these properties?
- Q4: How can we relate the test results that are obtained in the lab to field performance?
- Q5: What materials can be used to replace tar-containing materials for antiskid layers?

Because the application of antiskid layers on runways and thin high friction surfaces on road pavement are quite similar, the question was also raised if we can expand the usage of such materials to road pavements. This is a very important question, because if producers can develop materials for a larger market, they could be much more interested. Therefore, two additional sub questions were raised:

- Q6: Can we use these materials for high friction thin surfaces on road pavements?

With respect to answer Q6, another sub question, which is also important for designing durable and sustainable thin surfaces for road pavement, arose, which is:

- Q7: What are the most important properties for materials to be used for thin surfaces on road pavement?

Summarizing these 7 sub questions leads to the main question of this research, which is how to determine a given material is applicable to design durable and sustainable thin surfaces for pavements and runways? This main question can be answered by answering the seven sub questions.

1.3 Objectives of This Research

Generally speaking, the objectives of this research are to answer the seven sub questions that are mentioned in the previous section. In order to be able to do so, two research projects were carried out, which are both part of this PhD study. Both projects were supported by CROW, Amsterdam Airport Schiphol and the Dutch Ministry of Defense [4].

The aim of the first project was to develop benchmarks for binders to be used in antiskid runway surfaces. The tar-containing binders used in these layers

were produced by the POSSEHL Company and are patent protected. It was not possible to get the pure binder and fresh antiskid samples from them for testing. In order to be able to test the antiskid layer, cylindrical cores with tar-containing antiskid layers on top were collected from six military airports in the Netherlands. Tests were designed to determine the properties of these materials. Benchmarks were developed from these test results [5].

The second project was carried out to verify the requirements that were concluded from the first project. In the meantime, new materials for antiskid layers were investigated. Potential binders were supplied by several Dutch companies and antiskid layers were constructed with these new binders [6, 7].

Figure 1-2 shows the research outline for this PhD study. It has three main parts. Part One is a general research plan for the first project. Many tests are included to answer questions Q1 to Q4. Surface macrotexture, structure characteristics, bonding strength and ageing resistance properties of tar-containing antiskid layers were determined. A pull test and a shear test were developed to investigate the tensile bonding strength and shear strength between the thin surface layer and the underlying layer.

Part Two is a test plan for the second project that was needed to answer question Q5. Tests used in Part One were reviewed by using new binders and antiskid surfaces. The new binders include a 2-component epoxy modified bitumen and a high content co-polymer modified bitumen emulsion. Additionally, the resistance to weathering and ageing were investigated. Rheological properties of the pure binders were tested to understand their behavior at both lower and higher temperatures. FEM simulations were carried out at meso-level using the properties derived from these new binders. All results obtained on these new binders were compared with the benchmarks developed in Part One.

Part Three is aimed at providing answers to Q6 and Q7. A typical road pavement structure with a thin noise reducing surface layer on top was analyzed using the results of pull tests and shear tests.

From the research outline, one can clearly see that this PhD research is highly inspired by practice and practice has also supported this research significantly. The author is therefore very grateful for all the supports he received. The big problem however was that only a limited amount of cores from runways could be obtained by the Ministry of Defense and Amsterdam Schiphol Airport. This is understandable because (unnecessary) core holes should of course be avoided as much as possible on operational runways. Therefore a compromise had to be found between the desired number of cores and the number of cores that could be made available. The number of cores that were made available is a reasonable number, but for more real research in depth more material would have been needed.

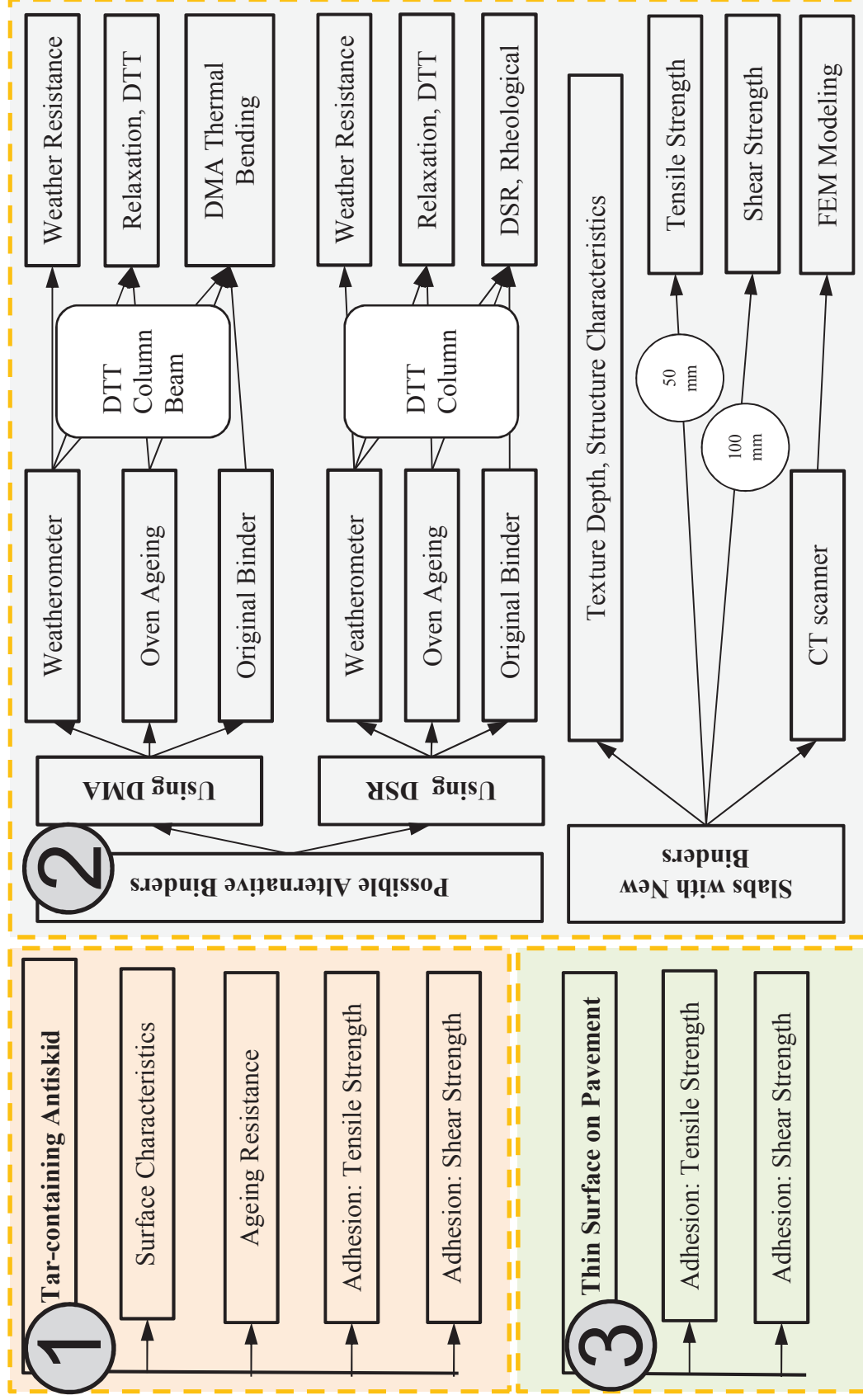


Figure 1-2 Outline of the research approach towards antiskid surface applications

The second problem was that all the materials investigated in this research are patent protected. Because of this no information could be obtained from one supplier, while the other suppliers provided some information that was very helpful but did not give full details about their materials because of commercial reasons. Although this is very understandable, it had of course an adverse effect on the depth of this research.

1.4 Organization of This Thesis

According to the research outline shown in Figure 1-2, this dissertation can be divided into three research parts, which are research on tar-containing antiskid layers, research on possible alternative binders, and FEM simulations to determine the performance of the investigated binders in antiskid applications on runways.

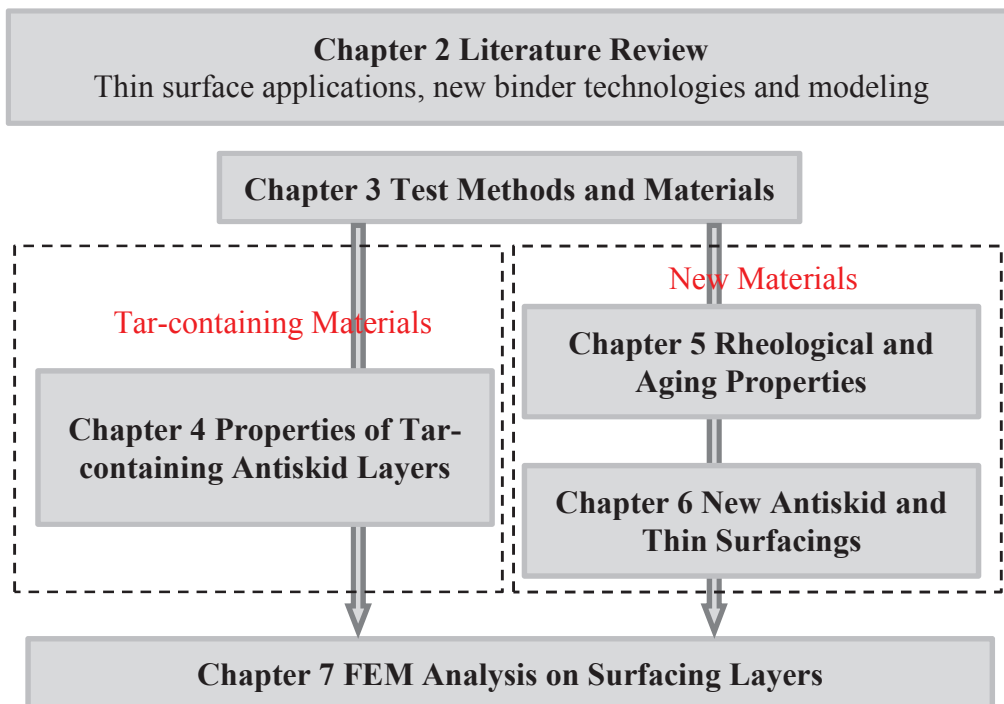


Figure 1-3 Outline of this dissertation

Figure 1-3 gives a flow chart of the outline and organization of this thesis. After this introduction chapter and is used to introduce the contents of this thesis. Chapter 2 gives a literature review on thin surface layer applications, new technology on binders and research methods that are used to test surface treatments. Chapter 3 includes information about the materials that are used in this research as well as the test methods.

In chapter 4, the test results obtained on the tar-containing antiskid layers are presented. These results include the surface characteristics, adhesion

properties, and ageing resistance. Adhesion property here means the adhesion at the interface between the top layer and the underlying layer.

Chapter 5 and Chapter 6 focus on the properties of potential alternative binders and their application. Antiskid surfaces made with these binders were placed on a layer of a reference asphalt mixture. Several tests were performed to investigate the adhesion between the antiskid layer and the asphalt mixture. Chapter 5 presents the rheological and ageing properties of the alternative binders, and Chapter 6 shows the adhesion properties of the antiskid layers made with the alternative binders.

Chapter 7 demonstrates the results of Finite Element Modeling performed on the antiskid surface layers. The obtained stress and strain distributions in the binder under vehicle loading are discussed.

Chapter 8 presents the conclusions and recommendations.

REFERENCES

1. EAPA, *Airfield Uses of Asphalt*, in Ref: (3)2-03-00.015. 2003, European Asphalt Pavement Association.
2. Xiao, Y., *Literature Review on Possible Alternatives to Tar for Antiskid Layers*, Report No. 7-10-185-1. 2010, Delft University of Technology.
3. Leest, A.J.v. and G. Gaarkeuken, *Resistance of surface layers on airfields in the Netherlands-in situ and laboratory testing*, in *2005 European Airport Pavement Workshop*. 2005.
4. CROW, *D11-01 Specification for Runway Surface Dressings on Airfields*. 2011: the Netherlands.
5. Xiao, Y., et al., *Assessment Protocol for Tar-containing Antiskid Layers for Runways*, Report No. 7-10-185-2. 2010, Delft University of Technology.
6. Xiao, Y., M.F.C.v.d. Ven, and A.A.A. Molenaar, *Investigation on ICOPAL Antiskid Surface-Layer-type 1, Alternative for Tar-containing Antiskid*, Report No. 1-12-185-3. 2012, Delft University of Technology.
7. Xiao, Y., M.F.C.v.d. Ven, and A.A.A. Molenaar, *Investigation on Schiphol Antiskid Surface Layer-Alternative for Tar-containing Antiskid*, Report No. 1-12-185-4. 2012, Delft University of Technology.

2. Literature Review

A major objective of this research was to either identify or develop a method to select particular binders that can be used for thin layer applications, mainly for antiskid surfacings. In order to achieve this objective, the current state of knowledge with regards thin surface layers is reviewed in this chapter. At the same time, the focus is on the latest research on binders and new application technologies for thin surface layers (TSLs).

In this research, include surface dressings, slurry seals and thin asphalt mixture surfacings, which are applied on road pavements, runways and bridge decks to improve the skid resistance properties in the tire-pavement surface interface.

2.1 Overview of TSLs

Thin surface layers are treatments applied to the pavement surface that increase the pavement thickness by less than 40 mm. In some situations, the load bearing capacity of the pavement can be entirely met by the structural layers, while the surfacing layer can be optimally designed to meet specific road user requirements. Application of this concept has given rise to a new class of thin or ultra-thin surfacings. Thin surfaces are specially designed to provide significantly improved surface properties of pavement and bridge decks in terms of skid resistance, noise reduction and durability, without significantly affecting other characteristics of the surface such as ride quality. The surface characteristics of aggregates used for TSLs have significant influence on the skid resistance and rolling resistance [1].

Thin protective surfacing materials can be used to increase durability and improve safety on road pavements. A thin surface protects the treated pavement against attacks from spillage of oil, gasoline, hydraulic fluid, organic solvents and compounds, de-icing chemicals, etc. It can protect bituminous from the degrading effects of weather, and also protect concrete pavements and bridge decks from chloride attack.

There are many types of thin surface layers, such as surface dressings, slurry seals and thin asphalt mixtures.

2.1.1 Surface Dressing

A surface dressing, also named as surface seal, seal coat, seal, chip seal and surface treatment [2], is a quick and convenient method of rejuvenating a surface

which is beginning to show signs of damage. When applied in time, surface dressings eliminate the need for replacement of the existing wearing course and therefore reduce maintenance costs. Bitumen emulsion sprayers and aggregate spreaders are used to lay down the seal coat. It is used to improve pavement surface performance, to form a fresh wearing course and to improve the friction of the pavement surface. It can be used to treat both lightly and heavily trafficked roads. The surface of all classes of roads, ranging from single tracks, unclassified roads and footpaths to national high speed motorways can and have been successfully treated in the past in this way.

2.1.1.1 Advantages

A Surface dressing is a long established and proven highway maintenance technique. In simple terms, the application of a surface dressing is as follows. First a hot bitumen or cold bitumen emulsion is sprayed onto the road surface with a spray tanker followed immediately by spreading high quality aggregate chippings (see Figure 2-1). Then rollers are applied to ensure proper embedment of the aggregate into the binder. A surface dressing is an economical way to provide the pavement with a water impervious seal with the added benefit of a much-improved surface texture and increased friction coefficient (wet).



Figure 2-1 Bitumen emulsion is sprayed onto the pavement for surface dressing

Surface dressing is an extremely cost-effective surface maintenance treatment when properly designed, specified and executed and when applied at the right moment in time. Advantages of surface dressing are [2]:

1. Sealing the road surface against moisture damage which is known to be one of the major causes of asphalt pavement deterioration.
2. Stopping the deterioration of the pavement surface.
3. Reducing spray caused by vehicles travelling on wet road surfaces.
4. Restoring the necessary level of skid resistance of the road surface which results in a reduction of skid related traffic accidents.
5. Enabling treated surfaces to last longer thereby increasing service life before maintenance is required.

6. Maximizing the cost effectiveness of limited highway maintenance funds. The cost for a surface dressing is lower than for a traditional asphalt surfacing.
7. Specially designed ‘quiet’ surface dressings can be used to reduce the road noise generated by traffic, although the level of noise reduction that can be achieved is much smaller than that of porous asphalt.
8. It only takes a very short time to apply the surface dressing, which means disruption to road traffic and local services is minimized.

Furthermore, proper attention to design and construction has provided surface dressings with a lifetime of over 10 years, even on very heavily trafficked areas.

2.1.1.2 Applications

Surface dressings should be applied before the road surface deteriorates to the stage at which expensive major patching and/or reconstruction is required. It should be carried out before the skid resistance of the surface falls below the acceptance level set for the road.

Applications can be made in one or two layers as well as in combination with other surface treatment techniques such as slurry seals to achieve the desired result. Surface dressings can be constructed in a number of ways to suit site conditions. Selection of the suitable surface dressing method depends on the condition of the pavement and traffic conditions. The most commonly used surface dressing types are listed below [3]:

1. Single surface dressing: used on light and medium trafficked roads where the pavement damage is still slight or moderate and more or less uniformly distributed over the pavement’s area.
2. Single surface dressing with double application of chippings and single surface dressing with pre-coated aggregate: used on heavily trafficked roads, crossings, sharp curves and slopes.
3. Double surface dressing: used on strongly damaged surfaces showing raveling, cracks, unevenness and on heavily trafficked roads.
4. Double surface dressing with pre-coated aggregate: on gravel roads and heavily damaged asphalt pavements;
5. Surface dressing with crushed gravel and all-in aggregate (meaning sand and coarse aggregate combined): on gravel roads and roads with light traffic.

Single Surface Dressing

A single surface dressing is constructed by spraying a bitumen emulsion or hot bitumen onto the existing pavement surface followed by spreading a layer of fine aggregates. The upper part of Figure 2-2 shows the construction steps of a single surface dressing. For heavily loaded roads a double dressing is a more durable solution than a single dressing [4, 5].

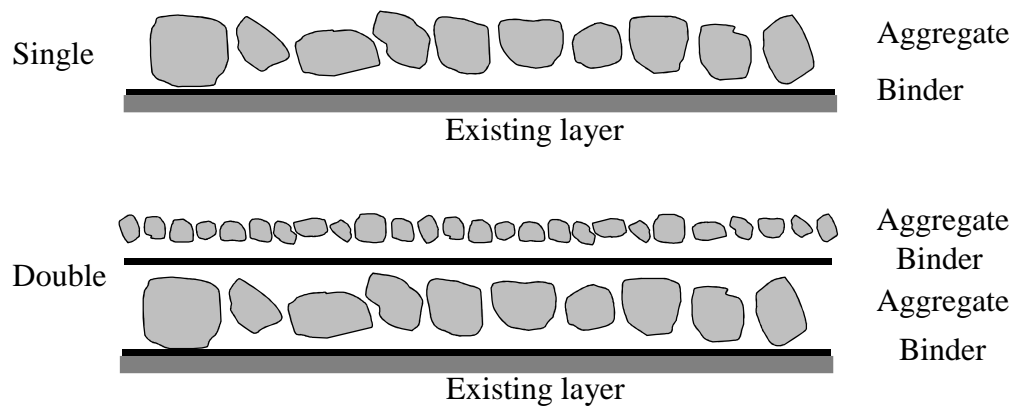


Figure 2-2 Construction steps of single and double surface dressing [5]

Double Surface Dressing

As the bottom graph in Figure 2-2 shows, a double surface dressing is applied in two steps. A layer of single size chippings is applied after the first spray application of bitumen emulsion to form the bottom layer. Then this single size chipping layer is dressed with an additional sprayed layer of binder and fine single size chippings to form a final surface layer. This surface dressing method can be used for pavements that only need a seal as driving surface where has low traffic volume. It can also be used on existing pavement surfaces to enhance the durability and minimize the frequency of maintenance in (sub)tropical countries [5].

Other Surface Dressings

Besides single and double surface dressing, there are many other types of surface dressings used in different situations [5].

A triple surface dressing is typically used for pavements where a new road is expected to carry high traffic volumes. A third layer of small chippings is then applied on a double surface dressing. This layer will reduce noise generated by traffic and the additional binder will ensure a longer service life.

Sandwich surface dressings (a layer of chippings is spread prior to a single surface dressing being applied) are principally used on existing binder rich surfaces [6].

2.1.1.3 Antiskid Surfacing

An antiskid surfacing is a special surface dressing with high skid resistance. The high skid resistance is achieved by using aggregates that produce a high friction between the tyre and the pavement surface and have a high Polished Stone Value. Sometimes artificial aggregates such as steel slag are used. A binder (modified bitumen, epoxy and polyurethane) is used to bind the aggregates to the road surface. Such surfacings are more expensive but also more

durable than a surface dressing, and are therefore used on areas such as crossings, roundabouts and runways where a high skid resistance is required. Moreover, Liu also claims that antiskid surfacings have noise reduction capabilities [7, 8].

Figure 2-3 shows a high macrotexture antiskid surfacing on a runway (left picture) and a colored antiskid surfacing at a traffic light area (right picture).



Figure 2-3 Antiskid surfacing on runways (left) and colored antiskid surfacing at a traffic light area (right)

Aggregates used for antiskid layers need to be hard aggregates that are not likely to crush under heavy loads. They should retain the sharp edges and facets, which were produced at the time of crushing, during their service life. Basalt and bauxite are normally used for this purpose.

In specific cases, antiskid surfacings may be given a different colour to the road surface such as red and yellow. These colored antiskid surfacings are constructed by using colored aggregates (e.g. bauxite) or pigmented binders. Colored surfaces are used for traffic calming, speed reduction and hence prevent accidents from happening. Colored antiskid surfacings can also warn drivers of dangerous sections, and mark different functional zones, such as parking lots, pedestrian crossings and walking paths.

2.1.2 Slurry Seals

Slurry seals are mixtures of bitumen emulsion, fine mineral aggregate, filler, water and specific additives. These materials are mixed in special designed proportions, and then uniformly spread over the prepared surface. The completed slurry seal is a relatively homogeneous material, which firmly adheres to the prepared surface. Slurry seals are similar to micro-surfacings, but the mineral skeleton does not need to have the high crushing resistance as the skeleton for the above mentioned antiskid layers. The reason is that the skeleton for slurry seals has limited interlocking of the aggregate particles [9]. Consequently, slurry seals are applied in thin overlays (thickness varies from 3 mm to 20 mm) to avoid permanent deformation caused by traffic.

According to the International Slurry Surfacing Association, application of slurry seals can significantly extend the life of existing pavements by protecting the underlying layers against ageing and the environment. They also will fill smaller cracks.

2.1.2.1 Advantages

Slurry seal technology can be applied on highways, streets, parking lots etc. Like surface dressings, slurry seals have the following advantages:

1. It is very quickly open to the traffic: after about half an hour the road can be reopened to traffic.
2. It can repair smaller defects of the pavement, such as small cracks and light raveling.
3. With the limited thickness of slurry seal, no adjustments of the surrounding pavements because of height differences are needed.
4. By considering its price and lifetime, it is a cheap method for improving the durability and appearance of the pavement.

The thickness of a slurry seal layer depends on the aggregate size and usually ranges from 3 to 20 mm. Layers with approximately 10 mm thickness are mostly used. Slurry seals with finer aggregate are used on roads and parking lots with low traffic levels, whereas slurries with coarser aggregate are used on roads with heavier traffic levels. Depending on the aggregate size, the rate of application is 4-14 kg/m². To manufacture and spray the slurry seal, special equipment mounted on a truck is used [9, 10]. Figure 2-4 shows how slurry seals are applied.

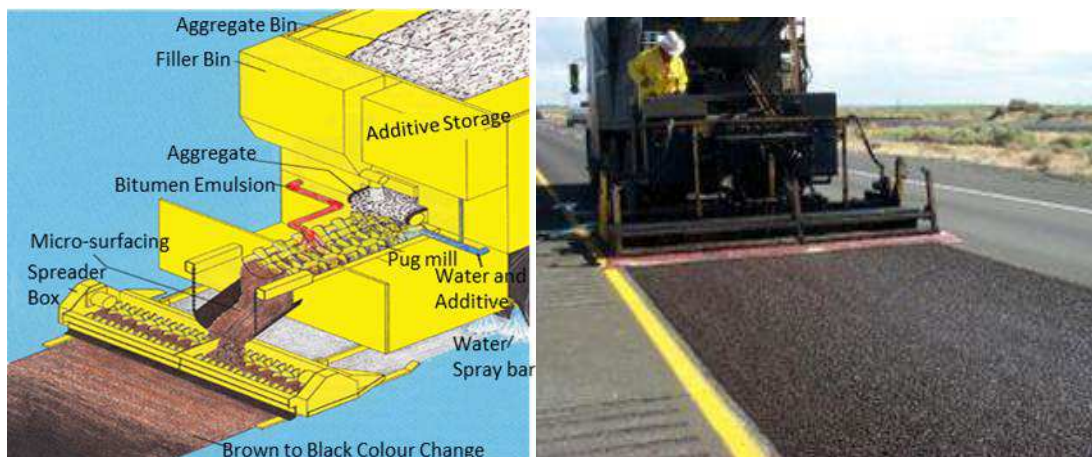


Figure 2-4 Placement of a slurry seal^{1,2}

¹Pavement Interactive -Slurry Seals: http://pavementinteractive.org/index.php?title=Slurry_Seals

²Micro surfacing: <http://www.blacklidgeemulsions.com/micro-2.htm>

2.1.2.2 Micro-surfacing

Micro-surfacings are advanced forms of slurry seals that use the same basic ingredients and combine them with advanced polymer additives¹. They are applied to restore and preserve the surface characteristics of pavements. Micro-surfacings are designed to correct rutting, improve inadequate pavement cross profiles, and enhance frictional properties of the pavement surface.

Slurry seals are used to cover the entire surface, while micro-surfacings are normally applied to fill minor wheel ruts. Micro-surfacings are low-cost preventive maintenance treatments that prevent deterioration of the pavement, maintain or improve the functional condition of roadways, and extend the service life of the pavement when applied to suitable candidates.

The placement of a Micro-surfacing system on medium to high traffic roads offers a competitive alternative to traditional methods of restoring surface characteristics of roadways. The life of the pavement is extended by 4 to 8 years [11].

2.1.3 Thin Hot Mix Overlays

Both thin hot mix overlays and slurry seals are thin asphalt mixture overlays. The difference is that thin hot mixture surfacings can enhance the structural quality to a limited extent as well as the ride quality and skid resistance. Slurry seals do not contribute to the structural strength of the pavement.

Thin asphalt mixture overlays include thin surface layers with a thickness between 25 mm to 40 mm. Ultra-thin surface layers have a thickness less than 25 mm and are assumed not to contribute to the structural strength.

Typical thin mixture surfaces include High Performance Thin Overlays (HPTO), Open Grade Friction Courses (OGFC), Stone Mastic Asphalt (SMA) surface layers and Graded HMA surface layers. In some particular situations, thin mixture surfaces like Ultra-thin overlays, Novachip and Ultra-thin friction courses (UTFC) were utilized to restore and preserve pavements by improving the skid resistance. They can also correct ruts and protect the pavement surface [12-14].

2.1.3.1 Novachip

Novachip was originally developed in France in 1986 and was introduced into the United States in 1992. Novachip is a thin modified bitumen based hot mix layer. First, a layer of modified emulsion is sprayed on the road surface to form a membrane, and within seconds, a layer of Hot Mix Asphalt (HMA) is applied on the emulsion, see Figure 2-5. At that moment, the water driven from the emulsion cools the HMA, setting both materials and providing bond to the underlying surface. Compaction is the final step in this process [12, 13].

Unlike surface dressings, slurry seals, micro-surfacings and hot mixed materials, Novachip combines a surface seal with a level paving surface, resulting in a negative textured surface, which is very good for noise reduction.. The layer thickness of Novachip ranges from 10 to 20 mm, depending on the maximum size of the aggregate.



Figure 2-5 Specifically designed paving equipment and thickness of Novachip

Russell [13] did pavement condition survey on Novachip after it has been applied for 8 years. They reported that the reported that Novachip was effective in reducing both the frequency and severity of cracking. Novachip is ideal for both urban areas and high traffic volume areas where other preventive maintenance treatments could have application problems.

Advantages of Novachip are the following. Novachip adheres (sticks) very well to the underlying asphalt layer. It provides a surface with high friction and can reduce the traffic noise and hydroplaning. The bitumen membrane prevents moisture damage in the underlying asphalt layer. The pavement can be reopened for traffic within 15 to 20 minutes.

Disadvantages of Novachip are that it is only recommended for flexible pavements. Like most surface layers, the service life of Novachip may be substantially reduced due to cumulative distresses within the existing pavement structure. During application, Novachip needs specifically designed paver equipment which makes it more expensive and results in higher initial cost. Because of the very thin layer, the pavement surface temperature and the ambient temperature shall not be lower than 8 °C when applying Novachip.

2.1.3.2 Ultra-Thin Friction Courses

The principle of UTFC was developed in France in the early 1990s. UTFC is a very thin, 15 to 20 mm thick asphalt layer that is laid by spraying a thick tack-coat to the road surface all in one pass, similar to the Novachip concept. It was initially produced as an alternative to slurry seals [14].

The rapid construction of UTFC can ensure an early reopening of the road. It gives a better smoothness compared to slurry seals. Furthermore, it can reduce

traffic noise and water spray during rain. Similar to Novachip, UTFC needs a special paver which results in higher initial cost.



Figure 2-6 UTFC applications and its surface

2.2 Thin Surfacing for Airfields

One of the most important functions of runway pavement surfaces is to guarantee sufficient friction between the tire and the runway surface. There are several ways to achieve this. One way is to apply a grooved asphalt surface. Grooving also protects aircrafts from hydroplaning by letting the water film flow into the grooves. Even in wet weather, the peaks between the grooves will still be in contact with the aircraft tires. Existing pavements may have surfaces that are not suitable for sawing grooves. Grooves will often lead to raveling, are unnecessary when an asphalt mixture is used as the surface layer. But the raveling is not wanted on airfield runways at all [15].

Another way to maximize friction is using chip or slurry seals to provide sufficient friction and other properties. Antiskid surfaces however are a widely used solution. Nowadays, the development of new surfacings has been followed by improvements in mechanical tests for bituminous binders as well as in specifications and surface layer design procedures. Guidelines have been developed based on various special binders, which can be used to lead to new binder solutions for airfield runway applications.

2.2.1 Research on Tar-containing Antiskid

In 2001, a CROW working committee has been set up in the Netherlands to establish whether there are any existing surface layers or coatings that are qualitatively comparable to tar-containing antiskid surfaces [16]. The precondition for the selection of the potential alternatives was that they had to be existing products and be proven techniques for surface layer. Five alternative systems for surface layers and coatings were selected and compared to tar-containing antiskid layers.

Bonding tests, raveling tests and steel brush tests (kerosene resistance) were performed in this research. The results showed that none of the six selected possible alternative surface layers that were tested achieved the same results on all properties as the tar-bearing antiskid. The alternative coatings were comparable on skid resistance and texture depth, but their raveling and chemical resistance was substantially lower [16, 17].

2.2.1.1 Bonding Test

This test was only conducted on the tar-containing antiskid surfacing (POSSEHL ANTISKID), tarless antiskid surfacing and surface coatings with epoxy binder. Tarless antiskid surfacing is a new surface coating developed by the Possehl company that can be compared to the tar-containing antiskid but with a tarless bituminous binder. This coating meets the specified requirements (skid resistance, texture depth and environmental standards) [16].

Holes with 9 centimeters diameter were cored in the pavement to a depth of 20 mm so that the core penetrates through the surface coating. Steel plates were glued to the dry surface with a quick-hardening adhesive. Once the adhesive was dry, the antiskid layer was removed and the tensile force measured. Figure 2-7 shows the test set up and the failed surfacings.



Figure 2-7 Setup for bonding tests (left) and examples of tested surface coatings

The results of the failure load measured during the bonding strength test on the pavement depend on aspects that include the ambient temperature. The temperature was assumed to have no effect on the tensile strength tests on the epoxy, while a temperature correction was made for the tar-containing antiskid.

The average failure stresses are presented in Table 2-1. The tar-containing antiskid surfacing and the tarless modified bitumen surfacing were pulled entirely free from the underlying pavement. In the case of the epoxy coating, the aggregate was pulled away from the surface coating that stuck to the underlying layer. The results of the coating on epoxy basis are comparable to tar-containing antiskid. The results for the tarless surfacing were clearly poorer [16].

Table 2-1 Average failure stress from CROW pull test

Surfacing types	Average failure stress [MPa]
Surface coating with epoxy binder	1.34
Surface coating with tarless modified bitumen	0.64
Tar-containing antiskid	1.14

2.2.1.2 Raveling Test

The raveling test is used to expose the pavement surface to repeated shear stresses. A ring-shaped rubber load plate (outside diameter 200mm, inside diameter 100mm) is placed on the asphalt and rotated repeatedly. The weight of the apparatus was set at approximately 500 kg (based on a friction coefficient of 0.5-0.7). Figure 2-8 explains the setup that was used for the raveling test. Figure 2-9 shows the results of raveling tests on three different coatings at the same rotation frequency and rotation time [16]. The raveling resistance of bituminous binder coatings without tar is the poorest. Unfortunately, the raveling resistance of tar-containing antiskid layer is not available in the references.

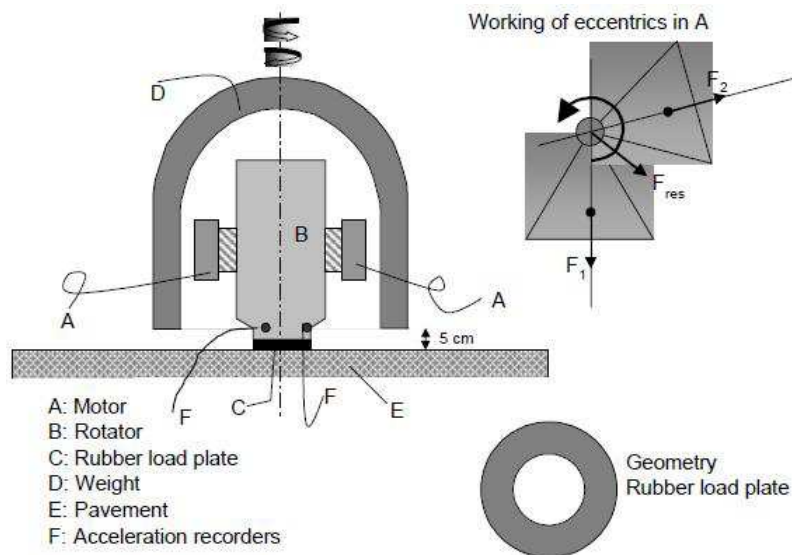


Figure 2-8 Asphalt raveling tester setup



Figure 2-9 Results of raveling test on three different coatings

2.2.2 POSSEHL ANTISKID

POSSEHL ANTISKID is a thin high-friction surface that is used on airport runways to give a high friction and guarantee safety during take-off and landing. It is a patent protected technology owned by company POSSEHL SPEZIALBAU in Germany³. The POSSEHL ANTISKID Surface Treatment has a lifespan of approximately 8 to 15 years or longer (claim from the company). Since 1956, it has been applied on more than 130 runways at national and international airports and has proven itself as an excellent protective high-grip surfacing system.

From a pavement technical point of view, the most important characteristics of POSSEHL ANTISKID are as follows [18]:

1. High friction coefficient on new runways and high-speed exit taxiways when wet.
2. Reduced aquaplaning danger through improved drainage of the water under the tires due to the pronounced macro texture of the surfacing; considerably higher effective drainage capacity in comparison with grooving, retaining the same high friction over the entire surface.
3. Local penetration of the water film through high macrotexture provides direct contact between the tires and the pavement surface.
4. Resistance against aircraft fuel, chemical de-icing agents, heat and jet engine exhaust streams.
5. Savings on de-icing material of up to 80% are possible.
6. Minimized danger caused by foreign object debris, because specially graded aggregate with a maximum aggregate size of 3.5 mm and a tar-containing binder, which provides excellent adhesion, are used.

Test results obtained on POSSEHL ANTISKID will be discussed in Chapter 4. Although POSSEHL ANTISKID can provide very good service from a technical point of view, it is a non-environmental friendly tar-containing material.

³POSSEHL ANTISKID® Surfacing, <http://www.possehl-spezialbau.de>

2.2.3 Super AirMat

Recently, new technologies have been developed to provide sustainable surface layers for runways. Super AirMat has been designed especially for airfields, by Nynas Bitumen UK. It is a very durable asphalt material that holds the aggregate firmly in place. It was laid for the first time on a runway in the UK by Bardon Contracting in October 2005. Resurfacing runways using Super AirMat helps airport authorities to prolong the life of the pavements and ensures the highest standards of safety for aircraft.⁴

Super AirMat [19, 20] contains a 10 mm nominally sized gritstone with a very high polished stone value. A polymer modified grade of bitumen (Nynas Bitumen's durable binder Nypol TS) was used in Super AirMat to bind aggregates together. It is designed to provide for good adhesion and cohesion with the stone. Cellulose fiber was added to the asphalt mix to achieve extra durability. Because the cellulose fiber can prevent drain down of mastic, as well as enhance the direct tensile strength in the mortar.

2.3 Aggregates for Surfacing

The ability of the road surface to provide a high skid resistance is a combination of the surface texture and the micro texture on the aggregate itself. The resistance against polishing of the microtexture is expressed in the PSV (Polished stone Value) of the aggregate in the road surface. Higher PSV values usually result in a higher resistance to polishing of the aggregates. Most hard aggregates such as gravel, crushed stone, and crushed slag can be used successfully as aggregate for surface treatments, however also the right combination of harder and softer minerals in the aggregate can give very good results. In practice, natural gravel and crushed stone are typically used. The selected aggregate, must meet certain requirements in size, shape, cleanliness, crushing resistance and surface properties.

2.3.1 Aggregate Shape

Aggregate shape can be described as either flat or cubical. It can also be either round or angular. These shapes will affect the TSL in different ways. If an aggregate is flat, the seal coat will lose chips excessively in the non-wheel path area of the road bed, or it may bleed in the wheel path. This is due to the pressure from traffic tires causing the flat chips to settle into the binder on their flattest side, failing to increase the road surface friction. The TSL becomes thinner at the places where the tires pass. Aggregate with a Flakiness Index of 20% or lower should be used for high volume roads⁵.

⁴Super AirMat by Nynas: http://www.nynas.com/templates/Page_8898.aspx?epslanguage=EN

⁵Bituminous Surface Treatments: <http://pavementinteractive.org/index.php?title=BST>

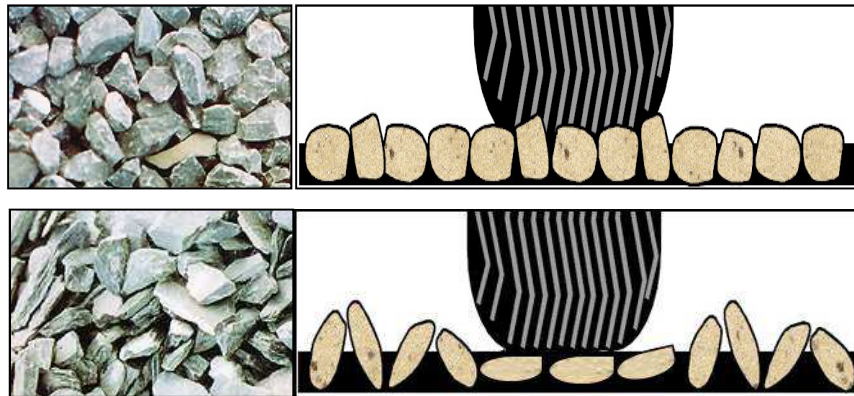


Figure 2-10 Superior cubical aggregates (up-left) and flaky aggregates (bottom-left); traffic influence on cubical aggregates (up-right) and flake aggregates (bottom-right)

Therefore, the preferred aggregate shape is cubical because of its stability. With cubical aggregates, traffic will not affect the chip orientation. No matter how the chips are oriented, the seal coat height will essentially stay the same and chip embedment will be uniform. Round aggregate tends to roll and becomes displaced by traffic. Angular aggregates lock to one another and resist compaction. This will result in many uncompacted voids. On high volume roads, a double chip seal may be the better option. The aggregate in the bottom layer should be about twice as large as the one used in the top layer. The smaller stones on top will likely cause less windshield damage and the surface is typically smoother than a single seal coat [21].

2.3.2 Aggregate Gradation

Aggregate gradation and size are important to the performance of TSLs. There are two options for a surface treatment, graded aggregate and one-size aggregate, as Figure 2-11 shows.

Graded aggregate means that the aggregate has some distribution in size. There are many types of gradations, such as dense graded or gap graded. One difficulty that may arise from using graded aggregate is that due to the lower air voids in graded aggregate means the binder may not fit between the chips. Problems such as bleeding and aggregate loss may then occur due to over filling.

In order to avoid this, single sized aggregate is recommended [21]. Single sized aggregate is an aggregate mixture that comprises roughly of equally sized stones. If all the aggregates are approximately of the same size, there is enough void space for the bitumen to fill and bond the stones to each other and to the pavement structure. Other benefits of single sizes aggregate include good friction between the surface and vehicle tires due to maximizing tire-aggregate contact area and good drainage between the stones.

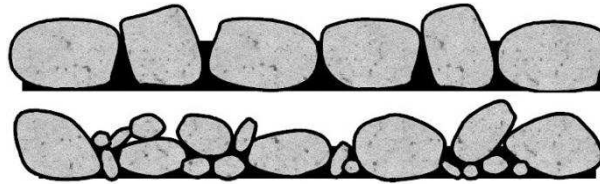


Figure 2-11 Cross section of one-size aggregate (up) and graded aggregate (bottom) [21]

2.4 Binders for Surfacing

Generally speaking, thin surfaces for road applications should have a long service life (longer than 10 years [22]). Furthermore, TSLs should meet the following requirements:

1. A good adhesion at the interface between the TSL and the underlying layer is essentially important in order to be able to carry horizontal forces due to breaking. Also adhesion between the aggregates and the binder is important to provide resistance to raveling.
2. Low traffic noise production: the macrotexture of a pavement surface has a dominant influence on the road noise, which means the noise production depends to a large extent on the surface texture and the void content.
3. Sufficient skid resistance is needed to provide enough friction between the tires and the pavement surface.
4. Good fuel resistance is also required especially in areas like parking lots, gas stations and runways.

To obtain optimum performance of TSLs, a proper choice of type and application ratio of binder and aggregates is essential. Failures such as raveling and lack of friction will be minimized in such a way. Technically, the binders used for thin surface applications should at least have the following qualities [4].

1. Having sufficiently low viscosity in order to be sprayed properly and cover the surface uniformly when applied. Yet viscous enough to remain in a uniform layer;
2. Retaining a proper consistency after application to be able to wet the applied aggregates.
3. Quick development of curing and adhesion. The curing speed should be fast enough to allow reopen to the traffic, and slow enough to have enough time for application.
4. Holding the aggregate tightly to the road surface after rolling and curing to prevent raveling caused by traffic.

Currently, bitumen emulsions, polyurethane resins and epoxy resins have already been used for pavement surface layers and provided these layers with good adhesion and good fuel, water and chemical resistance. Particularly, bitumen emulsions are used widely, because they are the easiest to apply and have the lowest price. Furthermore, additives like emulsifiers and modifiers can significantly improve the performance of bitumen emulsions.

2.4.1 Bitumen Emulsion

Bitumen emulsions are heterogeneous systems with two or more liquid phases, made up of a continuous liquid phase (water) and at least a second liquid phase (bitumen) dispersed in the former liquid as fine droplets. Standard bitumen emulsions are normally considered as the oil in water type and contain from 40% to 75% bitumen, 0.1% to 2.5% emulsifier, 25% to 60% water plus some other minor components. The size of the bitumen droplets ranges from 0.1 to 20 micrometer in diameter.

The ideal emulsion should be stable under storage, transport and application but should break rapidly after application and leaving a binder having the properties of the original bitumen adhering strongly to the road and to the aggregates [23]. It should have a low viscosity to allow early handling and application and should flow to minimize irregular spraying but should not flow due to road irregularities or gradients.

The most important properties of bitumen emulsions are stability, viscosity (or, more accurately rheology), breaking and adhesion.

Stability

Emulsions are inherently unstable. Over a period of time, which may be hours or years, due to the gravity force and the difference in density between the two phases, the bitumen phase, or part of it, will move slowly towards the bottom of the emulsion container. This process is called settlement. If the stability of bitumen emulsion is poor, settlement may lead to coalescence and breaking, in which case agitation can no longer restore the quality of the emulsion.

The speed of settlement depends on the bitumen content of the emulsion and decreases with increasing bitumen content. Increasing the bitumen content will increase the viscosity of a bitumen emulsion, which will therefore result in better storage stability and lower settlement speed [24]. In emulsions containing more than 65% of bitumen, settlement is normally negligible. The following methods can be used to reduce or prevent settlement [25]:

1. Increasing the viscosity of the water phase by adding a thickening agent.
2. Preventing flocculation by changing the types and concentrations of stabilizer and emulsifier or by changing the pH.
3. Reducing the size of the droplets for example by better milling or changing the emulsifier.
4. Improving the storage conditions, for example by keeping the emulsion at higher temperature than the ambient temperature.

Besides settlement, the bitumen droplets may start adhering to each other, which is called flocculation. Bitumen droplets in the emulsion have a small charge. The source of the charge is the emulsifier, as well as ionizable components in the bitumen itself. These small charges on the droplets normally provide an electrostatic barrier which prevent them to approach close to each

other (like charges repel). However, when two droplets do achieve enough energy to overcome this barrier and approach closely, then flocculation will happen. This flocculation may sometimes be reversed by agitation, dilution, or addition of more emulsifier.

When droplets in an emulsion merge to form bigger droplets, this is called coalescence. Flocculation is often followed by coalescence. Coalescence will start because of mechanical action such as agitation, pumping or vibration. Coalescence occurs in the breaking process and is dependent on the aggregate type. Coalescence cannot be reversed.

Factors that force the droplets adhering together such as settlement under gravity, evaporation of the water, shear or freezing will accelerate the flocculation and coalescence process [26]. Low viscosity bitumen will coalesce more rapidly than high viscosity bitumen. However, eventually we want the emulsion to coalesce fast after the bitumen emulsion has come in contact with the aggregates and has been placed on the road.

Viscosity

Viscosity of a fluid is defined as the resistance to flow. For bitumen emulsion, it is usually measured with a rotating spindle viscometer at 40 °C [27].

The viscosity of bitumen emulsions is almost independent of the viscosity of the dispersed bitumen. It is possible to produce emulsions of hard bitumen (<10 pen) which are readily pourable at 10 °C. The manufacturer must be able to produce emulsions with the desired viscosity for example for spraying. The viscosity must be predictable and remain constant within certain limits (depends on the storage, transport and application situations throughout the storage life of the emulsion [15]).

The viscosity is influenced by many factors. The most important are the bitumen content, the temperature of the emulsion, and the droplet size distribution. Figure 2-12 illustrates the relationship between viscosity and bitumen content and temperature [25] (the literature did neither mention the temperature for the left graph, nor the bitumen content for the right graph). The kinematic viscosity (cSt) is the dynamic viscosity (mPa·s) divided by the density of the fluid (g/cm³). Type and dosage of emulsifier, type and dosage of stabilizer, salt content and viscosity of the bitumen also have an influence on the viscosity of the emulsion.

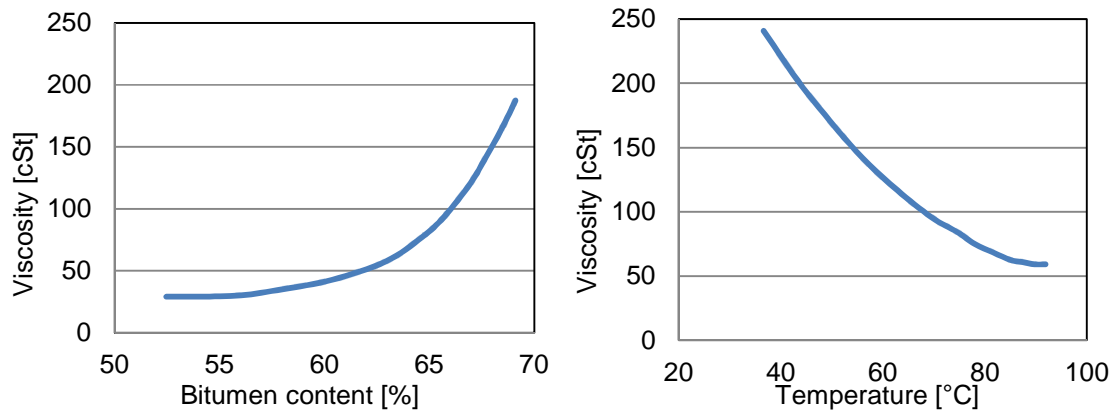


Figure 2-12 Example of relationship between viscosity vs. bitumen content and temperature [25]

Breaking

When a bitumen emulsion is applied on a mineral aggregate surface, the coalescence process will start which eventually will lead to breaking. The electrical charges on the stone surface rapidly absorb a number of the emulsifier ions from the water phase of the emulsion, thus reducing the number of emulsifier ions on the droplets to such an extent that the breaking process starts (See Figure 2-13 [15]). A point is reached where the charge on the surface of the droplets is depleted that rapid coalescence takes place. The aggregate is then covered with hydrocarbon chains and, therefore, the liberated bitumen adheres strongly to its surface.

The rate of setting and curing depends on the reactivity of the emulsion towards the aggregate and environmental conditions such as ambient temperature, wind velocity and humidity. Aggregates have a specific surface charge in the presence of water. Acidic aggregates such as quartzite and granite contain silica and have a strong negative charge in the presence of water. These negative charges attract the positive charged cationic bitumen particles, leading to destabilization of the surfactant system and subsequent coagulation of the bitumen particles. This breaking mechanism is absent when anionic emulsions are used with acidic aggregates, in this case the coagulation can only take place by evaporation of the water phase [28].

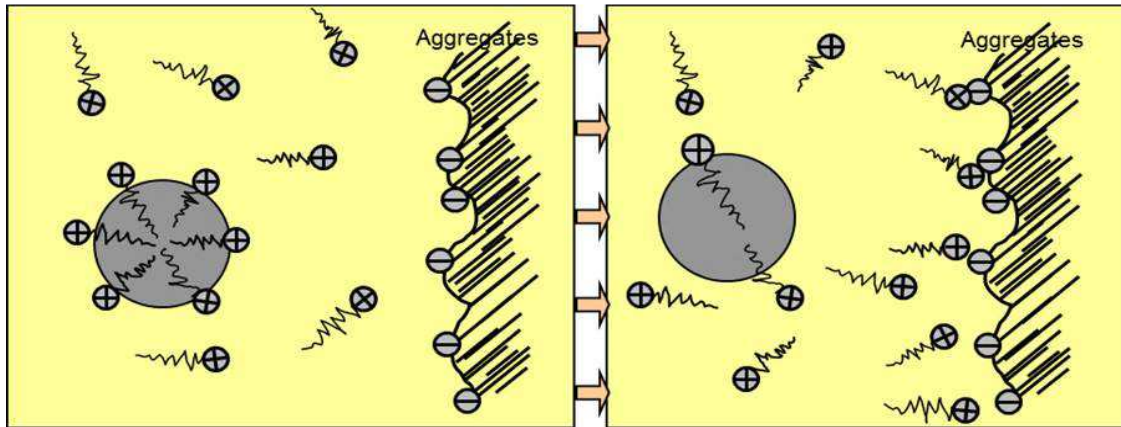


Figure 2-13 Schematic diagram of breaking process for cationic bitumen emulsion [15]

Adhesion

Adhesion is a very important property in all applications where bitumen is used as an adhesive between aggregates. The bitumen “wets” the surface of the aggregate to create a maximum contact area. Basically, aggregates can be classified as alkaline or acidic. Therefore, if an anionic emulsion is applied onto an acidic aggregate, the resulting adhesion can be poor.

On the other hand, a cationic emulsion breaking on an acidic or basic aggregate results in a strong absorption of the organic cation ($R-NH_2$, chemical group in emulsifiers) on the surfaces. This cation gives oleophilic properties to the surface on which it is absorbed, and has a water displacing effect resulting in strong adhesion of the deposited bitumen film to the aggregate surfaces. In this way, cationic emulsifiers will act as anti-stripping agents after breaking of the emulsion [25].

Table 2-2 summarizes the breaking rate and adhesion results of cationic and anionic emulsions with two types of aggregates [25]. The cationic emulsion breaks fast both on acidic aggregate and alkaline aggregate. And it can achieve good adhesion with alkaline aggregate and excellent adhesion with acidic aggregate. Since most aggregates used in road construction have a majority of negative charges on its surface, cationic bitumen emulsions are mostly used.

Table 2-2 Results of cationic and anionic emulsions with two types of aggregates

Emulsion	Aggregate	Results	
		Breaking rate	Adhesion
Anionic	Acidic	Slow	Poor
Anionic	Alkaline	Medium	Good
Cationic	Acidic	Fast	Excellent
Cationic	Alkaline	Fast	Good

2.4.2 Modified Bitumen Emulsion

The use of Polymer Modified Bitumen Emulsions (MBE) has increased dramatically in the road maintenance industry. Modifiers that are used can be divided into elastomers and plastomers. All of the elastomers considered are rubbers, either natural or synthetic (e.g. SBR and SBS). Plastomers used in highway construction are typically classified as paraffins (e.g. LDPE, EVA) [29]. Typical polymers are listed in Table 2-3.

Table 2-3 Typical Polymer modifiers for bitumen emulsion

Type	Form	Chemistry
Block copolymer	Crumb or powder	SBS (Styrene-Butadiene-Styrene)
Random copolymer	Latex	SBR (Styrene Butadiene Rubber)
copolymer	Crumb or powder	EVA (Ethylene Vinyl Acetate)
Homo-polymer	Pre-blended with AC	LDPE (Low Density Polyethylene)
copolymer	Crumb or powder	EMA (Ethylene Methacrylate)

Polymers can be blended in many ways into the bitumen, and it can be done indirectly in the case of modified bitumen emulsions. The final modified bitumen/polymer blend can be described in four ways [30]:

1. Polymers can be a separate phase dispersed in the bitumen. This occurs when the polymer is incompatible with the bitumen. These products are generally unstable with very poor storage characteristics.
2. Bitumen can be a separate phase dispersed in the polymer. This only occurs at a high polymer content (>12%). These materials are used in industrial products such as roof sealers etc.
3. Polymers can form a network within the bitumen. This is typical for the type of polymer modified bitumen generally used in road construction. The long polymer molecules become entangled to form elastic net. The elastic structure changes mechanical properties of the bitumen such as ductility, softening point, viscosity, etc.
4. Polymers can be molecularly bound to the bitumen. This has the advantage that bitumen and polymer are chemically linked and form a homogeneous material.

Figure 2-14 compares the complex modulus of unmodified bitumen (PG 58-22) and 3 wt. % SBR latex modified bitumen at a wide temperature range from -60 °C to 80 °C. The latex film is flexible even below -30 °C and maintains an elastic modulus at an elevated temperature of above 80 °C. This is due to the high molecular mass of this polymer, which yields a sufficient amount of polymer chain entanglements. The complex modulus changes only by a factor of 10 between -20 °C and 80 °C. In contrast, the complex modulus of the unmodified bitumen changes by a factor 100000 over the same temperature range [31].

Figure 2-15 illustrates that the rutting resistance temperature (Temperature at which $G^* / \sin(\delta) = 1kPa$, where G^* is the complex modulus and δ is the phase angle) of emulsion type mixtures increases after modification, especially after modification with cement together with SBR (the cement content was not mentioned in the reference) [32].

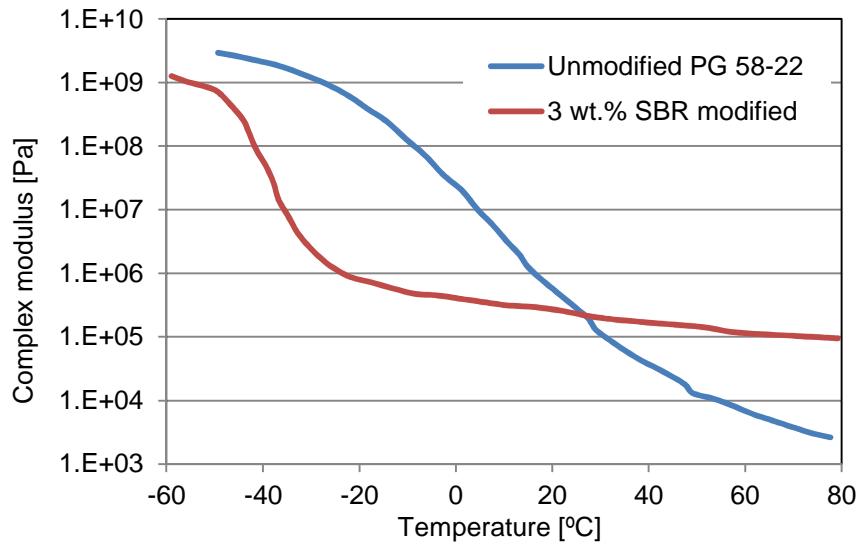


Figure 2-14 Complex modulus of unmodified and modified bitumen [31]

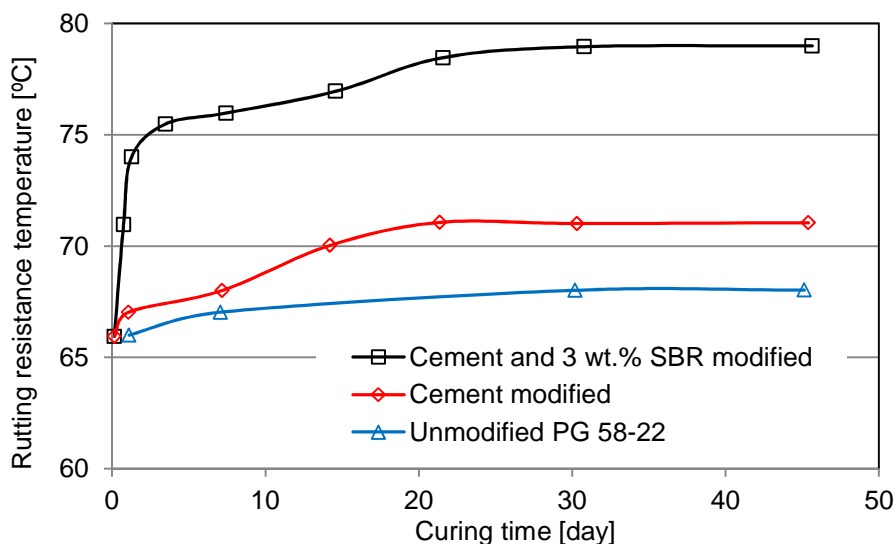


Figure 2-15 Superpave rutting resistance temperature of the emulsion binders [32]

The mechanical adhesion of four emulsions was analyzed with the Vialit Plate Shock Test, by Kucharek [33]. This test method is an indicator of adhesion between binder and chippings. Bitumen emulsion is applied to stainless steel plates and aggregates are embedded in the binder using a hand operated rubber wheel roller. The prepared test plate is turned over and placed on 3 pointed

support rods. A stainless steel ball is made to fall from an ‘angled slide’ three times within 10 seconds period onto the inverted test plates. Figure 2-16 explains the setup for Vialit Plate Shock Test [34]. The result of adhesivity is defined as the sum of number of chippings remaining bonded to the plate and the number of fallen chippings which are still bonded with binder (100 chips were used).

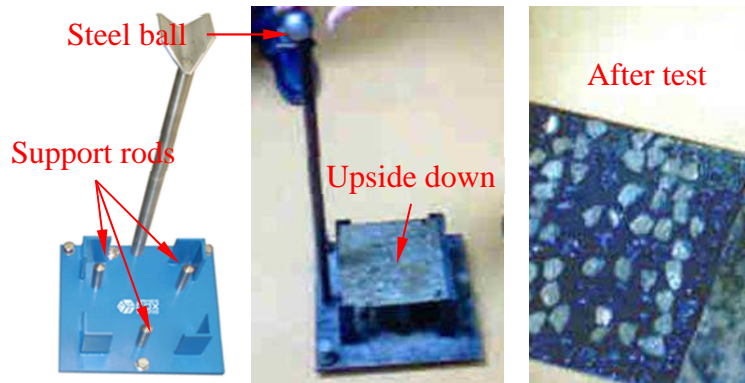


Figure 2-16 Set up for Vialit Plate Shock Test

The four tested emulsions were cationic rapid-setting and were prepared using a commercially available emulsifier for cationic rapid setting bitumen emulsion (CRS), with identical dosages. One was non-modified and the other three were polymer modified, all containing the same polymer content of 3 wt. % to the emulsion. The difference between these three emulsions lies in the type of polymer modification. One was modified using SBR latex (CRS-Latex), while the second was made by modifying the bitumen with SBR prior to emulsification (CRS-PMA). The third contained the same 3% SBR level but half is contained in the binder and half is contained as latex (CRS-Comb) [33].

Table 2-4 shows the results of adhesivity. The four emulsions showed to have a adhesivity level of 100 to the granite and the traprock chips, after 24 hours. The CRS-PMA shows some failures with the limestone chip. This means that the adhesion properties of CRS-PMA are lower than those of the others [33].

Table 2-4 Adhesivity at 24 hours cure by Vialit Plate Shock Test

Adhesivity	Limestone	Granite	Traprock
CRS	100	100	100
CRS-Latex	100	100	100
CRS-PMA	93	100	100
CRS-Comb	100	100	100

Kucharek also evaluated the cohesion properties by means of Frosted Marble Cohesion Test [33]. Figure 2-17 shows the setup. In the test [35], 15

frosted (sand-blasted) marbles were placed in the asphalt emulsion. The emulsion thickness is 1.6 mm and corresponds to an application rate of 1.5 L/m². The average torque (kg·cm) required to move 5 frosted marbles was recorded as the chip retention strength. The test is conducted within a trough plate containing 3 rows that each held 5 frosted marbles. Each marble is tested individually and the average of the five results per row is reported as one test.

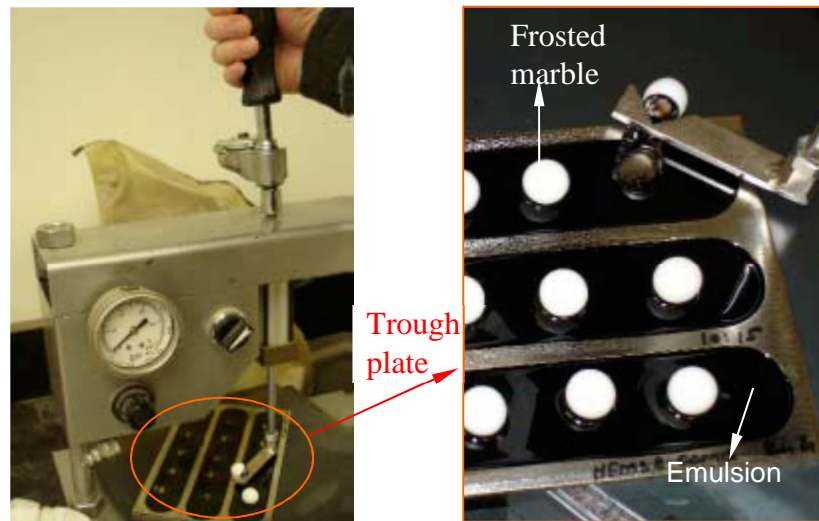


Figure 2-17 Setup for Frosted Marble Cohesion Test

Cohesion results with the Frosted Marble Test are presented in Table 2-5. CRS and CRS-PMA have consistently higher cohesion values than the other emulsions. The cationic emulsions containing latex have lower initial cohesion values compared to the others. The difference observed between the latex and the PMA cationic emulsions is because of the difference in polymer morphology. The PMA emulsion contains SBR polymer in the binder therefore, with breaking of the emulsion, the cohesion buildup can take advantage instantly of the polymer presence. This seems to be especially effective during the first 2-3 hours of its curing time. With the emulsions containing latex, it needs almost complete curing of the binder before it can deliver its full mechanical benefit. The combination CRS-Comb shows relatively low cohesion after two hours but has the highest cohesion of all emulsions after 4 and 6 hours. All four cationic emulsions display similar cohesion values after 24 hours.

Table 2-5 Cohesion by Frosted Marble Test

Cohesion [kg·cm]	2 Hours	4 Hours	6 Hours	24 Hours
CRS	9	10.83	12.23	21.92
CRS-Latex	4.4	7.8	11.6	22.42
CRS-PMA	11.2	13	16.4	23.8
CRS-Comb	6.6	18.6	19.6	23.8

In Jones' research, the Wet Track Abrasion Test (WTAT) and Cohesion Test were performed on various emulsion mixtures [36-38]. Slurry mixtures of fine graded aggregate, asphalt emulsion, and water were prepared to a homogeneous mix and are formed into a disk by pouring in the circular template. After curing and removal of the template, the disk-shaped specimen is dried to a constant weight at 60 °C. The cured slurry is then placed in a water bath for 1 hour, and then mechanically abraded under water with a rubber hose for 5 minutes. The abraded specimen is washed free of debris, dried at 60 °C and weighed. The loss in weight expressed as grams per square meter is reported as the wear value (WTAT loss) [37]. The left graph in Figure 2-18 shows the WTAT set up.



Figure 2-18 WTAT setup (left) and Cohesion test setup (right)

A cohesion tester provides the numerical strength value of the slurry. The cohesion tester puts forces on the slurry to simulate power steering movements and rotating tyres. The torque measurements are made after a certain curing time by means of a torque tester. The highest torque is then reported as the cohesion value. The right graph in Figure 2-18 shows the test setup.

The results in Table 2-6 indicate that SBR polymers enhanced the cohesion properties of bitumen emulsions. According to all laboratory tests, SBR latex performs the best.

Table 2-6 Test results of various polymers modified emulsions

Polymer	Cohesion [kg·cm]		WTAT loss [g/m ²]		Vertical Displacement [%]
	30 min	60 min	1 hour	6 days	
Natural	16	18	161.5	441.3	7.8
SBR	16	21	118.4	161.5	1.3
SBS	12	17	247.6	301.4	8.6
EVA	13	16	549	602.8	11.2

The temperature of the bitumen emulsion when sprayed on the road pavement surface will affect its viscosity and the way it flows on the surface, and will therefore have an effect on the final performance of thin surface layers. Therefore, an optimal temperature is needed for spraying bitumen emulsion.

2.4.3 Epoxy Modified Bitumen

An epoxy modified bitumen binder is a two-phase chemical system in which the continuous phase is an epoxy curing agent and the discontinuous phase is a mixture of special bitumens, which makes the performance of epoxy modified asphalt mixture different from traditional asphalt mixtures [39]. Unlike conventional bitumen, epoxy modified bitumen neither become as brittle as bituminous binder at low temperature and nor melt at high temperature [15].

Epoxy modified bitumen was originally developed in the late 1950s by the Shell Oil Company as a material designed to withstand the damage caused by jet fuel. In 1967, it was used to strengthen the surface of San Francisco Bay's mile-long San Mateo Hayward Bridge. After more than 40 years, the bridge's surface is reported to be in excellent condition [40].

Generally, compared to traditional asphalt mixture, the cured epoxy asphalt mixture has an extremely high temperature stability and strength, excellent fatigue and anti-bleeding properties, and superior rutting resistance. Marshall Stability values of epoxy asphalt mixtures tend to increase with curing time. The Marshall Stability value of a cured specimen can reach to 37 kN (See Figure 2-19). Even at the beginning of curing, the stability value is more than 10 kN, which is more than enough for opening to traffic in most situations. When used on roads, it sets quickly enough for normal traffic in the early life even without full curing, which enables the road to be reopened within two hours [41, 42].

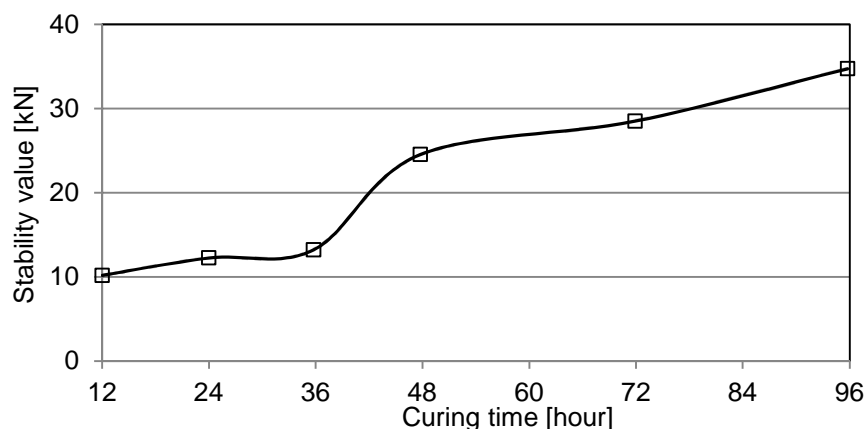


Figure 2-19 Marshall stability-curing time curve of an epoxy modified asphalt mixture at 60 °C

Luo used the Marshall stability test and indirect tensile strength test to evaluate the moisture sensitivity of epoxy asphalt mixtures [41]. PG 80/100

bitumen was used as reference. The aggregate grading limits are shown in Table 2-7. The binder content is 6.5 wt. %. From the results shown in Table 2-8 and Table 2-9, it can easily be seen that the epoxy modified asphalt mixture performed significantly better than the reference SMA mixture. The results show that the epoxy modified asphalt mixture is less susceptible to moisture damage. Figure 2-20 also shows that epoxy modified asphalt mixture has higher stability values.

Table 2-7 Grading limits of the asphalt mixtures [41]

Sieve size [mm]	16	13.2	9.5	4.75	2.36	0.6	0.075
Percentage passing [%]	100	100	95-100	65-85	50-70	28-40	7-14

Table 2-8 Marshall Stability test for different kinds of asphalt mixtures [41]

Mixture type	Marshall Stability [kN]		Retained Stability
	Standard condition	Conditioned at 60 °C for 48 h in a water bath	
Epoxy asphalt mix	36.1	35.7	98.9%
SMA 10	5.6	4.4	78.6%

Table 2-9 Indirect tensile strength test for different asphalt mixtures [41]

Mixture type	Indirect tensile strength at 25 °C [kN]		Retained Stability
	Standard condition	Conditioned at -18 °C for 16 h, then at 60 °C for 24 h in a water bath	
Epoxy asphalt mix	31.9	25.8	80.9%
SMA 10	7.4	5.6	75.7%

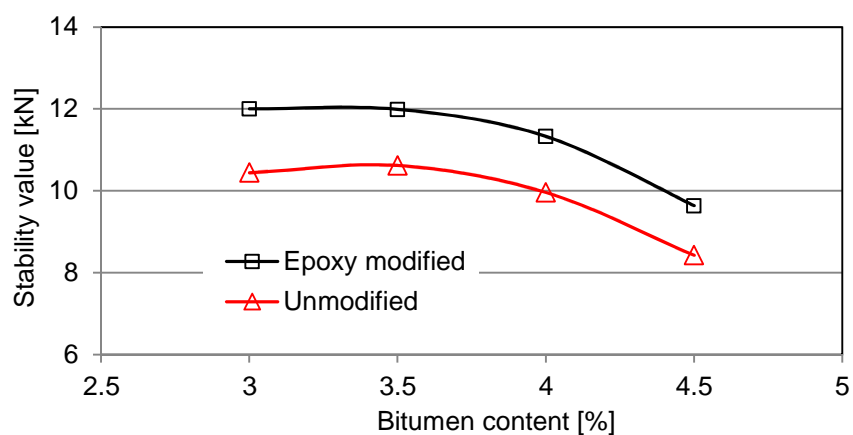


Figure 2-20 Marshall Stability of pure bitumen mixture and epoxy asphalt mixture [43]

The fatigue properties of the epoxy modified asphalt mixture and asphalt mixture were evaluated by three-point beam fatigue tests using a sinusoidal load

(load controlled mode, the modulus of epoxy modified asphalt mixture and the applied stress level were not mentioned in the reference) with 5 kN maximum peak load and a frequency of 10 Hz. The epoxy modified asphalt mixture was cured at 120 °C for 6 hours. The beams were 30 mm x 35 mm in cross-sectional area and 250 mm in length with a span length 200 mm. The fatigue test results in Table 2-10 indicates that the fatigue life of the epoxy asphalt mix is more than three times longer than that of SMA10 [41, 43].

Table 2-10 Fatigue life for different kinds of asphalt mixtures at 20 °C [41]

Mixture type	Load cycles [times]	Condition of the samples
Epoxy asphalt mix	12 000 000	No damage
SMA 10	3 200 000	Cracking in the middle of the sample

The low temperature properties were evaluated by means of three point bending tests on an epoxy asphalt mixture, SMA and mastic asphalt mixture (MA). Table 2-11 shows the test results. It indicates that at the same temperature of -15 °C, the epoxy asphalt mixture has the highest tensile strength and stiffness modulus value. It can be concluded that the epoxy asphalt mixture performed significantly better in terms of strength at low temperature, while its deformation characteristic (strain at failure) is similar to that of other mixes [41].

Table 2-11 Bending test results for different kinds of asphalt mixtures [41]

Mixture type	T [°C]	Flexural Tensile strength [MPa]	Maximum Flexural Tensile strain	Flexural Stiffness [MPa]
Epoxy asphalt mix	-20	20.54	2.26×10^{-3}	10172
	-15	20.29	2.60×10^{-3}	7808
SMA 10	-15	7.51	2.06×10^{-3}	3477
MA	-15	13.56	3.63×10^{-3}	3736

Figure 2-21 shows an asphalt mixture and an epoxy asphalt mixture after being submersed in diesel (the reference did not mention the submersion time [44]). Since the tests were comparison tests, it is reasonable to assume that equal submersion times were used. Within the same time, the asphalt mixture almost fully dispersed while the epoxy modified bitumen mixture was still in good condition. This shows that the epoxy asphalt mixture offers relatively good fuel (or diesel) resistance. Epoxy modified bitumen binders are classified as “thermosetting” as the epoxy resin components cause the binder to cure by chemical action and it is not subsequently softened by high ambient temperatures or by the spillage of fuel. An epoxy modified bitumen layer thus acts as an effective seal against the ingress of fuel.

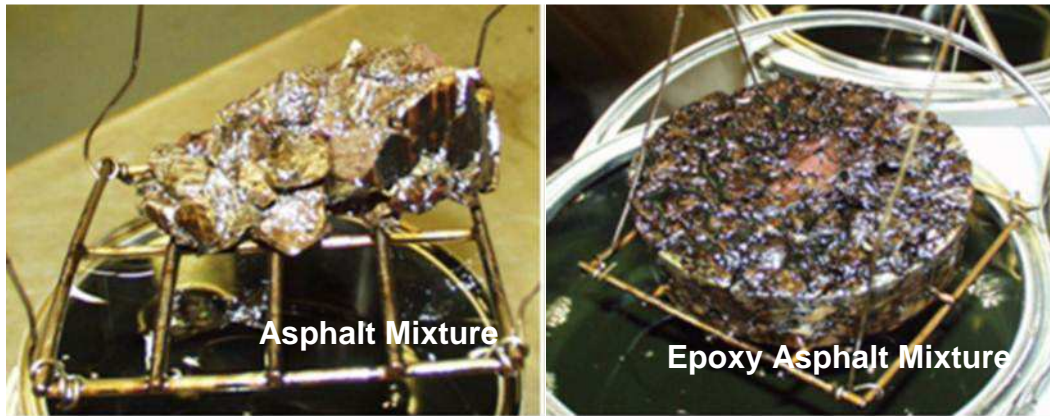


Figure 2-21 Effect of diesel immersion [44]

Furthermore, tests performed by the California Department of Transportation showed that surfaces with epoxy modified bitumen obtained maximum skid resistance. Research carried out by Washington State Department of Transportation showed that the epoxy modified bitumen doesn't need maintenance for a longer period of time. Advantages of epoxy modified bitumen can be listed as follows [39, 42]:

1. More resistance to low temperature cracking because of its higher tensile strength and flexibility, the temperature influences on the fracture resistance of epoxy modified asphalt mixture are not as significant as that of HMA.
2. More resistance to fatigue cracking, rutting and ageing; less susceptible to water induced damage; sufficient resistance to fuel spillage and blast from jet-type aircraft.
3. Stiffer (higher modulus) at service temperatures, with greater load spreading ability.
4. Excellent adhesion properties, more resistance to surface abrasion from tire action.

2.4.4 Other Binders

Besides the modified bitumen emulsion and epoxy modified bitumen, there are many other binders that were developed for coating in building and construction market. New technologies provide unique technical solutions to overcome well known problems, like good adhesion to concrete, water resistance and acidic resistance.

2.4.4.1 Polyurethane Resins

Polyurethane resins are now being widely used in the coatings and adhesives industries. They provide a tough, durable and highly flexible seal. The advantages of polyurethane coatings are their high tensile strength, excellent weathering and chemical/mechanical resistance [23, 45, 46].

Polyurethane is formed by a chemical reaction between a polyol resin and a polyisocyanate hardener. When the two components are mixed, the hydroxyl groups (-OH) in the resin react with the isocyanate groups (N=C=O) in the hardener and then a three dimensional molecular structure is produced. Only one isocyanate group can react with one hydroxyl group so there is an ideal ratio of hardener molecules to resin molecules which will give optimum mechanical properties. Despite of this fact, it is possible to vary this ratio slightly either way in order to modify the mechanical properties of the system. This is because the isocyanate hardener is also capable of cross-linking with itself in the presence of atmospheric moisture. More hardener than the optimum ratio will produce coatings which are harder, more brittle and have greater resistance to chemical attack. Less hardener will have the opposite effect, the film will be more flexible and its resistance to weathering will decrease [47].

Van Lent [48] investigated the potential of using polyurethane binder for pavement purposes by means of testing the binder, as well as a polyurethane binder based mixture. He found that the investigated polyurethane binder behaved elastic. For temperatures below 20 °C its phase angle was lower than 10 degrees (see Figure 2-22). Compared to general bitumen binder, the polyurethane binder had a larger shear modulus and a more elastic behavior (smaller phase angle). The tensile strength of the polyurethane binder (more than 30 MPa) is much higher than the tensile strength of bitumen (not higher than 6 MPa, dependent on temperature and loading speed). The fatigue resistance of the polyurethane binder was much larger than the fatigue resistance of a bituminous mortar.

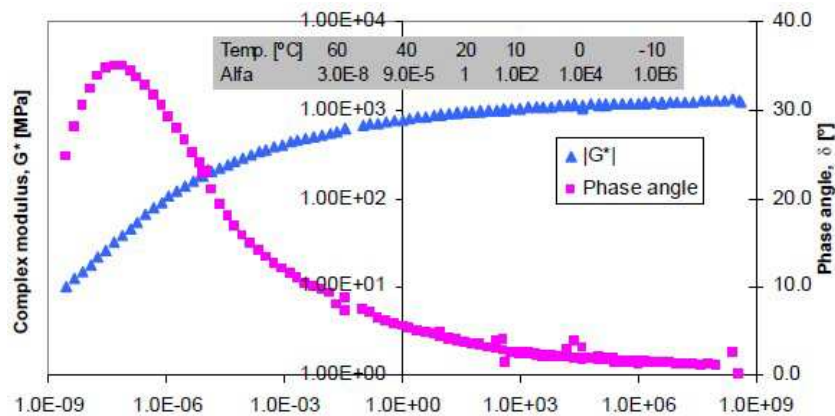


Figure 2-22 Master curve of the polyurethane binder at 20°C [48]

Unfortunately, the relaxation behavior of the polyurethane binder (see Figure 2-23) investigated by van Lent was much worse than the relaxation behavior of bituminous binders. This can cause low temperature related stresses of significant magnitude which, in combination with traffic induced stresses, can result in possible cracking in pavement structures. The coefficient of thermal expansion of the polyurethane binder based mixture (about $5.76 \times 10^{-5} / ^\circ\text{C}$) is

different from the value of asphalt mixture (ranges between 2 and 3×10^{-5} /°C [15]). This will cause higher temperature induced stresses in the polyurethane modified mixture when the temperature changes [48].

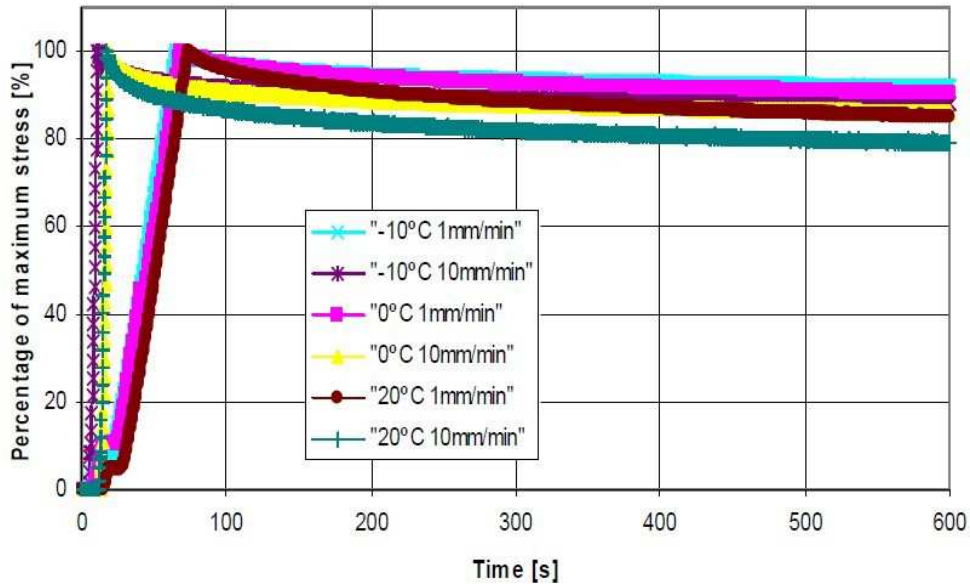


Figure 2-23 Relaxation of the polyurethane binder at 20°C [48]

During the last decade, Addagrip Surface Treatments UK Ltd designed a special two-component polyurethane resin, named Addagrip's 1000 System resin, for sealing and protecting asphalt surfaces from erosion caused by frost damage, chemical attack and aviation fuel spillage. It has been used to carry out durable and extensive repairs to the concrete runways of two Polish airports. In 2001 they used this kind of resin at Radom airport and the surface is still perfect⁶. Applying this polyurethane resin onto the pavement surface can result in a significant reduction of water and fuel absorption, which can result in long service life.

2.4.4.2 Epoxy Resins

Epoxy is a co-polymer. It is formed from two different chemicals. These are referred to as the "resin" and the "hardener". The resin consists of monomers or short chain polymers with an epoxide group at either end. Most common epoxy resins are produced from a reaction between Epichlorhydrin and Bisphenol-A. The hardener consists of reactive hydrogen, for example Epichlorhydrin. When these compounds are mixed together, the amine groups ($\text{NH}_2\text{-R}$) react with the epoxy groups (-CH(O)CH-) to form a covalent bond (see Figure 2-24). Each NH group can react with an epoxide group, so that the resulting polymer is heavily cross linked, and is thus rigid and strong. Polyamide, amido/amine and

⁶Addagrip. Available from: <http://www.addagrip.co.uk/1000system.html>

aliphatic/aromatic amine hardeners react with epoxy resins upon mixing to provide films that are extremely resistant to chemicals [45].

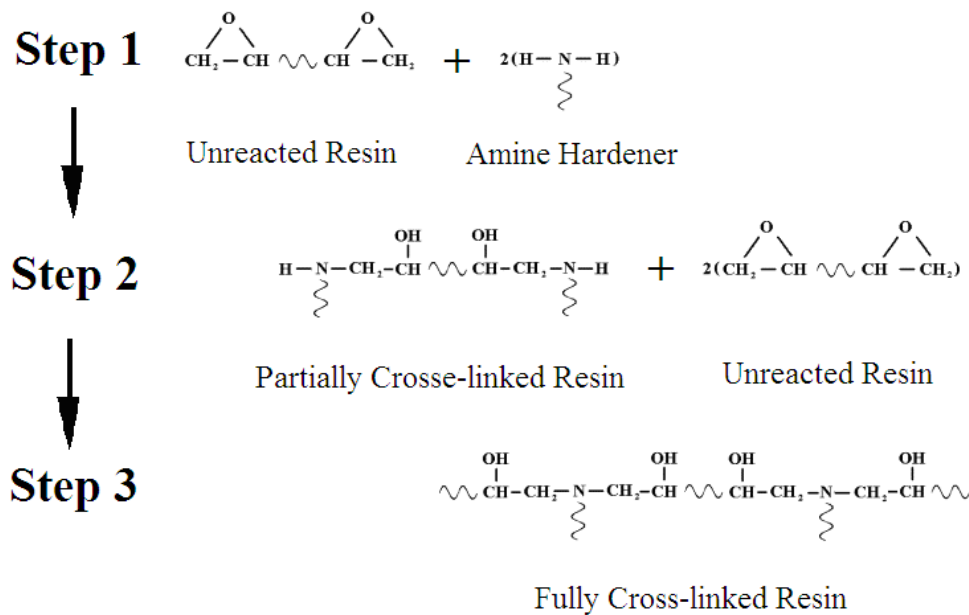


Figure 2-24 An fully cross-linked epoxy resin formed by reacting between amine groups and epoxy groups

Many epoxy products also contain additives such as organic solvents, fillers such as fiberglass or sand, and pigments. When epoxy resin systems are used, single molecules (monomers) of the epoxy resin and the curing agent combine to form long chains of molecules (polymers). This process of polymerization is called "curing", and can be controlled through temperature and choice of resin and hardener compounds, the process can take minutes to hours. Some formulations benefit from heating during the curing period, whereas others simply require time at ambient temperatures.

Epoxy resins consist of a linear chain molecule with a reactive epoxy group at each end of the chain. Each particular type of epoxy resin varies in terms of its detailed structure and the length of the chain between the epoxy groups. The actual properties of the final epoxy resin coatings are highly dependent on the type of resin and hardener used. Solid epoxy resins have larger molecules and the distance between cross-linking points is greater, which results in more flexible and resilient films. Liquid resins with shorter chains give harder and stronger films due to denser cross-linking [47].

In general, epoxies have excellent adhesion and mechanical properties, as well as excellent chemical and heat resistance. The advantage of epoxy resin is that this compound can be cured at atmospheric temperature and humidity within a reasonable curing time. It can be mixed with common materials like cement mortar and concrete to enhance the early strength, impact resistance and moisture resistance of these materials.

2.5 Modeling of Thin Surfacing

Various laboratory and field test methods are employed to characterize the performance of thin surfaces. Generally each test method can only represent one specific state of stress, e.g. bending or tension or compression etc. However, the real stress situation in a TSL cannot be represented by any of those lab and field test methods alone. The challenge now is how to use the properties quantified by these lab tests to predict material behavior in the complex field situations.

Many Finite Element Models (FEMs) have been introduced to simulate the performance of road pavements and hence predict their performance. The main damage type on TSL's is raveling, which is the loss of stone from the surface. The Road and Railway Engineering Section at TU Delft did substantial research in trying to explain and solve this problem at meso-level [49, 50].

2.5.1 Different Modeling Levels

The determination of the stresses and strains in an asphalt mixture can be divided into three different levels, macro-level, meso-level and micro-level. Figure 2-25 presents these three levels.

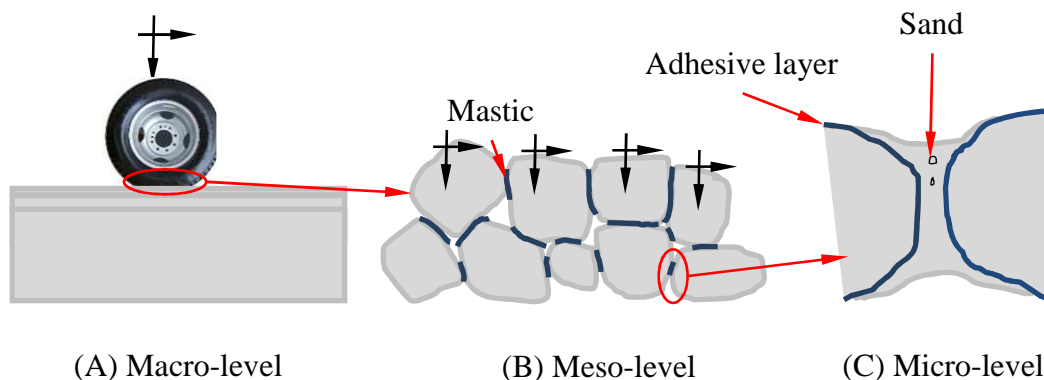


Figure 2-25 Three levels for asphalt mixture simulations

2.5.1.1 Macro-level

The macro-level model (see Figure 2-25(A)) for pavement design means application of multi-layer theory, with the possibility to model the tire road surface interaction as non-uniform. At macro level, the load is mostly modeled as a circular area with constant vertical stress equal to the tire pressure. Also combinations of such circular loads can be made to model the complex contact pressure distribution which occurs in practice. This method works well for obtaining a schematic picture of the stress and strain conditions in the pavement.

However, as the failure of thin surface layers occurs at the surface, the interaction between tire and road is very important and therefore the surface layer structure and the load on the road surface must be modeled as realistically as possible, which is not possible with these macro-level models.

2.5.1.2 Meso-level

Meso-level modeling allows taking into account the properties of the various components of the asphalt mixture. At meso-level, the asphalt mixture layer is modeled with a stone skeleton, mastic, voids and an interface between aggregate and mastic. The stone skeleton consists of aggregate particles larger than 2 mm, while the mastic is the mixture of bitumen, filler and sand smaller than 2 mm.

As Figure 2-25(B) shows, the loads at this level are applied on individual stones. By using realistic values for the parameters describing the response to loading of the mastic and interface, the stresses and strains in the mastic and the interface can be calculated.

2.5.1.3 Micro-level

At micro-level as Figure 2-25(C) shows, the binder is modeled in terms of sand, filler, bitumen, interface and voids. At micro-level, several separate models need to be developed to characterize the different components. A micro-level model should be able to predict accurately the stresses and strains developing at places of adhesive zone between stone and bitumen, and at cohesive zone in the mastic.

However, from an engineering point of view, modeling at meso-level is refined enough to analyze problems like raveling.

2.5.2 Macro-level Models

Macro-level models like BISAR, CIRCLY⁷ etc. were used in the past to study the behavior of pavement [51]. They use multi-layer theory which assumes each pavement layer to be linear elastic, homogeneous and isotropic.

In this research, the binder areas between the aggregate particles are of special interest. In this case, the homogeneous macro-level model can no longer be used. Modeling of the individual composites as a whole skeleton is therefore required. The size, shape and position of every aggregate should be taken into account.

2.5.3 Meso-level Models

The Lifetime Optimization Tool (LOT) project, carried out at TU Delft [49], is based on an meso-mechanical analysis. The model was developed to explain the phenomena that take place in Porous Asphalt (PA) mixtures during the passage of a tire and because of temperature changes. The developed FEM models basically translate the PA surface load, the mixture geometry and the response behavior of the mortar into signals of stress and strain at various

⁷ Overview of CIRCLY: <http://www.mincad.com.au/circlly.htm>

locations in the PA mixture. By interpretation of the computed stress and strain signals, the life expectancy of the modeled PA is estimated.

2.5.3.1 Idealized Models

The idealized model in LOT considers perfectly round and rigid spheres bond together via mortar bridges. Figure 2-26 gives an overview of the 2D idealized model. As it is shown, the model has a length of 11 particles at the PA surface. It consists of three layers of stone particles. In each layer the outer two particles are enclosed in a mortar film modeled by a single layer of elements. The mortar films closer to the middle of the model are modeled by two layers of elements. Figure 2-27 is an enlargement of the transition area where the mesh is refined [49].

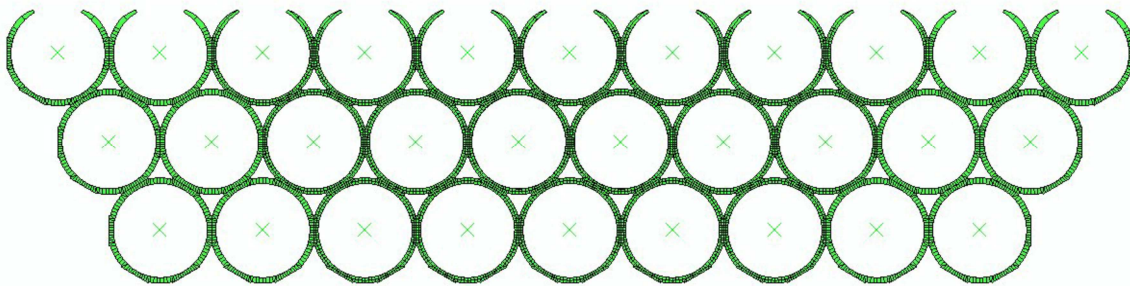


Figure 2-26 Overview of 2D idealized model [49]

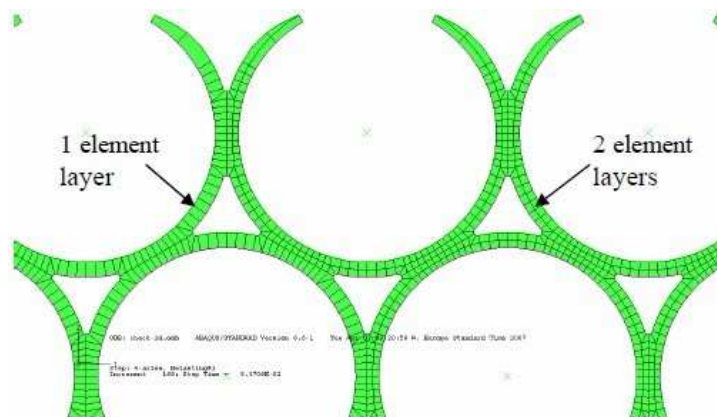


Figure 2-27 Magnified transition area with refined mesh [49]

In this idealized model, the particles themselves are not visible and formed by implementation of restraints. In this case the crosses that mark the center of the various particles have the freedom to rotate and translate. All nodes at edge of the particle are rigidly connected to the master nodes indicated by the crosses; this effectively creates rigid body stone particles. Five particles closest to the center of the model are fitted with a layer of 0.01 mm thin elements that represent the adhesive zone [49].

In order to get more accurate simulation results, a 3D idealized model as shown in Figure 2-28 was developed. In this 3D idealized model, the aggregates were modeled by rigid bodies through implementation of restraint conditions. As was the case in the 2D model, only the upper central stone was fitted with an interface layer that represents the adhesive zone. For the other aggregate particles, the binder is directly connected to the aggregate particles to form the bonding bridge [49].

Both 2D and 3D idealized models can simulate the mixture behavior under certain loading conditions quite well. But the influence of aggregate geometries such as size and shape were not included. A 2D photo model, which was developed from the skeleton structures of mixtures, is closer to real mixture structures.

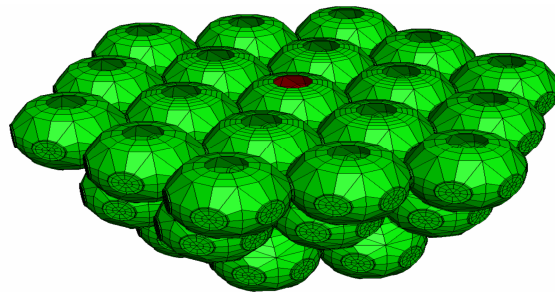


Figure 2-28 Overview of the 3D idealized model [49]

2.5.3.2 Scan/photo Models

In the LOT research, real scan images/photos of PA were semi-automatically translated into a 2D element sketch [49]. Then a mesh is generated automatically. Figure 2-29 gives an indication of the obtained models and meshes in relation to the original image. Adhesive zones with a thickness of 0.01 mm are also presented only in the central upper part of the models. This is because the real interest is in the phenomena that play a role at the surface while the models are most accurate in the center of the model.

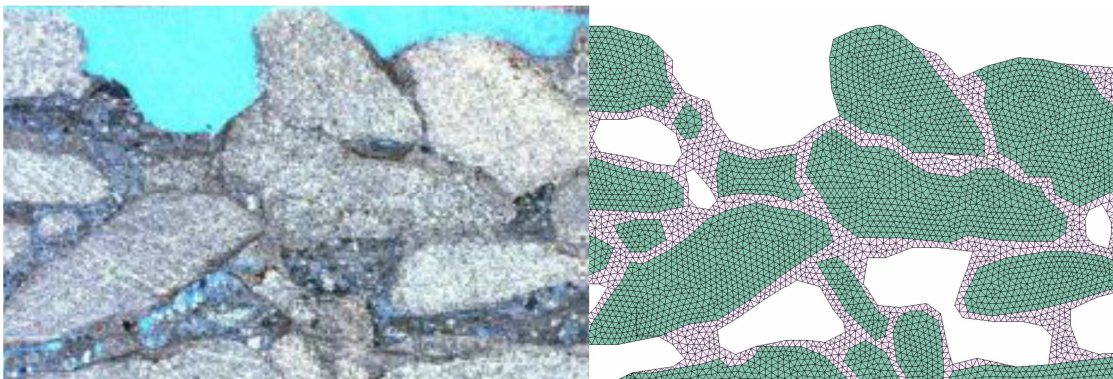


Figure 2-29 From photo to mesh geometry for FEM [49]

Compared to the idealized models, models generated from scan images/photos are a closer representation of reality. Hence they give more reasonable simulation results. Therefore, models generated from scan images will be used in this research.

2.6 Summary

In this chapter a literature review on thin surface layer applications, including surface dressings, slurry seals and thin hot mix overlays has been given. New technologies for thin surface layer application are also addressed, such as newly developed binders and new surface layer structures. At the end of this chapter, modeling methods that are currently used for pavement surface analyses were discussed. The following items can be concluded from the literature review:

1. Thin surface layers, including surface dressing, slurry seal and thin mixture surface, are widely used on road pavements, bridge decks and airfields. They can significantly extend the service life by enhancing the surface properties and protecting the underlying layers from oil spillages, chemicals UV light and etc. Furthermore, most of these methods are cheap and can be quickly applied.
2. An antiskid surfacing is used for a pavement to increase the friction and hence to reduce the possibility of skidding. It is commonly used at special areas/places where higher friction values are required. High quality binder and aggregates are needed for antiskid surfacings.
3. Newly developed binders can significantly improve the relevant properties of TSLs. Polymer modifiers can improve the adhesion. Epoxy modified bitumen can achieve enough strength in a short time allowing reopening of the road to traffic in a short time. They provide a better fuel and moisture resistance and flexibility at low temperature, etc. Polyurethane resins and epoxy resins also have potential to provide good performance on TSLs.
4. Super AirMat is a recently developed surfacing for runways. It uses polymer modified bitumen and cellulose fibers as binders and provides good adhesion with aggregates.
5. Modeling at meso-level can be used to simulate the behavior of TSLs under tire and temperature loading. 2D element meshes can be developed from real scan images/photos of TSLs, using the method that was developed in LOT project.

Based on the literature review, it seems that there are a number of potential binders for antiskid surfacings. When the potential binder and mixture are optimally designed, good performance like adhesion, tensile strength and fatigue can be achieved. But at this moment, none of them are well supported by research for the thin surfacing and antiskid applications.

Therefore, the potential of using modified bitumen emulsion, epoxy modified bitumen and epoxy resin for antiskid thin surfaces was studied in this research. Furthermore, research on a performance evaluation method for durable

and sustainable thin surfacings is proposed. In order to design a durable and sustainable thin surfacings, a workable performance evaluation model should be proposed to evaluate both the property of the binder and the thin surfacing layer. The curing behavior, the adhesion property and the viscoelastic behavior in a wide temperature range should be considered.

REFERENCES

1. ISO, *ISO 13473-2, Characterization of pavement texture by use of surface profiles - Part 2: Terminology and basic requirements related to pavement texture profile analysis*. 2002.
2. InfraGuide, *Preservation of Bituminous Pavement Using Thin Surface Restoration Techniques*. 2005: Federation of Canadian Municipalities and National Research Council.
3. Ltd, V.T. *Production of bitumen-emulsions - Application of emulsions in different road construction technologies*. in *XXVII International Baltic Road Conference*. 2009. Riga, Latvia.
4. Bulletin, W.T., *Seal Coating and Other Asphalt surface Treatments*, T.I. Center, Editor. 1992. p. 4.
5. DFID, *A Guide to Surface Dressing in Tropical and Sub-tropical Countries*. 2000, Department for International Development: London, ISSN 0951-8797.
6. REA, *Surface Dressing with Bitumen Emulsion - REAL Technical Data Sheet No. 4*. 2006.
7. Liu, H., et al. *Study on Thin-layer Antiskid and Flame Retardant Colored Pavement Material for Tunnels*. in *Electric Technology and Civil Engineering (ICETCE), 2011 International Conference on*. 2011.
8. Liu, H., et al. *Research Progress and Prospect of Application Technology of Thin-layer Antiskid Colored Pavement at Home and Abroad*. in *Electric Technology and Civil Engineering (ICETCE), 2011 International Conference on*. 2011.
9. ISSA. *Recommended Performance Guidelines for Emulsified Asphalt Slurry-A105*. International Slurry Surfacing Association 2010; Available from: www.slurry.org.
10. ISSA. *Recommended Performance Guidelines for Micro-surfacing-A143*. International Slurry Surfacing Association 2010; Available from: www.slurry.org.
11. Broughton, B., S.-J. Lee, and Y.-J. Kim, *30 Years of Microsurfacing: A Review*. ISRN Civil Engineering, 2012. **2012**: p. 7.
12. Cooper, S.B. and L.N. Mohammad, *Novachip Surface Treatment - Six Year Evaluations*. 2004, Louisiana Transportation Research Center.
13. Russell, M.A., et al., *NovaChip - Final Report, No. WA-RD 697.1*. 2008, Washington State Department of Transportation.
14. Gilbert, T.M., P.A. Olivier, and N.E. Galé. *Ultra Thin Friction Course: Five Years on in South Africa*. in *8th Conference on Asphalt Pavements for Southern Africa*. 2004. Sun City, South Africa.
15. Shell, *The Shell Bitumen Handbook, Fifth Edition*. 2003.
16. Leest, A.J.v. and G. Gaarkeuken, *The F.O.D. resistance of surface layers on airfields in the Netherlands: in situ and laboratory testing*, in *2004 FAA*

- Worldwide Airport Technology Transfer Conference*. 2004: Atlantic City, New Jersey, USA.
17. Leest, A.J.v. and G. Gaarkeuken, *Resistance of surface layers on airfields in the Netherlands-in situ and laboratory testing*, in *2005 European Airport Pavement Workshop*. 2005.
 18. POSSEHL. *POSSEHL ANTISKID®*. Available from: http://www.possehl.nl/nl/vliegveldverhardingen/speciale_bekleding_voor_start-en_landingsbanen/antiskid_55983.shtml.
 19. Nynas-Bitumen, *Alternatives emerge to traditional airport surfacing*: <http://www.modernasphalts.com/archives/archive/20/articles/MA20Nynas.pdf>.
 20. Nynas-Bitumen, *Exeter Runway Receives Super-Strength Treatment*. 2006.
 21. Wood, T.J., D.W. Janisch, and F.S. Gaillard, *Minnesota Seal Coat Handbook*. 2006.
 22. *Long-lift Surfaces for Busy Roads*. 2008: International Transport Forum.
 23. Xiao, Y., *Literature Review on Possible Alternatives to Tar for Antiskid Layers*, Report No. 7-10-185-1. 2010, Delft University of Technology.
 24. Hermadi, M. and A.B. Sterling, *New mix composition to increase the storage life of Indonesian bitumen emulsion*, in *9th Road Engineering Association of Asia and Australasia (REAAA) Conference*. 1998: New Zealand.
 25. ScanRoad, *Technical Bulletin 2 - Bitumen Emulsions*. 1983: p. 15.
 26. TRB, *Asphalt Emulsion Technology*, TRB Report No. E-C102. 2006.
 27. CEN, *NEN-EN 14896: Bitumen and bituminous binders - Dynamic viscosity of bituminous emulsions, cut-back and fluxed bituminous binders - Rotating spindle viscometer method*. 2006.
 28. Louw, K., K. Spence, and P. Kuun, *The Use of Bitumen Emulsions as a Cost Effective Solution for Constructing Seals During Winter*, in *8th Conference on Asphalt Pavements for Southern Africa*. 2004.
 29. Gardiner, M.S. and D.E. Newcomb, *Polymer Literature Review*, Report No. MN/RC-95/27. 1995, Civil Engineering Department, University of Minnesota.
 30. Nootenboom, C.W. *Compatibility of polymers in bitumen*. in *Modified Bitumen Seminar*. 1991.
 31. Takamura, K., *Improved Fatigue Resistance of Asphalt Emulsion Residue Modified with SBR Latex*, in *AEMA Annual Meeting*. 2003.
 32. Lubbers, C., *Emulsions 101 Polymer-Modified Emulsions for Surface Treatments*, in *NEPPP (Northeast Pavement Preservation Partnership) Annual Meeting*. 2008.
 33. Kucharek, A.S., J.K. Davidson, and J.M. Croteau, *Development of Adhesive and Cohesive Properties of rapid-setting bitumen emulsions during chip seal construction*, in *AEMA*. 2008.
 34. CEN, *NEN-EN 12274-3 Surface dressing - Test method - Part 3: Determination of Binder Aggregate Adhesivity by the Vialit Plate Shock Test Method*. 2003.
 35. Howard, I.L. and G. Baumgardner, *Highway 84 Chip Seal Field Trials and Laboratory Test Results. Final Report FHWA/MS-DOT-RD-09-202-VI*. 2009, Mississippi State University.
 36. *ISSA TB-109. Test Method for Measurement of Excess Asphalt in Bituminous by Use of a Loaded Wheel Tester and Sand Adhesion*.
 37. ASTM, *D3910-07, Standard Practices for Design, Testing, and Construction of Slurry Seal*. 2007.

38. David, R.J. and C. Antonio, *The effects of various polymers on quick-set quick-traffic emulsified asphalt micro-surfacing mixes*, in AEMA. 1988.
39. Hongtao, L., C. Xianhua, and Q. Zhendong, *On the fracture properties of epoxy asphalt mixture with SCB test*, in *Advanced Testing and Characterization of Bituminous Materials, Two Volume Set*. 2009, CRC Press.
40. Chamarthi, R.S., *Evaluation of Wearing Surface Systems for the Orthotropic Steel Deck of the San Mateo Hayward Bridge*. 2012, University of Missouri-Columbia.
41. Luo, S., J. Wang, and Z. Qian, *Research on the performance of locally developed epoxy asphalt mixes*. 2007, SATC.
42. Alabaster, D., P.R. Herrington, and J.C. Waters, *Long Life Open-graded Porous Asphalt*, in *APT '08. Third International Conference*. 2008.
43. Çubuk, M., M. Gürü, and M.K. Çubuk, *Improvement of bitumen performance with epoxy resin*. *Fuel*, 2009. **88**(7): p. 1324-1328.
44. Elliott, R., *Epoxy Asphalt: Concept and Properties*, in *Long Life Surfacing for Busy Roads-A Workshop OF TRA2008*. 2008: Ljubljana, Slovenia.
45. Keith D, W., *Paint and Coatings: a Mature Industry in Transition*. *Progress in Polymer Science*, 1997. **22**(2): p. 203-245.
46. Volker, M., *New Resin Systems for High Performance Waterborne Coatings*. *Progress in Organic Coatings*, 1993. **22**: p. 273-277.
47. *Epoxy and Polyurethane Coating Systems for Marine Applications*. 2001; Available from: <http://www.azom.com/article.aspx?ArticleID=1100>.
48. Lent, D.Q.v., A.A.A. Molenaar, and M.F.C.v.d. Ven, *Determination of the Technical Possibilities of the Use of Elastopave® in Pavement Applications*. 2009, Delft University of Technology: Report No. 7-09-195-2.
49. Huurman, M., *Lifetime Optimisation Tool, LOT, Main Report, Report No. 7-07-170-1*. 2007, Delft University of Technology.
50. Mo, L.T., et al., *Research of Bituminous Mortar Fatigue Test Method Based on Dynamic Shear Rheometer*. *Journal of Testing and Evaluation*, 2011. **40**(1).
51. Behiry, A.E.A.E.-M., *Fatigue and rutting lives in flexible pavement*. *Ain Shams Engineering Journal*, 2012. **3**(4): p. 367-374.

3. Materials and Test Methods

The main question of this thesis is how to design durable and sustainable thin surface layers for runways and pavements. This question is originally generated from finding alternatives to tar-containing materials for antiskid surfaces for runways. Because of the urgency to find alternatives, samples with tar-containing antiskid layers were first evaluated to serve as benchmark. Requirements which have to be fulfilled by the new antiskid layers were then concluded. From its name it is clear that an antiskid layer should provide excellent skid resistance for landing and departing aircraft. These requirements put high demands on the macro texture of the layer and the microtexture of the aggregates to be used for this layer.

Furthermore, the adhesion between aggregates and between the antiskid layer and the underlying layer should be excellent. This is essential because loose aggregates and loose layers can result in significant FOD (Foreign Object Damage). A number of years ago e.g. an MD-11 aircraft lost its tail engine at Schiphol airport because loose aggregate from the antiskid layer was sucked in it. These good adhesion characteristics are mainly dependent on the characteristics of the binder and the interaction between aggregates and binder.

Maintenance operations on runways of busy airports should be limited as much as possible. This means that the antiskid layer should have a long lifetime itself and should be able to protect the layer underneath from environmental induced damages as well as damage due to fuel spillage, de-icing chemical etc. This immediately means that the antiskid layer itself should be highly resistant to fuel spillage and de-icing chemicals as well. On top of that the layer should have a high resistance against weathering and ageing. The adhesion should stay good and the layer should not become brittle as a result of ageing.

All these requirements are very much or even mainly related to the characteristics of the binder.

Finally it is obvious that the antiskid layer should be able to sustain the combination of high induced stresses due to rolling and braking aircraft and high temperature stresses that can be induced during cold winter periods. In order to be able to sustain the combination of aircraft and environmental induced stresses, the antiskid layer should have very good stress relaxation properties. Also these properties are very much dependent on the characteristics of the binder.

Therefore based on the literature review, new binder materials developed by local producers, including polymer modified bitumen emulsions, two-component epoxy modified bitumen binders and modified epoxy resins, were investigated by

performing tests both on binders and newly designed antiskid surface layers made with these binders.

Information about the materials and test methods used in this research are presented in this chapter. Figure 1-2 in Chapter 1 has explained the outline of the research approach for this study. Tar-containing antiskid layers were first investigated by means of sand patch test, CT scan, microscope, pull test and shear test. Then newly designed materials such as modified bitumen emulsion, epoxy modified bitumen and epoxy resin was studied. Newly designed antiskid layers were included in this research as well.

3.1 Materials

3.1.1 Tar-Containing Antiskid Surface Layers

All the tar-containing samples used in this research are collected from runways on Dutch military airfields. Normally a military runway has an asphalt construction over its entire length, except at the ends. Both ends of the runway are constructed with Portland Cement Concrete. The asphalt is covered with a coal-tar based antiskid layer. This layer is normally not used on taxiways or aprons. The antiskid layers on the Dutch military airfields were all constructed by the contractor, Possehl Spezialbau GMBH. The binder is a coal-tar based emulsion made by Possehl in Germany. The aggregate they used for these antiskid layers was special basalt from a German quarry, with grain sizes between 1.5 and 3.5 mm. The mineralogical composition of this aggregate is presented in Figure 3-1. It contains the following minerals:

- Diopside, $\text{CaMg}_{0.88}\text{Fe}_{0.24}\text{Si}_{1.88}\text{O}_6$
- Forsterite, $\text{Mg}_{1.39}\text{Fe}_{0.61}(\text{SiO}_4)$
- Bytownite, $\text{Na}_{0.14}\text{Ca}_{0.85}\text{Al}_{1.83}\text{Si}_{2.16}\text{O}_8$
- Microcline, $\text{K}_{0.58}\text{Na}_{0.42}\text{AlSi}_3\text{O}_8$

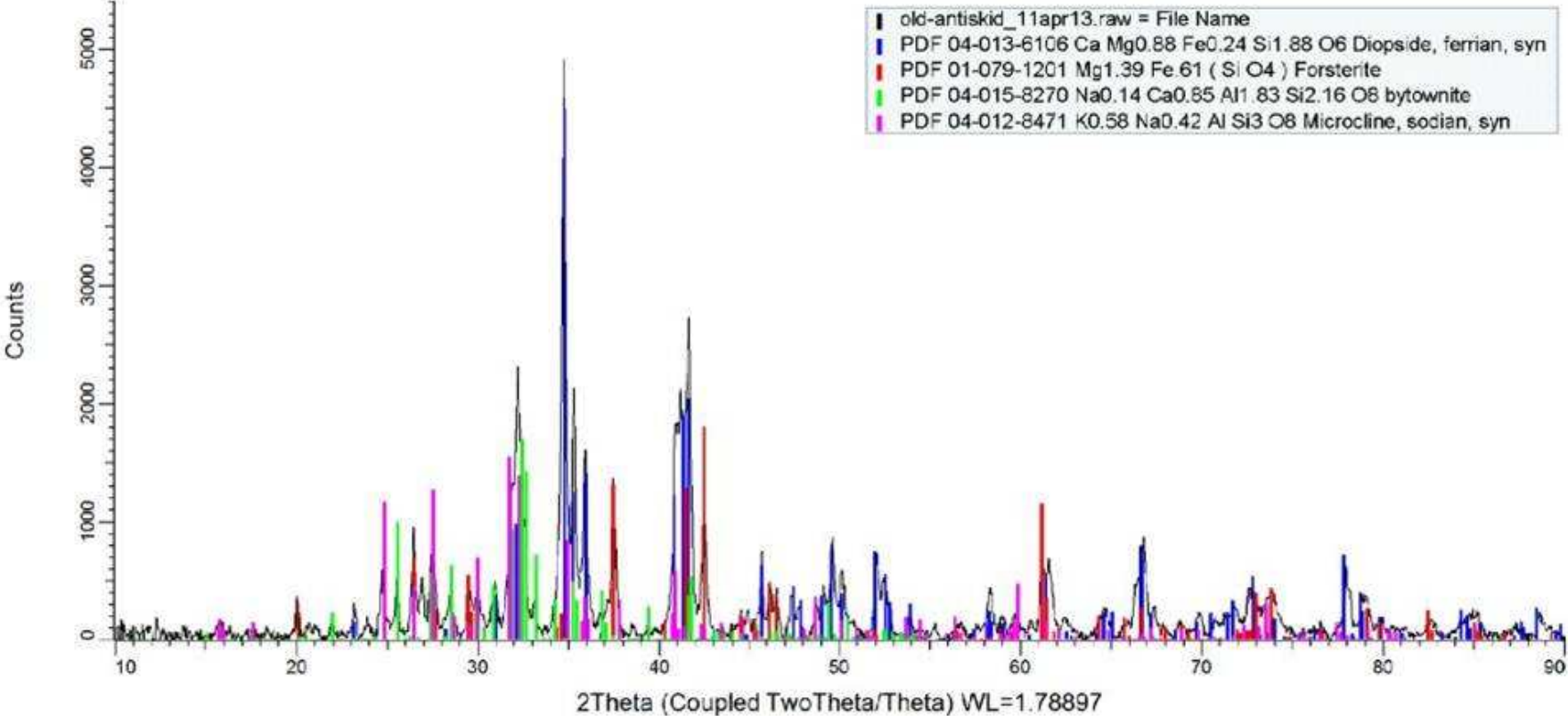


Figure 3-1 XRD plot of the mineralogical composition of the aggregate used by Possehl for tar-containing antiskid surfaces

Cored samples were collected from six military airfields, Soesterberg, Gilze-Rijen, Leeuwarden, Woensdrecht, Volkel and Eindhoven. These airfields are named after the cities near which they are located. Figure 3-2 shows the locations of the airfields. The antiskid layers of these six airfields were constructed in different years. Hence properties of antiskid layers of various ages could be investigated in this research. It is not clear whether Possehl has changed the tar-containing binder during all those years or not. But the FTIR test results in Chapter 4 will show large differences among specimens from different airfields.



Figure 3-2 Locations of six airfields [1]

From each airfield 10 cores were taken, including the antiskid layers and the underlying asphalt mixture layers. The cores were taken after visual inspections on the runways to ensure that the cores have same surface conditions. Due to some misunderstanding between coring companies and airfield authorities, the diameters of the cores from different airfields are not identical. They vary between 133 and 143 mm. Cores from Gilze-Rijen and Leeuwarden airfields have a diameter of 133 mm, while cores from the other four airfields have a diameter of 143 mm. Table 3-1 shows when the antiskid layers were placed, together with the sample diameter.

Table 3-1 Construction years of antiskid layers and diameters of cores

Airfield	Woensdrecht	Gilze-Rijen	Leeuwarden
Construction year	2009	2008	2007
Runway Length [km]	2.4	2.5 and 1.8	3.2 and 2.1
Runway width [m]	40	50	50
Core diameter [mm]	143	133	133
Airfield	Eindhoven	Volkel	Soesterberg
Construction year	2005	2004	1989
Runway Length [km]	3.0	--	3.0
Runway width [m]	40	--	40
Core diameter [mm]	143	143	143

The coring locations on the runways are shown in Figure 3-3. In order to avoid differences due to variation in construction, cores were taken in the same construction lane. To eliminate the influence of rubber deposits which can be found in the touch down zone, the second construction lane from the side and far enough from the landing and takeoff places was chosen (see Figure 3-3 (a)). However, because of a misunderstanding, No. 1 to 5 samples from Gilze-Rijen and all the samples from Leeuwarden airfield were not taken in longitudinal direction, but perpendicular to the construction lane, as Figure 3-3 (b) shows.

After coring, the antiskid layer was gently washed in the laboratory with a brush under running water. Then a high pressure air rifle was used to blow off dust and rubber fines. After measuring the thickness of the asphalt layers, all the samples were cut to 100 millimeter thickness for further testing. Some of the samples from Soesterberg Airfield were shorter than 100 mm. After these preparations, the cores were kept in a storage room at 15 °C.

The cores were numbered by the first capital character of the airfield location followed by roman numerals. Example: No.E2 presents core No.2 from Eindhoven Airfield.

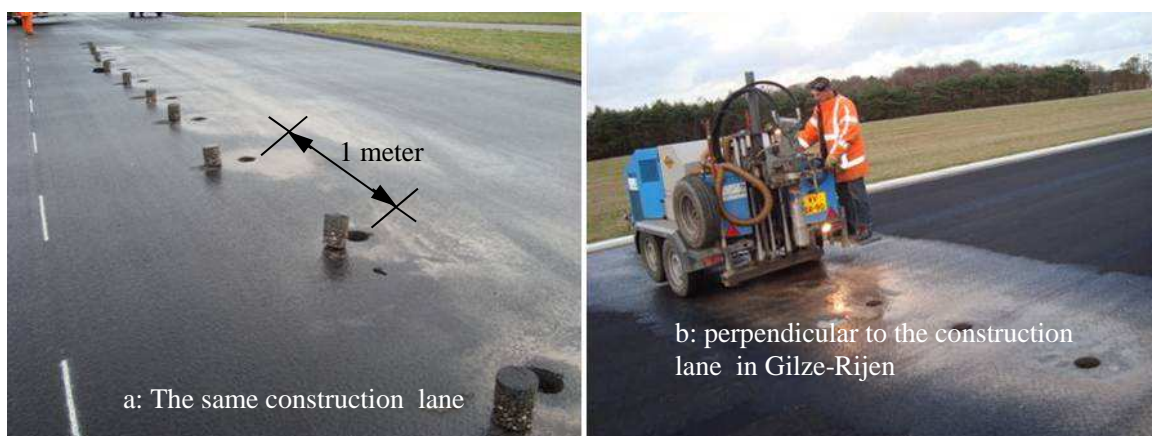


Figure 3-3 Sample locations on the runway

3.1.2 New Potential Binders

In this research, different types of binders were investigated. These binders were two-component Epoxy Modified Bitumen (EMB), two-component Modified Epoxy Resin (MER) and high content co-polymer Modified Bitumen Emulsion (MBE). All these investigated binders were newly developed products by companies. Only limited information about the binders could be obtained because of commercial reasons.

3.1.2.1 Two-Component Epoxy Modified Bitumen

The two-component EMB binders were obtained from ICOPAL Company¹. They were carefully selected to achieve proper mechanical properties and excellent compatibility with bitumen without phase separation and. The hardening mechanism is based on a chemical reaction between component A and B after mixing, leading to an open 3-dimensional structure of epoxy resin throughout a bitumen based matrix. Therefore, the mixture shows the advantages of both epoxy and bitumen.

According to the producer, component A is a bitumen based material. Component B is the hardener. After mixed and cured, EMB specimens can be prepared. EMB binder is a special mix of bitumen, additives, fillers and different bitumen-compatible epoxides. The composition is given in Table 3-2.

Table 3-2 Compositions in the EMB binder

Chemical epoxy resin	40-55%
Nynas bitumen (160-220 Pen)	10-20%
Mineral fillers	25-40%
Bio-oil (as a plasticizer)	2-10%

At the beginning of this research, three types of component A for EMB binders were investigated, named A1, A2 and A3. These three binders differ from each other in their chemical composition and mechanical properties. Their basic physical properties are given in Table 3-3. Same component B was used to mix with three types of component A.

¹ Icopal bv, <http://www.icopal.nl/>

Table 3-3 Technical information of binder A1, A2 and A3

Properties	Component A				Component B
	A1	A2	A3	A3-UV	
Appearance	Viscous liquid				Viscous liquid
Colour	Black				Yellowish
Viscosity at 25 °C [mPa•s]	7500	6700	6300	6500	400
Density at 25 °C [g/cm ³]	1.28	1.3	1.37	1.44	1
Reaction speed with component B	fast	middle	slow	slow	--
Mass percent [%]	85.5	86	86.5	87.5	14.5 for A1 14 for A2 13.5 for A3 12.5 for A3-UV

The obtained EMB binder was named as A1, A2 and A3 in this research according to its type of component A. A list of tests was then conducted on these three binders. EMB A3 binder was selected for further analysis because it behaves better than other two binders. A UV resistant additive (Hindered Amine Light Stabilizer, HALS, 1 wt. %) was specifically added into A3 to improve its UV resistance. The UV additive modified A3 binder was therefore named as A3-UV in this research. An EMB based antiskid surface was also constructed on slabs in the laboratory with A3-UV binder.

Table 3-4 presents the chemical bonds determined by means of FTIR for component A [2]. Figure 3-4 and Figure 3-5 present the FTIR spectrums of component B and component A (component A for binder A1, A2, A3 and A3-UV). In Figure 3-4, the absorbance peak located between 3289 and 3352 cm⁻¹ is the N-H stretching, and the N-H deformation is located at 1500- 1610 cm⁻¹.

Table 3-4 Characteristic bonds in component A

Wavenumbers [cm ⁻¹]	Chemical bonds
2969- 2871	C-H stretching of CH ₂ and CH aromatics and aliphatics
1508	C-C stretching of aromatics
1034	C-O-C stretching of ethers
915	C-O stretching of oxirane groups
829	C-O-C stretching of oxirane groups

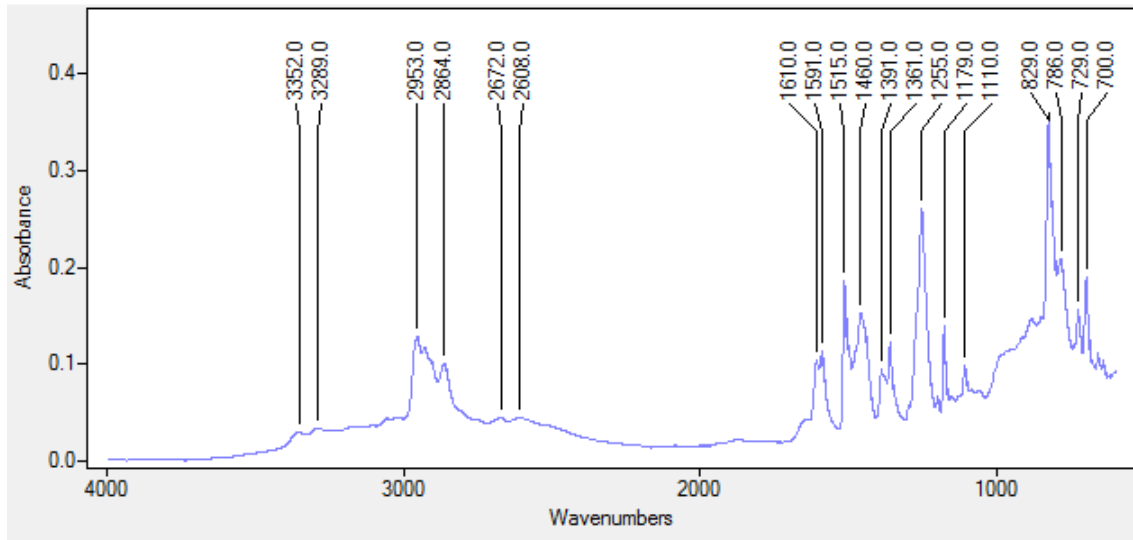


Figure 3-4 FTIR spectrums of component B

Components of the Aliphatic compound, the ether (R–O–R') group and the Ethylene oxide (C₂H₄O) group can be observed from Figure 3-5. The absorbance peaks for A2, A3 and A3-UV are very similar. But A1 differs strongly from the other three with the absorbance levels. The absorbance peak of CH stretching at 2969 cm⁻¹ is the highest. The absorbance peak of C-H in-plane bending of CH₂ and CH₃ at 1440 cm⁻¹ is also the highest compared to the peaks of the other three A-components. This means that there are more alkane bonds in the A component of A1.

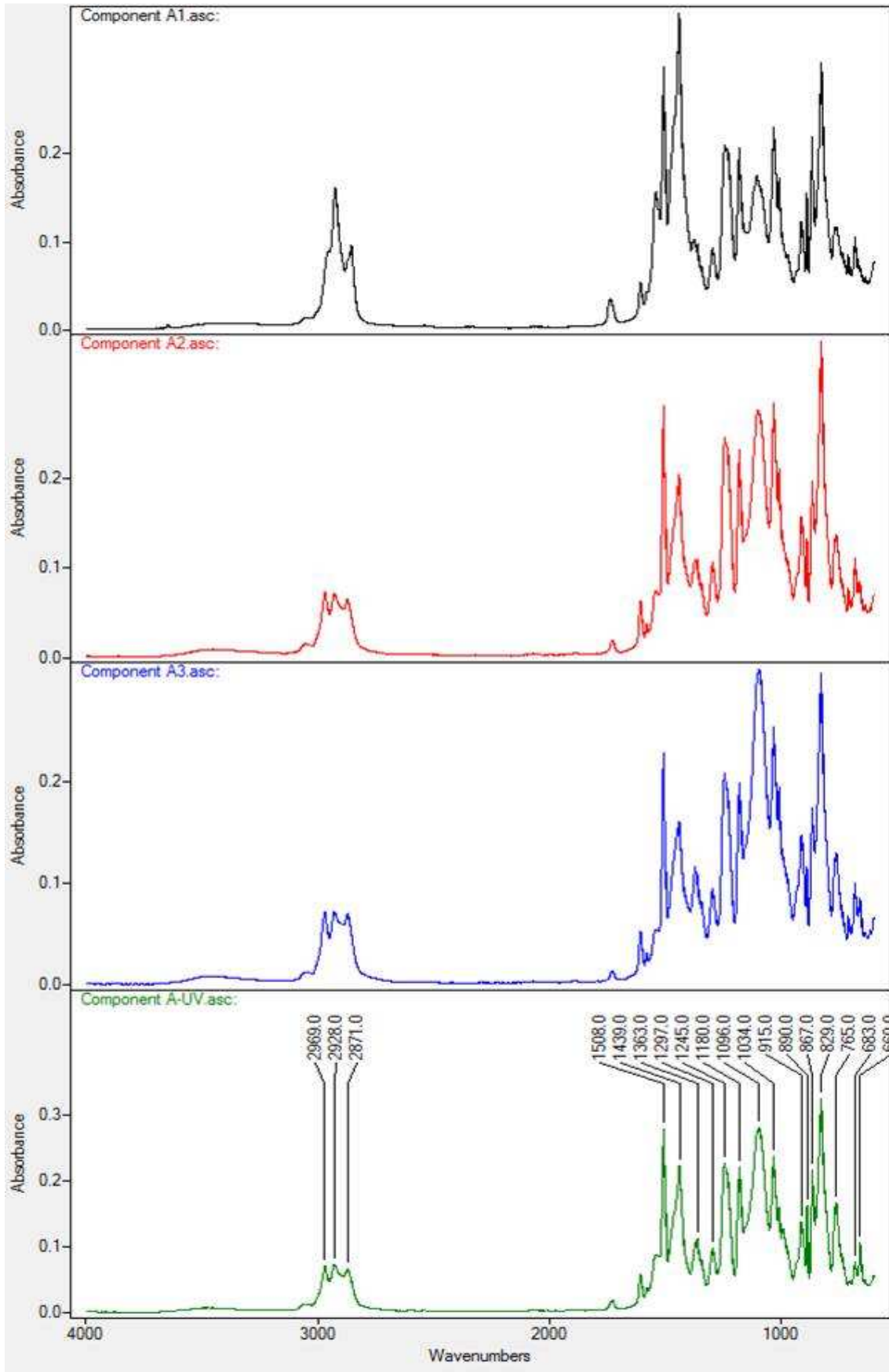


Figure 3-5 FTIR spectrums of component A

The sample preparation of two-component EMB is described hereafter [3]. After this preparation process, samples were cured in a temperature cabinet (22 °C and 14 °C). Then Direct Tensile Tests (DTT), Relaxation Tests (RT), Dynamic Shear Rheometer (DSR) tests, Dynamic Mechanic Analysis (DMA), ageing evaluation and weatherometer simulation were used to investigate the properties. The sample preparation involves the following steps:

1. Add component B to component A at the right mass ratio (see Table 3-3) at room temperature.
2. Mix thoroughly with a mixing machine till a homogeneous mix is obtained (1-2 minutes). Homogeneous mixing of components A and B is necessary for making the samples.
3. Then prepare the samples by pouring the mixture into the mould for DTT, DSR and DMA test specimens. Air voids need to be carefully avoided.

3.1.2.2 Modified Epoxy Resin

The MER materials were obtained from Latexfalt² Company. One type was investigated in this research. Some basic information on this material is given in Table 3-5. More information such as chemical composition was not available in this research.

The sample preparation steps for the MER are similar to the steps used for the two-component EMB. However, sample preparation of EMB and MER binders differs slightly. After mixing component A and B together, the MER is in a liquid state and cannot be poured into the DTT/DSR/DMA sample mould immediately. In order to get DTT/DSR/DMA specimens, the mixed epoxy resin was kept in the mixing container at an ambient temperature of 22 °C for 2 hours.

Table 3-5 Technical information of MER

Properties	Value	
	Component A	Component B
Appearance	Viscose liquid	Viscose liquid
Colour	Clear	Light yellow
Viscosity at 25 °C [mPa•s]	0.7-1.1	0.2-0.4
Density [g/ml]	1.12	0.99
Volume ratio for mixing	61.28	38.72

After 2 hours curing, the viscosity of the MER was high enough to be placed in the silicon rubber mould and DSR mortar mould. Then samples were cured in the mould at 14 °C to study its curing behavior.

² Latexfalt, <http://www.latexfalt.com/>

3.1.2.3 Polymer Modified Bitumen Emulsion

A high co-polymer content MBE was also obtained from Latexfalt Company. It was made from a hard bitumen binder with a low penetration.

Ten grams of MBE were placed in a container at 22 °C to follow the water evaporation speed and the residue content. Figure 3-6 shows the remaining weight in relation to time. It shows that there is a weight loss of 44.8% due to evaporation, which means that the bitumen binder content in the MBE is around 55.2%.

Figure 3-6 shows that around 120 hours (loss percentage is 30% after 20 hours) are needed to get the water phase fully evaporated. However, this simple test cannot simulate the real situation on a road. In the field, when the bitumen emulsion is applied, the specific surface charge of aggregates will attract the emulsifier. At higher temperatures and wind, the evaporation speed will be enhanced.

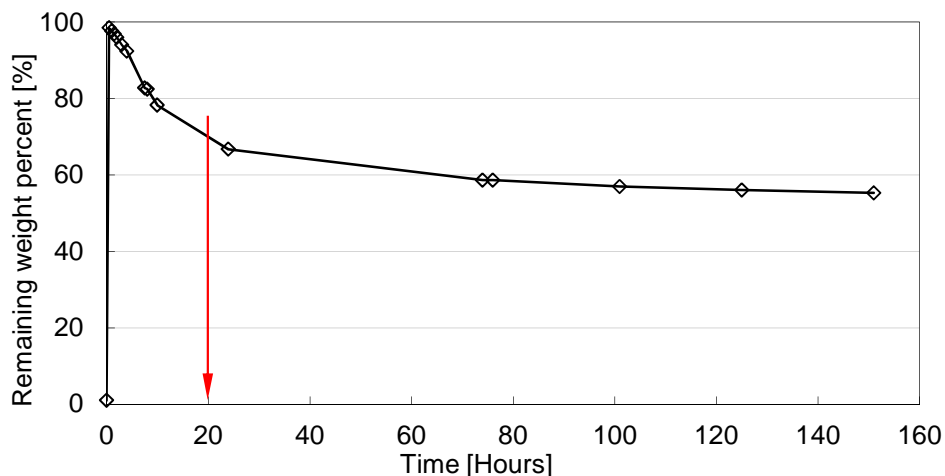


Figure 3-6 Weight lost percentage versus time of MBE

Following specification EN13074 (see Figure 3-7), three steps were used to obtain bitumen residues from MBE in the lab. 60 gram bitumen emulsion was spread onto a sheet of silicon paper with a size of 200 mm×200 mm [4]. This resulted in a film with a thickness of 1.5 mm. Residues obtained from this procedure are uniformly cured. After each of the three stages, the residue binder was removed from the silicon paper for further testing.

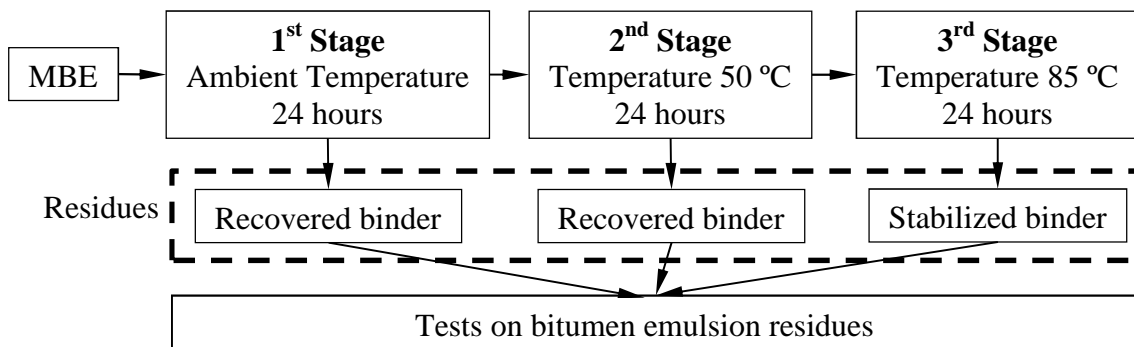


Figure 3-7 Curing program for tests on bitumen emulsion residues

3.1.3 Potential Antiskid Layers

Based on the research results (which will be discussed in Chapter 4 and Chapter 5) obtained on the new materials listed above, the ICOPAL EMB binder was used to design a new antiskid surface layer for further research. It should be mentioned that also other companies were invited by CROW to produce antiskid surfaces with their own products, but unfortunately they were not able to contribute to this research.

Antiskid layers were constructed on dense asphalt mixture slabs with a size of 600×600×50 mm. The underlying asphalt mixture slabs were constructed by KOAC-NPC³ under contract with CROW, while the surface antiskid layers were constructed by ICOPAL Company themselves. The asphalt mixture below the antiskid layer is an AC 11 mixture made with bitumen 40/60. The density of this asphalt mixture is 2326 kg/m³, and the average volumetric void content is 4.9%. Figure 3-8 shows the slab of a newly designed ICOPAL EMB based antiskid layer on top of an asphalt mixture. This antiskid layer is then named EMB-based antiskid layer in this research.

Table 3-6 Aggregate gradation of the asphalt mixture for the slabs

Aggregates	<2 mm	2-5.6	5.6-8	8-11.2	11.2-16
Percentage [wt. %]	0.61	10.34	23.66	13.09	1.12
Quartz sand	29.21 %		filler	9.74 %	
Moraine crushed sand	6.43 %		bitumen	5.8 %	

The EMB-based antiskid layer was constructed as follows: first, a thin cold epoxy modified bitumen film of approximately 1.5 mm thickness was sprayed onto the surface of the asphalt mixture layer. Secondly, aggregates with a high Polished Stone Value were spread over the binder evenly. After the binder was

³ KOAC-NPC: <http://www.koac-npc.com>

fully cured, the loose aggregates were swept away. Detailed information of this newly designed antiskid layer will be presented and discussed in Chapter 6.

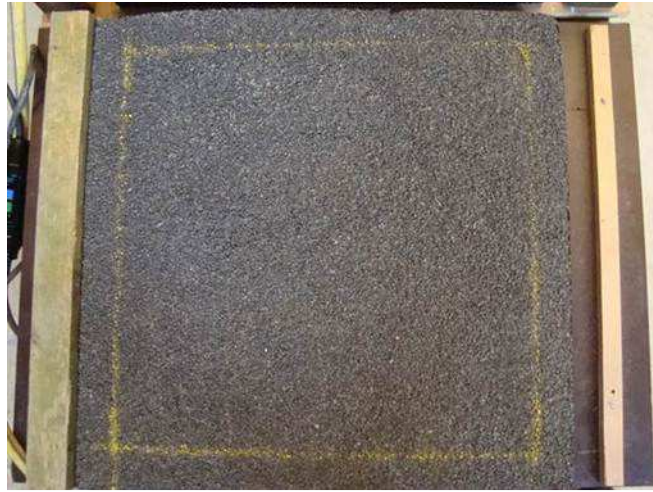


Figure 3-8 Slab with newly designed antiskid layer on top

Besides the newly designed EMB based antiskid layer from ICOPAL, Schiphol airport also provided specimens with a non-tar-containing antiskid surface layer (see Figure 3-9) produced and placed by Possehl. The specimens were collected from a newly constructed runway, and named as “Schiphol antiskid” in this research. The coring was done within one year after construction of the antiskid surface layer. The binder used for the new Schiphol antiskid layer is still patent protected and therefore no information and test results were made available about this new binder. Only research on the completed antiskid surface layer could be carried out.



Figure 3-9 Schiphol cores with new Possehl antiskid layer

The mineralogical composition of the aggregate that was used for the EMB-based antiskid layer and Schiphol-antiskid are presented in Figure 3-10 and

Figure 3-11. The aggregates from Schiphol-antiskid have the same mineral composition as the basalt for the tar anti-skid antiskid. The aggregates used for ICOPAL EMB-based antiskid layer contain the following mineral components:

- Corundum, Al_2O_3
- Hematite, Fe_2O_3
- Quartz, SiO_2
- Diaspore, $\text{AlO}(\text{OH})$
- Chloritoid, $\text{Mg}_{0.26}\text{Mn}_{0.06}\text{Fe}_{1.75}\text{Al}_{3.88}\text{Si}_{2.05}\text{O}_{10}(\text{OH})_4$

The sand patch test was first conducted on these slabs (or cores) to investigate the macro surface texture and structure characteristics. Then cylindrical cores were drilled and used for further testing. These tests included adhesion tests and Nano CT scanning.

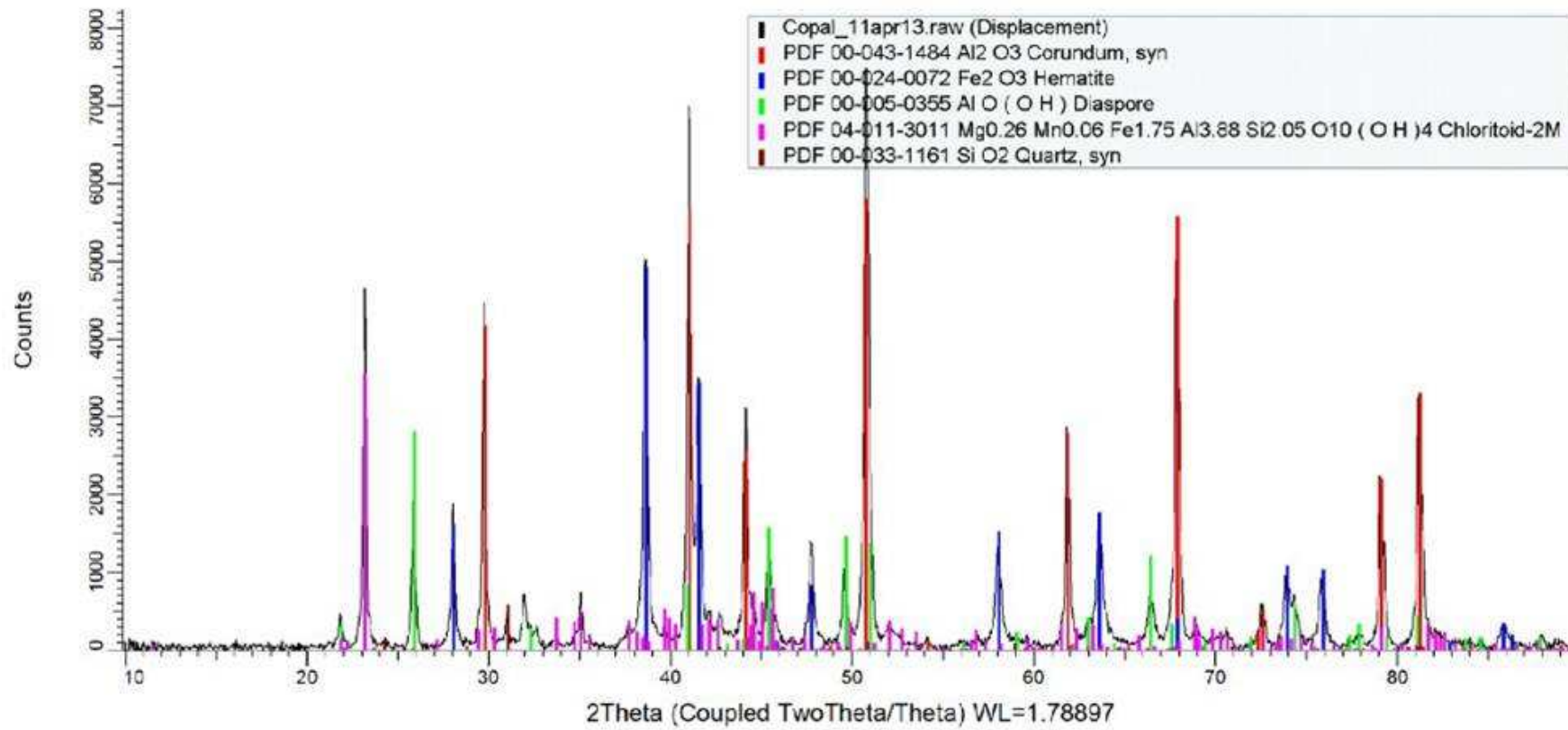


Figure 3-10 XRD plot of the mineralogical composition of aggregate for EMB-based antiskid surfaces

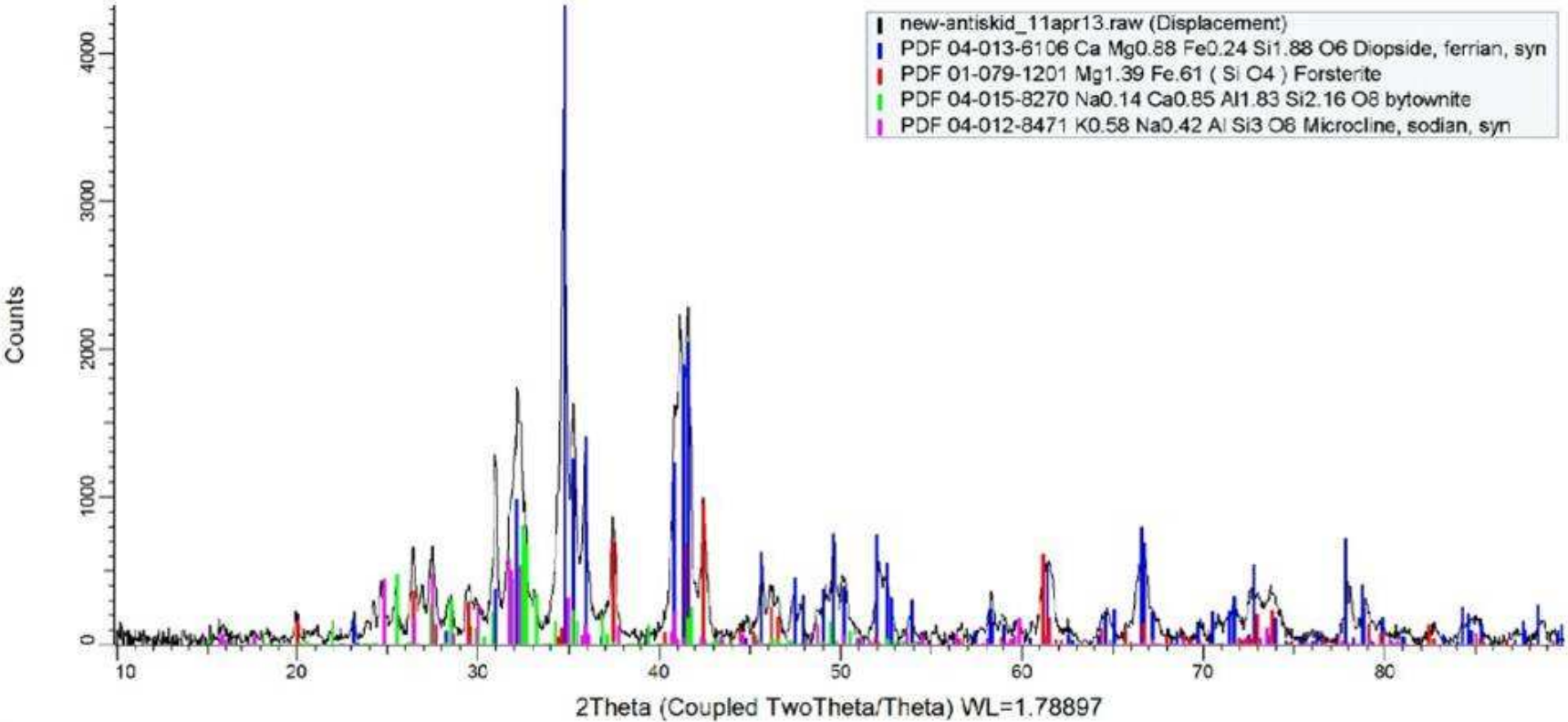


Figure 3-11 XRD plot of the mineralogical composition of aggregate for Schiphol antiskid surfaces

3.1.4 Noise Reducing Thin Surface Layers

In addition to the research on new binders for antiskid layers for runways, thin surface layer applications for roads are also analyzed in this research. Two types of noise reducing thin surface layers, named NRTSL-R and NRTSL-1, were investigated (see Figure 3-12).

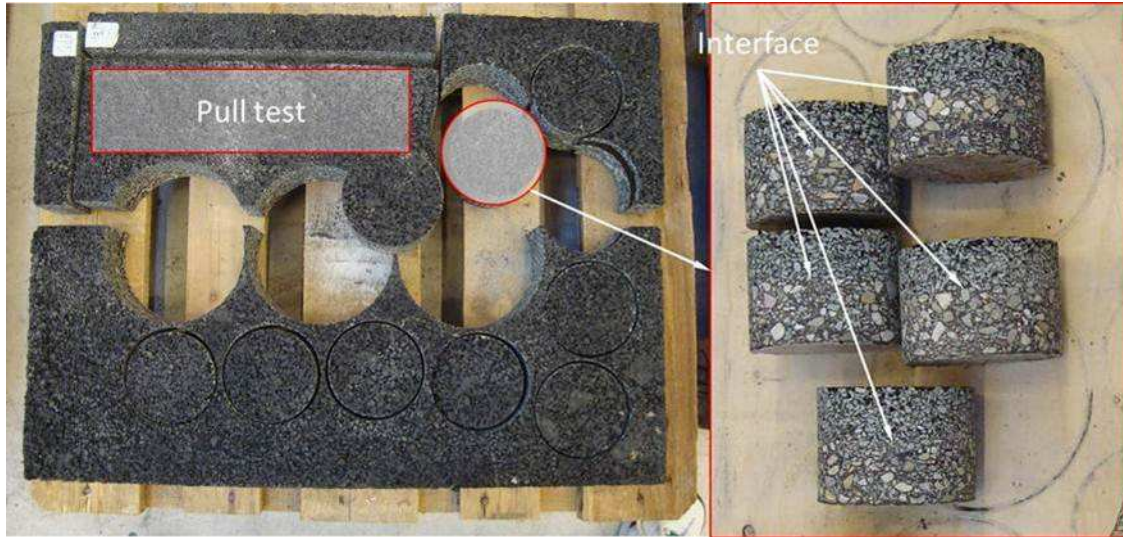


Figure 3-12 Thin surface layers and cylindrical specimens

Table 3-7 gives basic information about the two tested NRTSLs. The difference between these two NRTSLs is the void content. The NRTSL-R has a void content of 12% by volume, while NRTSL-1 has a void content of 18%. Shell Cariphalte DA binder was used. Cariphalte DA is specially designed for friction layers [5]. It can provide sufficient adhesion to prevent cracking and raveling. The underlying asphalt mixture is a conventional base layer from the mill (according to the Standard RAW Bepalingen 2005, CROW [6]). It satisfies the mix composition requirements of the RAW standard 2005.

Table 3-7 Information for thin surface layers

Properties	Value	
	NRTSL-1	NRTSL-R
Coarse aggregate content, % by mass	78	78
Max. aggregate size, mm	2/6	2/6
Air voids content, % by volume	18	12
Binder content, %, by mass ratio with the mineral aggregate	6.1	6.1
Aggregate type	Bestone	Bestone
Layer thickness	30 mm	
Bitumen type	Cariphalte DA	
Surface texture	0.87	0.71

3.2 Tests on Binders

3.2.1 Ageing Evaluations

Binder tests were performed on both the original and aged binders. The commonly used ageing procedures for bitumen binders cannot be used for EMB and MER since they are thermal setting materials. They will get hard after being fully cured and cannot be reheated like bitumen binders to make specimens. Furthermore, exposure of epoxy type of materials to high pressure condition (e.g. Pressure Aging Vessel) may damage the large molecules. This would not represent realist ageing in the field.

Therefore, an oven and a weatherometer were used to simulate ageing due to environmental conditions.

3.2.1.1 Oven Ageing

In this research, an oven was used to simulate high temperature ageing. Cured samples (DTT specimens, DMA beams and DSR columns of A1, A2, A3 and MER binders) were placed in an oven at 85 °C for 7 days. Figure 3-13 shows the original EMR binder and 7 days aged EMR binder. A change in color occurred during the high temperature ageing in the oven, which indicates that chemical reactions may have taken place.

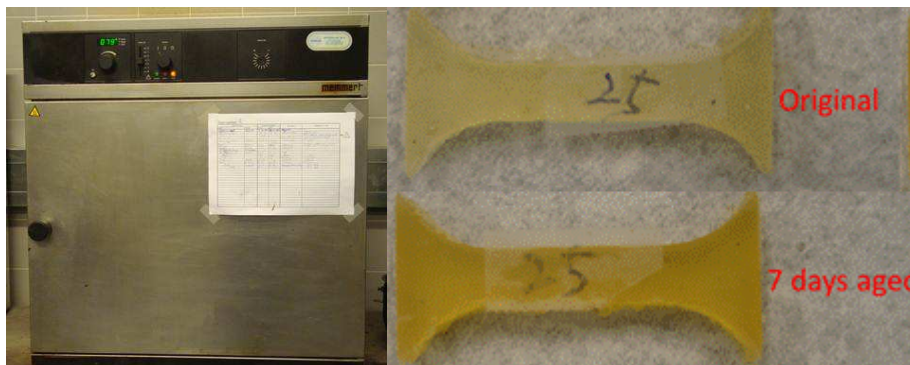


Figure 3-13 Oven (left) and MER binder before and after ageing in the oven

3.2.1.2 Weatherometer Ageing

The effects of weather conditions were simulated by using a weatherometer. The available equipment at TU Delft for accelerated weathering is the SUNTETST XXL+ from Atlas Materials. The instrument simulates environmental parameters like UV radiation, temperature, and moisture/humidity. An artificial light source (Xenon arc lights) is used that closely simulates the UV and visible part of the solar radiation. This equipment is recommended to accelerate ageing of materials which are exposed to natural sunlight during their service life [7].

Columns and beams of A3-UV binder were placed in the weatherometer chamber for accelerated ageing. The research results presented in Chapter 4 indicate that A1, A2 and MER binders did not provide as good behaviors as A3 binder. Hence weatherometer ageing was not conducted on the A1, A2 and MER binders. Figure 3-14 shows the instrument and specimens placed in the chamber.



Figure 3-14 Weatherometer and DSR/DMA samples

The equivalent number of hours to simulate one year field conditions in the Netherlands can be calculated as [7]:

$$t(hr) = \frac{H(Ws/m^2)}{E(W/m^2) \times 3600(s/hr)} = \frac{215 \times 10^6}{60 \times 3600} = 995hr \quad (3-1)$$

Where, H is the annual mean radiant exposure, 215×10^6 Ws/m^2 exposed in the UV range of 300-400 nm, E is the intensity of xenon lamps, 60 W/m^2 . Therefore, 1000 hours of UV exposure in the weatherometer chamber is realistic to simulate the effect of one year UV radiation during service life.

As Table 3-8 shows, the ageing conditions are: 40 °C of CHT (temperature of the air circulating within the chamber), 60 °C of BST (black surface temperature of the specimens), and UV irradiance in the range of 300-400 nm with 60 W/m^2 .

Table 3-8 Simulation conditions in the weatherometer

Ageing protocol	UV-Humidity ageing
Air temperature [°C]	40
BST temperature [°C]	60
UV light (300-400 nm) [W/m^2]	60
Humidity [%]	70
Time [hour]	1000

According to research by Hagos [7], the mean average relative humidity for an entire year in the Netherlands is between 77% to 89.4%. Because of the limitations of the used weatherometer, 70% humidity was used in this research. Specimens were placed in this environment for 1000 hours.

3.2.2 Direct Tensile Test

The DTT was employed to determine the tensile strength of binders under a constant displacement loading speed. Figure 3-15 schematically shows the size of the DTT samples. Figure 3-16(1) shows typical DTT samples in the silicon mould. When the liquid binders were poured into the mould, overfilling was necessary to ensure that enough binder was available to completely fill the mould after curing. Sample preparation is critical and has a large influence on the test results. Specimens with bubbles should not be used. [8, 9]

Normally, in the DTT test for bitumen binder/mortar samples as shown in Figure 3-15 are used. But for the MER and EMB binders, the tensile strength is much higher than the adhesive strength between the binder and steel plate. In preliminary tests, the specimens mostly failed at the adhesive zone between the binder and steel instead of in the binder. In order to avoid this undesirable adhesive failure, the tested samples were first glued to the steel with X60 polymer glue before testing.

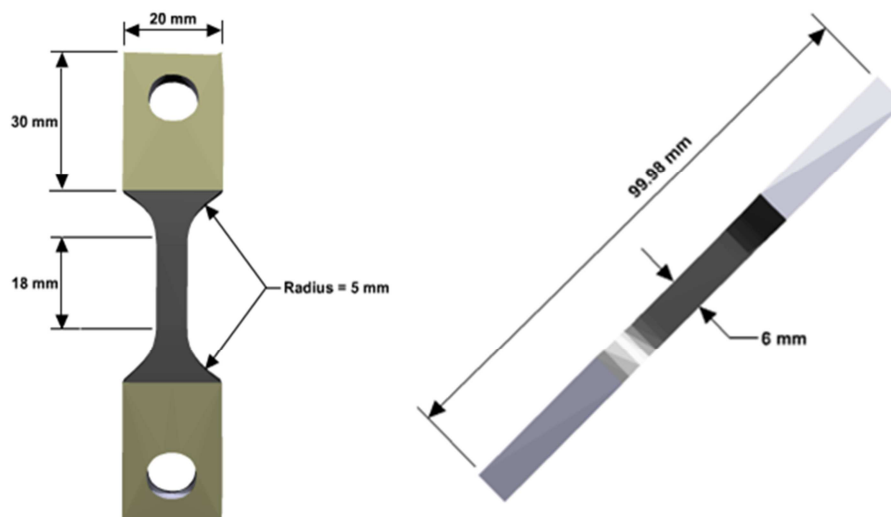


Figure 3-15 The schematic sizes of DTT samples

X60⁴ is a 2-component fast curing adhesive glue. It provided a high enough adhesive strength between the binders and steel plates. X60 is not sensitive to ambient temperature. Figure 3-16(2) shows test specimen with glue at both sides.

⁴X60 glue: <http://www.hbm.com/nl/menu/producten/rekstroken/adhesives-bonding-material/x60/>

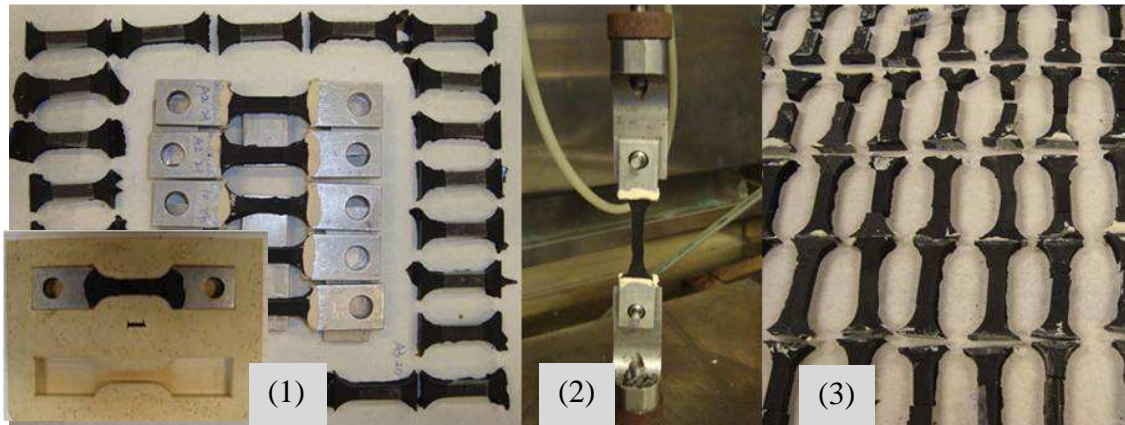


Figure 3-16 Sample preparations for DTT test

(1) Specimens, (2) Specimen glued to steel plates, (3) Failed specimens

After a certain curing time, the samples were tested at a constant displacement rate (different values dependent on testing temperature) until failure. The maximum failure stress and displacement are recorded. Figure 3-16(3) shows the specimens after the tensile tests were performed. The DTT samples mainly failed in the middle area. Tests were performed on A1, A2, A3 and MER binders.

The following equations are used to calculate the tensile strength and tensile strain.

Tensile strength:

$$\sigma_f = \frac{P_f}{A} \quad (3-2)$$

Tensile strain:

$$\varepsilon = \frac{D}{L_e} \quad (3-3)$$

Where,

σ_f = Tensile strength, also named as direct tensile strength, [MPa];

A = original cross-sectional area, [mm²], here $A=36 \text{ mm}^2$;

P_f = maximum load, [N];

ε = strain at maximum load;

D = the displacement at the maximum load, [mm];

L_e = the effective length of DTT samples, [mm].

If the entire sample length (40 mm, see Figure 3-15) is used for the strain calculations, the actual strain occurring in the center section (18 mm) is underestimated. However, in this research it was not possible to establish reliable reference points for a laser system to measure the displacement only in the

central part (18 mm). Therefore, an effective length of 33.8 mm is used as the equivalent length [10].

Figure 3-17 shows the plots of displacement and resulting force versus time as measured during a DTT test [3]. When a constant displacement rate is applied, the responding force sharply increases at the beginning. Before it fails, there is a more or less constant force plateau which is the failure propagation stage. The shorter the failure propagation stage is, the more brittle the material is. When the applied displacement reaches the maximum strain, the specimen fails immediately.

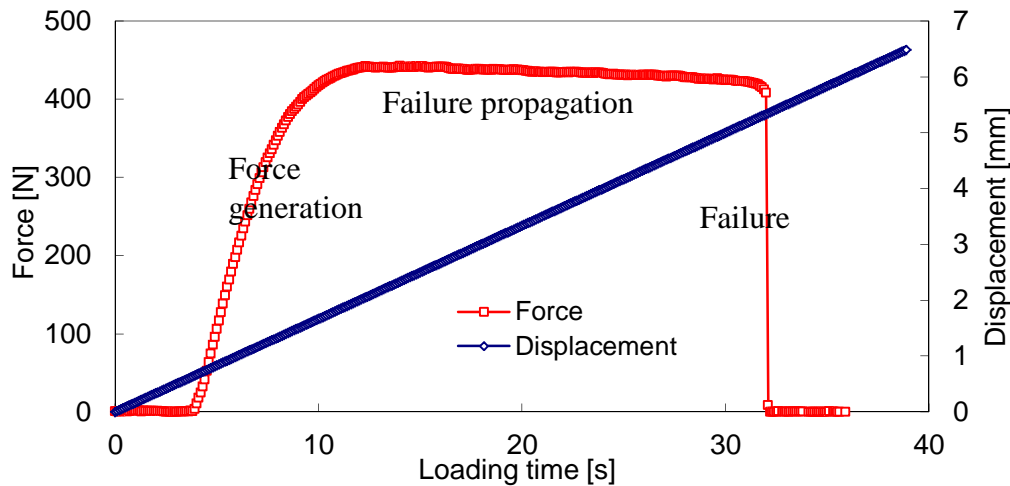


Figure 3-17 Displacement rate and resulting force curve for DTT on EMB

3.2.3 Relaxation Test

Relaxation tests (RT) were performed using DTT samples and the DTT machine. Relaxation time and loading force were monitored at constant testing temperatures. The test was performed in three steps. First, the specimens were conditioned in the testing machine at the specified test temperature for 60 to 75 minutes. Then a constant displacement rate of 10 mm/minute was applied till a certain force was reached, which was 40% of the failure force of fully cured samples. After that, the displacement was kept constant for 10 minutes and the relaxation of the resulting force was monitored. This test was conducted on A1, A2, A3 and MER binders.

At the same time, relaxation tests were also performed on the A3 binder with a DSR machine. A strain level of 2% was first applied onto the specimen within 2 seconds. This strain level was kept constant for 5 minutes. The resulting stress was then recorded.

The relaxation percentage after 10 minutes in the DTT test (or 5 minutes in the DSR relaxation test) was calculated by using the following equation:

$$R = \left(1 - \frac{F_{\text{Remain}}}{F_{\text{MaxApplied}}}\right) \times 100 \quad (3-4)$$

Where,

R = relaxation percentage after 10 (or 5) minutes, [%];

F_{remain} = remaining force after relaxation at certain time, [N];

$F_{\text{Maxapplied}}$ = the maximum applied force, [N].

Figure 3-18 shows a typical graph of the applied displacement and the resulting force as a function of time for a relaxation test performed on the EMB binder [3]. EMB is a viscoelastic material, so when the displacement is fixed, the stress generated in the binder will decrease significantly at the beginning. After a certain period of time, the remaining stress will stay constant at a low level. The relaxation property of purely elastic materials is 0%, while for purely viscous materials it is 100%.

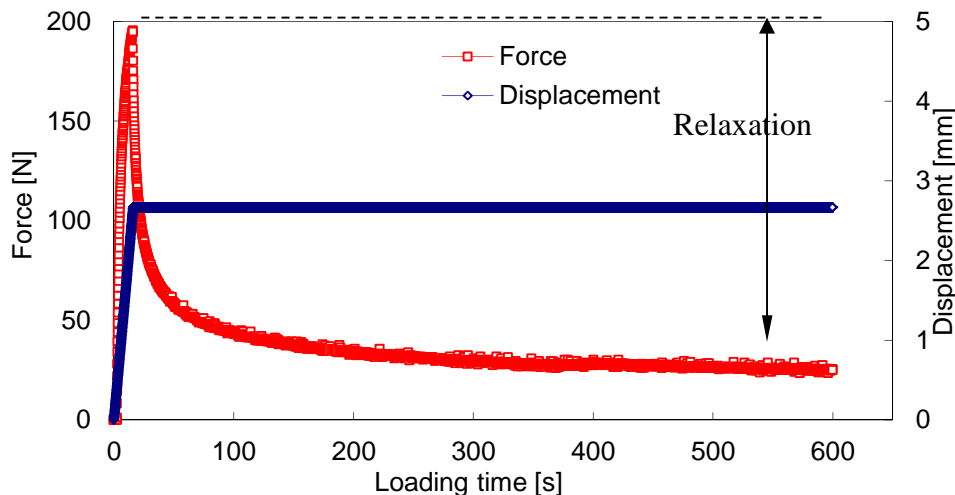


Figure 3-18 Example of applied displacement and resulting force versus time in a RT from DTT on EMB

3.2.4 Dynamic Shear Rheometer

Bituminous binders are viscoelastic. They behavior both viscous and elastic characteristics when deformation is applied. Furthermore, the viscoelastic properties of bituminous binders are also temperature dependent. This means that they behave like an elastic solid (deformation due to loading is recoverable, which means they are able to return to their original shape after a load is removed) at (very) low temperature and like a viscous liquid (deformation due to loading is non-recoverable, which means they cannot at all return to their original shape after a load is removed) at high temperature. The DSR is capable of quantifying

both the elastic and viscous properties in the lab. This makes the device well suitable for characterizing asphalt binders at medium to high temperatures.

From the DSR measurements in sinusoidal mode the specimen's complex shear modulus (G^*) and phase angle (δ) can be determined. The complex shear modulus can be considered as the sample's total resistance to deformation when repeatedly sheared in sinusoidal mode. It can be calculated by equation 3-5 and 3-6:

$$\tau_{\max} = \frac{2T}{\pi r^3} \quad \gamma_{\max} = \frac{\theta r}{h} \quad (3-5)$$

Where:

- τ_{\max} = maximum applied stress;
- γ_{\max} = the resulting strain;
- T = maximum applied torque;
- r = specimen radius;
- θ = rotation angle, in radians;
- h = specimen height.

The Complex shear modulus (G^*) can be determined by:

$$G^* = \frac{\tau_{\max}}{\gamma_{\max}} \quad (3-6)$$

The phase angle (δ) is the lag between the applied shear stress and the resulting shear strain during sinusoidal loading (see Figure 3-19). It is an indicator of the relative amounts of recoverable and non-recoverable deformation. The larger the phase angle is, the more viscous the material will be. Purely elastic materials have a phase angle of 0 degrees, while purely viscous materials have a phase angle of 90 degrees. So the phase angle can be regarded as a measure of the viscoelasticity of the material.

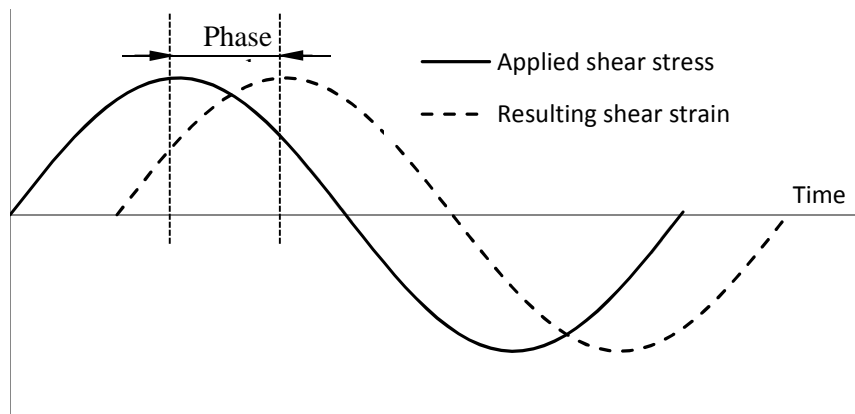


Figure 3-19 DSR applied stress, resulting strain and phase angle

The sinusoidal signal of the applied stress and resulting strain can be represented by a complex notation as shown below:

$$\gamma^* = \gamma_d e^{i\omega t} = \gamma_d (\cos \omega t + i \sin \omega t) \quad (3-7)$$

$$\tau^* = \tau_d e^{i(\omega t + \delta)} = \tau_d (\cos[\omega t + \delta] + i \sin[\omega t + \delta]) \quad (3-8)$$

Where, γ^* is the complex shear strain, γ_d is the shear strain amplitude, τ^* is the complex shear stress, τ_d is the shear stress amplitude, and δ is the phase angle.

The complex shear modulus can be given by the following equations:

$$G^*(\omega) = \frac{\tau^*}{\gamma^*} = \frac{\tau_d}{\gamma_d} e^{i\delta} = \frac{\tau_d}{\gamma_d} (\cos \delta + i \sin \delta) = G' + iG'' \quad (3-9)$$

$$G' = G^* \times \cos(\delta) \quad G'' = G^* \times \sin(\delta) \quad (3-10)$$

$$\tan \delta = \frac{G''}{G'} \quad (3-11)$$

Where, G' is the storage modulus and G'' is the loss modulus. The storage modulus represents the elastic component of the viscoelastic behavior, while the loss modulus represents the viscous component [5]. The in-phase and out-of-phase component of the complex shear modulus are shown in Figure 3-20 [7].

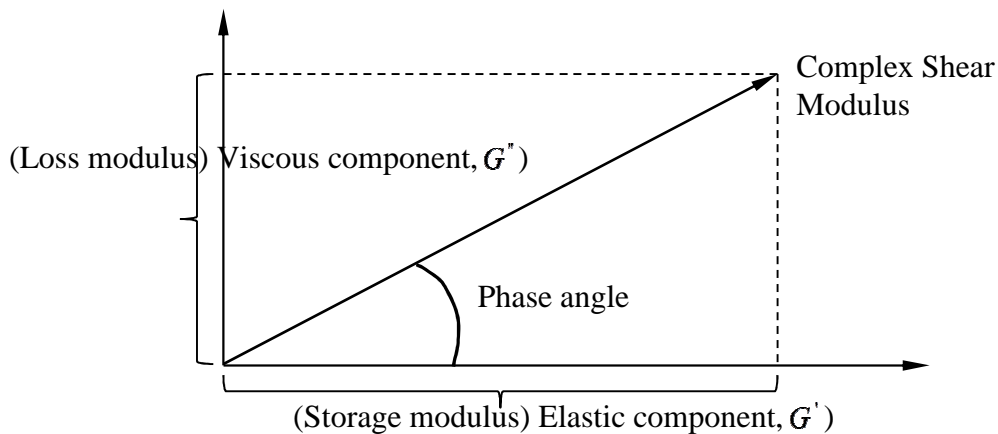


Figure 3-20 Relation between complex shear modulus and its storage and loss modulus components

3.2.4.1 Standard DSR Test

In the standard DSR test on bitumen [11] a thin bitumen sample is sandwiched between two circular plates. The lower plate is fixed while the upper plate oscillates back and forth across the sample at a certain frequency to create a

shearing torque (see Figure 3-21). Basic DSR tests were only conducted on the 1st stage, 2nd stage and 3rd stage residues (see Figure 3-7) of the MBE binder. Figure 3-22 shows the DSR specimen and test geometries.

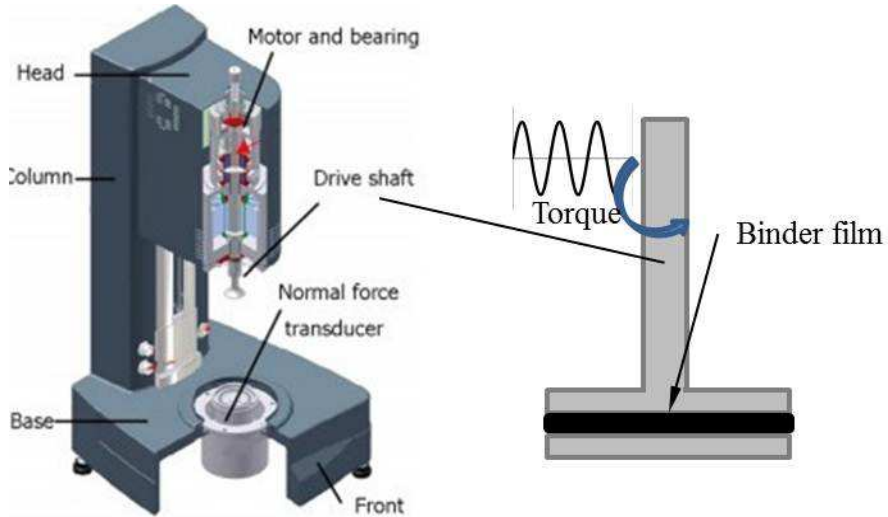


Figure 3-21 Dynamic Shear Rheometer test equipment⁵

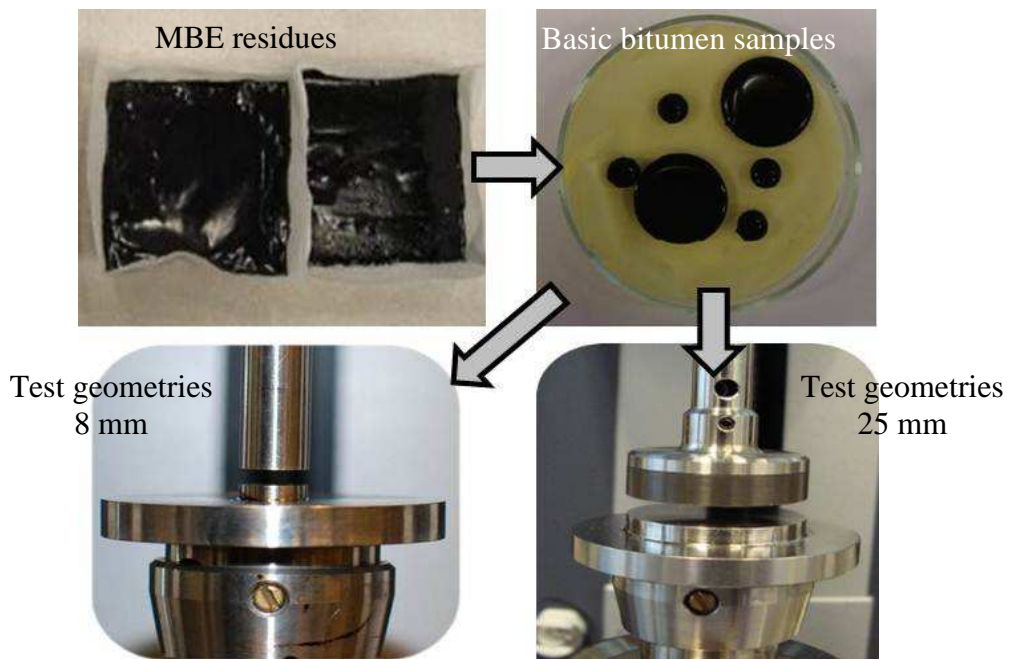


Figure 3-22 DSR specimens and test geometries

⁵TA INSTRUMENTS-Rheometers:
http://www.me.ust.hk/~cemar/Characterization/Materials%20Characterization/AR_Brochure.pdf

Residues of the modified bitumen emulsion were reheated to prepare DSR samples. In order to reduce the effect of sample geometry, 2 different diameter sizes were used. 8 mm diameter parallel plates and 25 mm diameter plates were used dependent on the testing temperature. The 8 mm diameter plate is normally designed for tests at temperatures below 20 °C. The 25 mm plate is normally designed for tests at temperatures higher than 20 °C. Before starting the DSR tests to determine master curves with frequency sweeps at several temperatures, strain sweeps are performed to check if the tests can be done in the linear visco-elastic region of that binder over the whole temperature range.

3.2.4.2 Column Shear Test

EMB and MER are thermal setting materials. They will get hard after being fully cured, which means that they cannot be reheated like bituminous binders. It is possible to prepare small DSR type disks and glue them on the top and bottom plate for shear testing. However, many unexpected influences might be introduced to the test itself and hence the results might not be reliable. Therefore, shear test on columns were used in this research to evaluate the rheological properties of EMB and MER binders.

The preparation of the column type specimens is shown in Figure 3-23. The two components of EMB or MER were first mixed homogenously. Then the liquid state binder was carefully poured into a special designed mould made of silicone plastic. After the binder was fully cured, the mould was disassembled and the cylindrical mortar columns were ready to be tested using the DSR test equipment.

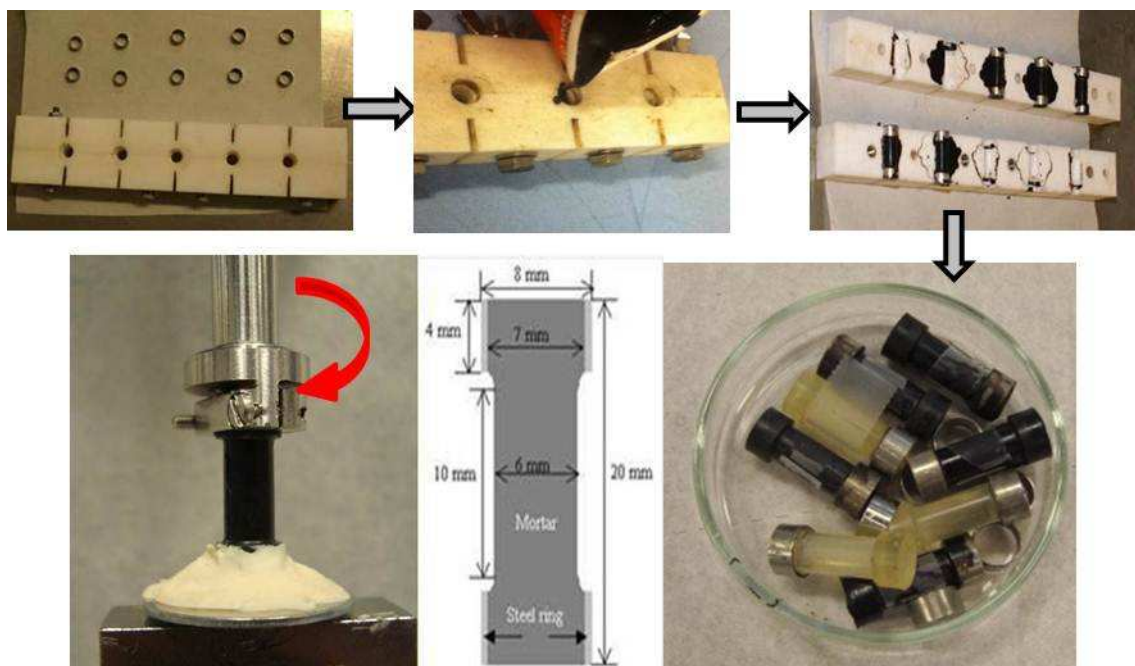


Figure 3-23 Preparation of column specimens for the DSR test

The left-bottom figure shows a typical DSR test on a binder column and the relevant sizes of column sections. The effective height of DSR column is 12.742 mm. [12]

3.2.4.3 Master Curves

Frequency sweep tests were conducted with the DSR at various temperatures and frequencies (from 0.1 rad/s to 300 rad/s). Then master curves for the shear complex modulus and phase angle were constructed using the time-temperature superposition principle. This principle allows shifting the response data at various temperatures with respect to time or frequency to a selected reference temperature. The curve obtained using this principle shows the frequency or loading time dependency of the complex shear modulus and phase angle over a wide loading time or frequency range.

The amount of shifting required at each temperature to the reference temperature was determined using the Williams-Landel-Ferry (WLF) equation [13, 14]:

$$\log(\alpha_T) = \frac{C_1(T - T_{ref})}{C_2 + (T - T_{ref})} \quad (3-12)$$

Where,

- α_T = the shift factor at a temperature of T ;
- T_{ref} = reference temperature, [°C];
- C_1, C_2 = are constants.

The reduced frequency is then determined by multiplying the test frequency by a shift factor:

$$f_R = f \times \alpha_T = f \times 10^{\frac{C_1(T-T_R)}{C_2+T-T_R}} \quad (3-13)$$

The data of complex shear modulus and phase angle were then fitted using the following S-curve model:

$$G^* = G_{min} + (G_{max} - G_{min}) \times (1 - \exp(-(\frac{f_R}{\beta_G})^{\gamma_G})) \quad (3-14)$$

$$\delta = \delta_{min} + (\delta_{max} - \delta_{min}) \times \exp(-(\frac{f_R}{\beta_\delta})^{\gamma_\delta}) \quad (3-15)$$

Where,

- G^* = complex modulus, [Pa];
- f_R = reduced frequency, [rad/s];
- G_{min}^*, G_{max}^* = complex modulus when f_R is 0 or infinite, [Pa];
- δ = phase angle, [°];

- $\delta_{\min}, \delta_{\max}$ = phase angle when f_r is infinite or 0, [°];
- β_G, β_δ = location parameters of the S-curve;
- γ_G, γ_δ = shape parameters of the S-curve.

Figure 3-24 presents an example of master curves for the residue from modified bitumen emulsion after the 3rd stage of curing (see Figure 3-7). The two blue lines show the master curves of complex modulus and phase angle at a wide frequency range. They were constructed by using the solver function in the Excel spreadsheet through minimizing the mean relative error. The other lines show the DSR frequency results, each line represents one test temperature.

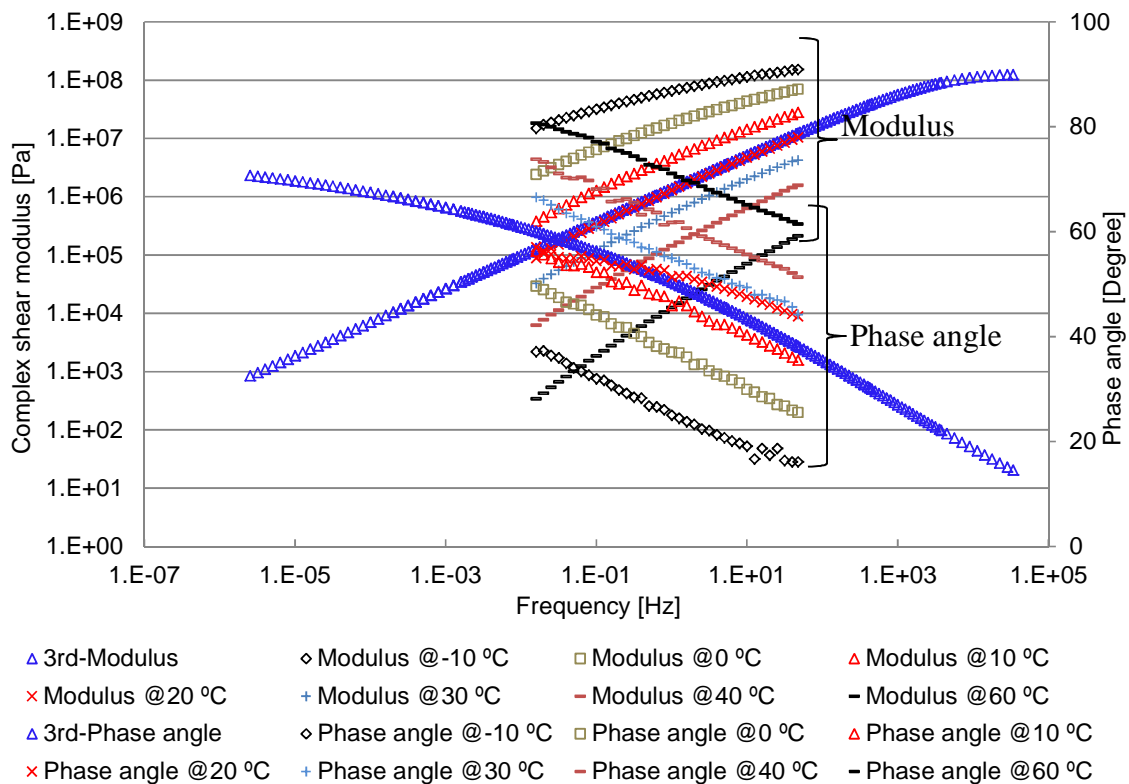


Figure 3-24 Master curves at 20 °C for the 3rd stage cured modified bitumen emulsion

3.2.5 Dynamic Mechanical Thermal Analysis

This research is aiming to define a performance evaluation model for thin surfacings, as well as antiskid surfacing. So, on the one hand, tests involved in this research are chosen because they can characterize the crucial performance aspects for antiskid layer applications. On the other hand, they are also based on whether they are workable and acceptable from a road material designer’s point of view. The DSR can characterize the viscoelastic properties of a binder quite well, but not all the suppliers have a DSR. Some of them may prefer to use DMA

(Dynamic Mechanical Thermal Analysis). Therefore, DMA is also included in this research.

DMA was used to investigate the viscoelastic properties of the binders, specifically at the higher temperature range from 60 °C to 200 °C. The DMA is commonly used to determine the storage and loss modulus, the phase angle, or the dynamic and complex modulus of materials. With the DMA, one can measure the amplitude and phase difference of the displacement of a sample in response to an applied oscillating force (see Figure 3-19) [15].

Figure 3-25 shows the DMA bending setup for binder beams. The complex modulus, storage modulus and loss modulus can be obtained by the following equations:

$$E^* = \frac{\sigma_{\max}}{\varepsilon_{\max}} = |E^*| e^{i\delta} = E' + i \times E'' \quad (3-16)$$

$$\delta = \arctan\left(\frac{E''}{E'}\right) \quad (3-17)$$

Where:

- E^* = complex modulus, [Pa];
- σ_{\max} = the peak value of sinusoidal stress, [Pa];
- ε_{\max} = the peak value of the sinusoidal strain;
- $|E^*|$ = the absolute value of complex modulus, [Pa];
- δ = the phase angle;
- E'' and E' = loss modulus and storage modulus.

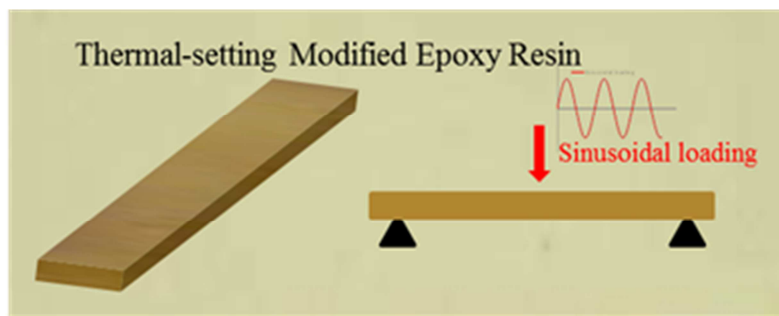


Figure 3-25 DMA bending setup and binder beams

Because of restrictions in availability, two DMA testers were used in this research. One was used to conduct tests on MER binder beams which were 30 mm long, 8 mm wide and 2 mm thick. The other one was used for A3-UV binder beams which had a smaller size. This will be discussed in Section 5.3.2.3 in Chapter 5.

3.3 Adhesion Tests

The adhesion at the interface between a thin surface layer (e.g. antiskid surface) and the underlying asphalt mixture layer is an important feature influencing the durability of the surface layer. Test methods that allow evaluating this characteristic include the tensile adhesion and shear adhesion test.

Pull tests were widely used because they can be done easily in the field [16]. A CROW working committee did some tests on antiskid materials for runways in the past [17]. They used a simple pull test to measure the bonding strength between the antiskid layer and the asphalt mixture layer in the field (see the left picture in Figure 3-26).



Figure 3-26 Simple pull test setups

Other test methods like the Torque Bond test (the right picture in Figure 3-26, which was originally developed in Sweden for the in-situ assessment of bond conditions, have been adopted in the UK as part of the approval system for thin surfacing systems. Furthermore the UTEP Pull-Off test was developed at the University of Texas at El Paso (UTEP). These tests are widely used for evaluating the adhesion properties of interlayers [18, 19].

These tests can be used to quantify the tensile adhesive strength and identify a failure mode, showing the weakest place in the tested system. However, the measured tensile strength is not reliable enough to represent the adhesion property. Because these tests are controlled by hand operation or pressure, they are neither force nor displacement controlled [20].

The Leutner shear test was developed in Germany in the late 1970s as a simple method of performing a direct shear test on the interface between two asphalt layers [21, 22]. The test is performed on 150 or 100 mm diameter cores with at least two layers taken either from a pavement or prepared in the laboratory. However, an antiskid layer is a thin surface layer and does not fit in

the standard shear test setup. Modifications were therefore introduced to allow Leutner tests to be able to evaluate the shear strength through the interface between the thin layer and the underlying asphalt layer.

The force controlled mode (constant loading rate) was used in the pull tests, and the displacement controlled mode (constant displacement rate) was used in the shear tests. It would have been better to use the same loading modes in these two adhesion tests. However, some other organizations did similar tests and they used the force controlled mode for the pull test and the displacement control mode for the shear test. In order to be able to compare test results, similar loading conditions as used by other organizations were applied in this research.

3.3.1 Pull Adhesion Test

The pull test is performed on cores taken from the runways and slabs. Cylindrical cuts with a diameter of 50 mm were first cored into the core to a depth of 10 mm to make sure that the drill passed the antiskid surface layer (35 mm for TSLs). A steel plate was then glued to the dried and cleaned surface with X60 glue. After the glue got its full strength, the entire sample was placed upside down on the test table in a temperature controlled chamber. The surface layer was pulled off and the tensile force was measured [20].

Figure 3-27 shows the sample preparation and setup for the pull test. Three displacement sensors were used to record the displacement data during the pull test. A force controlled speed of 0.025 MPa/s was used in this research.

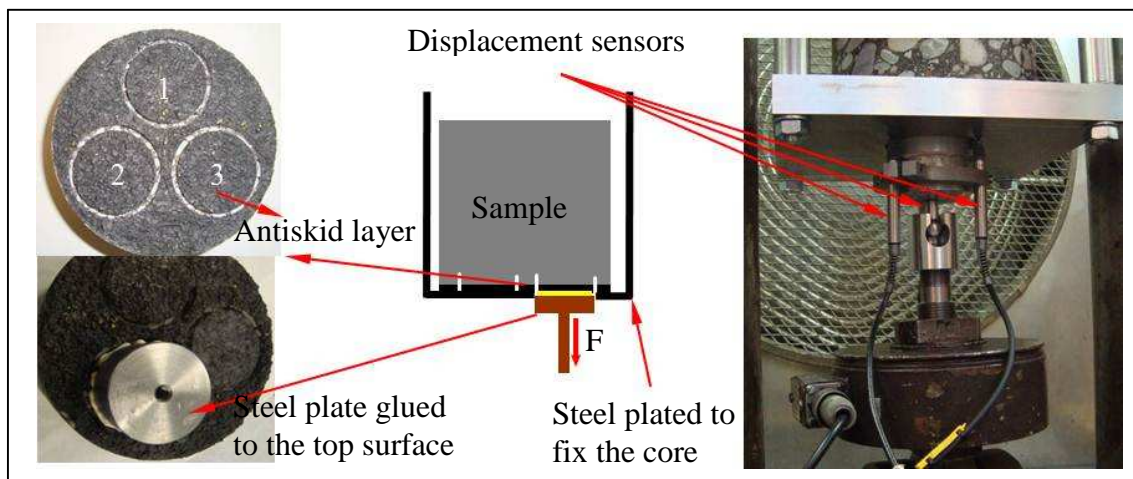


Figure 3-27 Sample preparation and test setup for pull test

The Direct Tensile Strength (DTS) is defined as the maximum tensile force divided by the area of fractured surface:

$$DTS = \frac{4F}{\pi \times D^2} \quad (3-18)$$

Where,

DTS = direct tensile strength, [MPa];

F = the maximum force, [N];

D = the diameter of test specimen, [mm].

Figure 3-28 shows a typical example of the applied force and resulting displacement curves versus time. This test was performed on core No.W5 at 0 °C. The force and displacement were recorded and used to plot a stress-strain curve. The area under the stress-strain curve from the test starting point to the failure point (see Figure 3-29) represents the failure energy, which is the energy that the specimen has absorbed up to failure.

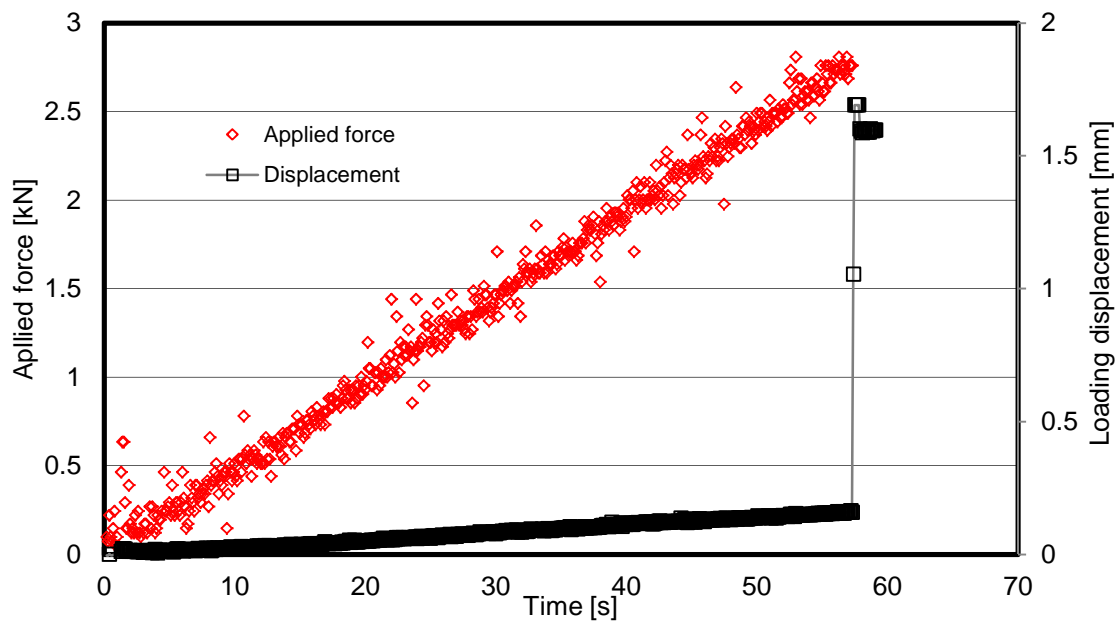


Figure 3-28 Typical curves for the applied force and resulting displacement

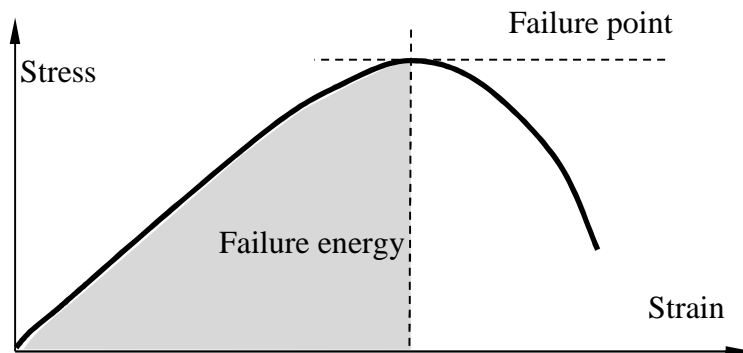


Figure 3-29 Illustration of failure energy

Pull tests were performed on cores both with a cut into and without a cut into the underlying asphalt mixture layer. The differences between these two sample preparation methods were compared and analyzed. The tests were performed at 20 °C with a load (stress) controlled speed of 0.025 MPa/s. The test results are shown in Table 3-9, Figure 3-30 and Figure 3-31. Both tests showed failures at the interface.

Table 3-9 Differences between tests on cores with cut and without cut in Pull test

	Applied failure force [kN]		$\frac{\text{Without}}{\text{With}}$
	With cut	Without cut	
Sample 1	1.684	2.578	1.53
Sample 2	1.428	1.868	1.31

From Figure 3-30, it can be clearly seen that the failure force is much higher when there is no cut compared to the case with a cut. Table 3-9 shows that samples without a cut had a 1.31 to 1.53 times higher failure load. This is caused by the larger failure area when there is no cut through. So a higher force is needed. Figure 3-31 shows the displacement-force curves. After the initial phase, both curves show the same slope in the load-displacement curve. This means that the stiffness of the testing specimens is quite close. But it is clear to see that more energy is needed to fail the sample when no cut is introduced into the core.

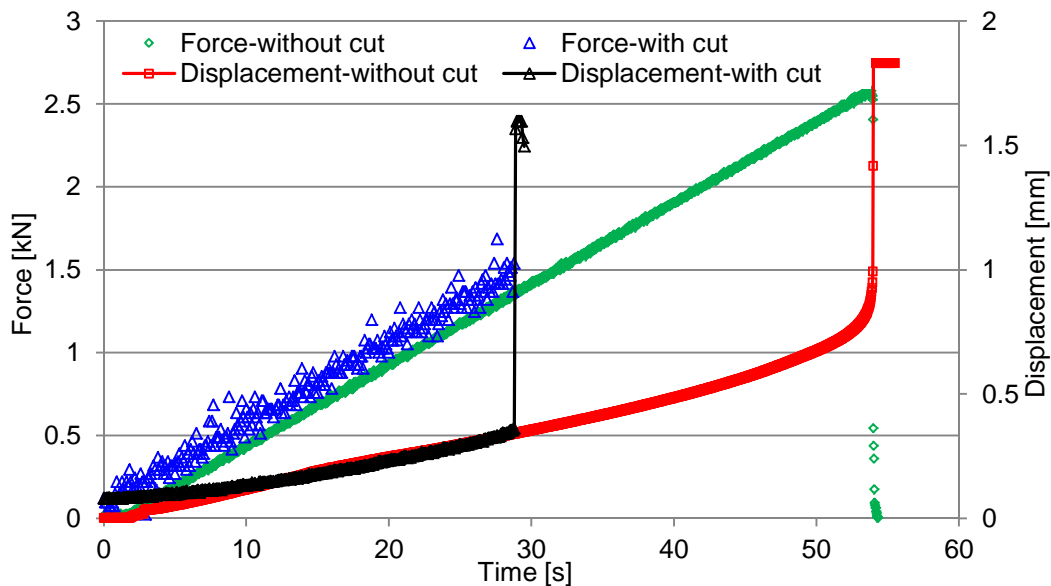


Figure 3-30 Applied force and displacement versus loading time

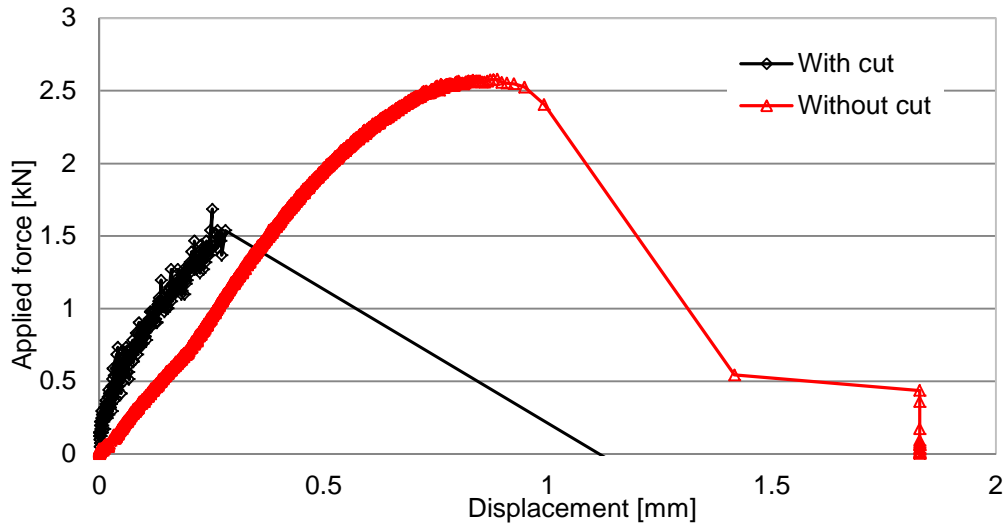


Figure 3-31 Test results on cores both with cut through and without cut

Figure 3-32 shows the failure area obtained with the pull tests. The picture at the right side shows the failure surface in case no cut was made. The failure surface is irregular. It is much larger than what it should be. These are the main reasons for the higher force to reach failure in case no cut is made.



Figure 3-32 Failure surfaces at the interface

3.3.2 Leutner Shear Adhesion Test

The antiskid layers have a thickness of approximately 5 mm. This is too thin to perform shear test on the interface by directly using the Leutner setup. Therefore, X60 glue and steel cylinders are used to modify this test.

Figure 3-33 shows the sample preparation and setup for the modified Leutner shear test. A steel cylinder of 100 mm diameter and 40 mm thickness was glued onto the antiskid surface with X60 glue. The liquid glue may penetrate into the interface or even get into the underlying mix layer. In order to avoid this

undesired situation as much as possible, the specimen was kept upside down during the preparation process until the glue was cured.

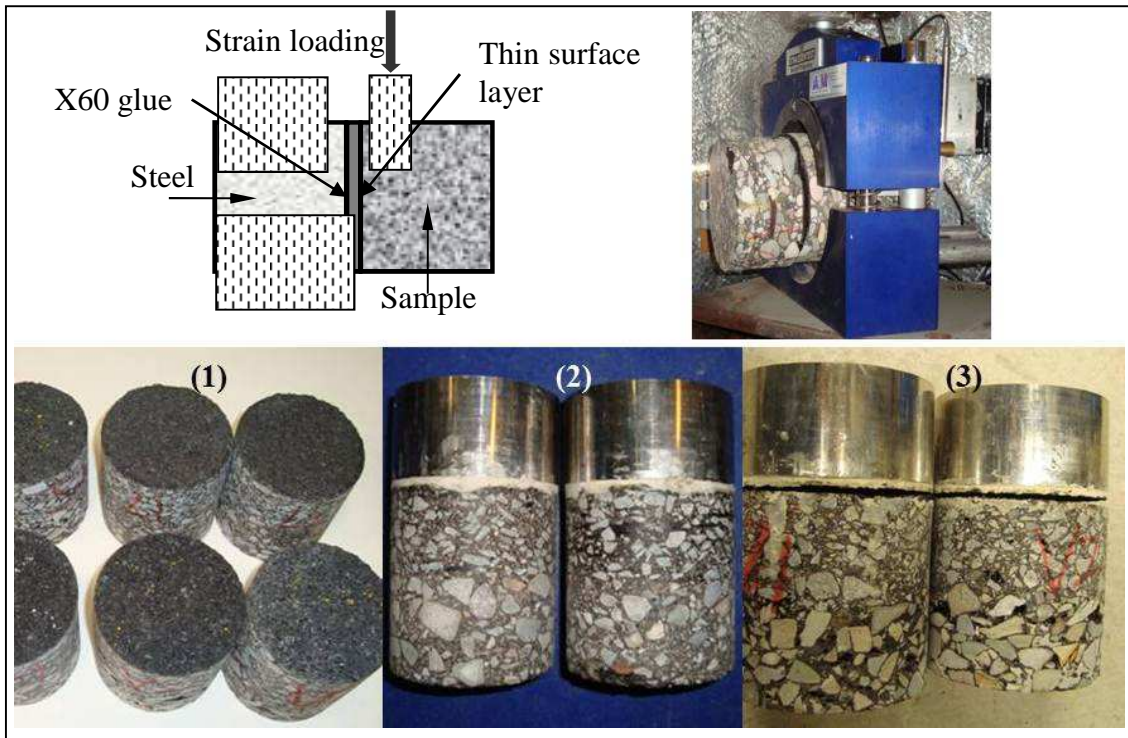


Figure 3-33 Sample preparation and test setup for Leutner shear test

During the test, a constant vertical displacement rate of 50 mm/min is applied across the interface. The resulting shear force is measured. The average Direct Shear Strength (DSS) can be calculated by the following equation:

$$DSS = \frac{4P}{\pi \times D^2} \quad (3-19)$$

Where,

DSS = direct shear strength, [MPa];

P = the maximum force, [N];

D = the diameter of test specimen, [mm].

Figure 3-34 shows a typical test graph of displacement and resulting force versus time curves for the shear test on specimens from Eindhoven Airport. The failure energy can be calculated with the same method described in Figure 3-29.

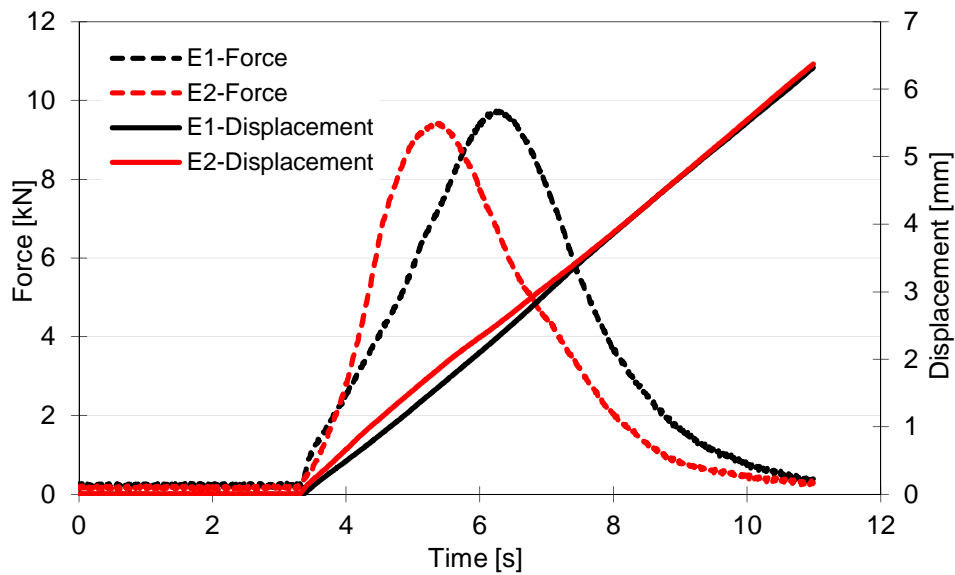


Figure 3-34 Typical displacement and resulting shear force curve in the Leutner shear test

3.3.3 Failure Modes

Based on the sample preparation for pull tests and shear tests, five different modes of failure can be defined when applying a load with these two setups. These different failure modes provide valuable information about the thin surface layer and the underlying asphalt mixture layer. Figure 3-35 shows a simplified diagram of these possible failure modes.

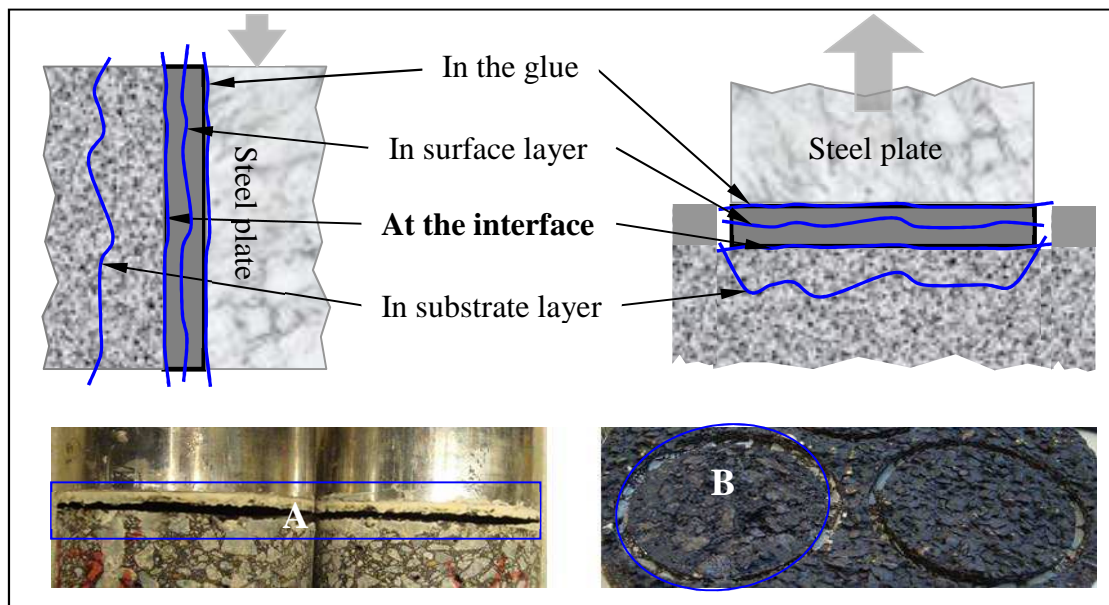


Figure 3-35 Four possible fracture modes during adhesion evaluations

First possibility, if the failure occurs at the bond surface (interface), the pull-off strength (or shear strength) is in fact the tensile (or shear) adhesive strength. In this case, the ultimate load is a value that is giving information about the adhesion between the surface layer and the underlying asphalt layer. Second possibility, when the failure occurs between the steel plate and the thin surface, a stronger glue is needed. In this research, the X60 glue has a high enough adhesive strength after it gets fully cured. Hence no failures occurred between the steel plate and the thin surface layer. Third possibility, if the failure occurs in the surface layer material, the surface layer is the weakest point of the system; in this case the adhesive strength at the interface exceeds the tensile strength of the surface layer.

Fourth possibility, if the failure occurs in the underlying layer, the surface layer and the interface are stronger than the layer below. In this case, the failure stress is the tensile/shear stress of the underlying layer. Fifth possibility, in some cases the failure occurs partially along the bond surface and partially in either the surface layer or the underlying layer, and the failure mode is a combination of two or more of the failure modes discussed above.

All Leutner shear test samples failed at the interface between the antiskid surface layer (or thin surface layer) and underlying mixture layer. These failure modes indicate that the modified Leutner shear test is a workable method for evaluating the adhesion properties between a thin layer and an underlying layer.

During the pull test, most of the tests on antiskid specimens failed at the interface. But for the TSL specimens, just 3 out of 10 tests failed at the interface (this will be discussed in Chapter 6). This means that the used pull test is suitable for antiskid surfaces, but not for TSLs.

In this research, failures that are not at the interface were excluded from the final data analysis described in the following Chapter 4 and Chapter 6.

3.4 Surface Characteristics

Surface friction plays an important role in the safe operation of traffic on road pavements and aircrafts on airfields. Surface friction is generated as the tire rolls or slides over the pavement surface and a force that resists the relative motion between the tire and surface is developed [23].

Generally the higher the friction coefficient is, the safer the surface is. Friction or skid resistance depends on the microtexture and macrotexture of the surfaces. Surface texture includes microtexture, macrotexture and megatexture. As Table 3-10 shows, macrotexture has a wavelength from 0.5 mm up to 50 mm, while microtexture has wavelength below 0.5 mm; megatexture has wavelengths from 50 mm up to 500 mm. Figure 3-36 shows the difference between microtexture and macrotexture.

Table 3-10 Wavelengths for three level textures

	Microtexture	Macrottexture	Megattexture
Length	< 0.5 mm	0.5 to 50 mm	50 to 500 mm
Affects	Skid resistance	Skid resistance Tire-pavement noise	Skid resistance Tire-pavement noise Roughness

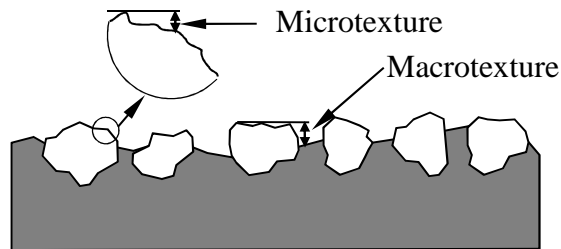


Figure 3-36 Illustrations of microtexture and macrottexture

The microtexture is associated with the surface of the aggregate and is controlled by the individual aggregate surface properties, such as shape and asperity. Microtexture has a large influence at speed below 50 km/h, although it contributes to skid resistance at all speeds. Macrottexture refers to larger-scale irregularities of the pavement surface that are affected by aggregate size and aggregate orientations. It contributes to the speed-dependent part of friction and to wet surface friction. The primary function of the macrottexture is to help maintaining sufficient skid resistance to aircraft travelling at high speeds. It specifically can provide paths allowing water to escape which also helps to prevent hydroplaning [24, 25].

3.4.1 Texture Depth

Macrottexture is characterized by the Texture Depth (TD) and Mean Profile Depth (MPD). The definitions of TD and MPD are as follows:

1. Texture Depth (TD): TD is defined as the vertical distance between the surface and the plane through the top of the three highest aggregates. According to EN 13036-1 [26], it is the average depth of the pavement surface macrottexture measured by the volumetric sand patch test method.
2. MPD: According to ASTM E1845, the measured profile of the pavement macrottexture is divided for analyzing purposes into segments, each having a base-length of 100 mm. The slope, if any, of each segment is suppressed by subtracting a linear regression of the segment. The segment is divided in half and the highest peak in each half segment is determined. The difference between the resulting height and the average level of the segment is calculated for each half segment and the average of both halves is computed. The average peak values of both segments are reported as MPD, see Figure 3-37 [27, 28].

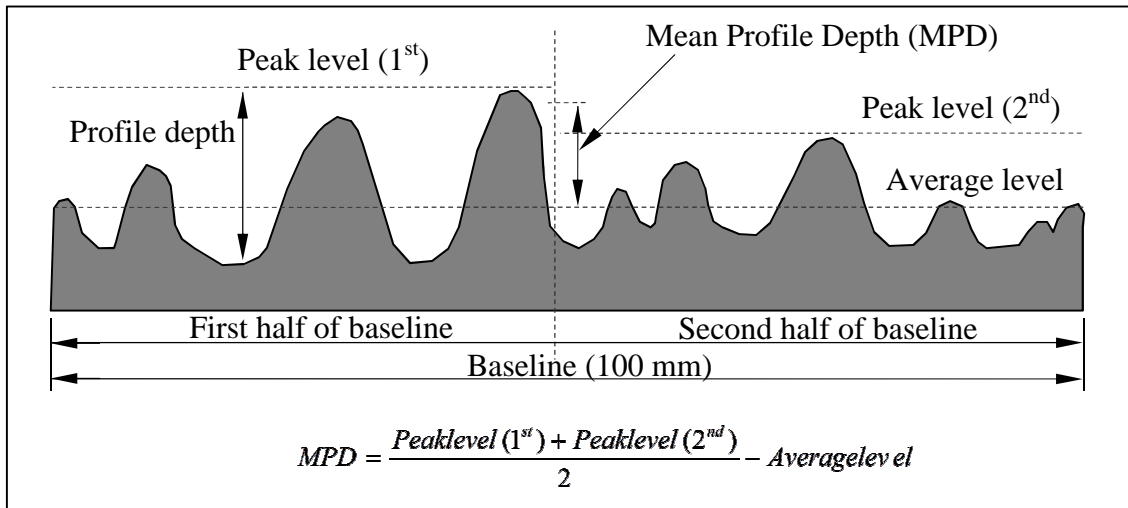


Figure 3-37 Illustrations of Mean Profile Depth

In this research a microscope and Nano CT scans were used to evaluate the surface texture of antiskid layers. The traditional sand patch test was used for comparison purposes.

3.4.2 Sand Patch Test

The sand patch test is a traditional test method to estimate the TD of road pavement surfaces. It can be easily performed in the field and it is widely used. The disadvantage of this test is that it cannot be performed under wet and windy conditions. Figure 3-38 shows the sand patch facilities and test in the field.

Figure 3-38 Sand patch test in the field⁶

In this research, sand patch tests were carried out according to ASTM E965-96. First, the surface was cleaned and dried. A certain volume of special

⁶<http://www.highfrictionroads.com/index.php?q=node/18>

sand (minimum of 90% by weight passing 0.25 mm sieve (No. 60 sieve) and retained on 0.18 mm sieve (No. 80 sieve)) was poured on the surface. Then the sand was spread by making a circular area with a disc which was kept horizontally to make sure the surface was filled to the level of the highest points. The higher the texture is, the smaller the circle that is created. [29]

The diameter of the sand patch was measured in four directions with an accuracy of 5 mm. The TD (in mm) was then calculated with the following equation.

$$TD = \frac{64000 \times V}{\pi \times (D_1 + D_2 + D_3 + D_4)^2} \quad (3-20)$$

Where,

V = the volume of sand, [ml];

D_i = the diameter, $i = 1, 2, 3, 4$ [mm].

3.4.3 Microscope

Besides traditional sand patch tests, other types of equipment such as laser-based devices can be used to give 2D and 3D surface profiles. Samples can be collected from the field and then placed under a microscope for inspection. MPD values can then be calculated.

In this research, a Leica stereo microscope was used on tar-containing antiskid specimens. Figure 3-29 shows the microscope setup. Four locations were scanned on every core to obtain an average value for the MPD, as the right graph in Figure 3-29 shows. During the test, three dimensional structures of every scanned position were obtained and an area of approximately 8 mm×8 mm was selected to calculate the surface characteristics. Figure 3-39 shows a 3D image of the surface of Eindhoven's No. 5 sample; also the selected area for the surface profile calculations is shown.

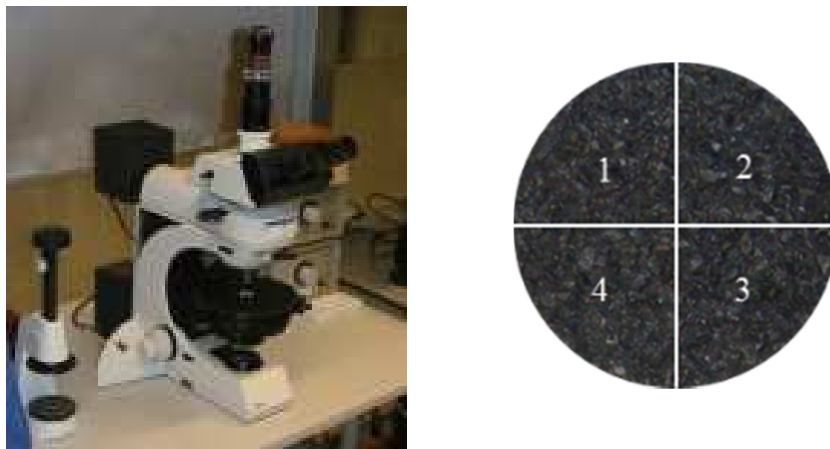


Figure 3-39 Microscope setup and test positions on the antiskid cores

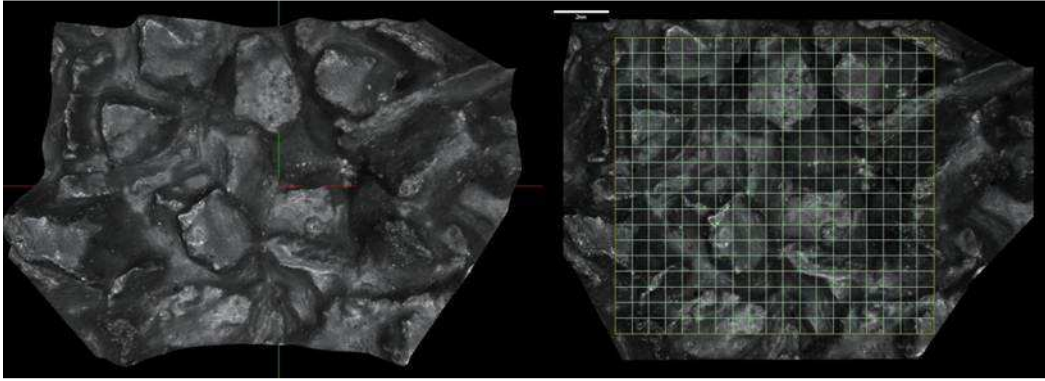


Figure 3-40 3D image of microscope for antiskid surface (left) and the selected area for the surface profile calculation (right)

3.4.4 CT Scan

X-ray Computerized Tomography (CT) imaging was originally developed for medical purposes to produce cross-sections of the human body. It creates a series of two-dimensional slices of X-ray images taken in a cross section of the object. From the slides a three-dimensional visualization and characterization of objects can be made.

CT scan grey-level images give an overview of the microstructure of an asphalt mixture. In this research it was used to investigate the structural characteristics of antiskid surface layers and noise reducing thin surfaces. Both a larger scale medical CT scanner and a Nano CT scanner were employed. The differences between these two scanners are the pixel density of the scanned images. Scanned images from a Nano CT scanner have a higher resolution. The resolution of the medical scanner is 0.3×0.3 mm in the scanning plane, while the minimum distance of the planes is 0.5 mm. With the Nano scanner, the resolution can be 0.7 to 1 micrometer in all three directions, depending on the size of the specimen to be scanned. The medical scanner used was a Siemens, while the Nano CT scanner was a Phoenix Nanotom⁷ (see the left graph in Figure 3-41).

The x-ray Nano CT system consists of an x-ray source, the sample holder which allows the sample to rotate, a high resolution detector and a computer for control and reconstruction [30]. A schematic diagram of the Nano CT scanner is shown in Figure 3-41 (right).

⁷<http://phoenix-xray.com/>

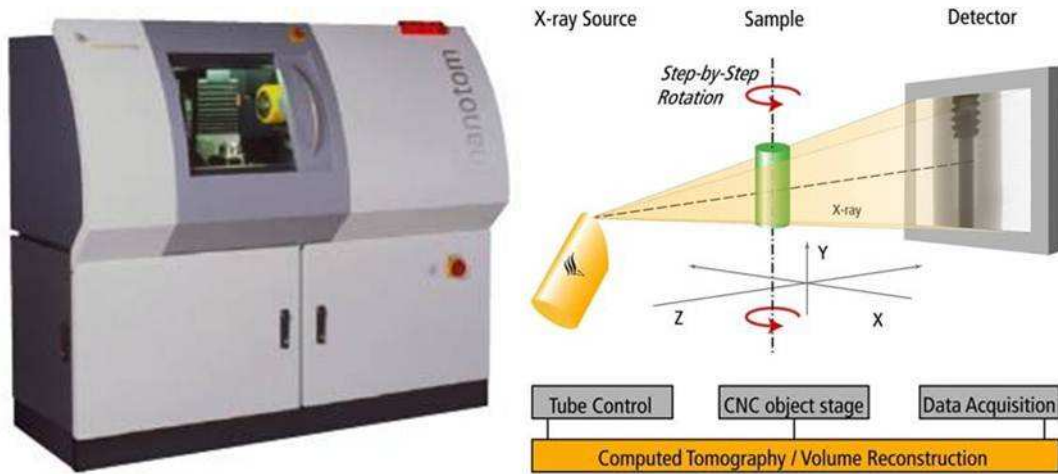


Figure 3-41 Nano CT scan equipment and its schematic diagram

Figure 3-42 presents an example of 2D and 3D Nano CT scan images of the tar-containing antiskid surface layer from Eindhoven Airport. The top-right figure shows the cross image at the horizontal level while the bottom figure indicates the vertical cross image of an antiskid layer.

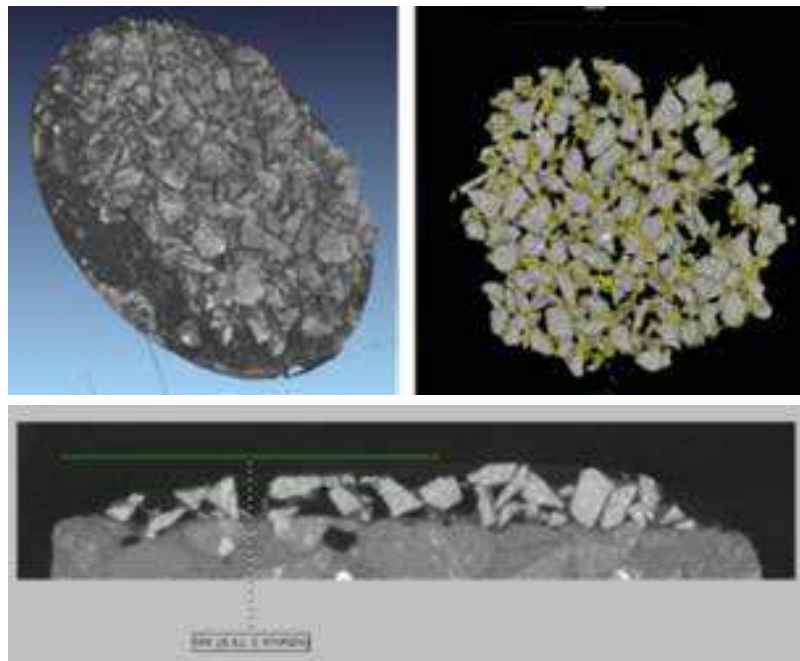


Figure 3-42 Typical 2D and 3D Nano CT scan images of antiskid surface layer

In the scan images, each voxel is represented by a gray value depending on the X-ray absorption that relates closely to density differences within the objects. The darkest (black) parts are exterior and voids, the grey (yellow part in the top-right graph in Figure 3-42) parts are mastics and the light (white) parts are the

aggregates. The contrast in gray values in the CT scan images is good and can be used to clearly separate the three phases.

In order to calculate and distinguish the histogram of all voxels into three phases of aggregates, binder and voids, the Amira program was used. Amira is software for visualization and data analysis of the scanning results. It can be used to reconstruct 2D and 3D images of scanned asphalt layers. At the same time, the volume of voids, binder and aggregates can be calculated. If necessary, the volume of voids, binder and aggregate per slice can be plotted over the height of the sample to get an indication of the volume distributions over the height. [31]

REFERENCES

1. Xiao, Y., et al., *Assessment Protocol for Tar-containing Antiskid Layers for Runways, Report No. 7-10-185-2*. 2010, Delft University of Technology.
2. Theophanides, T., *Infrared Spectroscopy - Materials Science, Engineering and Technology*. ISBN 978-953-51-0537-4. 2012.
3. Xiao, Y., et al., *Characteristics of two-component epoxy modified bitumen*. Materials and Structures, 2011. **44**(3): p. 611-622.
4. CEN, *EN 13074 Bitumen and Bituminous binders - Recovery of binder from bitumen emulsions by evaporation*. 2002.
5. Shell, *The Shell Bitumen Handbook, Fifth Edition*. 2003.
6. CROW, *Standaard RAW Bepalingen, in the Netherlands*. 2005, ISBN: 90 6628 443 9.
7. Hagos, E.T., *The Effect of Ageing on Binder Properties of Porous Asphalt Concrete*. 2008, Delft University of Technology: PhD dissertation.
8. TRB, *New Simple Performance Tests for Asphalt Mixes, TRB Report No. E-C068*. 2004.
9. Qiu, J., et al., *Evaluating Self Healing Capability of Bituminous Mastics*. Experimental Mechanics, 2011: p. 1-9.
10. Al-Qadi, I.L., et al., *Characterization of Low Temperature Mechanical Properties of Crack Sealants Utilizing Direct Tension Test*. 2008, University of Illinois at Urbana Champaign, Report No. ICT-08-028.
11. CEN, *NEN-EN 14770 Bitumen and bituminous binders - Determination of complex shear modulus and phase angle - Dynamic Shear Rheometer (DSR)*. 2005.
12. Mo, L.T., *Damage Development in the Adhesive Zone and Mortar of Porous Asphalt Concrete*. 2010, Delft University of Technology.
13. Woldekidan, M.F., *Response modelling of bitumen, bituminous mastic and mortar*. 2011, Delft University of Technology: Delft.
14. Liu, G., *Characterization and Identification of Bituminous Materials Modified with Montmorillonite Nanoclay, in Civil Engineering and Geosciences*. 2011, Delft University of Technology: Delft.
15. Khedoe, R.N., *Possible use of C-Fix in Porous Asphalt*. 2006, Delft University of Technology.
16. Al-Qadi, I.L., et al., *Tack Coat Optimization for HMA Overlayers-Laboratory Testing*. 2008, Illinois Department of Transportation: Report No. FHWA-ICT-08-02.

17. Leest, A.J.v. and G. Gaarkeuken, *Resistance of surface layers on airfields in the Netherlands-in situ and laboratory testing*, in *2005 European Airport Pavement Workshop*. 2005.
18. Tashman, L., K. Nam, and T. Papagiannakis, *Evaluation of the Influence of Tack Coat Construction Factors on the Bond Strength between Pavement Layers*. 2006, Washington State University: Washington, D.C.
19. Deysarkar, I., *Test Set-up to Determine Quality of Tack Coat*, in *Department of Civil Engineering*. 2004, University of Texas at El Paso.
20. Xiao, Y., et al. *Adhesion Properties of Tar-Containing Antiskid Surface Layers on Runways in Airfield*. in *T&DI Congress 2011: Integrated Transportation and Development for a Better Tomorrow*. 2011. USA: ASCE.
21. Collop, A.C., N.H. Thom, and C. Sangiorgi, *Assessment of bond condition using the Leutner shear test*. *Proceedings of the Institution of Civil Engineers: Transport*, 2003. **156**(4): p. 211-217.
22. Collop, A.C., et al., *Shear bond strength between asphalt layers for laboratory prepared samples and field cores*. *Construction and Building Materials*, 2009. **23**(6): p. 2251-2258.
23. Hall, J.W., et al., *Guide for Pavement Friction*, in *Final Report for NCHRP Project 01-43*. 2009.
24. Toan, D.V., *Runway friction performance in NZ*, in *International Conference on Surface Friction for Road and Runways*. 2005: Christchurch, New Zeland.
25. Nicholas, R.F., *Comparison of Macrotecture Measurement Methods*, in *Civil and Environmental Engineering and Geodetic Science*. 2009, The Ohio State University.
26. NEN-EN, *EN 13036-1, Road and airfield surface characteristics-Test methods-Part 1: Measurement of pavement surface macro texture depth using a volumetric technique*. 2010.
27. ASTM, *E1845-09 Standard Practice for Calculating Pavement Macrotecture Mean Profile Depth*. 2009.
28. Abbas, A., et al., *Three-Dimensional Surface Texture Characterization of Portland Cement Concrete Pavements*. *Computer-Aided Civil and Infrastructure Engineering*, 2007. **22**(3): p. 197-209.
29. ASTM, *E965-96 Standard Test Method for Measuring Pavement Macrotecture Depth Using a Volumetric Technique*. 2006.
30. Kim, K.G., et al., *Nano X-ray Computed Tomography System*, *World Congress on Medical Physics and Biomedical Engineering 2006*, R. Magjarevic and J.H. Nagel, Editors. 2007, Springer Berlin Heidelberg. p. 1417-1420.
31. Nielsen, C.B., *Microstructure of porous pavements - Experimental procedures, Technical note 47*. 2007, Danish Road Institute.

4. Set Benchmark by Evaluating the Properties of Tar-containing Antiskid Layers

In this chapter, various properties of tar-containing antiskid layers such as surface characteristics, which include texture and mean profile depth, structural characteristics and adhesion at the interface are discussed. Conclusions from these test results will be used as a benchmark for the selection of new potential binders for runway antiskid applications, as outlined in Figure 1-3 from the introduction.

As mentioned before, it was not possible to develop the benchmark by testing the original binder used in the tar-containing antiskid layers. All materials had to be retrieved from cores taken from airfields. It will be quite obvious that this has complicated the analysis substantially since it implied among others that only a limited amount of material could be obtained which in turn resulted in a limited test. In this research, only 10 cores from each airfield were available. Figure 4-1 shows the research program for this chapter.

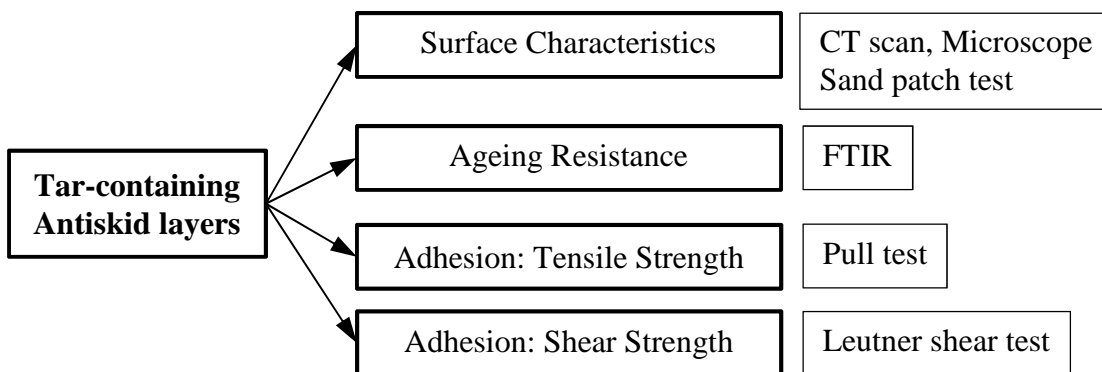


Figure 4-1 Research program of Chapter 4

4.1 Tar-Containing Antiskid Layers

Most of the asphalt pavement runways in the Netherlands are covered with an antiskid layer. The present antiskid layer used is a patent protected ANTISKID, which is produced and applied by the Possehl Company in Germany. An antiskid layer is designed to keep the skid resistance well above the

maintenance level for a long period of time and to preserve the underlying layers from wear, heat, fuel and other chemicals. Furthermore, antiskid layers should be able during their service to resist repeatedly life. The high stress levels introduced by large aircraft wheel loads and spread them to the underlying layers. Because a tar-containing binder provides excellent adhesion and excellent protection against ageing and external chemicals, tar-containing binders were used in the past in antiskid layers applications [1].

However, because of environmental concerns, tar-containing asphalt mixtures are not allowed anymore with the only exception being runway antiskid applications. But tar based binders were also banned to these applications from the beginning of 2010 [1, 2]. One of the goals of this dissertation was to develop a benchmark for evaluating new binders.

4.1.1 Tar Detector

When recycling asphalt mixtures in the Netherlands, one should check first of all whether there is tar present in the asphalt mixture. Mixtures that contain tar cannot be used for recycling and the binder has to be burned completely. Ultraviolet blue light is often used to detect the tar contamination in asphalt mixtures. The so called Pak-Marker is used for this purpose (see Figure 4-2). It is especially developed to detect Polycyclic Aromatic Hydrocarbons in asphalt products and is used in the following way. Pak-Marker detection was conducted with the help from KOAC-NPC.

After shaking the spray can, a layer of white spray (composition is not mentioned on the Technical Data Sheet) is sprayed on the asphalt mixture. Then it is left to dry before further testing. If there is tar in the mixture there will be a discoloring of the white substance. This color will be light brown or yellow. If there is no clear visible discoloring, the UV lamp can be used. Under UV light the spray will light up and get a yellow/blue color. A yellow color indicates that there is tar in the mixture, and a blue color means that there is no tar present (the tar content is smaller than 500 mg/kg). Figure 4-3 shows the color difference under UV light between a mixture contaminated with tar and a mixture without tar. Without tar, there are no visible images except gray aggregates and binder, while the sprayed white material has a blue color. When the sample is tar-contaminated, many yellow areas can be observed.

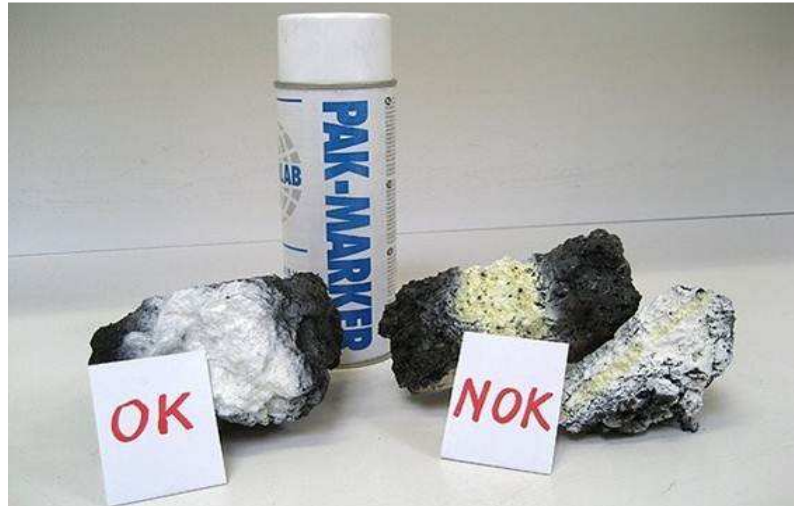


Figure 4-2 Pak-Marker for detecting tar-containing in asphalt mix¹

The presence of tar contamination on the fractured surface of specimens (Leutner shear test specimens, pull test specimens, cores with the anti-skid layer scratched off) tested in this chapter were carefully checked with the Pak-Marker.

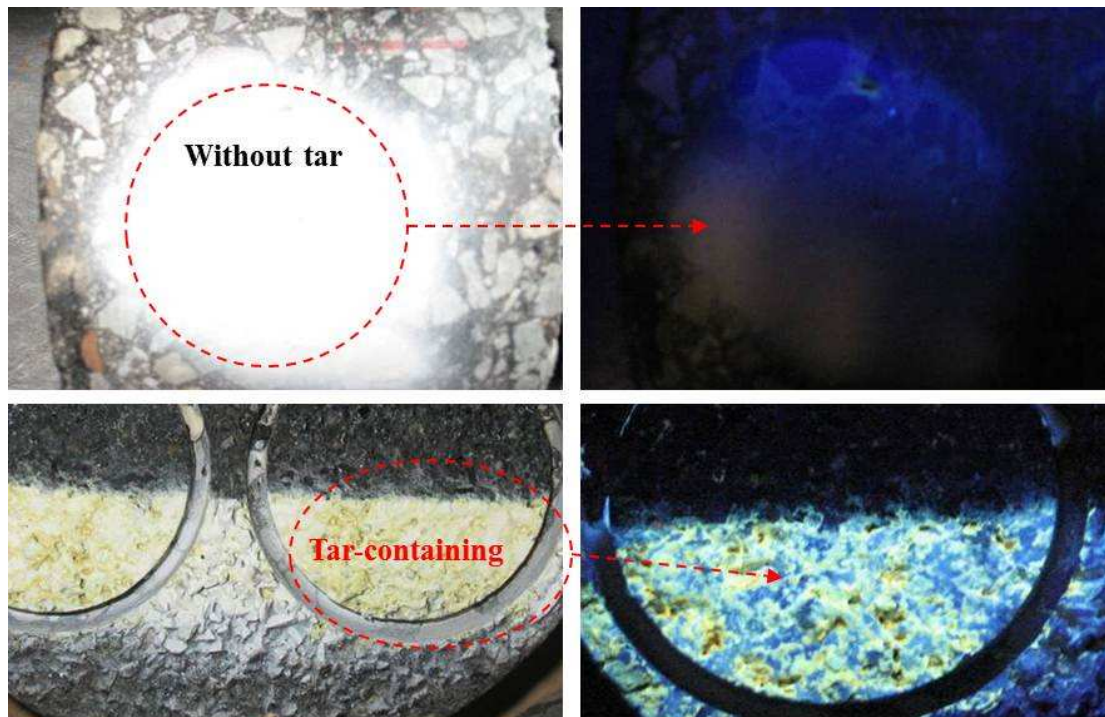


Figure 4-3 Difference between tar-containing mixture and mixture without tar under UV light

¹ <http://www.adams-polendam.be/containerdienst/soorten-afval/teerhoudend-asfalt>

Figure 4-4 presents the results of UV blue light marker on samples from Woensdrecht Airport. The top of the asphalt mixture underneath the antiskid layer was analyzed after the Leutner shear tests and pull tests were performed. These pictures clearly show the presence of tar at the asphalt mixture surface since all of them have shown many yellow areas. Similar discoloring was found on the failure surfaces of the pull test samples and shear test samples from the other five airfields.

The reasons for the presence of tar at the top of the asphalt mixture layer might be a result from the application process of the antiskid surface layer. During the application, tar-containing emulsions are first sprayed onto the asphalt pavement surface before the aggregates are spread. Hence this may result in tar remaining at the surface of the asphalt mixture. Tar-containing aggregates need to be removed during the reconstruction.

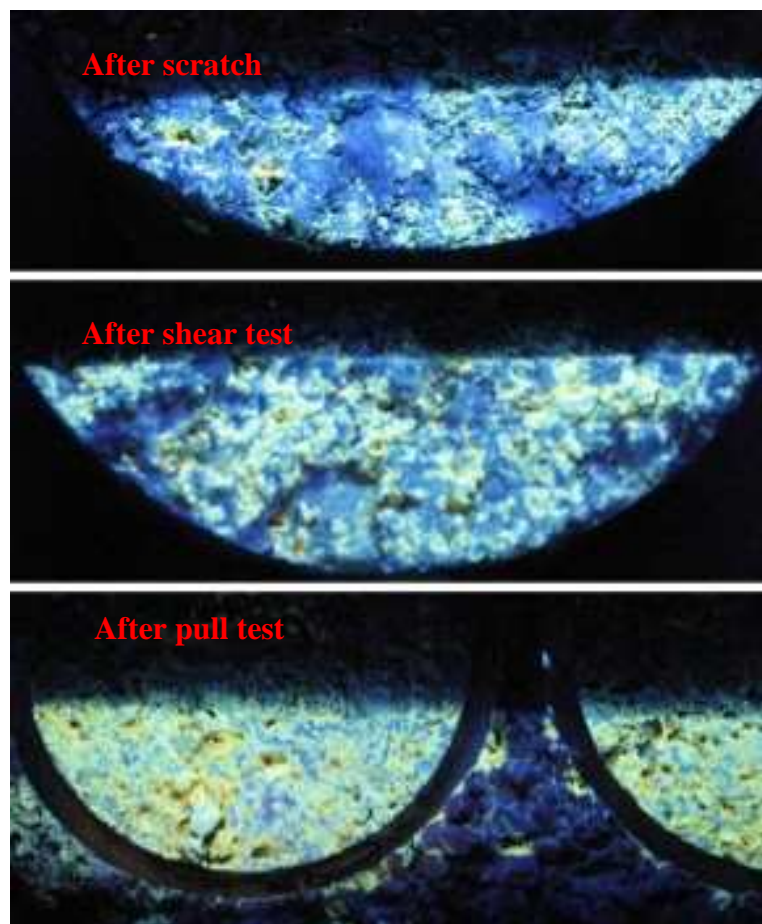


Figure 4-4 Results of UV blue light marker on specimens from Woensdrecht Airport

The results show that the asphalt layer under the tar-containing antiskid is partly contaminated with tar. So the asphalt layer cannot be recycled in other

asphalt mixtures anymore. And the cores left from this project cannot be disposed with other asphalt mixtures.

4.1.2 High Temperature Resistance

A simple test was used to understand the high temperature resistance of tar-containing antiskid layers by placing them vertically in an oven at 150 °C. This was just a trial test and the test is not standardized in any specifications. Two reasons can be given for doing this with such a simple method. The first reason was that there were no tar-containing binders available for testing. The second reason was that the number of tar-containing antiskid specimens was limited. Placing the specimen vertically in a high temperature environment was therefore the easiest and most efficient way to check its high temperature resistance..

Some test specimens after the shear test and CT scan were reused for this purpose:

Type 1 specimens: Two samples of antiskid layers after the Leutner shear tests were used. The antiskid layers were still glued onto the steel plate with X60 glue.

Type 2 specimens: Two samples after the Nano CT scanning were used. They have a thickness of approximately 1 cm, including the antiskid layer and part of the asphalt mixture layer. Samples were glued with X60 glue onto a steel plate at the asphalt mixture layer side.

The difference between the type 1 and type 2 specimens is that in type 1, there is just tar-containing antiskid layer, while type 2 specimens consist of the tar-containing antiskid layer, the interface and the asphalt mixture layer below.

These antiskid specimens were placed vertically in an oven at 150 °C for at least one hour. Figure 4-5 shows the result of type 1 specimens after exposure at 150 °C in the oven for one hour. No visible deformation could be observed. The results of Type 2 specimens are shown in Figure 4-6 and Figure 4-7. Figure 4-6 illustrates that after one hour, the antiskid layer stayed quite well intact, while a crack developed in the asphalt mixture layer. Within two hours, one of the samples failed in the asphalt mixture layer. The other sample showed no visible deformation even after four hours.



Figure 4-5 Deformations after one hour in the oven at 150 °C of type 1 specimen

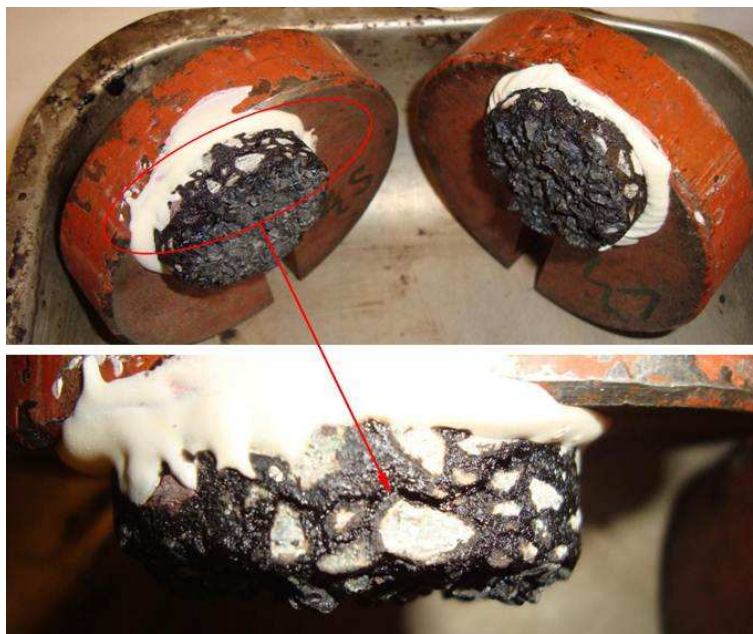


Figure 4-6 Deformations after one hour in the oven at 150 °C of type 2 samples

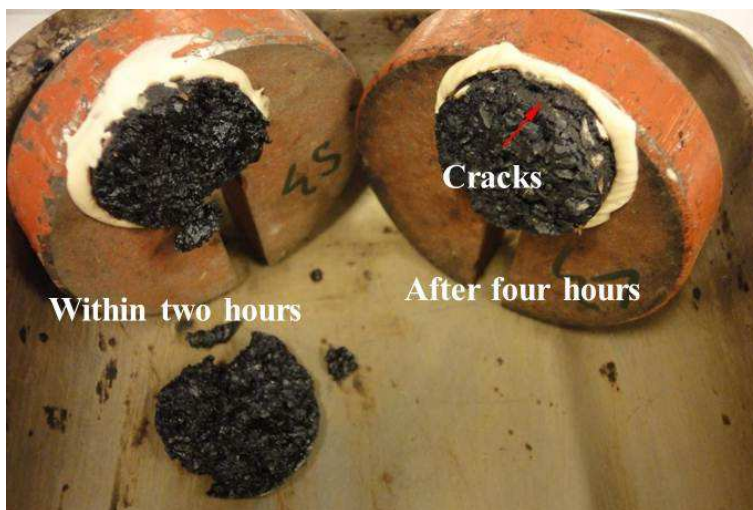


Figure 4-7 Visible deformations of type 2 samples

From these simple tests it can be concluded that the tar-containing antiskid can resist a high temperature of 150 °C for at least one hour. It has a much better high temperature resistance than the traditional asphalt mixture underlying the antiskid layer. These findings are supported by the fact that the softening point of the fresh tar-containing binder is very high (above 100 °C [3]).

4.2 Surface Characteristics

CT scans and Microscopy were used to evaluate the surface texture of tar-containing antiskid surface layers. Then the traditional sand patch test was used for comparison.

4.2.1 CT Scans

CT scans are used especially in road engineering to investigate the structure of asphalt mixtures [4, 5]. Its gray-level images give an overview of the density differences in the mixture, such as aggregates, mortar and voids. Furthermore, the volumetric content of these phases can be calculated from re-constructed 3D images.

As introduced in Section 3.4.4, a larger scale CT scanner (also named medical CT scanner) was firstly used. The upper left picture in Figure 4-8 shows the scanner. Cores were placed in the CT scanning machine with the antiskid layers in the vertical direction.

The resolution of this CT scanner is 0.3×0.3 mm in the scanning plane, and the minimum distance of the planes is 0.5 mm. Normally 1 mm distance is used. The picture at the bottom in Figure 4-8 presents the scanned images. Although 3D pictures of the antiskid surface can be generated, the resolution is not enough to effectively separate the aggregates and binder areas. This means that the larger CT scanner is not suitable for evaluating antiskid surfaces. A Nano CT scanner, which has a resolution of 0.7 to 1 micrometer in all three directions, was then used.

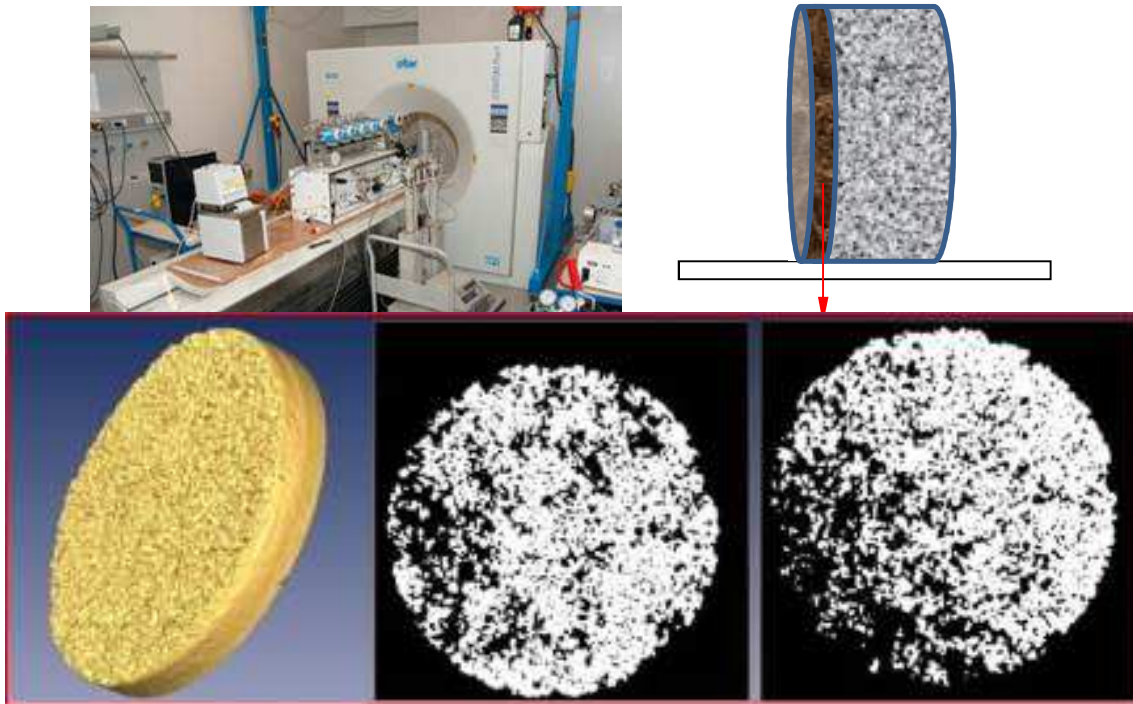


Figure 4-8 Larger scale CT scanner and scan images

Cylinders of 40 mm diameter were cored from the airfield specimens. Then the antiskid layer was cut off together with a small part of the underlying asphalt layer. The total thickness of these specimens was 1 cm. The samples were then placed in the scanning cabinet. Figure 4-9 shows the samples of tar-containing antiskid layers used for the Nano CT scans and a schematic graph of the setup with the tested sample in the scanner cabinet. Basically, an X-ray beam transmitted through a sample along several paths in different directions is detected and stored in a computer. The intensity of the X-ray beam is measured before it enters the sample and after it passes through the sample. The profile of transmitted X-ray beams has an intensity which is dependent on the material density. It is then used to reconstruct images of slices of the sample.

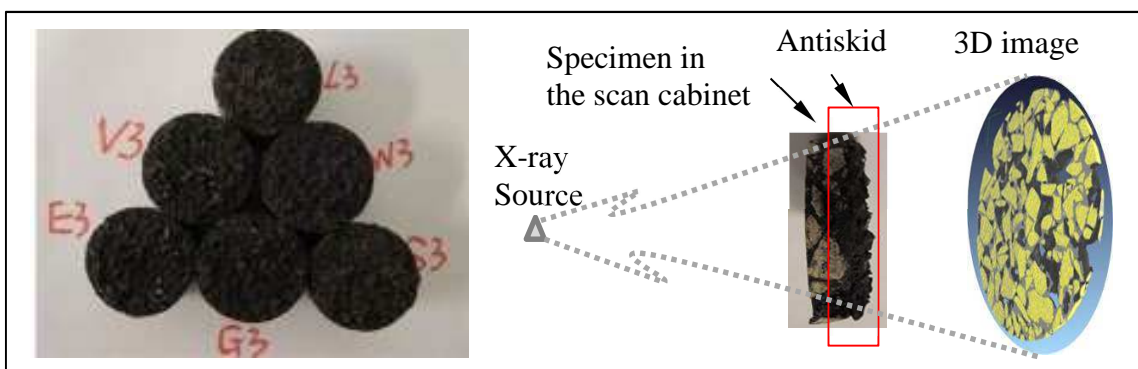


Figure 4-9 Nano CT scan samples and setup

Figure 4-10 shows an example of the Nano CT scan images from the surface to the interface for an antiskid layer from Eindhoven Airfield. The No. 1 slide presents the surface of antiskid layer while the No. 5 presents the interface between antiskid layer and asphalt mixture layer. The yellow area is representing the tar-containing binder, defined by setting the range of gray values.

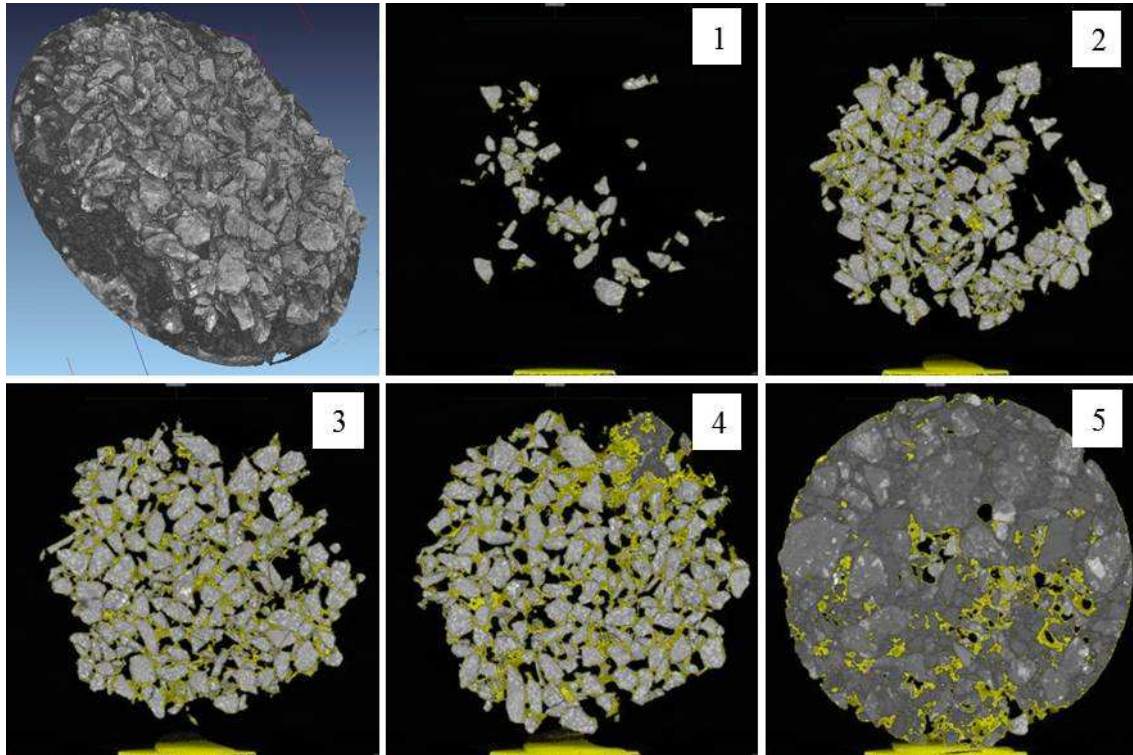


Figure 4-10 Nano CT scans for core from Eindhoven Airfield

Figure 4-11 shows cross-section images of a core from Soesterberg Airfield. The dark areas represent the air voids, the gray areas represent the binder and the lightest areas represent the aggregates. These photos indicate that the antiskid layer is a special thin layer with a thickness of 3 to 5 mm. For such a thickness and small aggregate size, it has an extremely high macrotexture. The height from the peak point to the valley bottom is almost equal to the thickness of the antiskid layer. This maximum height is determined with a microscope as will be discussed in the following section.

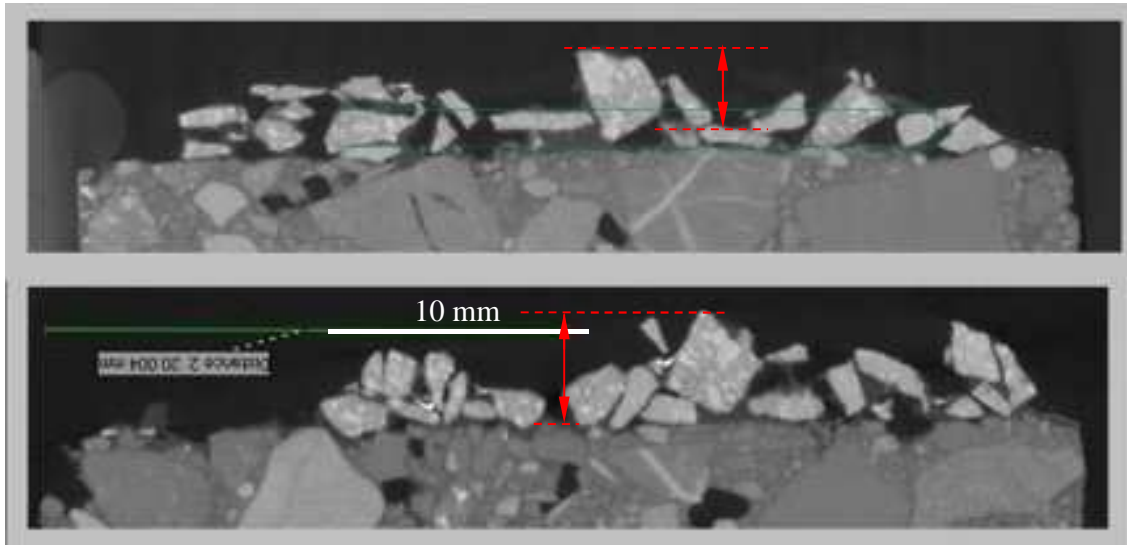


Figure 4-11 Nano CT scan cross images of the antiskid layer of Soesterberg Airfield

After the scan, an area with a certain thickness in the 3D scan images was selected for calculating the void, binder and aggregate content. Figure 4-12 shows the three side views of the selected space. Two or three different selected volumes for each airfield sample were calculated. The results are presented in Table 4-1 and Table 4-2.

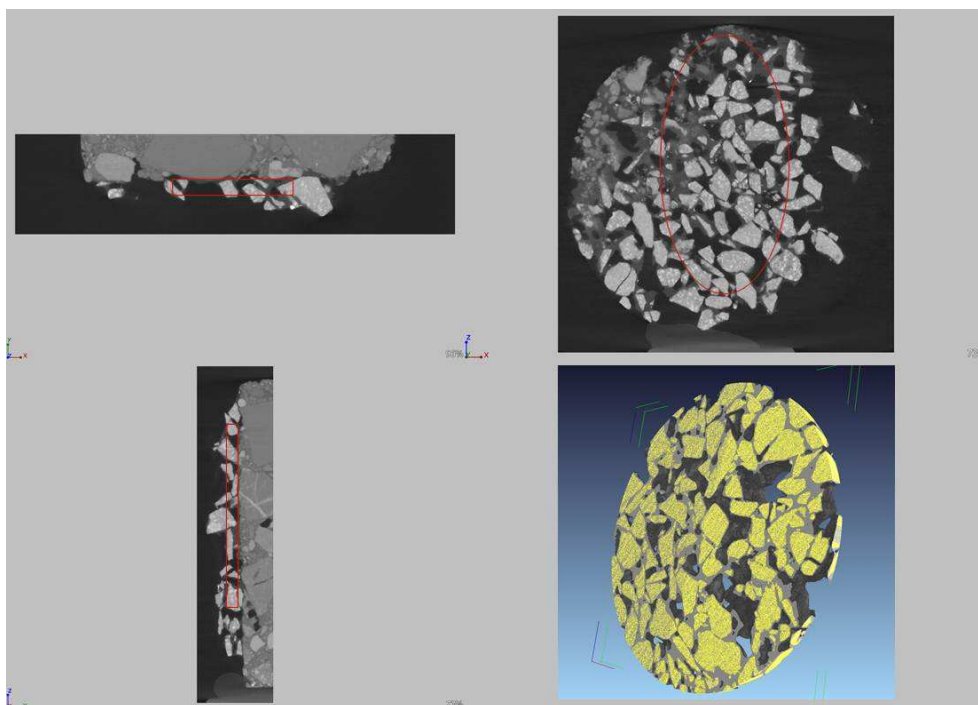


Figure 4-12 Side views of selected spaces for layer characteristic calculations

The Soesterberg sample, which was constructed in 1989, has the highest void content and lowest aggregate content. This may be a result from the construction method being used which was different from the methods used in newer antiskid layers, or some raveling occurred during its service life. The results of the other five airports are more or less the same. For these five airports, the calculated average void content is 17.4% and the average binder content is 26.9%. This indicates that antiskid layers have a very high binder content and void content. A high void content is recommended to provide sufficient macrotexture and prevent airplanes from hydroplaning in rainy days.

Table 4-1 Volumetric of tar-containing antiskid layers from Nano CT scan

	Woensdrecht		Gilze-Rijen		Leeuwarden		Eindhoven	
Total Volume [mm ³]	345	730	1400	1200	677	547	630	346
Void [%]	18.3	18.1	18.7	17.8	16	18.8	15.5	17.5
Binder [%]	27.5	29.3	27.3	28	25.3	25	25.5	25.5
Aggregate [%]	54.2	52.6	54	54.1	58.7	56.4	59.2	57
	Volkel				Soesterberg			
Volume [mm ³]	210	127	287	545	300	100	577	
Void [%]	17.1	15.5	18.1	23.7	23.6	25.7	29	
Binder [%]	27.8	27.6	27.6	27.7	27.9	23.9	22.3	
Aggregate [%]	55.2	57.2	54	49.5	51.8	50.4	48.6	

Table 4-2 Average volumetric of tar-containing antiskid layers

	Void [%]	Binder [%]	Aggregate [%]
Woensdrecht	18.2	28.7	53.1
Gilze-Rijen	18.3	27.6	54.1
Leeuwarden	17.3	25.2	57.7
Eindhoven	16.2	25.5	58.4
Volkel	17.2	27.7	55.1
Average (excluding Soesterberg)	17.4	26.9	55.7
Soesterberg	25.8	25.4	49.7

4.2.2 Microscopy

Laser scanning microscopy is widely used to investigate the surface characteristics of pavements, which include surface profile and surface roughness [6]. High data density 3D images of surface structures can be produced. Vilaça et al. [7] developed a new scanning prototype machine for obtaining 3D road surface data and characterizing the road texture through two algorithms that allow to calculate the Texture Depth and Texture Profile Level. Their results showed good agreement between the scanning equipment and the traditional Sand Patch Test method.

In this research, laser scanning microscopy was used to determine the surface profiles of the tar-containing antiskid surface layers. Table 4-3, Figure 4-13 and Figure 4-14 present the average test results. Table 4-4 presents the detailed results.

Table 4-3 Average microscope test results

	St [mm]	Sa [mm]	Pa [mm]
Woensdrecht	3.702	0.602	0.362
Gilze-Rijen	3.449	0.595	0.310
Leeuwarden	3.455	0.597	0.300
Eindhoven	4.076	0.691	0.378
Volkel	3.545	0.599	0.312
Soesterberg	3.620	0.631	0.338
Average	3.64	0.62	0.33

St: Maximum height of selected area
 Sa: Average height of selected area
 Pa: Mean Profile Depth (MPD, state as mean average height of primary profiles is the Microscope data reports.)

The maximum height of the selected area varied from 3.45 mm to 4.08 mm, while the average height of the selected area varied from 0.56 to 0.69 mm. The antiskid layer in Eindhoven Airfield has the highest values for the maximum and average height. Gilze-Rijen Airfield, which has the second newest antiskid runway surface, has the lowest values. However, the differences between each airfield are less than 1 mm. This means that these six airfields have quite similar surface profiles.

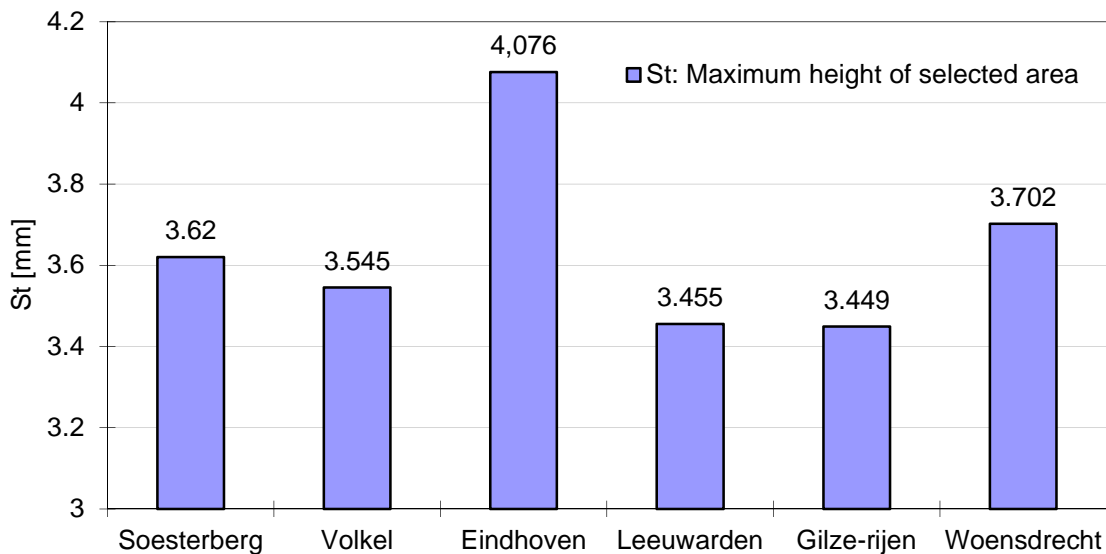


Figure 4-13 Maximum heights of measured areas

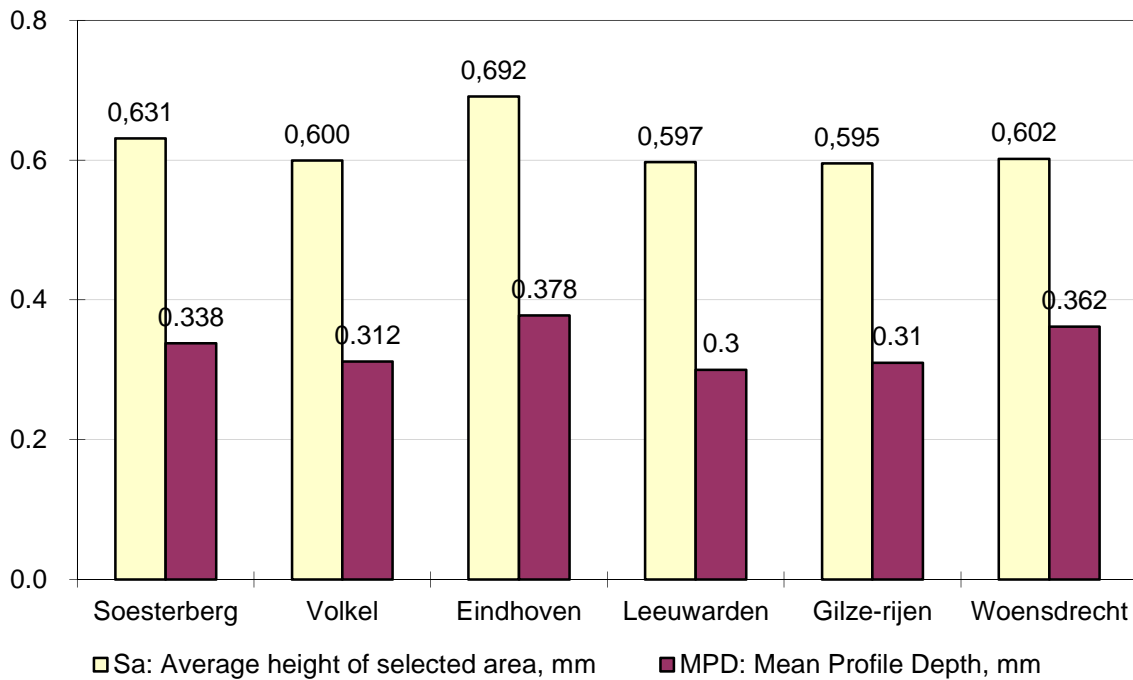


Figure 4-14 Average height and Mean Profile Depth

The texture values of the antiskid layer from Soesterberg Airfield are just slightly lower than the average value, even after 16 years of service and another 4 years exposure to climate with no traffic on it. This indicates that tar-containing antiskid layers can maintain relatively constant texture levels for a long period of time.

As explained in Chapter 3, because of a misunderstanding, 5 samples from Gilze-Rijen airfield and all samples from Leeuwarden Airfield were not taken in the longitudinal direction, but in a direction perpendicular to the runway centerline. Figure 4-15 shows MPD values at different positions. The left of the graph is closer to the runway side and the right is closer to the middle part which is used more often by aircrafts. No obvious decrease of the MPD value from the side to the middle of the runway can be observed from these figures. Figure 4-14 and Table 4-4 show that the average values of the MPD for Gilze-Rijen and Leeuwarden Airfields are slightly lower than those of the other airports. It is therefore concluded that the different coring locations on Leeuwarden and Gilze-Rijen did not significant influence the texture results. The tar-containing antiskid layer can maintain its high texture depth during its service life, even at the center line area where heavy loads normally occur.

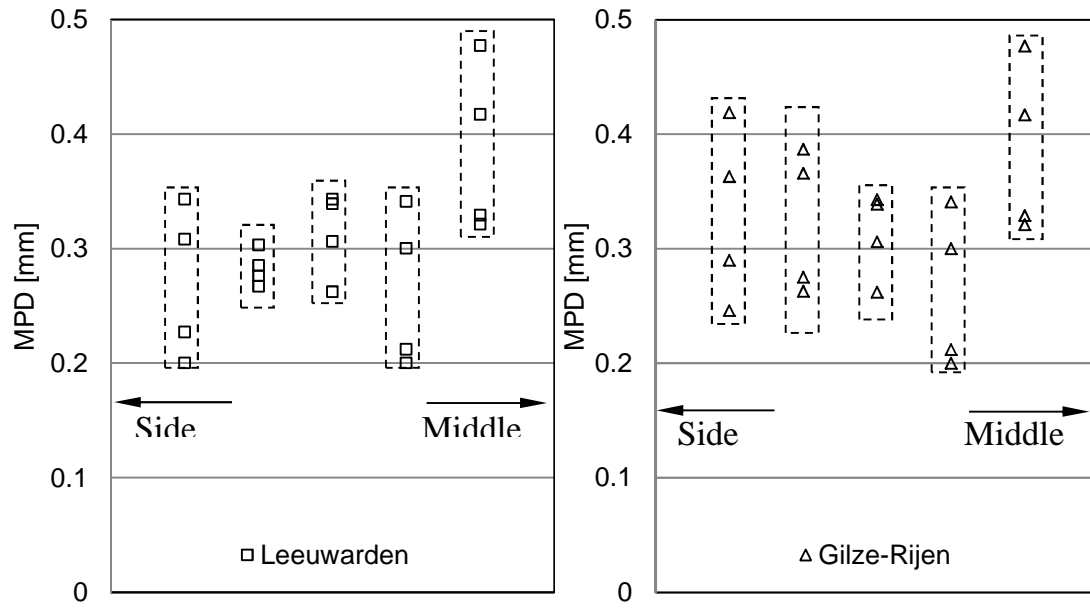


Figure 4-15 MPD values of cores at different positions

Table 4-4 Microscope test results on tar-containing antiskid surfaces

Woensdrecht	W1	W2	W3	W4	W5	W6	W7	W8	W9	W10	Average
St [mm]	3.901	3.104	3.641	4.318	3.191	3.495	3.931	4.032	3.920	3.489	3.702
Sa [mm]	0.662	0.612	0.601	0.727	0.499	0.569	0.618	0.620	0.610	0.502	0.602
Pa [mm]	0.3	0.383	0.379	0.340	0.321	0.360	0.465	0.322	0.392	0.364	0.362
Gilze-Rijen	G1	G2	G3	G4	G5	G6	G7	G8	G9	G10	Average
St [mm]	4.220	3.650	3.183	3.199	4.301	3.404	2.787	2.973	3.293	3.480	3.449
Sa [mm]	0.686	0.651	0.525	0.542	0.842	0.587	0.444	0.490	0.554	0.633	0.595
Pa [mm]	0.330	0.323	0.313	0.263	0.386	0.293	0.325	0.264	0.295	0.313	0.310
Leeuwarden	L1	L2	L3	L4	L5	L6	L7	L8	L9	L10	Average
St [mm]	2.890	3.120	4.137	3.238	4.180	3.246	3.687	3.415	3.180	3.453	3.455
Sa [mm]	0.497	0.606	0.663	0.606	0.730	0.519	0.530	0.652	0.513	0.654	0.597
Pa [mm]	0.270	0.307	0.311	0.303	0.308	0.300	0.283	0.330	0.260	0.332	0.300
Eindhoven	E1	E2	E3	E4	E5	E6	E7	E8	E9	E10	Average
St [mm]	4.670	4.433	4.696	4.275	5.317	3.458	3.462	3.722	3.308	3.424	4.076
Sa [mm]	0.806	0.777	0.731	0.731	0.848	0.668	0.580	0.617	0.566	0.591	0.691
Pa [mm]	0.385	0.488	0.392	0.373	0.412	0.360	0.344	0.376	0.314	0.340	0.378
Volkel	V1	V2	V3	V4	V5	V6	V7	V8	V9	V10	Average
St [mm]	2.978	3.632	3.969	3.895	4.011	3.551	3.205	3.19	3.634	3.385	3.545
Sa [mm]	0.474	0.581	0.785	0.678	0.607	0.575	0.553	0.531	0.587	0.625	0.599
Pa [mm]	0.303	0.284	0.349	0.338	0.369	0.293	0.347	0.293	0.282	0.264	0.312
Soesterberg	S1	S2	S3	S4	S5	S6	S7	S8	S9	S10	Average
St [mm]	3.224	3.323	3.868	3.524	3.678	4.145	3.665	3.176	3.071	4.534	3.620
Sa [mm]	0.540	0.549	0.680	0.562	0.604	0.739	0.627	0.572	0.515	0.925	0.631
Pa [mm]	0.293	0.321	0.308	0.337	0.395	0.337	0.350	0.350	0.329	0.290	0.338
St: Maximum height of selected area; Sa: Average height of selected area; Pa: Mean Profile Depth, MPD											

4.2.3 Sand Patch Test

In the past, the Sand Patch Test (SPT) has been used for many years as the main test method to determine the surface texture depth. Nowadays, the Sand Patch Test is slowly being replaced by newly developed technologies such as laser devices, which can give more accurate results, [8] and also by continuously taken laser measurements at high speed in the field. In this research, the SPT was used as a reference for the calibration of results from the microscope tests that were discussed in the previous section.

ASTM E 965-96 states that at least 25 ml of sand shall be used to determine the TD [9]. In this study, it was not allowed to do test on the runways. Therefore, sand patch tests were done on the cores. Therefore only a limited amount of sand, which is 15 ml, could be used due to the limited diameter of the cores, see Figure 4-16. The diameter of the sand spread on the surface is approximately 110 to 120 mm. Table 4-5 and Figure 4-17 present the test results. The TD of the tar-containing antiskid layers varies between 1.26 and 1.46 mm. The average TD of all airfields is 1.36. The TD of Soesterberg Airport, which was constructed in 1989, is just slightly lower than the average.



Figure 4-16 Sand patch test on tar-containing antiskid layers

Table 4-5 Sand patch test results on two cores for each airport

	Texture Depth [mm]		
	NO. 1	NO. 2	Average
Woensdrecht	1.413	1.450	1.43
Gilze-Rijen	1.383	1.372	1.38
Leeuwarden	1.262	1.262	1.26
Eindhoven	1.444	1.483	1.46
Volkel	1.354	1.268	1.31
Soesterberg	1.310	1.366	1.34

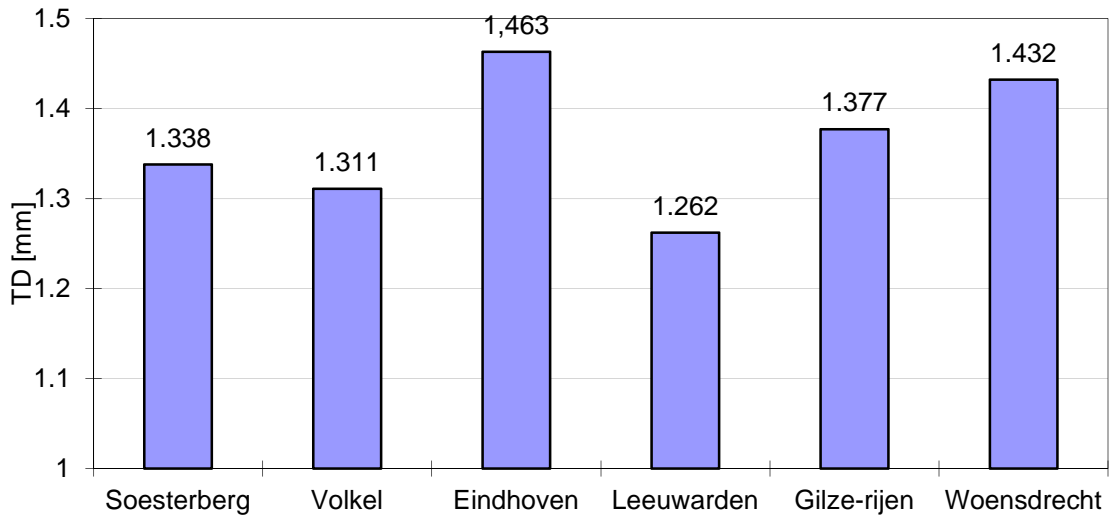


Figure 4-17 Sand patch test results

By means of a linear transformation, the MPD from the laser test (e.g. microscopy) can be used to estimate the macro-texture depth determined using a volumetric technique such as sand patch test [9, 10]. The relation between MPD and MTD differs due to the finite size of the sand spheres used in the volumetric technique. Because the MPD is derived from a two-dimensional profile rather than a three-dimensional surface, a transformation equation must be used. The following equation is concluded from Table 4-3 and Table 4-5 by using the solver function in Excel:

$$TD \approx ETD = 0.647 + 2.146 \times MPD \quad (4-1)$$

Where MPD is the mean profile depth based on the evaluation of the results with the microscope. ETD is the Estimated Texture Depth. Table 4-6 shows the ETD results. They fit quite well with the TD values from the sand patch test. This indicates that the sand patch test gives a similar texture depth as the microscope for the surface of antiskid layers. Both methods can be used for surface texture evaluation of antiskid surface layers. The sand patch results on cores represent the TD very well and can therefore be used for benchmark purposes.

Table 4-6 ETD results from Mean Profile Depth

	MPD [mm]	TD [mm]	ETD [mm]
Woensdrecht	0.362	1.432	1.423
Gilze-Rijen	0.31	1.377	1.312
Leeuwarden	0.3	1.262	1.291
Eindhoven	0.378	1.463	1.458
Volkel	0.312	1.311	1.317
Soesterberg	0.338	1.338	1.372

4.3 Aging Resistance

Fourier Transform Infrared (FTIR) spectroscopy was used to determine the long term ageing of the tar-containing binders. Because of the different construction times of the investigated antiskid layers, it was expected to acquire information about the long term ageing resistance of the tar-containing binders as a result of exposure to oxygen, temperature, deicing, chemicals etc. during the service period.

Figure 4-18 shows the differences between an aged bitumen 70/100 [11] and coal-tar in the FTIR test. They have similar absorption peaks and areas. But the proportions are very different. The ratio between alkanes (area of 2900 cm^{-1}) and aromatics (area of 800 cm^{-1} and 1600 cm^{-1}) is different between bitumen and coal tar. The red curve in Figure 4-18 shows that the absorption peak of the aromatics is equal to the absorption peak of alkanes in coal-tar. This is because tar has a high content of Polycyclic Aromatic Hydrocarbons (PAHs), i.e. molecules containing two or more simple aromatic rings fused together by sharing two neighboring carbon atoms. Furthermore, the aromatic C-H stretching modes between 3000 to 3100 cm^{-1} is very clear for coal tar [12].

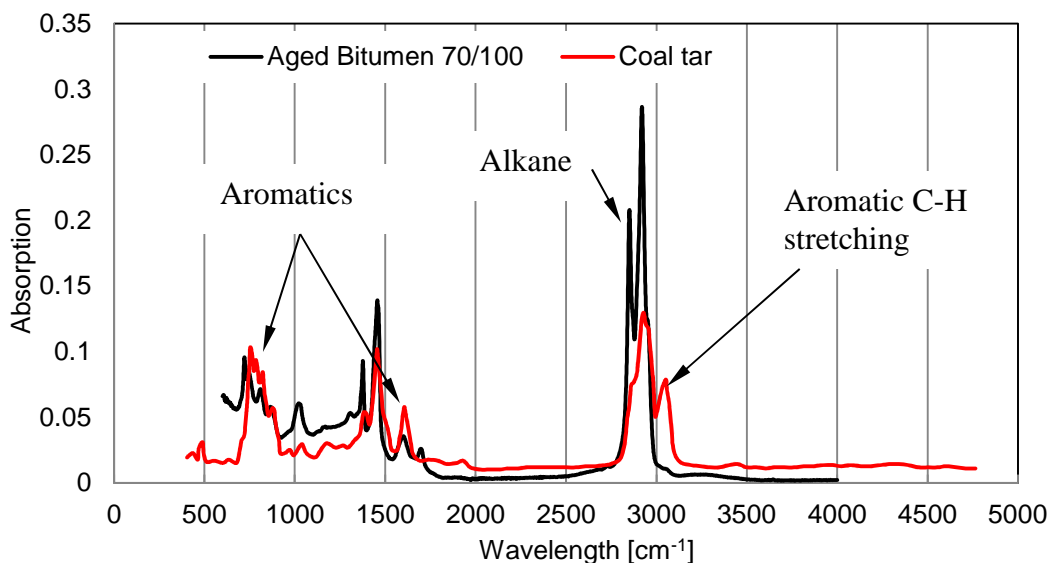


Figure 4-18 Differences between aged bitumen and coal-tar in FTIR test

In the beginning, it was tried to recover the tar-containing binders from the antiskid layer by using solvents. However, the composition of the tar-containing binders was unknown. Lack of knowledge about the composition complicates tar-containing binder extraction. Furthermore, laboratories in the Netherlands (e.g. KOAC-NPC) also did not want to do the recovery because of the possible toxic properties of the binder. Because of the health issue, it was decided not to recover tar-containing binders by means of solvents.

Instead the antiskid layer was grinded into powder with a sand grinding machine and then this powder was analyzed in the FTIR test. Figure 4-19 shows the tar-containing powders and the FTIR tester. However, the grinding processes can cause high temperatures and influence results. Antiskid from Woensdrecht and Gilze-Rijen could not be grinded into powders due to such high temperatures. They were more temperature sensitive compared to the samples from the other four airfields. During grinding, the antiskid mixtures of these two airports were sticking to the mould, making it impossible to grind them into powder. This indicates that the tar-containing binder in Woensdrecht and Gilze-Rijen might differ from the other four binders. At the meantime, the high temperature might introduce short term high temperature ageing, and affects the FTIR test results.



Figure 4-19 Powder of tar-containing antiskid mixtures and FTIR tester

Figure 4-20 shows the FTIR spectrums of tar-containing antiskid mixtures. The sample protocol-1 represents an aged bitumen 70/100 [11]. Table 4-7 shows the FTIR absorptions for representative functional groups, and Table 4-8 presents the absorption peak heights from the FTIR tests.

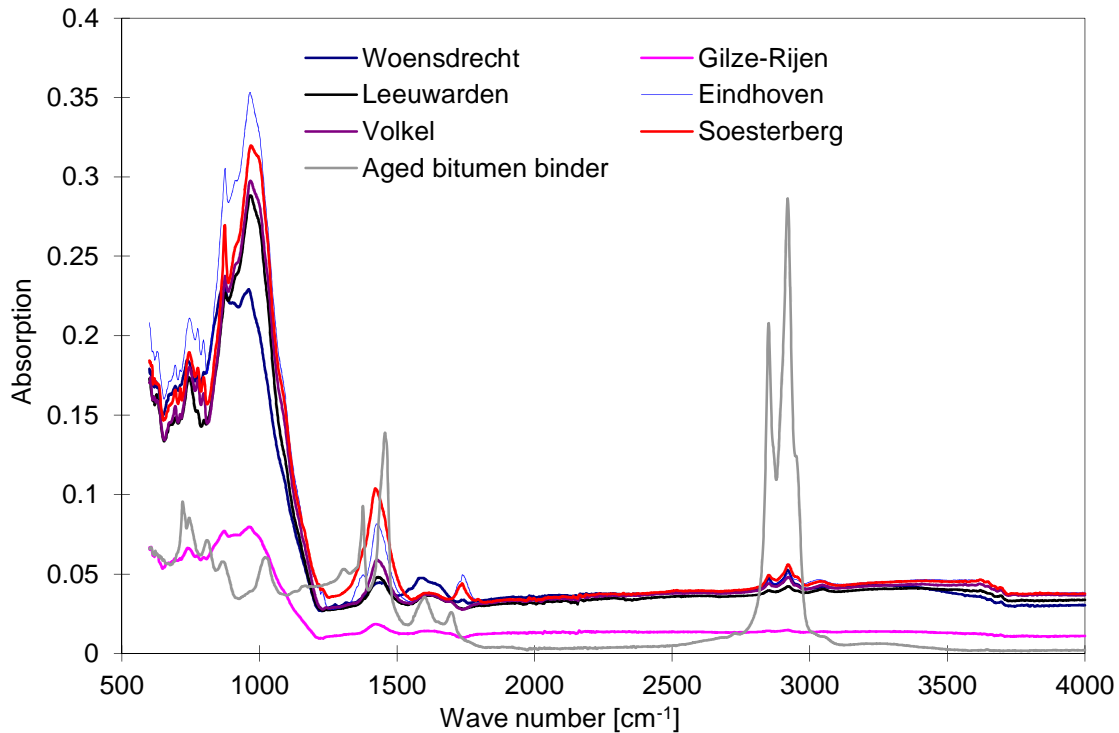


Figure 4-20 FTIR test results of tar-containing antiskid layer mixtures

From Figure 4-20 and Table 4-8, one can clearly observe that the tar-containing samples had a much higher absorption peak at 960 cm^{-1} and 860 cm^{-1} , which represent the deformation vibrations of the CH groups in the aromatic rings. Absorption peaks at the 2850 cm^{-1} area are resulting from CH stretch in alkanes. There are two strong absorption peaks at 1450 cm^{-1} and 1700 cm^{-1} . These are the peak absorbance of the carbonyl bond (C=O). There is no obvious absorption peak at 1030 cm^{-1} of S=O stretch in the FTIR spectrums.

Table 4-7 FTIR absorptions for representative functional groups

Functional group	Molecular motion	Wavenumber [cm^{-1}]
Aromatics	C-H stretch	3100-3000
	C=C stretch	~ 1600 & ~ 1475
	C-H bend	~ 880 & ~ 780 & ~ 690 & $850-800$ & $770-735$ & $715-685$
Alkanes	C-H stretch	2950-2800
	CH ₂ bend	~ 720
	C-H in-plane bend	1430-1290
Carboxylic acids	C=O stretch	1730-1700
	C-O stretch	1320-1210
Ketones	C=O stretch	~ 1715
Sulfoxides	S=O stretch	~ 1030

Table 4-8 Peak height from FTIR results

		CH ₂	CH in aromatic		C-H	C=O		CH in alkanes	
W	Peak at [cm ⁻¹]	738	871	960	1431	1595	1699	2851	2920
	Absorbance	0.1847	0.2307	0.2291	0.0446	0.0476	0.0345	0.0478	0.0525
L	Peak at [cm ⁻¹]	744	875	967	1431	1603	1699	2851	2923
	Absorbance	0.1737	0.227	0.2883	0.0481	0.0366	0.0327	0.0398	0.0424
E	Peak at [cm ⁻¹]	745	875	966	1427	1600	1697	2851	2922
	Absorbance	0.211	0.3053	0.3532	0.0816	0.0368	0.034	0.0458	0.0504
V	Peak at [cm ⁻¹]	744	875	967	1427	1610	1698	2851	2922
	Absorbance	0.1802	0.2377	0.2975	0.0589	0.037	0.0325	0.0442	0.048
S	Peak at [cm ⁻¹]	745	874	971	1421	1608	1699	2852	2922
	Absorbance	0.1897	0.2696	0.3196	0.1039	0.0381	0.0343	0.0494	0.0559
AB	Peak at [cm ⁻¹]	745	864	970	1456	1600	1697	2851	2920
	Absorbance	0.0854	0.0578	0.0393	0.1391	0.0354	0.0258	0.2079	0.2865
G	Peak at [cm ⁻¹]	739	872	963	1424	1599	1698	2848	2922
	Absorbance	0.0664	0.0771	0.0797	0.0184	0.0141	0.0124	0.0142	0.0147

Note: AB represents the aged bitumen binder.

The Gilze-Rijen sample showed a much lower absorption peak at 960 cm⁻¹ and 860 cm⁻¹ than the others. Gilze-Rijen has the second newest antiskid layer, and also huge differences occurred during the grinding. On the one hand, it could mean that a different binder was used at Gilze-Rijen airfield. On the other hand, the binder of the Gilze-Rijen and Woensdrecht antiskid layers (the two youngest antiskid layers) used for FTIR is just a part of the whole mixture (not really powder) because of the high temperature during the grinding.

In the research of Van den bergh [13], equation (4-2) was introduced for the Ageing Index (AI) to determine the oxidation ageing properties in bituminous materials. The ageing indicator is being divided by the sum of two areas: the ethylene groups (CH₂) at 1460 cm⁻¹ and methyl (CH₃) at 1375 cm⁻¹. These groups are believed not to be changed during ageing.

$$AI = I_{CO} + I_{SO} = \frac{\sum (\text{Around } 1700\text{cm}^{-1} + \text{around } 1030\text{cm}^{-1})}{\sum (\text{Around } 1460\text{cm}^{-1} + \text{around } 1375\text{cm}^{-1})} \quad (4-2)$$

Figure 4-21 shows the AI definition with bituminous binder (upside graph) and tar-containing binder from Soesterberg (bottom graph). One can clearly observe that the definition of Equation (4-2) for tar-containing binder has significant differences from the definition for bituminous material. The peak area at 1700 cm⁻¹, 1375 cm⁻¹ and 1030 cm⁻¹ are cannot be defined. This might indicate that the AI introduced for bituminous binder is not suitable for tar-containing binders.

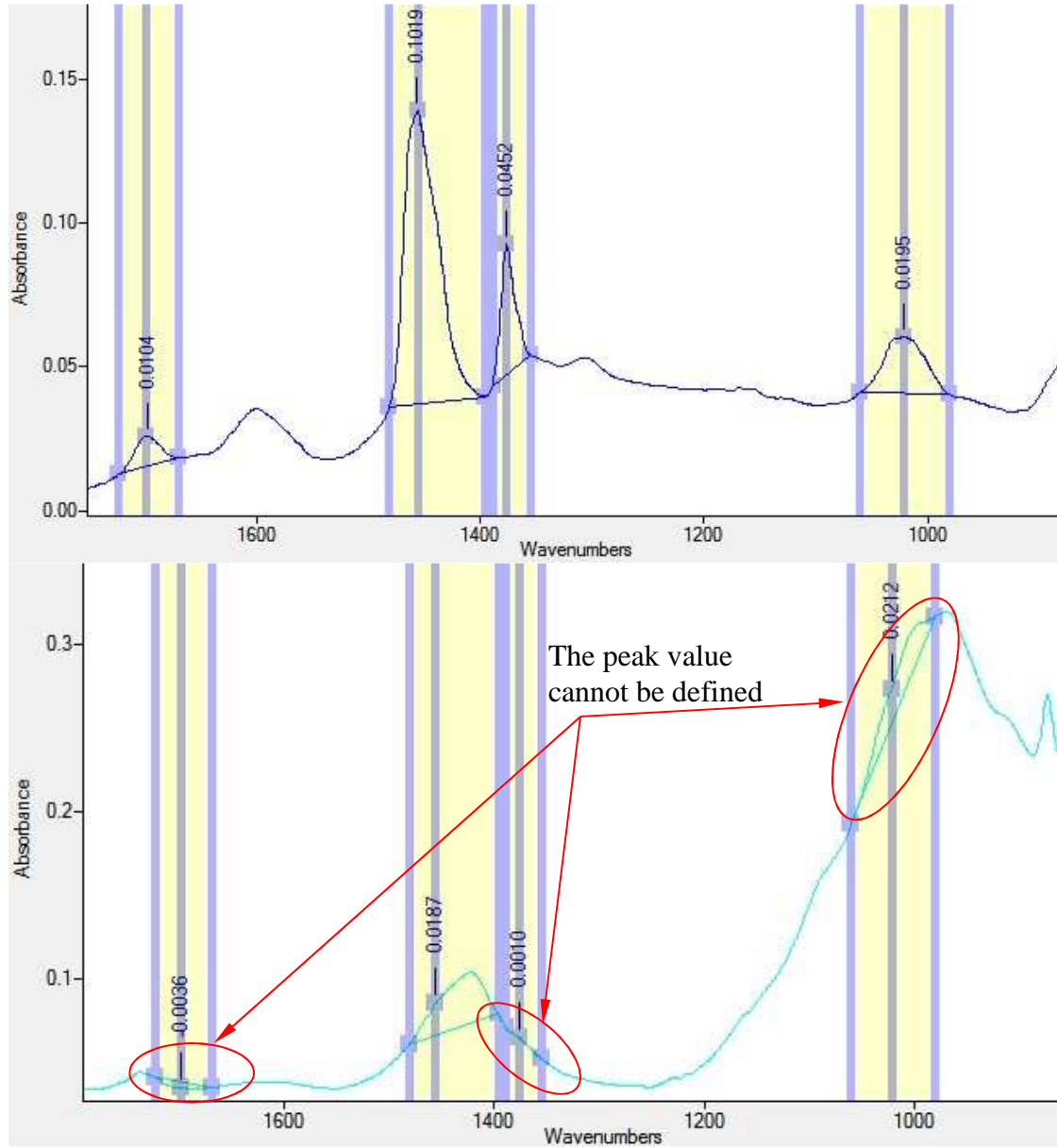


Figure 4-21 AI definition with bituminous binder and tar-containing binder

Therefore, another equation of the ageing index was used to determine the oxidation ageing properties [14]:

$$I_{\text{Ageing}} = \frac{\sum(\text{Carbonyl}: 1208\text{cm}^{-1}\text{to}1800\text{cm}^{-1})}{\sum(780\text{cm}^{-1}\text{to}1800\text{cm}^{-1} + 2810\text{cm}^{-1}\text{to}3100\text{cm}^{-1})} \quad (4-3)$$

The following equation (4-4) can be used to determine the aromatic content in the mix of antiskid layer [14]:

$$I_{\text{Aromatic}} = \frac{\sum(\text{Aromatic}: 780\text{cm}^{-1}\text{to}1208\text{cm}^{-1})}{\sum(780\text{cm}^{-1}\text{to}1800\text{cm}^{-1} + 2810\text{cm}^{-1}\text{to}3100\text{cm}^{-1})} \quad (4-4)$$

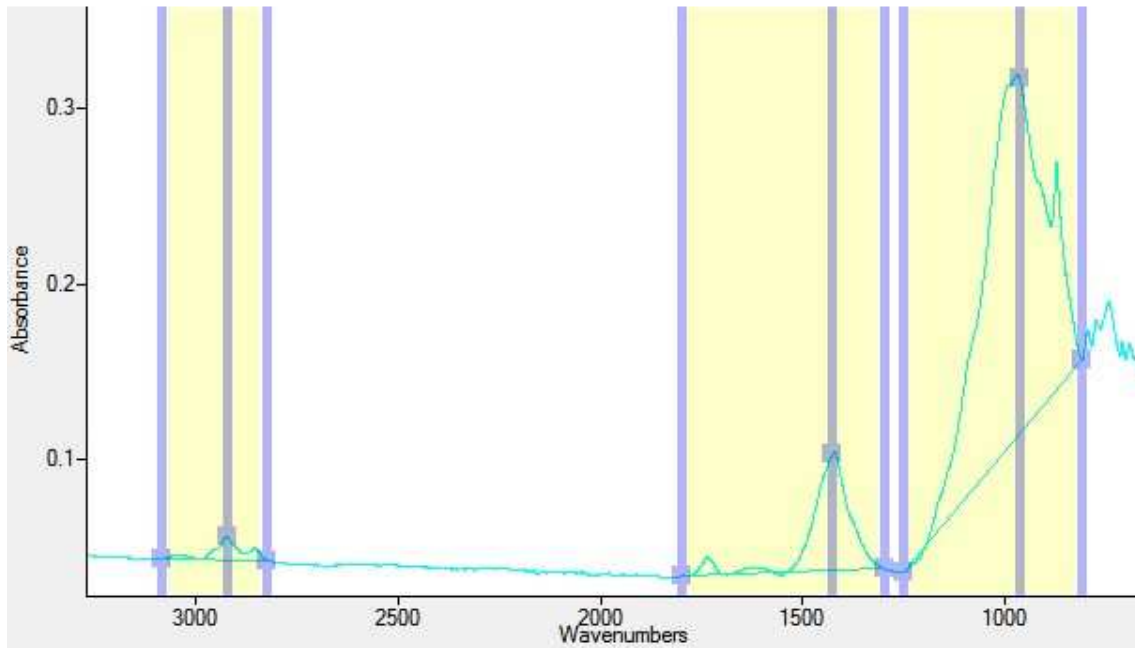


Figure 4-22 Definition of denominator for Equation (4-3) and (4-4)

Figure 4-22 shows the definition of the denominator for Equation (4-3) and (4-4). Table 4-9 shows the parameters that were calculated from the FTIR tests. All of the six antiskid mixture samples at least have a more than two times higher aromatic index compared to the long term aged bitumen binder. This indicates that the tar-containing antiskid layer mixture has more aromatic rings in the binder, which make it more toxic.

Table 4-9 Indexes from FTIR results

	I_{Ageing}	$I_{Aromatic} [780-1208]$
Woensdrecht	0.213	0.664
Gilze-Rijen	0.217	0.668
Leeuwarden	0.187	0.704
Eindhoven	0.187	0.712
Volkel	0.187	0.702
Soesterberg	0.223	0.67
Long term aged binder	0.337	0.295

The six tar-containing antiskid samples have more or less the same ageing index. And their ageing indexes are much lower than the ageing index in the long term aged 70/100 binder. This probably means that the ageing resistance of a tar-containing binder is much better than that of standard 70-100 pen bitumen. After a long service life at least the ketones content (C=O) in the tar-containing binder will not increase a lot. The Gilze-Rijen and Woensdrecht have the youngest specimens, but show higher values compared to the other ones. This is might

because of the high temperature occurred during the grinding process. Or different composition could be used for these two antiskid layers.

4.4 Modulus and Phase Angle

The modulus and phase angle of the antiskid layer mixtures were investigated in this research by means of DSR test. Antiskid layers were scratched off from cores and reheated to compact small cylindrical samples.

4.4.1 Sample Preparation

Antiskid layer mixtures (sand and binder) were used to prepare cylindrical samples for the DSR test. The antiskid material had to be taken from the core surface and had to be compacted. The toxic emissions from tar-containing antiskid mixtures will increase when the temperature is increased. In order to avoid environmental and health problems, the preparation temperature was first checked. Mixtures were compacted at 65, 80, 100, 110 and 135 °C. When the temperature was below 110 °C, the aggregates did not stick well to each other. When a temperature above 135 °C was used, much more hazardous emissions might be observed and technicians can easily smell them. Therefore 135 °C was used to heat the mix for compaction purposes.

A mould as shown in Figure 4-23 was designed to compact the antiskid mix. This mould consists of two pieces of semi-cylinders with 15 mm inner diameter. Two clamps were used to fix this mold during the sample compaction. The sample preparation procedure was as following:

1. About 12 gram of antiskid mixture was heated in the oven at 135 °C for 2 hours.
2. First half of the antiskid mixture was added into the mold, after tamping the rest of the mixture was added.
3. A hydraulic pressure compactor was used to compact the sample to 45 mm height. After cooling down, both sides of the sample were cut off to finally have a column with 35 mm height.

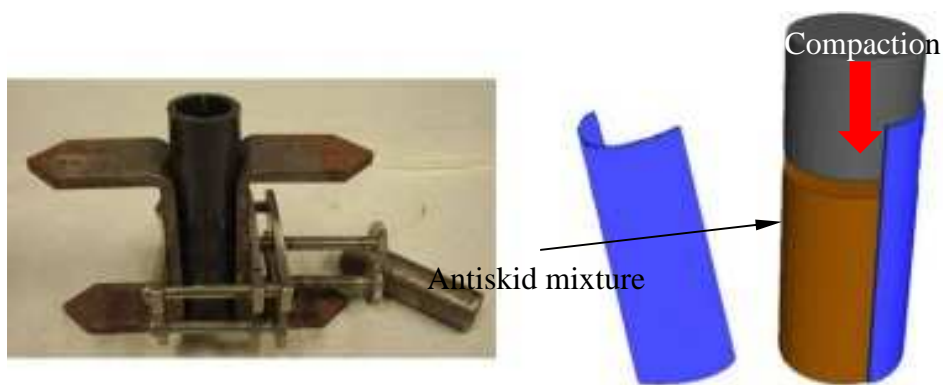


Figure 4-23 Designed mould to compact antiskid mix

Table 4-10 shows the estimated void contents in the compacted mix columns. The volume ratios between binder and aggregate presented in Table 4-2 were used for the estimation of the voids content. The density values of tar-containing binder and basalt were assumed to be 1.25 g/cm³ and 2.95 g/cm³ respectively. The estimated results indicate that the compacted mix columns have a much higher void content than the void content obtained from CT scanning that was presented in Table 4-2. This means that the antiskid mixture columns are different from the real antiskid mix. Nevertheless, it was considered too risky to increase the heating temperature to achieve better compaction due to health issues. So these compacted samples were used for frequency sweep tests to get an indication of the visco-elastic properties.

Table 4-10 Estimated void contents of the compacted mix columns

Sample	Weight [g]	Height [mm]	Diameter [mm]	Estimate void content [%]
L	10.3	38	15	36.9
E	11.4	44	15	39.8
V	10.1	35	15	31.4
S	9	32	15	33.9

Note: Information for W and G are not available

4.4.2 Frequency Sweep Test

The antiskid mixture column was glued on the DSR machine for the frequency sweep test, see Figure 4-24. At the different temperatures stress levels were selected to ensure that the material was tested within the linear viscoelastic range. The test parameters and conditions are shown in Table 4-11. The test temperatures were 10 °C, 20 °C, 40 °C and 60 °C. A frequency range from 0.1 rad/s to 300 rad/s was used. Cylindrical specimens with approximately 35 mm height and 15 mm diameter were tested.

Table 4-11 Frequency sweep test specifications

Loading mode	Stress			
Frequency [rad/s]	0.1 to 300			
Temperature	10 °C	20 °C	40 °C	60 °C
Applied stress [Pa]	755	151	91	60

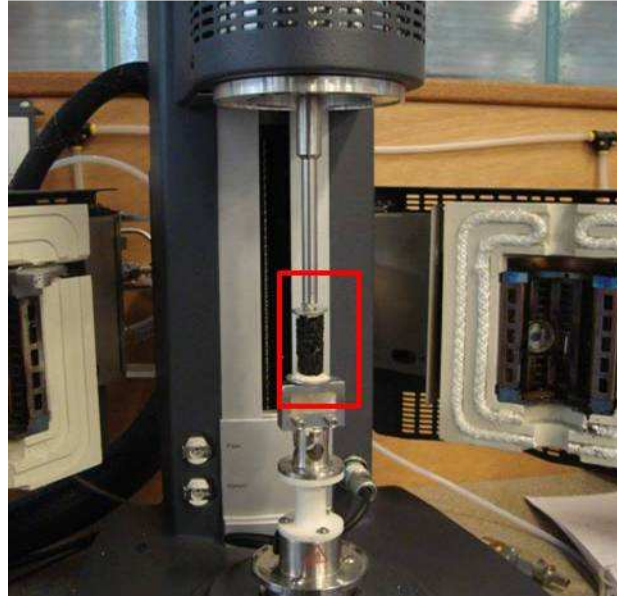


Figure 4-24 Frequency sweep test on an antiskid mixture column

4.4.3 Test Results

At the beginning, tests were carried out on two columns made from the antiskid mixture of Gilze-Rijen Airport. Figure 4-25 shows the results of the complex modulus. At 10 °C and 40 °C, the test results are nearly the same, while at 20 °C and 60 °C the results show some different values, but of the same order of magnitude. This illustrated that the columns of the antiskid mixture will give reasonably comparable values to test and compare with confidence in the frequency sweep test.

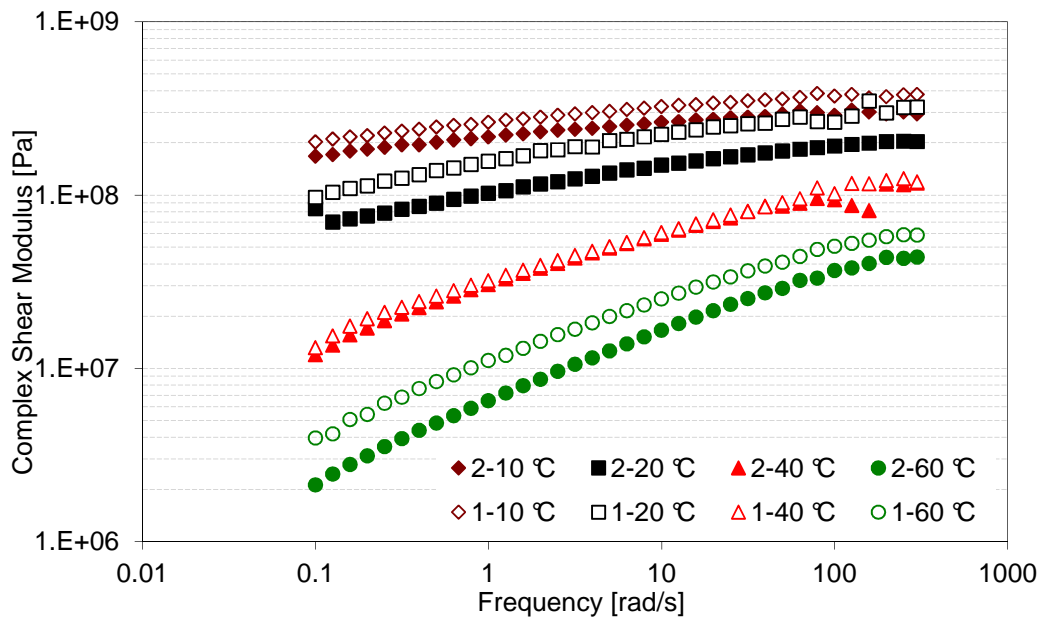


Figure 4-25 Tests on two columns from Gilze-Rijen mixture

Figure 4-26 shows the master curves of the complex shear modulus of the six mixtures of all airports. Figure 4-27 shows the results of phase angle. The reference temperature is 20 °C. A virgin bitumen binder and its long term aged binder from the research from Hagos were used for comparison [15]. Although the tests were conducted on the antiskid mixtures, the phase angle of the mixture is strongly dependent on the binder, especially at lower temperatures and higher frequencies and the shape of the modulus is parallel to the modulus curve of the binder. It is not right to compare the modulus values between the bitumen binder and tar-containing antiskid mixtures. But the slopes of the curves, which indicate the temperature sensitivity, can be compared.

The six modulus curves show similar shapes and slopes. The phase angle curves also express similar slopes. This means that these six tar-containing antiskid binders have the same temperature sensitivity. The slopes of modulus curves for tar-containing antiskid binders are smaller than the slopes of bitumen binders. This illustrates that the tar-containing antiskid mix is less temperature sensitive than bitumen binder, which agree the results in 4.1.1. The phase angle of the tar-containing mix is much lower than the value of bitumen binders.

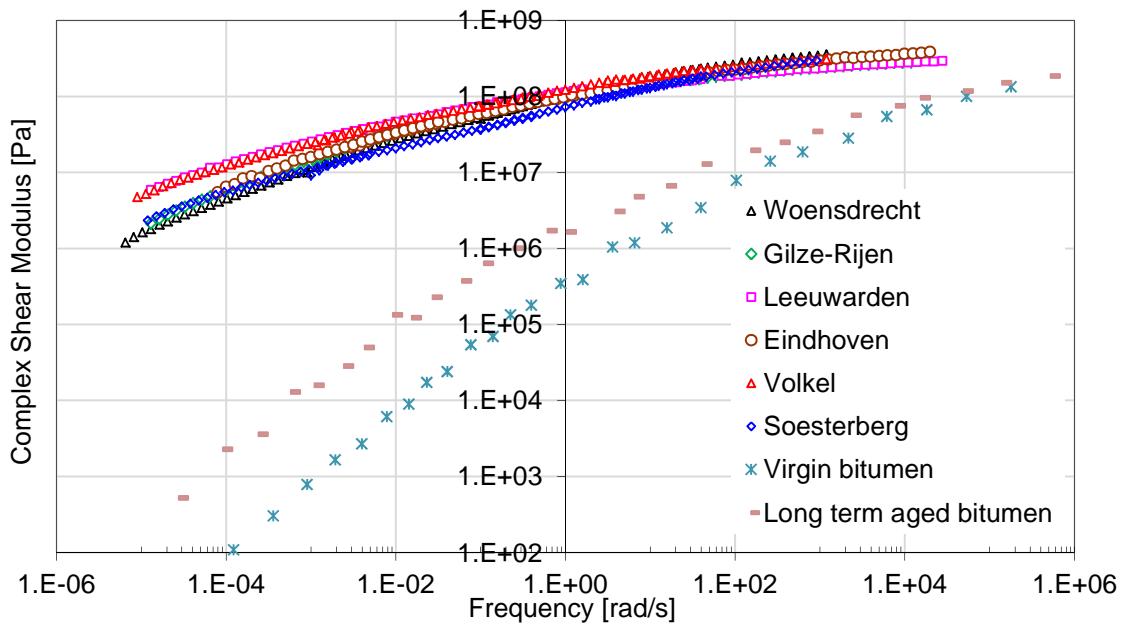


Figure 4-26 Complex shear modulus of six antiskid mixes at Tref=20 °C

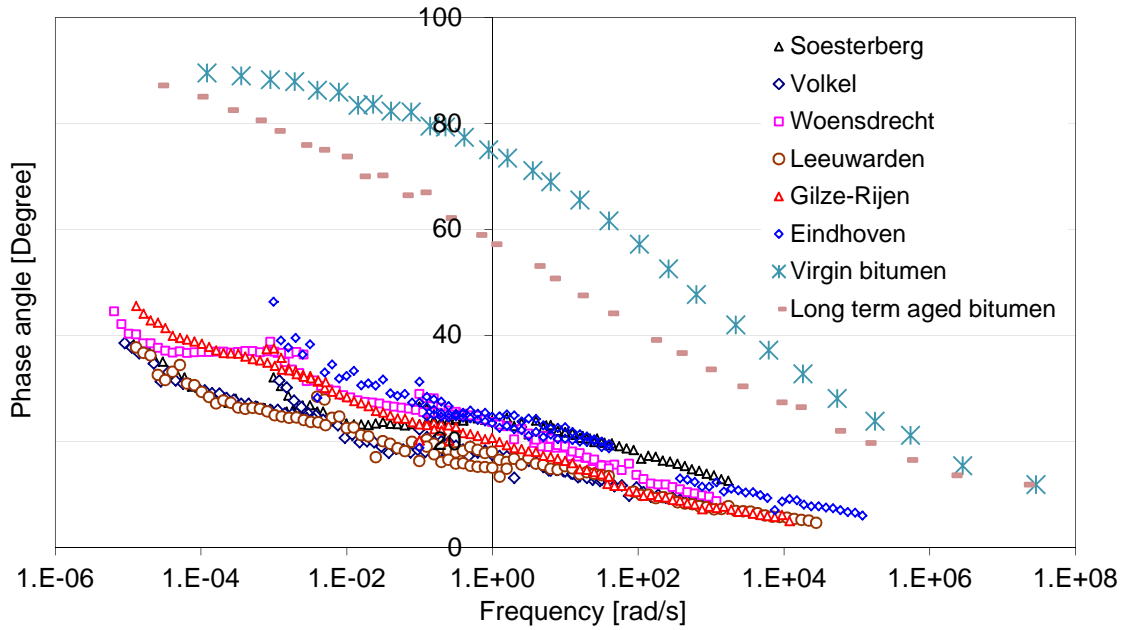


Figure 4-27 Phase angle of six antiskid mixes at Tref=20 °C

Table 4-12 presents the modulus and phase angle at 20 °C. In the frequency range of 0.1 rad/s to 100 rad/s, the phase angle of tar-containing binders varies from 10 degree to 30 degree. This illustrates that the tar-containing binders have a larger elastic component than their viscous component at 20 °C. The Woensdrecht and Gilze-Rijen airfields have the newest tar-containing antiskid mixtures. Lower modulus and higher phase angle were expected from the airfields. However, Table 4-12 does not show any relationship between the values and the service life. Different materials might be used for different airfields, which was also agrees with the phenomenon during the FTIR tests.

Table 4-12 Modulus and phase angle at different frequencies at 20 °C

	Frequency [rad/s]	0.1	1	10	100
Modulus [Pa]	Woensdrecht	5.0×10^7	10×10^7	1.8×10^8	4.5×10^8
	Gilze-Rijen	9.7×10^7	16×10^7	2.2×10^8	2.6×10^8
	Leeuwarden	1.0×10^7	11×10^7	1.4×10^8	1.8×10^8
	Eindhoven	1.0×10^7	9.6×10^7	1.5×10^8	2.1×10^8
	Volkel	7.3×10^7	12×10^7	1.9×10^8	2.7×10^8
	Soesterberg	3.6×10^7	7.2×10^7	1.3×10^8	1.9×10^8
Phase angle [Degrees]	Woensdrecht	28.92	23.55	19.01	15.35
	Gilze-Rijen	19.99	15.46	12.1	12.32
	Leeuwarden	16.22	17.99	15.23	12.33
	Eindhoven	18.74	24.58	22.62	17.54
	Volkel	22.16	17.43	14.27	12.36
	Soesterberg	26.51	23.97	21.7	10.56

4.5 Adhesion Properties

Antiskid runway surfaces are used to maintain a high friction level and sufficient surface texture to minimize hydroplaning during heavy rain. In order to achieve this performance, good adhesion between the aggregate particles in the antiskid layer is required, as well as good adhesion of the antiskid layer to the underlying layer.

On the one hand, a high adhesive strength in the antiskid layer can avoid raveling from the runway surface. On the other hand, good adhesion between antiskid layer and the underlying asphalt mixture layer gives good resistance to horizontal stresses introduced by heavy and high speed aircraft during take-off and landing. In order to test the adhesion properties, a pull test and the Leutner shear test were used to test the tensile and shear strength of the interface between antiskid surface layers and the underlying asphalt mixture layer. The test methods are explained in Section 3.3, Chapter 3.

4.5.1 Failure Modes

Figure 4-28 shows different failure surfaces between the tar-containing antiskid layer and the underlying asphalt mixture layer after the pull test. According to Section 3.3.3, there are five failure modes, at the bond interface (A), between steel plate and top thin surface (B), in the top layer (C), in the underlying asphalt mixture layer (D), and combined failure (E).

During the pull test, the samples from Woensdrecht Airfield tested at 10 °C and 20 °C all showed a combined failure (E) or failed at the interface between steel plate and antiskid surface layer (B). This means that at 10 °C and 20 °C, the DTS at the interface is higher than in the antiskid layer mixture at Woensdrecht Airport. This might be related to the fact that the Woensdrecht antiskid is the youngest and its binder might therefore be not as hard as the binder of the other antiskid layers. The black line in Figure 4-26 shows that at lower frequency, the Woensdrecht specimen has the lowest complex shear modulus.

Combined failure also happened on samples from Gilze-Rijen at 10 °C. Both from Gilze-Rijen Airfield and Eindhoven Airfield, one sample that was tested at 20 °C showed combined failure at the interface and in asphalt mixture. This may be caused by damage introduced before the tensile force was applied. Before the required tensile force was applied, the specimen was kept upside down and the glued steel plate was hanging on the specimen for one hour for temperature control purposes. This situation is similar to a creep test on the asphalt mixture, because the asphalt mixture is less stiff and more temperature sensitive than the tar-containing mixture. Therefore, some unexpected damage might have been introduced during the temperature control stage.

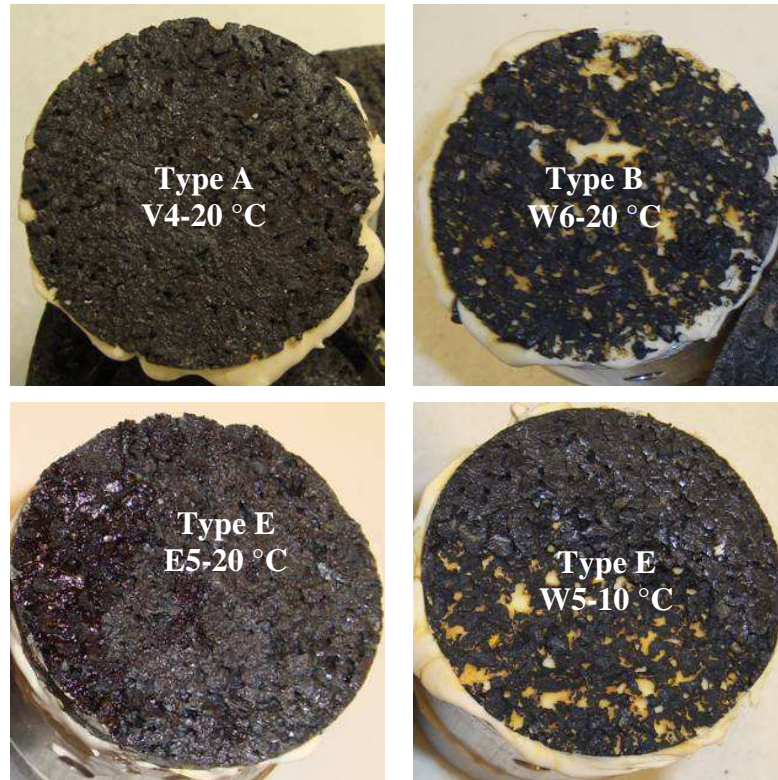


Figure 4-28 Fractured surfaces after pull test

Except for the above mentioned failures, all other pull tests resulted in failure at the interface (see the top-left graph in Figure 4-28). No failure occurred in the antiskid mixture, neither in the underlying asphalt mixture layer. These failure modes indicate that the interface is the weakest area when subjected to tension.

Figure 4-29 shows the failure surfaces obtained with the Leutner shear test. All the shear tests perfectly failed at the interface. This indicates that the newly designed pull test and shear test can be used to evaluate the adhesion properties between an antiskid surface layer and the underlying asphalt mixture.



Figure 4-29 Interface failure surfaces after the Leutner shear test

4.5.2 Leutner Shear Test Results

During the shear test, a constant vertical displacement rate of 50 mm/min is applied across the interface. The resulting shear force is measured. The selected test temperature was 20 °C. For each airport 2 samples were tested. The test method is explained in Section 3.3.2, Chapter 3. Figure 4-8 shows the force-displacement curves of the antiskid layers from Woensdrecht airport. The resulting force increases fast when a constant displacement rate is applied. When the maximum shear force is reached, the resulting force decreases till the interface completely fails. Figure A-1 in the attached Appendix presents the displacement-force curves for the other shear tests.

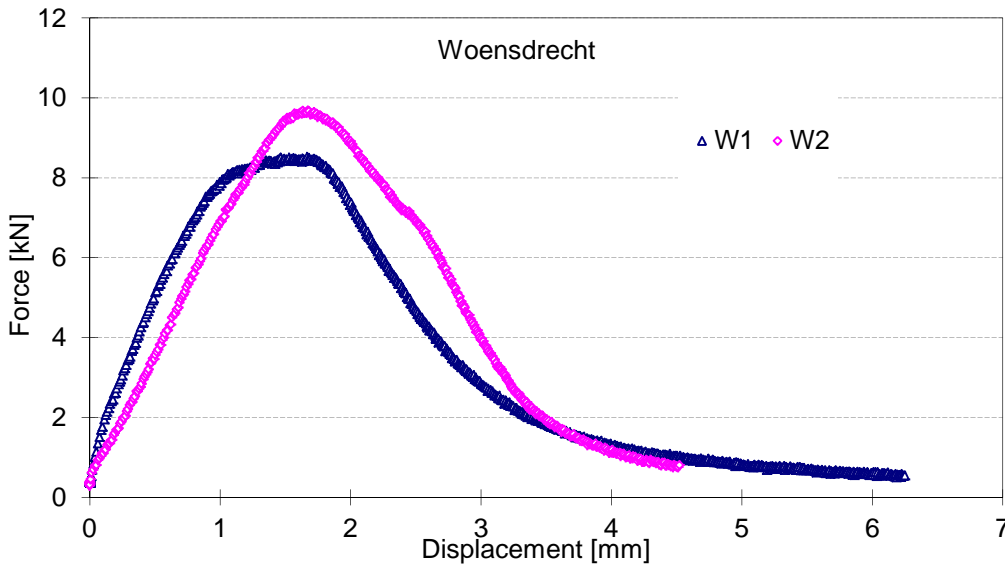


Figure 4-30 Displacement-force curves from shear tests

Table 4-13 shows the Leutner shear test results, together with the average values. Figure 4-31 shows the average shear strength and displacement at failure. The Soesterberg Airport samples have the second highest strength (1.69 MPa) while the antiskid layer has been in service for 20 years. The shear strength of Woensdrecht Airport samples, which have the newest antiskid layer, displays the lowest strength of 1.16 MPa. Samples from Eindhoven Airport have the highest displacement and relatively low shear strength. There is no obvious trend of shear strength in relation to the service life. It is recalled that the FTIR tests discussed in Section 4.2 indicated that no significant ageing had occurred during the service period, based on the used ageing index. Also the column testing with the DSR does not show a large change in rheological properties during service life. It is therefore concluded that both the mechanical and chemical characteristics of these antiskid surfaces are hardly affected by time and environmental conditions.

Table 4-13 Shear strength of the interface (20 °C, 50 mm/min)

Airfields	Maximum shear force [kN]			Shear Strength [MPa]
	No. 1	No. 2	Average	
Woensdrecht/ 2009	8.1428	9.3696	8.7562	1.159
Gilze-Rijen/ 2008	11.8479	10.798	11.32295	1.478
Leeuwarden/ 2007	11.9761	13.9416	12.95885	1.674
Eindhoven/ 2005	9.5284	9.2537	9.39105	1.219
Volkel/ 2004	16.0841	11.2374	13.66075	1.75
Soesterberg/ 1989	12.7207	13.1968	12.95875	1.691

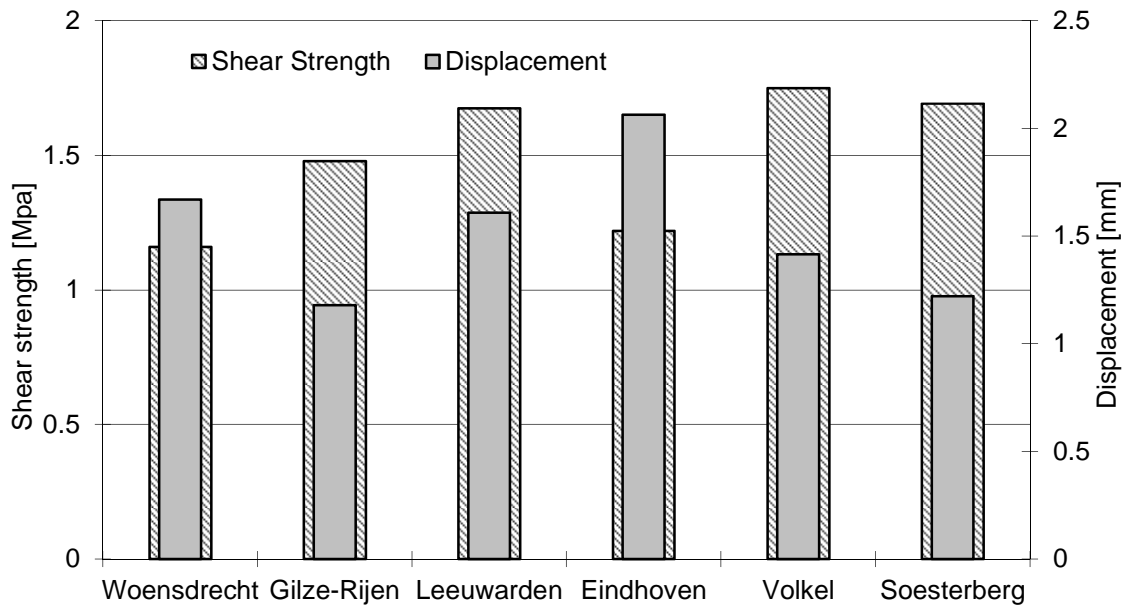


Figure 4-31 Shear strength and displacement for shear test

Surface characteristics of the underlying asphalt mixture layer also can have a significant influence on the interface shear strength. Figure 4-29 shows that the underlying asphalt mixture of Woensdrecht, Volkel and Leeuwarden airfield specimens appeared to have a smoother surface. Specimens from the other three airfields had rougher surfaces. Theoretically, a rougher surface can result in a higher shear strength. But from Table 4-13, the three airfields with a more smooth failure surface did not have a lower shear strength than the specimens with a rougher surface. This means that the surface characteristics of the underlying layer do not have a significant influence on the shear strength of the interface between tar-containing antiskid layer and asphalt mix layer, at least in this research.

On some cores from Woensdrecht Airfield, the Leutner shear test was also conducted on the interface between asphalt mixture layers and through the asphalt mixture. Table 4-14 shows the test results. These results illustrate that the shear strength at the interface between the antiskid layer and underlying asphalt mixture layer is higher than that at the interface between asphalt mixture layers. It is however lower than the shear strength through the asphalt mixture.

Table 4-14 Interface shear strength compared with the asphalt mix interface and in the mixture

Woensdrecht 2009	Shear Strength [MPa]			
	Through mixture	Asphalt mix interface	Through mixture	Asphalt mix interface
No. 1	2.416	1.196	2.004	1.120
No. 3	2.446	0.813	1.683	--
No. 8	2.465	--	2.065	--
No. 9	2.307	--	--	--
Average	2.408	1.005	1.917	1.120

4.5.3 Pull Test Results

The pull tests were performed on areas with a diameter of 50 mm. In this way, three pull tests could be performed on the surface of one core (the diameter of the core is between 133 mm and 143 mm, see Table 3-1), which made it possible to carry out more tests although the number of available airfield specimens was limited. The test method and sample preparation procedure are explained in Section 3.3.1, Chapter 3.

The tests were performed at 3 test temperatures, 0 °C, 10 °C and 20 °C, with the same loading speed of 0.025 MPa/s. Each of the three tests, done on one core, was performed at a different temperature. Three cores from each airfield were used.

All the detailed pull test results are presented in Table 4-15, together with the average values. Sample W4 and S5 were used for adjustment of the test setup. Figure 4-32 presents the DTS obtained at three different temperatures. The DTS decreased with increasing test temperature. The results on different cores at the same temperature only show a limited amount of variation.

Table 4-15 Pull test results on tar-containing antiskid layers

Airport	T [°C]	No.	Max. F [kN]	DTS [MPa]	Dis. [mm]	Ave. [MPa]	Description
Woensdrecht	20	W5	1.099	0.560	0.765	0.454	Around 50% surface 50% interface
		W6	0.684	0.348	0.601		
	10	W5	1.367	0.696	0.323	0.746	Around 50% interface 50% surface
		W6	1.563	0.796	0.315		Around 40% surface 60% interface
	0	W5	2.563	1.305	0.081	1.181	
		W6	2.075	1.057	0.107		
Gilze-Rijen	20	G4	1.367	0.696	0.608	0.655	
		G5	1.367	0.696	0.407		
		G6	1.123	0.572	0.532		Around 40% in the asphalt mixture
	10	G4	2.319	1.181	0.372	1.094	
		G5	1.855	0.945	0.211		Around 20% interface 80% surface
		G6	2.271	1.157	0.437		Around 80% interface 20% surface
	0	G4	2.612	1.330	0.291	1.384	
		G5	2.246	1.144	0.188		
		G6	3.296	1.679	0.22		
Leeuwarden	20	L4	1.514	0.771	0.43	0.842	
		L5	1.685	0.858	0.48		
		L6	1.758	0.895	0.589		
	10	L5	1.929	0.982	0.362	0.982	
		L6	1.929	0.982	0.33		
	0	L5	2.173	1.107	0.192	1.212	
L6		2.588	1.318	0.166			
Eindhoven	20	E4	1.709	0.870	0.507	0.738	
		E5	1.074	0.547	0.61		Around 10% in the asphalt mixture
		E6	1.563	0.796	0.406		
	10	E4	2.026	1.032	0.5	1.090	
		E5	2.295	1.169	0.427		
		E6	2.1	1.070	0.534		
	0	E4	2.319	1.181	0.232	1.355	
		E5	2.954	1.504	0.157		
		E6	2.71	1.380	0.105		
Volkel	20	V4	1.904	0.970	0.281	0.858	
		V5	1.685	0.858	0.362		
		V6	1.465	0.746	0.281		
	10	V4	2.271	1.157	0.139	1.181	
		V6	2.368	1.206	0.113		
	0	V4	3.516	1.791	0.09	1.560	
V6		2.612	1.330	0.049			
Soesterberg	20	S2	1.44	0.733	0.787	0.727	
		S6	1.416	0.721	0.701		
	10	S2	1.953	0.995	0.305	1.090	
		S5	2.441	1.243	0.335		
		S6	2.026	1.032	0.281		
	0	S2	2.808	1.430	0.158	1.430	

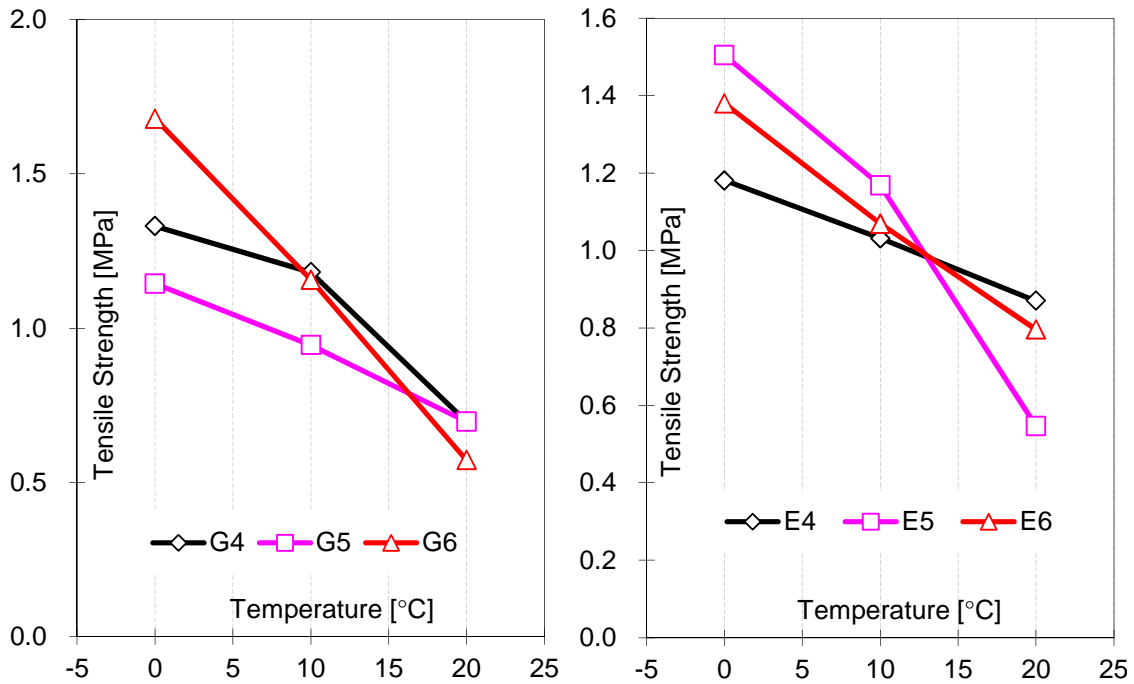


Figure 4-32 DTS at different temperatures on Tar-containing samples

Figure 4-33 presents the displacement-force curves in pull tests on samples at three test temperatures from Woensdrecht airport. The interface between the tar-containing antiskid layer and underlying asphalt mixture layer failed sharply at lower temperature with limited failure displacement. At higher temperature, the displacement was increased until it reached its failure displacement. The other force-displacement curves are represented in Figure A-2, Figure A-3 and Figure A-4 in the attached Appendix.

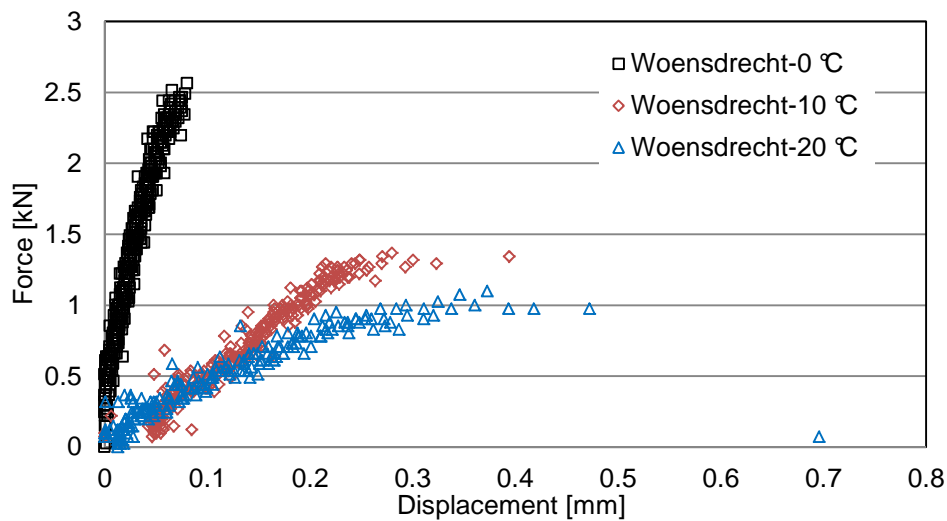


Figure 4-33 Force-displacement curves from pull tests

Figure 4-34 shows the average DTS of six airfields at three test temperatures. The tensile strength varies within 0.4 MPa at the same test temperature. By considering the variability that was presented in Table 4-15, it can be concluded that the service life did not have a significant influence on the bonding strength between tar-containing antiskid surface layer and underlying asphalt mixture layer. Nevertheless, it is reasonable that the results obtained on the Woensdrecht antiskid layer, being the youngest, are the lowest.

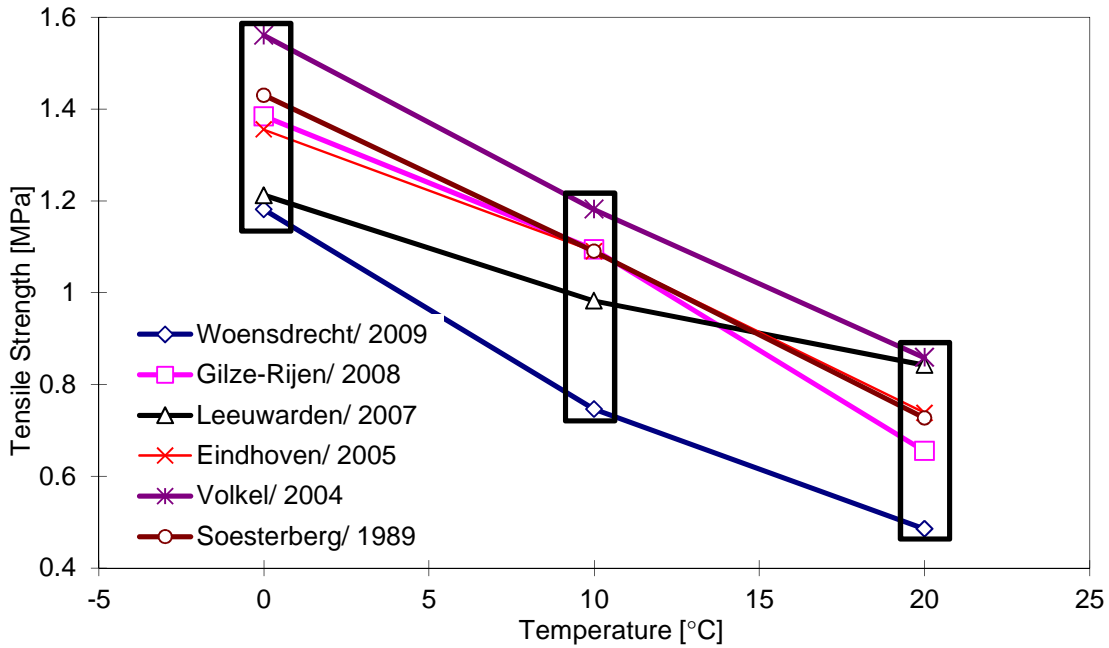


Figure 4-34 Average DTS at three evaluated temperatures

Table 4-16 presents the average tensile strength of six airfields calculated from Figure 4-34. The average tensile strength of the specimens from the six airfields is 1.04 MPa at 10 °C with the loading speed of 0.025 MPa/s. The newly designed antiskid layers for the runway applications should have the same or better average tensile strength.

Table 4-16 Average tensile strength of six airports

	0 [°C]	10 [°C]	20 [°C]
DTS [MPa]	1.46	1.04	0.727
Standard deviation	0.235	0.148	0.154
coefficient of variation	0.161	0.142	0.212

However, this conclusion means that the Woensdrecht cannot pass the requirement. The cores from Woensdrecht had relatively younger antiskid surface layer. Table 4-17 shows the pull test results on tar-containing cores at the

time of 6 weeks after application and 20 weeks after application. It illustrates that the tensile strength at the interface between tar-containing antiskid layer and underlying asphalt mixture layer will increase within the period after application. The tensile strength of Woensdrecht specimens might be higher when it gets old. Therefore, this slightly lower value was also accepted by the antiskid committees.

4.6 Tests from CROW

Adhesion tests were also conducted with (tar-containing) cores from a Schiphol antiskid runway by a CROW working committee. The cores were obtained 6 weeks after applying the antiskid surface in 2007 [16]. Cores with 150 mm diameter from two different locations were investigated. The test was performed by first introducing a circular cut with 100 mm diameter and 10 mm depth. Then the 100 mm diameter area was pulled off. Table 4-17 presents the test results at 10 °C and 0.025 MPa/s. All of the tests were conducted on cores with 100 mm diameter. All the tests failed at the interface. The average tensile adhesion strength at the interface after 6 weeks (6 weeks after application and 0 week in the storage room) of application was 1.3 MPa and 1.45 MPa. It increased to 1.54 MP and 1.59 MPa after 20 weeks of application (6 weeks after application and 14 weeks in the storage room). These results indicate that the tensile adhesion strength of the antiskid surfacing will increase a bit within the first period after application.

Table 4-17 Adhesion results obtained on Schiphol antiskid layer

Locations	Weeks stored at 20 °C	Tensile strength [MPa]	Average [MPa]	Failure displacement [mm]
Location 1	0	1.62	1.45	2.84
		1.36		1.97
		1.53		2.39
		1.57		2.53
		1.19		1.97
	14	1.46	1.59	1.61
		1.97		1.8
		1.98		1.84
		1.31		1.97
		1.24		1.58
Location 2	0	1.25	1.3	1.46
		1.3		1.67
		0.98		1.85
		1.28		1.72
		1.71		2.16
	14	1.32	1.54	1.75
		1.94		1.75
		1.19		1.78
		1.48		1.71
		1.76		1.83

Adhesion tests on cores from Gilze-Rijen runway were also performed by Possehl in Darmstadt University of Technology in Germany in 2009 [17]. Table 4-18 shows the test results at 10 °C. The same pull test method explained in the previous paragraph was used. All the tests showed failure at the interface.

The tensile adhesion test results presented in Table 4-15, Table 4-17 and Table 4-18 illustrate that the tensile adhesion strength varies a lot from one test to another test. The maximum tensile strength in Table 4-18 is 2.34 MPa, but the minimum value is less than 1 MPa at the same test conditions. The average tensile adhesion strength at the interface of the six investigated antiskid layers is 1.03 MPa, and the minimum values of the Schiphol specimens and Gilze-Rijen specimens are 0.98 MPa and 0.97 MPa. So, in conclusion we may recommend that the minimum tensile strength for alternative antiskid layers should be at least higher than 1 MPa.

Table 4-18 Adhesion results on Gilze-Rijen tar containing antiskid layer

Tensile strength [MPa]	Average [MPa]	Failure displacement [mm]
2.34	1.48	2.04
1.42		1.59
1.54		1.26
1.46		1.58
1.50		1.54
1.44		1.25
0.97		1.78
1.72		1.55
1.13		1.06
1.55		1.53
1.22		0.95

4.7 Benchmark Development

In this research, the aim of doing tests on tar-containing antiskid layers was to develop benchmarks for new environmental friendly antiskid layers.

4.7.1 Benchmarks

A basic program for the benchmark development is shown in Figure 4-35. First of all, the tests to be selected for benchmarking are required to be as simple as possible so that the suppliers should carry out these tests in their own labs. Secondly, the tests should represent the properties that are most important for antiskid surfacings.

In this research, the sand patch test, pull test and shear test were selected and specified in the specification for alternative antiskid layers [18]. Unfortunately, as discussed before, there was no information about the tar-containing binder and also no tests could be conducted on this material. So, it is

necessary to verify this specification by conducting tests on potential binders and newly designed antiskid layers based on newly designed binders. These tests will be discussed in Chapter 5 and Chapter 6.

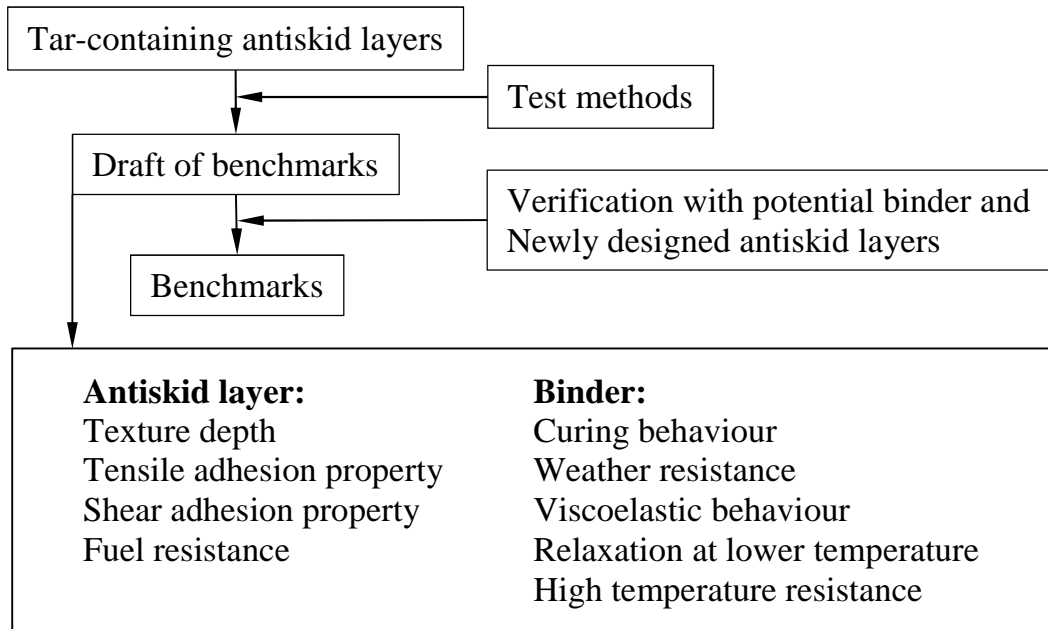


Figure 4-35 Basic program for benchmark development

4.7.2 Reliability and Number of Tests

In this chapter, limited tests were conducted due to the limited cores that were collected from the airfields. Average values were calculated and analyzed, but the question is how reliable these average values are given the limited number of tests that were performed.

Tests conducted in the laboratory provide an estimate of the average standard deviation of the property under investigation. As the number of tests increases, the estimated values more closely represent the true values. The principles of statistic confidence levels are very useful in determining how many tests will be necessary to ensure that the estimated mean is within a certain limit of the actual mean. In the AASHTO handbook of ‘design of pavement structures’, the concept of confidence level is explained by the statement that we are $100(1 - \alpha)$ percent confident that the mean value lies within the limits tests [19].

Statistical limit of accuracy curves help to assess the impact of the number of tests conducted on the precision of the estimate. The limit of accuracy, R , represents the probable range of the true mean from the average obtained by ‘ n ’ tests, at a given degree of confidence:

$$R = K_{\alpha}(\sigma / \sqrt{n}) \quad (4-5)$$

Where,

- K_{α} = the standardized normal deviate, which is a function of the desired confidence level, $100(1 - \alpha)$;
- σ = true standard deviation of the random variable being considered

If for a given variable (tensile strength, etc.) a confidence level is selected (e.g., 95 percent), K_{α} and α are constants. The R value is inversely proportional to the square root of the number of tests used if randomly selected. Figure 4-36 shows the typical schematic plot of R versus n . There are three zones along the accuracy curve. In zone 1, the accuracy curve has a steep slope. The precision of the estimate significantly increases with each additional test or sample [19].

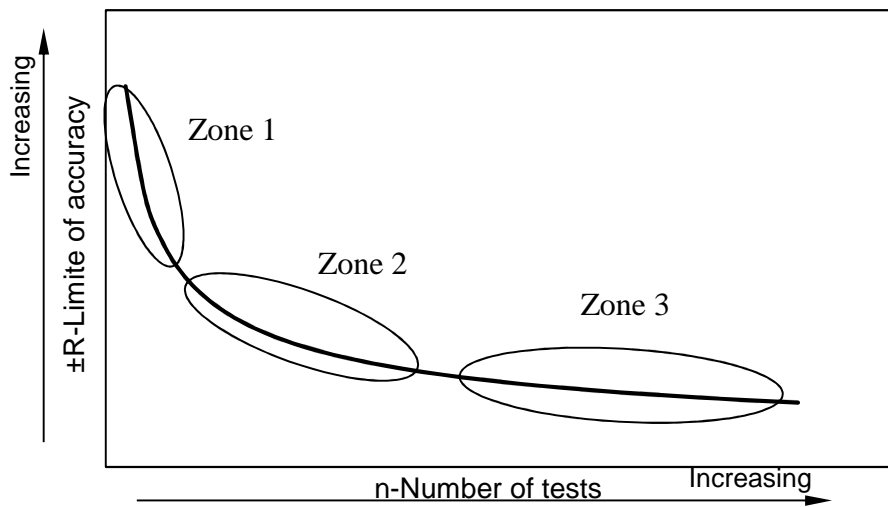


Figure 4-36 Typical limit of accuracy curve showing three general zones

Figure 4-37 shows the accuracy curves at a coefficient of deviation of 0.142, 0.161 and 0.212, which represent the coefficient of deviation in the pull test in Table 4-16. The confidence level was chosen at 95%.

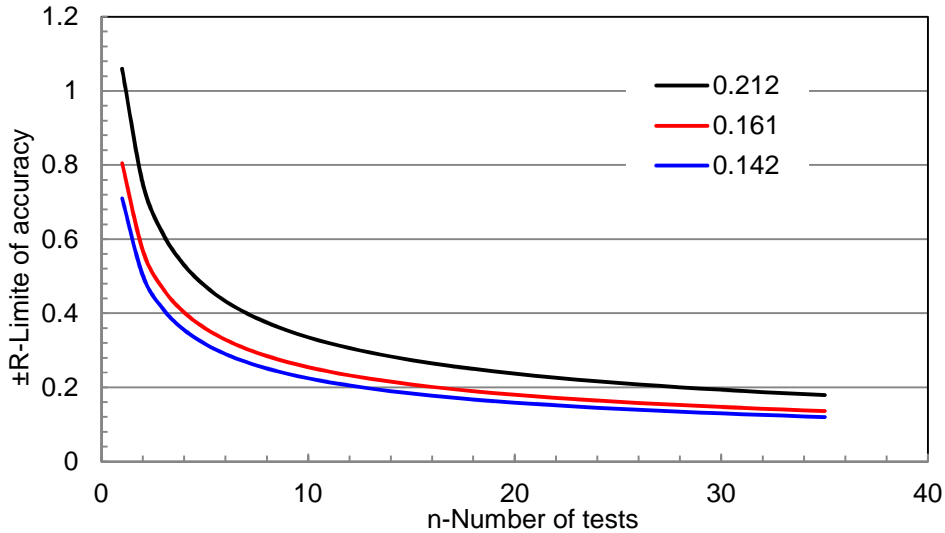


Figure 4-37 Limit of accuracy curves for pull test at 95% of confidence

In order to get reasonable test results, a certain reliable amount of tests should be required based on Table 4-19. If 0.2 of accuracy limit is required, in order to have 95% confidences of the test results, 12 tests are needed when the test coefficient of deviation is 0.142 at 10 °C as presented in Table 4-19. And about 3 tests are needed when the limit of accuracy is 0.4.

Table 4-19 Required test numbers based on the coefficient of variation

Confidence level	Limit of accuracy $\pm R$	Total number of tests required		
		0.142 [10 °C]	0.161 [0 °C]	0.212 [20 °C]
0.95	± 0.8	1	1	2
	± 0.6	2	2	3
	± 0.4	3	4	7
	± 0.3	5	7	12
	± 0.2	12	16	28

4.8 Conclusions

In order to understand the behavior of tar-containing antiskid layers, cores with antiskid surface layers from six airfields were analyzed in this chapter. The following conclusions can be drawn from the test results:

1. A tar-containing antiskid layer is a special thin layer with a thickness between 3 to 5 mm. The tar-containing antiskid surfaces have a relatively high macro-texture. The maximum height of the surface varied from 3.45 mm to 4.08 mm. The texture depth of tar-containing antiskid layers is between 1.26 to 1.46 mm. It appears from the results that these high texture levels remained consistent for a long period of 20 years.

2. Taking the evaluated tar-containing antiskid layers as a benchmark for alternative antiskid layers, the alternatives should provide at least a texture depth of 1.25 mm during the whole service life.
3. The tested six tar-containing antiskid samples show more or less the same ageing index, which is much lower than the ageing index of long term aged bitumen binder. This means that the ageing resistance of tar-containing binder is much better than that of bitumen.
4. The newly designed test methods are working well for evaluating the adhesion properties between the thin antiskid layers and the underlying asphalt mixture layer. With these test methods, the direct shear strength and direct tensile strength at the interface between the antiskid surface layer and the underlying layer could be evaluated.
5. The shear strength at the interface between tar-containing antiskid layer and asphalt mixture layer is higher than the shear strength at the interface between asphalt mixture layers. It is lower than the shear strength in the asphalt mixture.
6. The minimum shear strength at the interface between the tar-containing antiskid layer and the asphalt mixture layer was 1.16 MPa and the average was 1.5 MPa (20 °C and 50 mm/min). There is no obvious trend for the shear strength in relation to the service life, which means that the influence of ageing on the shear strength is not significant. Based on these results, a minimum shear strength of 1.2 MPa is proposed as a benchmark to which other antiskid systems should be compared.
7. Most of the pull tests failed at the interface, which means that the bonding strength at the interface between tar-containing antiskid layer and underlying asphalt mixture layer is the weakest area.
8. The average tensile strength at the interface between the tar-containing antiskid layer and the underlying asphalt mixture layer is 1.03 MPa at 10 °C with the loading speed of 0.025 MPa/s. The minimum tensile strength is about 1 MPa. It is therefore recommended that new designed antiskid surfaces should have a tensile strength higher than 1 MPa.
9. Results from the shear test and pull test show large variability. In order to ensure a sufficient level of reliability for the estimate average value of strength, enough tests should be performed when evaluating materials.

REFERENCES

1. Leest, A.J.v. and G. Gaarkeuken, *The F.O.D. resistance of surface layers on airfields in the Netherlands: in situ and laboratory testing*, in 2004 FAA Worldwide Airport Technology Transfer Conference. 2004: Atlantic City, New Jersey, USA.
2. Xiao, Y., et al., *Assessment Protocol for Tar-containing Antiskid Layers for Runways*, Report No. 7-10-185-2. 2010, Delft University of Technology.
3. Cao, J., A.N. Buckley, and L.J. Lynch, *Measurement of an intrinsic softening temperature for coal-tar pitch by proton magnetic resonance thermal analysis*. Carbon, 1994. **32**(3): p. 493-497.

4. Arambula, E., et al., *Numerical analysis of moisture vapor diffusion in asphalt mixtures using digital images*. Materials and Structures, 2010. **43**(7): p. 897-911.
5. Ongel, A., *Experimental analysis of open-graded asphalt concrete mixes in terms of safety, durability, and noise*. 2007, University of California, Davis: United States -- California.
6. Asi, I.M., *Evaluating skid resistance of different asphalt concrete mixes*. Building and Environment, 2007. **42**(1): p. 325-329.
7. Vilaça, J.L., et al., *3D surface profile equipment for the characterization of the pavement texture – TexScan*. Mechatronics, 2010. **20**(6): p. 674-685.
8. Holloway, D., *Calibration of Laser Devices Used for the Measurement of Pavement Surface Texture-Accuracy of Pavement Texture Measurement, in Third International Surface Friction Conference, Safer Road Surfaces-Saving Lives*. 2011: Austrulia.
9. ASTM, *E965-96 Standard Test Method for Measuring Pavement Macrotecture Depth Using a Volumetric Technique*. 2006.
10. Flintsch, G.W., et al., *Pavement Surface Macrotecture Measurement and Application, in TRB 2003 Annual Meeting*. 2003.
11. Qiu, J., *Self Healing of Asphalt Mixtures Towards a Better Understanding of the Mechanism, PhD Dissertation, in Civil Engineering and Geosciences*. 2012, Delft University of Technology: Delft.
12. Guillén, M.D., et al., *Fourier transform infrared study of coal tar pitches*. Fuel, 1995. **74**(11): p. 1595-1598.
13. Bergh, W.v.d., *The effect of ageing on the fatigue and healing properties of bituminous mortars. ISBN 978-90-8570-784-4, in 2011, Delft University of Technology: Delft*.
14. Lamontagne, J., et al., *Comparison by Fourier transform infrared (FTIR) spectroscopy of different ageing techniques: application to road bitumens*. Fuel, 2001. **80**(4): p. 483-488.
15. Hagos, E.T., *The Effect of Ageing on Binder Properties of Porous Asphalt Concrete*. 2008, Delft University of Technology: PhD dissertation.
16. Possehl, *Antiskid Projekt auf des Flughafen Schiphol, Possehl Spezialbau GmbH*. 2007.
17. Possehl, *Flughafen Gilze-Rijen, Startbahn 10/28, Projekt-Nr. 8.2014/2*. 2009.
18. CROW, *D11-01 Specification for Runway Surface Dressings on Airfields*. 2011: the Netherlands.
19. AASHTO, *AASHTO Guide for Design of Pavement Structures*. 1986, American Assiciation of State Highway and Transportation Officials: Washinton D.C.

5. Rheological and Ageing Properties of Alternative Binders

In the previous chapter, test results on tar-containing antiskid layers were discussed and a benchmark to which alternative products can be compared has been proposed. However, the tests used in Chapter 4 were only those that could be performed within the given constraints. The whole purpose of Chapter 4 was to define criteria to which new products had to comply. Since it became very clear that the binder behavior plays an essential role in the performance of an antiskid layer, the tests proposed in Chapter 4 are not enough for binder selection. Rheological characterization and properties such as curing, weather resistance and ageing resistance are essential as well.

In this chapter, several newly designed binders were investigated to verify the benchmark and to find out if they are suitable for antiskid surfacings. The newly designed binders include Modified Epoxy Resin (MER), Modified Bitumen Emulsion (MBE) and Epoxy Modified Bitumen (EMB). Figure 5-1 shows the research program for this chapter.

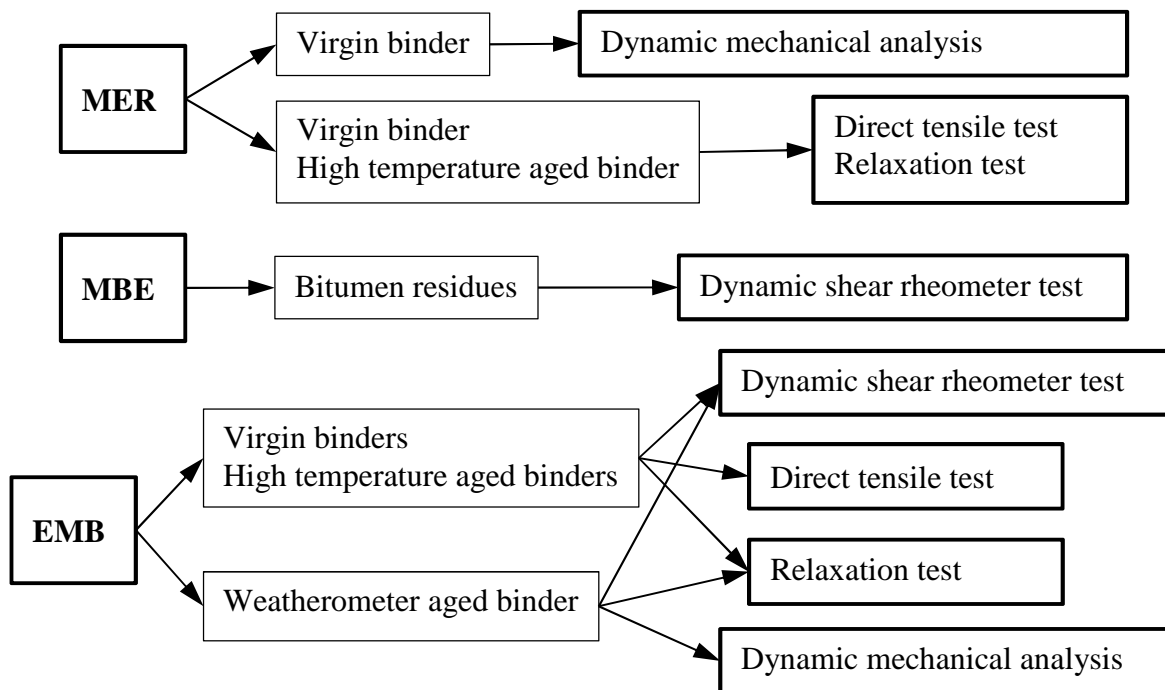


Figure 5-1 Research program of Chapter 5

5.1 Modified Epoxy Resin (MER)

Modified epoxy resin was investigated because it can give excellent adhesion and very good mechanical properties, as discussed in Section 2.4.4.2 in Chapter 2. In this study, Direct Tensile Tests, Relaxation tests and Dynamic Thermal Analysis tests were performed on MER to determine its curing behavior, tensile strength, relaxation and high temperature properties. The MER binder was provided by Latexfalt Company and its details can be found in Chapter 3.

5.1.1 Dynamic Mechanical Analysis

A DMA temperature sweep test ranging from 24 °C to higher than 200 °C was conducted on fully cured MER binders. This test was performed to determine the high temperature resistance. Three frequencies of 1 Hz, 10 Hz and 100 Hz were used. Figure 5-2 shows the test results. One can clearly observe that at high temperatures (more than 100 °C), MER behaves as a rubbery elastic material and has a stiffness value above 10 MPa while its phase angle value is close to 5 degree. It will not give viscous permanent deformation problems at temperatures above 60 °C, like traditional bitumens do.

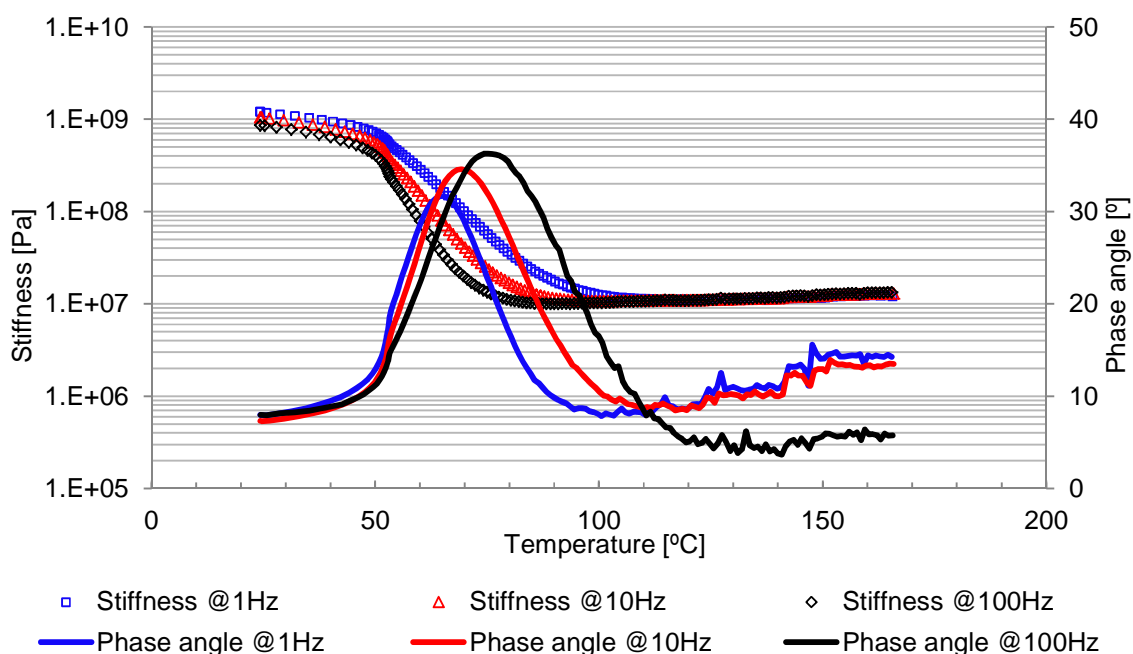


Figure 5-2 Temperature sweep results of MER binders

Figure 5-2 also indicates that the phase angle curves of MER at 1 Hz, 10 Hz and 100 Hz reach their maximum phase angle at 65.3 °C, 69.2 °C and 74.4 °C. This information shows that at lower temperature (lower than the temperature where the phase angle reaches its peak value), the bitumen component predominates the binder properties. Hence at this temperature range, the MER

will have bitumen-like viscoelastic properties. At higher temperatures (higher than the temperature where the phase angle reaches its peak value), the epoxy component predominates the binder property, and the binder will behave as an elastic material and show very good high temperature resistance.

Table 5-1 illustrates the influence of frequencies on the MER binder at 25 °C and 40 °C. It shows that at 25 °C and 40 °C, the frequency has only a slight influence on the binder stiffness and phase angle. At the temperature range from 50 °C to 100 °C, higher frequencies will result in a higher stiffness. But when the temperature is lower than 20 °C, as Figure 5-2 shows, the stiffness and phase angle of MER binder are independent of the frequency.

Table 5-1 Influence of frequencies on the binder stiffness

Frequency [Hz]	Stiffness [Pa]		Phase angle [Degree]	
	25 °C	40 °C	25 °C	40 °C
1	8.62E+08	6.39E+08	7.968547	9.47036
10	1.04E+09	7.77E+08	7.296724	8.830232
100	1.19E+09	9.37E+08	7.962769	8.927408

5.1.2 Direct Tensile Test

Mostly, the DTT test for a bituminous binder/mortar is performed on specimen as shown in Figure 3-15 [1]. Figure 5-3(1) shows typical DTT samples in the silicon mould. However, the test setup had to be modified slightly because of the following reason. In some preliminary tests, fracture occurred in the adhesive zone between the MER binder and the aluminum, instead of in the binder. This occurred because MER binders have a much higher tensile strength than the adhesive strength between the binder and aluminum plate. In order to avoid this undesirable adhesive failure, the tested samples were first glued to the aluminum with X60 polymer glue before testing.

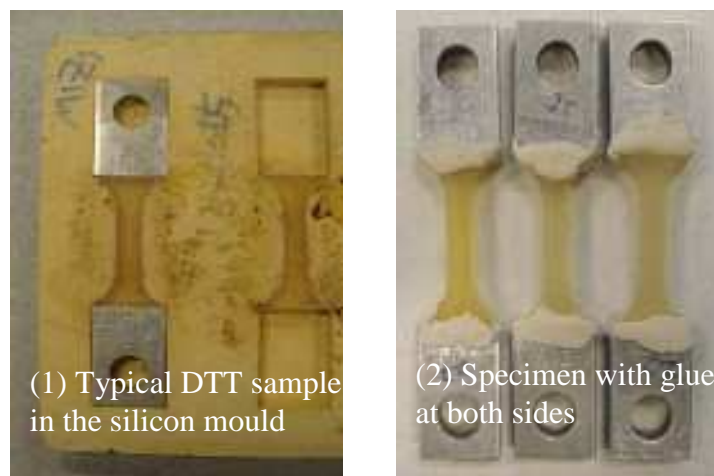


Figure 5-3 Typical specimens (1) and glued specimens (2) of MER for DTT

However, most of the tests still failed at the interface, even though X60 glue was applied. Figure 5-4 presents three test results. They all suddenly failed at the interface between the binder surface and the glue when the force was applied. This means that the X60 glue could not provide enough adhesive strength at the interface.

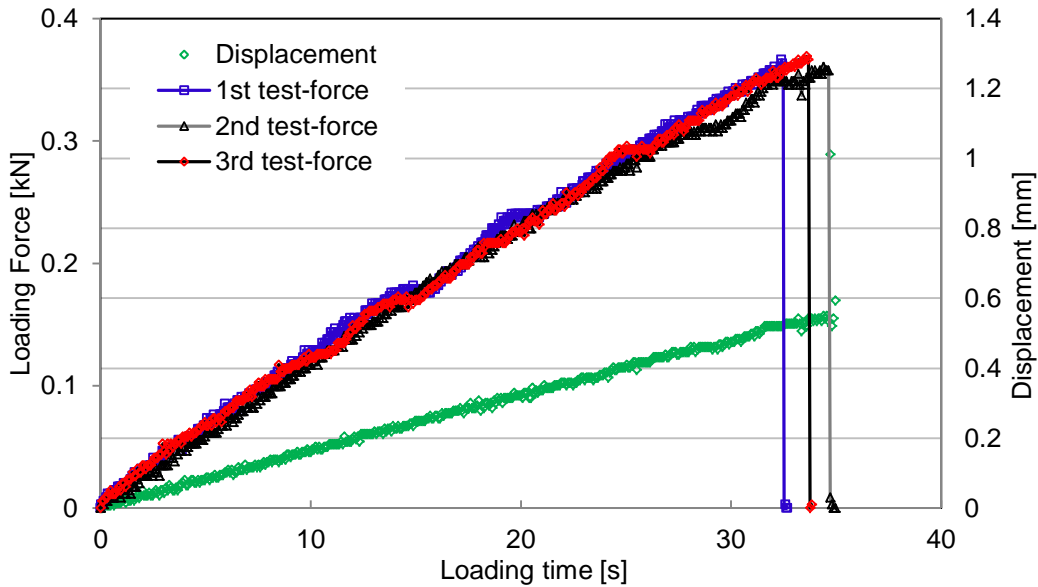


Figure 5-4 DTT results with failure at the interface at 10 °C at a displacement rate of 1 mm/min

In order to overcome the problem mentioned above, dumbbell shape specimens as shown in Figure 5-5 were used. Two clamps were introduced to eliminate the influence of the interface failure. The MER test specimen was produced directly into a dumbbell shape by pouring the MER into the DTT mould. During DTT and Relaxation tests (RT), both sides of the test specimen were fixed with clamps connected to the test machine. The contact surfaces on the clamps are rough enough to prevent slipping between specimen and clamps. With this method, the failure at the interface between the MER and the aluminum plate could be avoided.

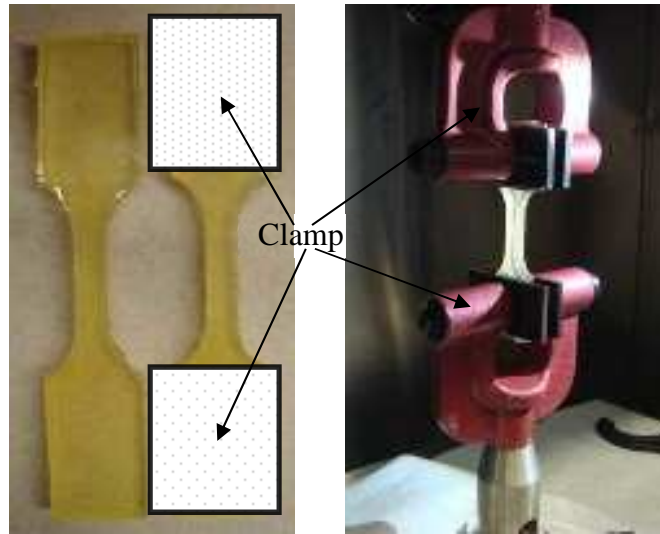


Figure 5-5 Schematic picture for DTT on MER samples

Figure 5-6 shows a typical test result obtained with a dumbbell shape specimen. The loading force is increased to a certain value. Before the specimen fails, there are a few seconds during which the load stays constantly while the displacement keeps increasing at constant displacement rate. As mentioned before this stage represents the failure propagation. The failure propagation of MER is taking just a few seconds. The displacement elongation is very limited and therefore the resulting tensile strain is not very large (less than 10%).

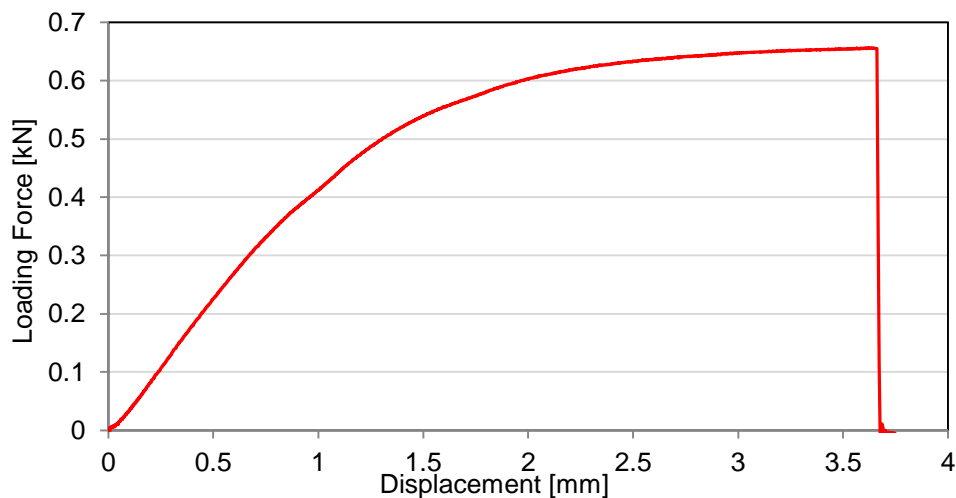


Figure 5-6 A typical DTT test curve obtained on MER at 20 °C and a displacement rate of 1 mm/min

5.1.2.1 Curing Behavior

The curing speed is a critical factor that will influence the possible application of the binder for thin surfacings. The faster the curing speed, the

more economical the surfacing application is. Especially when the binder is used on busy runways or at night at highways to be reopened early, it should cure fast enough to reopen the runway in a short time. Therefore, it is necessary to investigate the curing behaviour.

Specimens were kept in a storage room at 14 °C and 70% relative humidity after sample preparation. DTTs were conducted after different curing times. Tests were performed at 10 °C with a displacement speed of 1 mm/min. The maximum force and the displacement at failure were recorded.

Figure 5-7 presents the influence of curing time on strength and failure strain. The curing curves were fitted by means of a sigmoidal curve [2, 3]. The sigmoidal curve function is shown below:

$$S_T = \delta + \frac{\alpha}{1 + e^{\beta - \gamma \times T_{curing}}} \quad (5-1)$$

Where,

$\alpha, \beta, \gamma, \delta$ = sigmoidal function coefficients (fitting parameters);

S_T = the tensile strength, [MPa];

T_{curing} = the curing time, [hours].

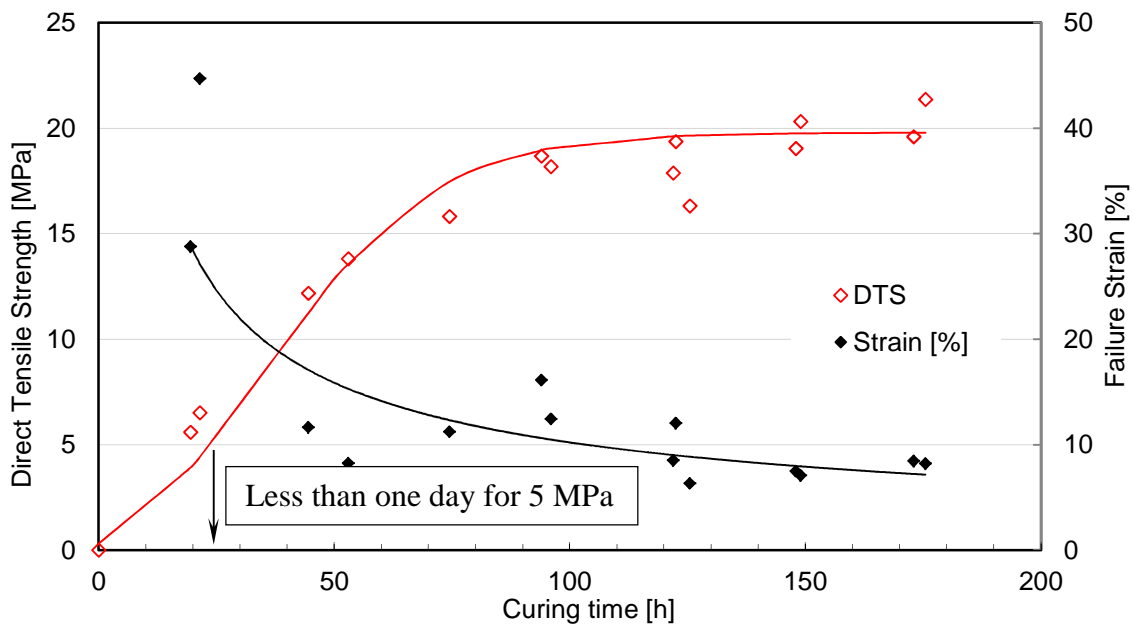


Figure 5-7 Curing curve of modified epoxy resin at 14 °C

Table 5-2 presents the fitting parameters for the curing curve. At short curing times, the MER has a lower tensile strength and a larger failure strain. The tensile strength is increasing until it reaches its maximum after being fully cured. Obviously, the tested two-component MER needs about 4 days to get fully cured. However, it has a DTS of 5 MPa after less than 1 day curing, which is higher

than the DTS value of traditional bituminous binders. In practice, the contact of MER with aggregate and environmental factors as wind and higher ambient temperature might accelerate the curing speed. Therefore in practice, the curing is expected to go faster than measured in the laboratory.

Table 5-2 Parameters for the prediction models of MER

δ	α	β	γ	R^2
-2.2	22	2.05	0.06	0.96

5.1.2.2 Direct Tensile Strength

DTT tests were carried out on fully cured specimens at temperatures of 0 °C, 10 °C and 20 °C. The applied displacement rate was 1 mm/min. The influence of the displacement rate on the tensile strength was investigated at 10 °C using displacement rates of 1 mm/min and 10 mm/min. Two tests were conducted at each test condition. Table 5-3, Figure 5-8 and Figure 5-9 present the DTS and failure strain at different temperatures and displacement rates.

Table 5-3 DTT test results on MER

Disp. speed	Failure Strength [MPa]				Failure Strain [%]			
	1 mm/min			10 mm/min	1 mm/min			10 mm/min
Temperature	0 °C	10 °C	20 °C	10 °C	0 °C	10 °C	20 °C	10 °C
Specimen 1	26.56	19.58	18.39	21.17	9.26	8.46	11.48	13.08
Specimen 2	29.47	21.36	18.61	21.11	11.54	8.2	7.22	10.44

The data show that the DTS of MER is dependent on the test temperature. The tensile strength is higher at 0 °C than the tensile strength at 10 °C and 20 °C. But the difference in tensile strength is not significant. The applied displacement rate does not seem to have a significant effect on the tensile strength. This behavior could be expected since the DMA test showed already that the stiffness of the MER binder is independent of the frequency in the lower temperature range (lower than 20 °C).

The failure strain is in the range of 7.2% to 11.5% and is not very sensitive to the test temperature. Basically, a viscoelastic material will behave more brittle at faster loading rates, which means that the strain at failure would decrease with increasing loading rate. But the results shown in Figure 5-9 do not fit this theory. Also this could be expected since the DMA results in Figure 5-2 and Table 5-1 illustrate that the tensile strength tests were performed under conditions where the response of the binder is independent of loading frequency. So the influence of loading rate on the failure strain cannot be determined.

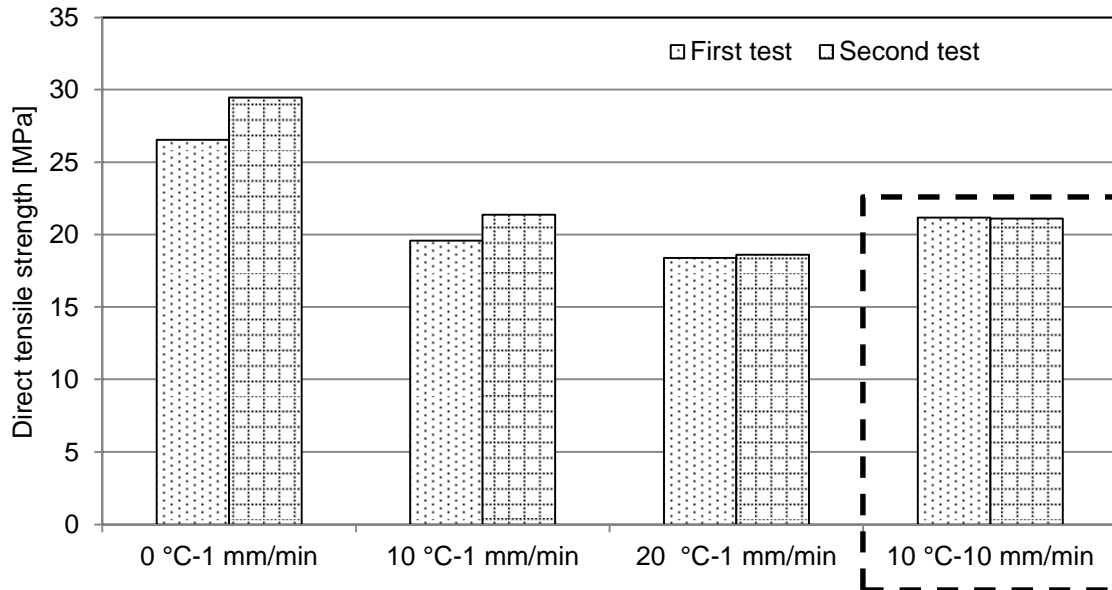


Figure 5-8 Direct tensile strength of MER binder

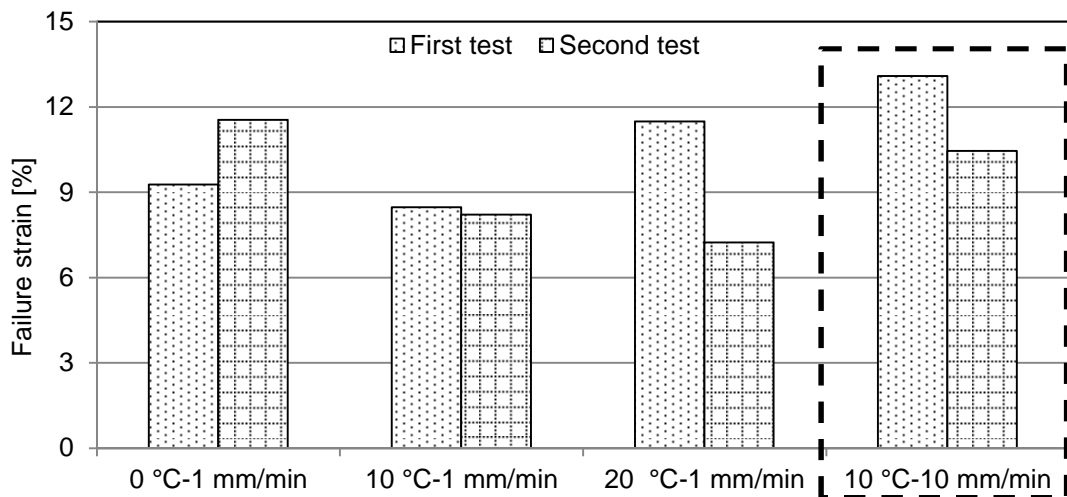


Figure 5-9 Failure strain of MER binder

Table 5-4 gives the DTS results of the original MER binder and oven aged MER binder. Obviously, after oven ageing at higher temperature, the tensile strength of MER has slightly increased under the same displacement loading rate. But considering the variability during the tensile tests, the influence of ageing on the tensile strength and failure strain is not significant.

Table 5-4 DTS of original MER and aged MER with 1 mm/min

Temperature		Failure Strength [MPa]			Failure Strain [%]		
		0 °C	10 °C	20 °C	0 °C	10 °C	20 °C
Aged	Test No. 1	29.47	20.36	23.72	11.54	11.36	11.36
	Test No. 2	30.75	19.83	21.86	7.9	8.22	11.98
	Average	30.11	20.1	22.79	9.72	9.79	11.67
Original		28.01	20.47	18.5	10.4	8.33	9.35

5.1.3 Relaxation Test

The same dumbbell shape specimens were used for RTs at 0 °C, 10 °C and 20 °C. Forty percent of the failure load obtained from the DTT tests on fully cured samples at the same test temperature and same displacement rate was used as the maximum force to load the specimen in the relaxation test. Figure 5-10 shows the relaxation curves of the original and aged MER binders at 10 °C. The applied maximum force on aged binder in the relaxation test was slightly higher than the one applied on the original binder.

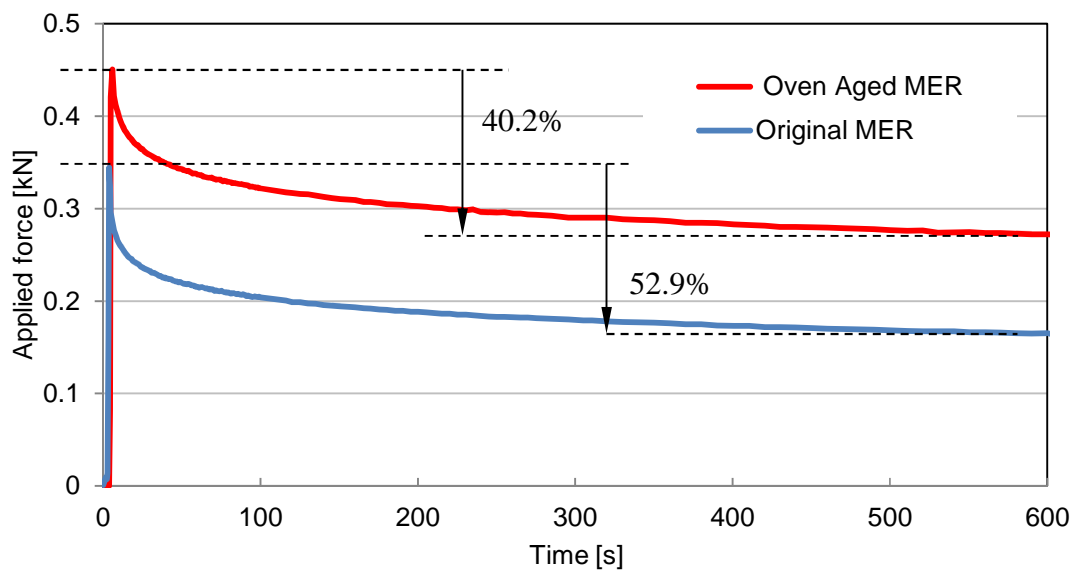


Figure 5-10 Relaxation test results at 10 °C of MER before and after ageing

Table 5-5 presents the RT results. Figure 5-11 presents the relaxation percentage of the original and oven aged MER binders at three different temperatures. After 7 days oven ageing, the aged binder shows less relaxation at 10 °C. It decreased from 48.8% to 40.8%. But at 20 °C and 0 °C, the difference is limited. In general it can be concluded that the ageing is hardly influencing the relaxation of MER.

The relaxation of the original MER at 0 °C is 39.24%, which is far less than the relaxation percentage of bituminous binders and epoxy modified bitumen. The relaxation percentage of original bitumen is normally higher than 90% at

0 °C, while epoxy modified bitumen can reach more than 50% relaxation under the same test conditions [1]. MER is a more elastic material, while bitumen and EMB are viscoelastic materials. Antiskid surface layers should have the ability to release the temperature induced tensile stresses which will occur in winter condition. But for MER binder, about 40% to 60% of the applied temperature stresses will remain and when high enough these stresses in combination with traffic induced stresses might result in cracking.

Table 5-5 Relaxation test results for MER

Temperature		Relaxation [%]			Applied strain [%]		
		20 °C	10 °C	0 °C	20 °C	10 °C	0 °C
Original	Specimen 1	50.7	44.6	39.7	3.1	2.5	2.3
	Specimen 2	50.4	52.9	38.8	3.1	2.5	2.4
	Specimen 3	52.6	--	--	2.3	--	--
	Average	51.21	48.76	39.24			
Aged	Specimen 1	52.1	40.2	37.3	2.8	2.8	2.5
	Specimen 2	51.2	41.4	38.5	3.1	3.1	2.5
	Average	51.67	40.78	37.92			

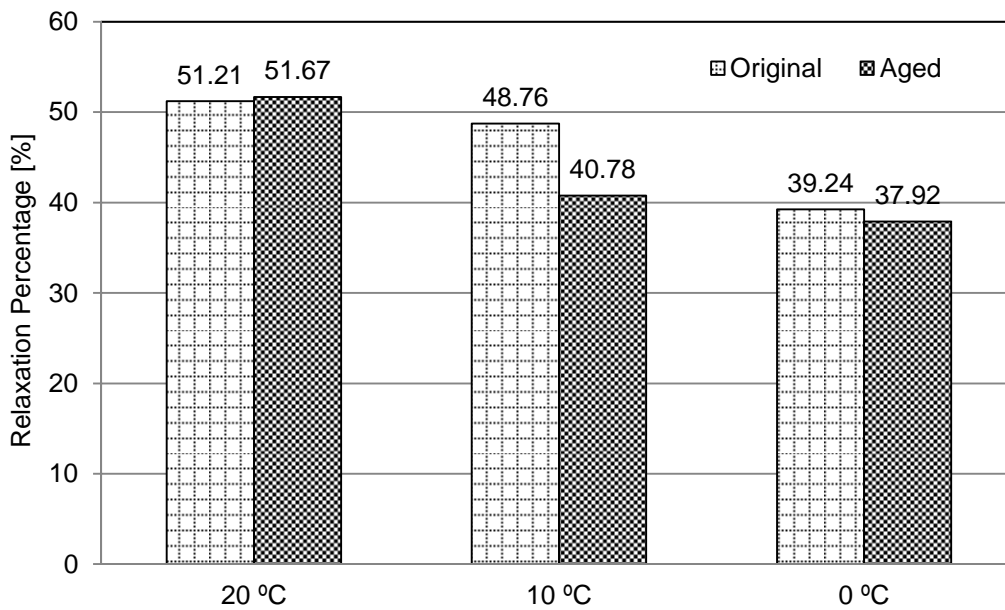


Figure 5-11 Average relaxation percentage of modified epoxy resin at three test temperatures

5.2 Modified Bitumen Emulsion (MBE)

The curing behavior of MBE was first investigated in the laboratory. Afterwards, DSR tests were conducted to understand the viscoelastic properties of the cured residues.

The residue from MBE is very sensitive to the temperature. At higher temperature, it has a lower tensile strength and a larger failure strain. At lower temperatures, it has a higher tensile strength and a smaller failure strain. According to [4], the maximum tensile strength of bitumen residue at lower temperatures ranges from 0.5 MPa to 2 MPa. It is much lower than the strength values for MER and EMB, and its failure strain is much higher. The displacement range of the equipment in the lab is too small to conduct DTT on the bitumen binder. So DTT is not included for bitumen residues in this research.

5.2.1 Curing Behavior

Firstly, a silicon rubber mould shown in Figure 5-12 was used to obtain the bitumen residue. A thin layer of bitumen emulsion (approx. 3 mm) was spread into the silicon rubber mould, having a diameter of 8 mm or 25 mm. The mould was designed to allow slightly more material to be placed in it than required in the DSR test.

After filling the mould with the required amount of emulsion, the sample was allowed to dry over 24 hours at ambient temperature (around 22 °C (1st stage)). For the 2nd stage the residual binders were kept in a ventilated oven at 50 °C for 24 hours. For the 3rd stage the residual binders were kept in a ventilated oven at 85 °C for another 24 hours.

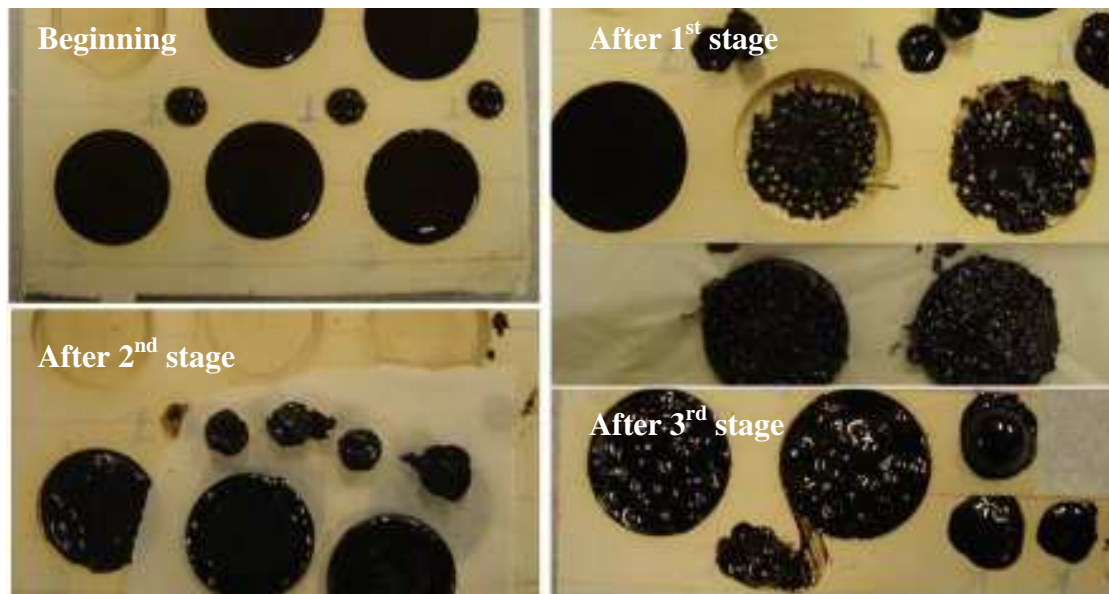


Figure 5-12 Silicon rubber mould and visual state of MBE at different stages

Figure 5-12 shows the visual condition of the MBE after different curing stages. After the 1st stage, thin bitumen films were observed at the surface, while the emulsion at the bottom stayed liquid. This happened because the mould is too

deep and the water inside the mould cannot evaporate easily. After the 2nd stage, the samples clearly showed a lot of bubbles. These problems were caused by the specific shape of the silicon rubber mould. Obviously the depth of the silicon rubber mould is too deep to let water evaporate smoothly.

To prevent the problems described, silicon paper was used. Instead of the silicon rubber mould, About 60 gram bitumen emulsion was spread on silicon paper with a size of 200 mm×200 mm. The same three steps as described in Figure 3-7 were applied to get bitumen emulsion residues. Figure 5-13 shows the visual state of the MBE after different curing stages.



Figure 5-13 MBE at different stage on silicon papers

5.2.2 Dynamic Shear Rheometer

Stress-strain relationship tests were conducted with the DSR strain sweep test to determine the Linear Viscoelastic (LVE) range of the binders. These tests were necessary to ensure that the following frequency sweep tests were conducted in the linear visco-elastic range. The dynamic shear modulus is relatively strain-independent at sufficient small strains. The strain level at which nonlinearity occurs varies significantly with the stiffness of the asphalt binder. In the Strategic Highway Research Program (SHRP) [5], the limit of the linear viscoelastic range was defined as the point beyond which the measured value of the complex modulus decreased to 95% of its initial value. This point was determined by conducting a strain sweep test, as shown in Figure 5-14.

Figure 5-14 shows the strain sweep test results obtained on the MBE residue after the first curing stage. The strain sweep test was performed at 20 °C at a frequency of 10 rad/s.

Figure 5-15 shows the stress-strain relationships at temperatures varying between -10 °C to 60 °C of the bituminous binder after the 1st stage curing. The three red curves of 20 °C, 40 °C and 60 °C were tested with the 25 mm diameter plate geometry, while the black curves of -10 °C, 0 °C, 10 °C and 20 °C were tested with the 8 mm diameter plate geometry. Figure 5-16 shows the relationship between shear modulus and shear strain obtained in a strain sweep test.

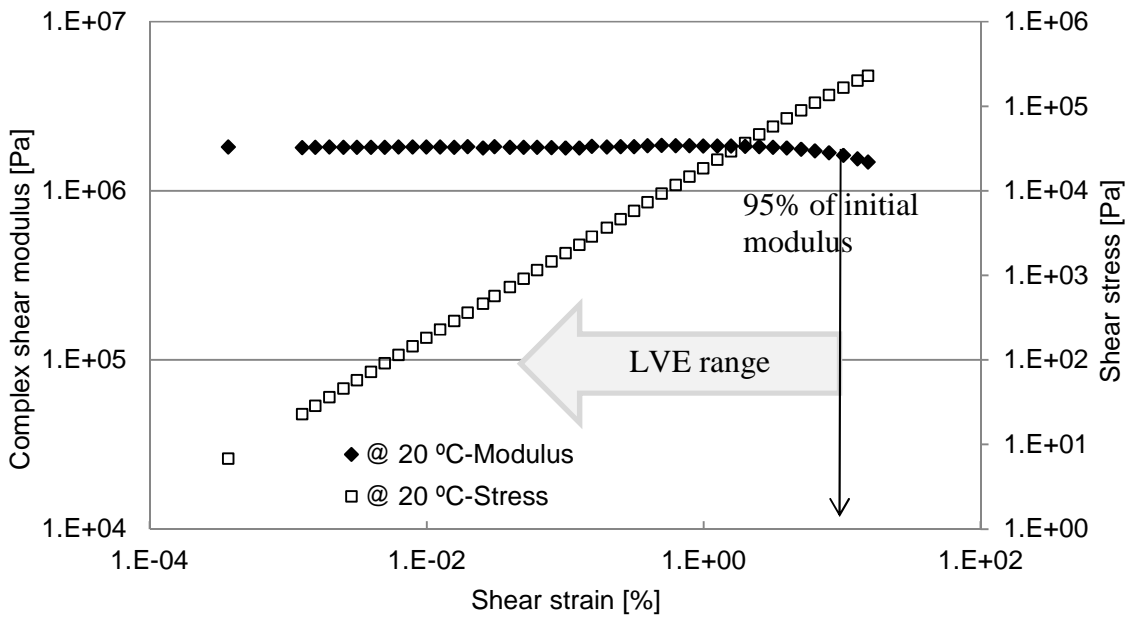


Figure 5-14 Strain sweep at 20 °C used to determine linear range

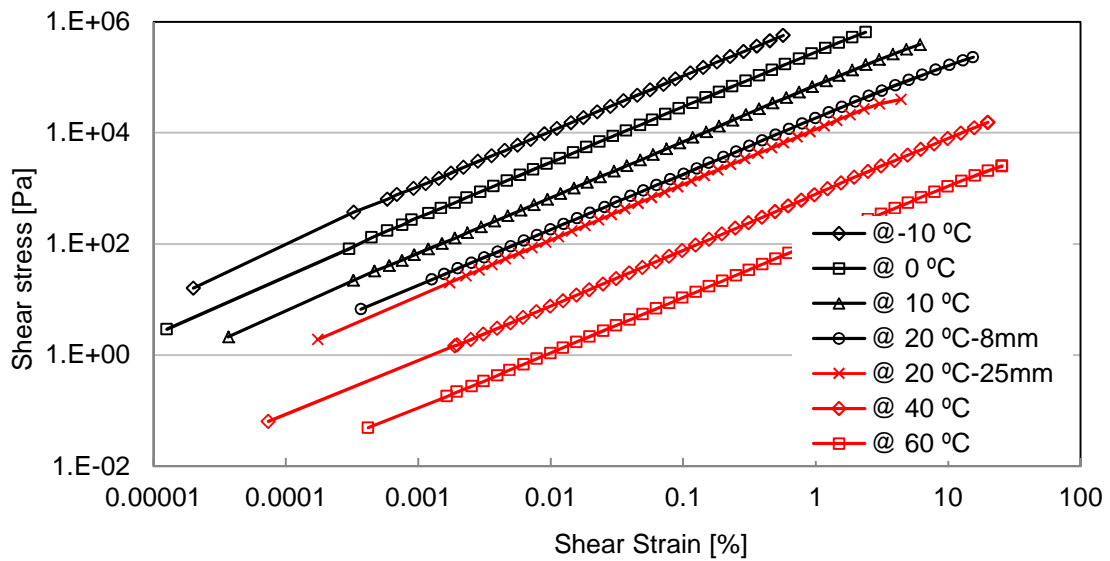


Figure 5-15 Stress-strain relationships of MBE after 1st stage curing

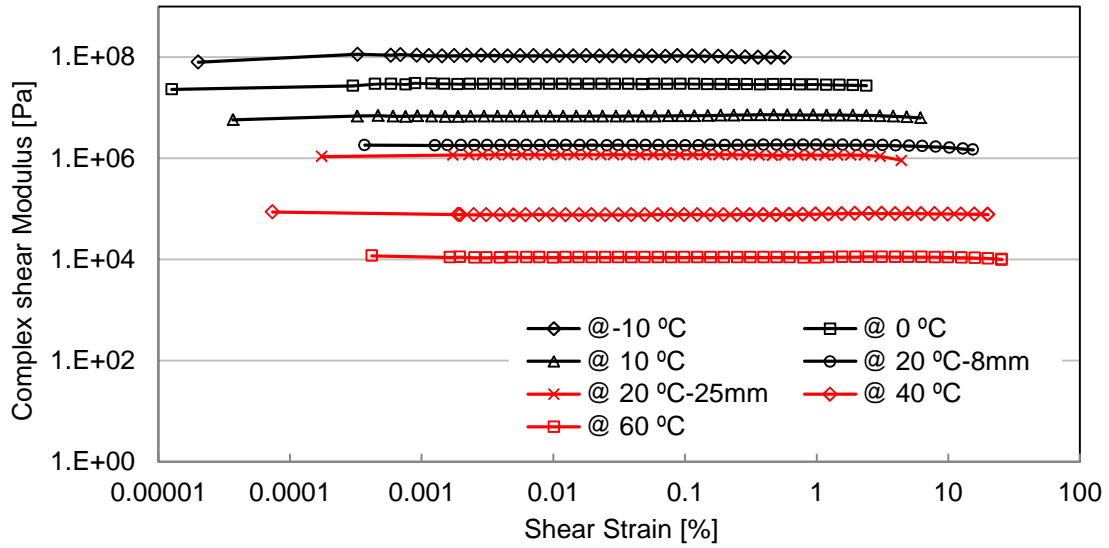


Figure 5-16 Modulus curves from strain sweep test on MBE after 1st stage curing

Strain sweep tests were also conducted on MBE residues after the 2nd and 3rd stage curing. Based on the results, proper strain levels were selected from the LVE range at each temperature for the frequency sweep tests. Table 5-6 presents the applied strain levels.

Table 5-6 Strain levels applied on emulsion residues at different temperatures

Strain level [%]	-10 °C	0 °C	10 °C	20 °C	40 °C	60 °C
1 st stage	0.01	0.05	0.1	0.3	1	3
2 nd stage	0.01	0.05	0.1	0.3	1	3
3 rd stage	0.01	0.05	0.1	0.3	1	3

Figure 5-17 shows the master curves of the modulus and phase angle for the residues after 1st stage, 2nd stage and 3rd stage curing, at the reference temperature of 20 °C. The Williams-Landel-Ferry (WLF) equation and S-curve Model (see the explanation in Section 3.2.4.3 in Chapter 3) were used to construct the master curves of the modulus and the phase angle over a wide frequency range. The following equations are used:

$$\log(\alpha_T) = \frac{C_1(T - T_{ref})}{C_2 + (T - T_{ref})} \quad (5-2)$$

$$f_R = f \times \alpha_T = f \times 10^{\frac{C_1(T - T_R)}{C_2 + T - T_R}} \quad (5-3)$$

$$G^* = G_{min} + (G_{max} - G_{min}) \times (1 - \exp(-(\frac{f_R}{\beta_G})^{\gamma_G})) \quad (5-4)$$

Where,

α_T = the shift factor at a temperature of T ;

- T_{ref} = reference temperature, [°C];
- C_1, C_2 = are constants;
- G^* = complex modulus, [Pa];
- f_R = reduced frequency, [rad/s];
- G_{min}^*, G_{max}^* = complex modulus when f_R is 0 or infinite, [Pa];
- β_G = location parameters of the S-curve;
- γ_G = shape parameters of the S-curve.

The fitting parameters of the master curves are given in Table 5-7. Master curves for a virgin pen grade bitumen (Pen 90) are also included in Figure 5-17 for comparison [1]. The physical properties of this bitumen are listed in Table 5-8.

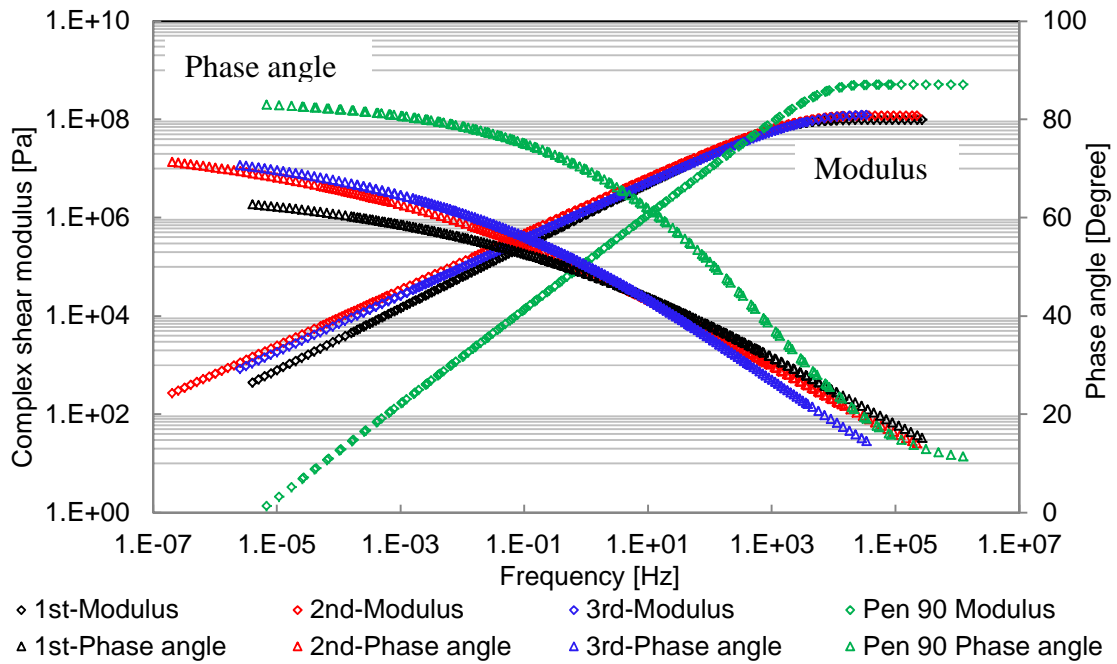


Figure 5-17 Modulus curves after the 1st stage, 2nd stage and 3rd stage curing

Table 5-7 Fitting parameters for MBE binders

Fitting parameters	After 1 st stage	After 2 nd stage	After 3 rd stage
C_1	22.36	19684.18	3044.1
C_2	208.81	160883.87	32032.5
G_{\max} [Pa]	9.77E+7	1.2E+8	1.25E+8
G_{\min} [Pa]	0	0	0
β_G	1095.86	1619.74	2458.93
γ_G	0.63	0.57	0.58
δ_{\max} [Degree]	67.39	77.89	76.21
δ_{\min} [Degree]	0.34	0	0.01
β_δ	9381.59	1498.28	764.46
γ_δ	0.12	0.11	0.13

Table 5-8 Basic properties of pen grade bitumen 90

Indicator	Test Method	Specifications	Results
Penetration [0.1mm]	ASTM D5	80~100	92.6
Softening point [°C]	ASTM D36	> 45	47.8
60 °C Viscosity [Pa.s]	ASTM D217	> 160	187
15 °C Ductility [cm]	ASTM D113	> 100	> 150

Compared to the Pen 90 bitumen, the residues of MBE have higher modulus values and lower phase angles at the same frequency. The slopes of the master curves of the MBE residues are smaller than the slopes of the master curves of the Pen 90 bitumen. This indicates that the MBE residues are less temperature susceptible.

Figure 5-17 show that the residue obtained after the 3rd curing stage has a slightly higher modulus than the residue obtained after the 2nd curing stage. This means that curing might occurred during the 3rd stage, hence only the master curves from the 3rd stage cured sample can represent the properties of a fully cured MBE residue. At a very low temperature, e.g. -10 °C, the MBE has a modulus value of 100 MPa, while its phase angle is below 20 degrees. At a high temperature, e.g. 60 °C, the MBE has a modulus value of approximately 300 Pa, while its phase angle is above 60 degrees. At 60 °C the binder has viscous domain properties and hence behaves almost like a liquid at these temperatures.

Because of jet blast, a high temperature resistance of antiskid surfacing at 80 °C or higher is required. The test results show that the MBE residue comes in a liquid state at temperatures higher than 60 °C. This indicates that MBE may not be suitable for antiskid surfacings.

5.3 Epoxy Modified Bitumen (EMB)

Firstly, preliminary tests were performed on three types of 2-component epoxy modified bitumen, named A1, A2 and A3. The differences between these three binders are the additive contents as shown in Table 3-3, which resulted in the fact that A1 cures the fastest and A3 cures the slowest.

5.3.1 Preliminary Tests

Two curing temperatures were used, 14 °C and 22 °C. After preparation, some samples were kept in a storage room at 14 °C and 70% relative humidity. Others were cured at ambient temperature in the laboratory (approximately 22 °C).

5.3.1.1 Curing Behavior

Some preliminary tests showed that the A3 binder is softer than the other two binders. For example, when DTT was performed at a displacement rate of 1 mm/min at 10 °C, A3 had a failure displacement which was out of the displacement range of the test machine. Therefore 10 °C and 6 mm/min were used for the A3 binder, while test conditions of 10 °C and a displacement rate of 1 mm/min were suitable as direct tensile test conditions for the A1 and A2 binder. Figure 5-18 shows the failure propagation during a DTT test. Figure 5-19 presents typical displacement-force curves for EMB binders. The figure clearly shows that A3 was more flexible and had a remarkably higher failure strain than the other two, even at a displacement rate of 6mm/min.

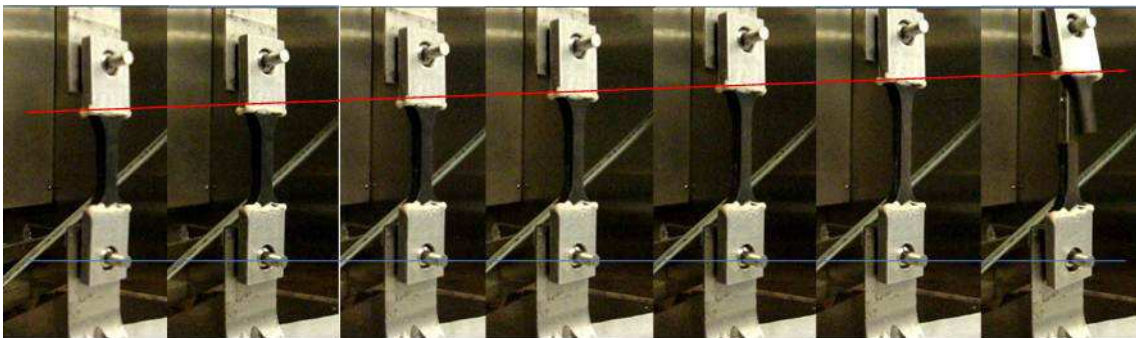


Figure 5-18 Failure propagation during a DTT test

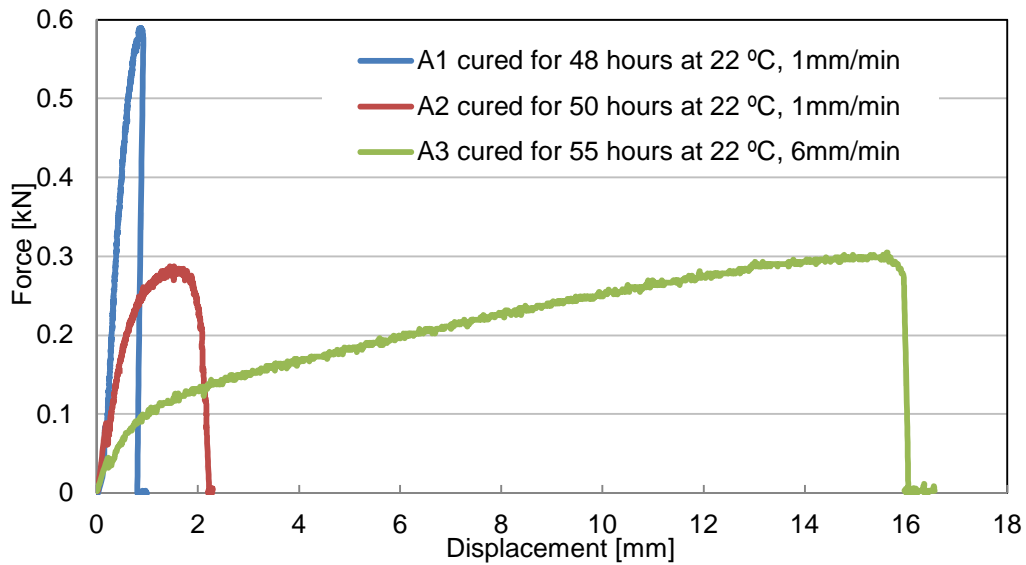


Figure 5-19 Force-displacement curves from DTT on EMB binders at 10 °C

The DTT test results are presented in Table 5-9, Table 5-10 and Table 5-11.

Table 5-9 DTS results of A1 binder

Cured at 14 °C				Cured at 22 °C			
Curing T [h]	Disp. [mm]	DTS [MPa]	Stiffness [MPa]	Curing T [h]	Disp. [mm]	DTS [MPa]	Stiffness [MPa]
26.5	1.55	9.28	202.38	21	0.94	14.49	520.98
54	1.17	15.55	449.14	21.5	1.14	16.35	484.68
55.5	0.94	15.71	564.93	27	0.84	15.87	638.67
77	0.88	14.81	568.99	27	0.9	16.28	611.43
77.5	0.87	14.90	578.77	47.5	0.89	16.12	612.07
88.5	0.81	17.18	716.69	48	0.89	16.36	621.35
89	0.93	16.44	597.56	75	0.99	16.36	558.59
242.5	0.77	17.91	786.11	115	0.89	16.44	624.41
315	0.79	17.74	759.19	115.5	0.83	16.28	662.99
502.5	0.9	18.80	706.15	165.5	0.8	17.01	718.84
503	0.86	19.46	764.65	171.5	1	18.31	619.01
				214	0.69	15.96	781.59
				216.5	0.74	18.07	825.46
				334	0.91	19.21	713.56
				339	0.84	19.21	773.02
				532.5	0.83	17.01	692.85
				533	0.77	16.28	714.65

Table 5-10 DTS results of A2 binder

Cured at 14 °C				Cured at 22 °C			
Curing T [h]	Disp. [mm]	DTS [MPa]	Stiffness [MPa]	Curing T [h]	Disp. [mm]	DTS [MPa]	Stiffness [MPa]
30	15.89	5.54	11.78	21.5	11.67	8.06	23.34
50.5	12.56	7.65	20.59	22	8.23	8.06	33.09
54	14	8.06	19.46	49.5	1.53	7.98	176.24
69	9.75	8.79	30.48	49.5	7.27	11.15	51.85
72	10.79	9.28	29.07	67	6.39	12.21	64.59
90.5	10.12	10.01	33.44	67.5	7.89	11.72	50.22
96	8.99	10.01	37.64	119	3.92	11.15	96.16
193	4.56	9.93	73.61	119.5	4	11.56	97.67
197	5.82	10.58	61.46	190	2.91	13.03	151.29
235.5	4.48	12.23	92.30	241	3.92	11.97	103.18
242	5.5	12.29	75.54	248	1.89	12.70	227.07
439	3.8	12.54	111.51	337.5	3.64	12.78	118.68
507	3.2	12.37	130.68	343	1.42	13.11	311.95
510.5	3	12.29	138.49	385	1.14	13.27	393.43
				574	1.82	13.19	244.88

Table 5-11 DTS results of A3 binder

Cured at 14 °C				Cured at 22 °C			
Curing T [h]	Disp. [mm]	DTS [MPa]	Stiffness [MPa]	Curing T [h]	Disp. [mm]	DTS [MPa]	Stiffness [MPa]
53	18.96	5.94	10.59	46	15.66	7.73	16.69
70	19.01	6.35	11.29	46	15.41	7.90	17.32
75.5	19.91	6.76	11.47	55	15.6	8.47	18.36
116	12.26	6.92	19.08	55	12.2	8.31	23.01
171	13.09	7.81	20.18	70	9.5	7.72	27.47
174.5	16.18	9.12	19.04	70.5	13.9	8.22	19.99
242.5	13.08	8.71	22.51	121.5	12.4	8.64	23.55
336	13.06	8.71	22.54	141.5	12.6	7.97	21.39
337.5	13.47	8.71	21.86	318.5	12.9	8.72	22.85
500	11.08	8.87	27.07	338	11	9.03	27.74
503	11.6	9.36	27.28	361.5	12	9.11	25.66
				385	9.84	9.11	31.30
				390	12.3	9.03	24.81
				410	10.6	8.61	27.46
				505	10.8	9.03	28.25
				507	10.1	8.47	28.35

Figure 5-20, Figure 5-21 and Figure 5-22 present the DTS results in relation to curing time and curing temperature. Table 5-12 presents the fitting parameters (see equation 5-1) for the curing curves of DTS values in relation to the curing time. The curves for the displacement at failure are obtained by adding a

logarithmic trend in excel. The DTS increases with curing time, and the higher the curing temperature was, the faster the DTS developed. Binder A1 has the fastest curing rate and the highest direct tensile strength, while A3 has the lowest curing rate and the lowest direct tensile strength. Based on the model parameters presented in Table 5-12, it can be concluded that the A3 EMB binder has a DTS of 9 MPa after being fully cured. The DTS of fully cured A1 and A2 is about 18 MPa and 12 MPa respectively.

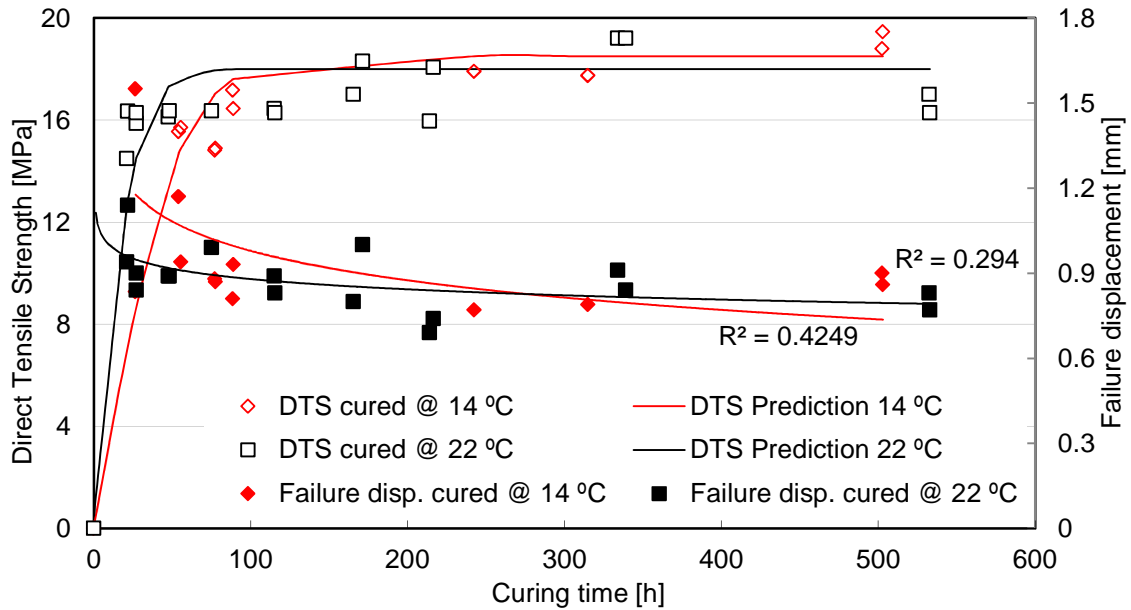


Figure 5-20 Curing curves for binder A1 tested at 10 °C and 1 mm/min

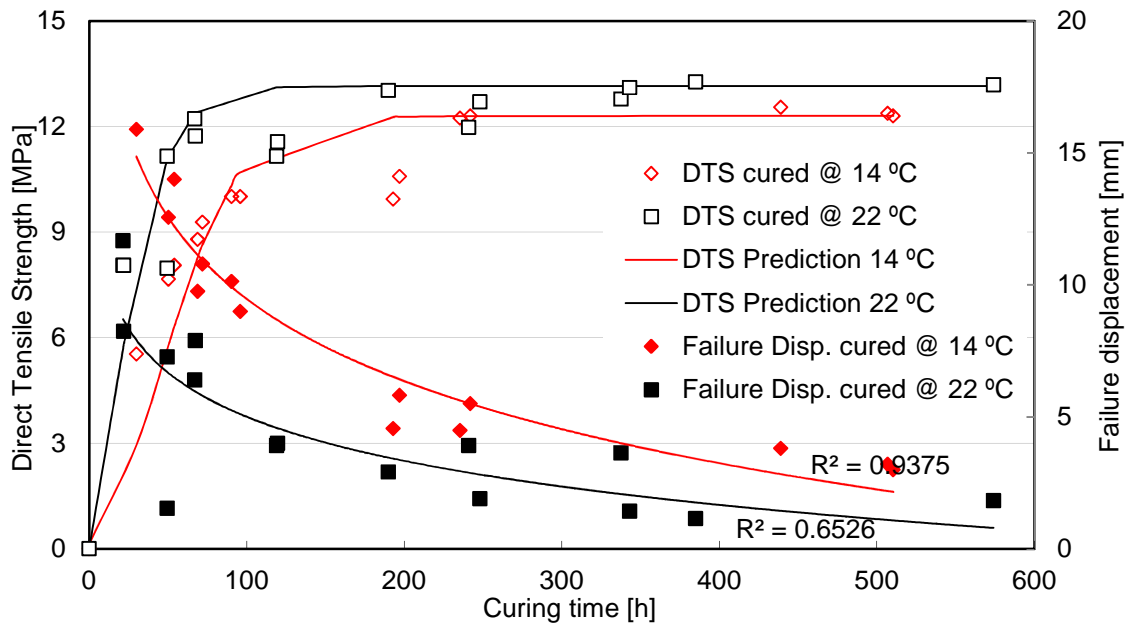


Figure 5-21 Curing curves for binder A2 tested at 10 °C and 1 mm/min

The displacement at failure of A1 and A2 is much smaller than that of A3. The failure displacement curves indicate that the A3 binder will perform better when large deformations are introduced onto the pavement surface. The antiskid surface might suffer to significant strain level. If the used binder cannot resist to this strain, cracks might occur.

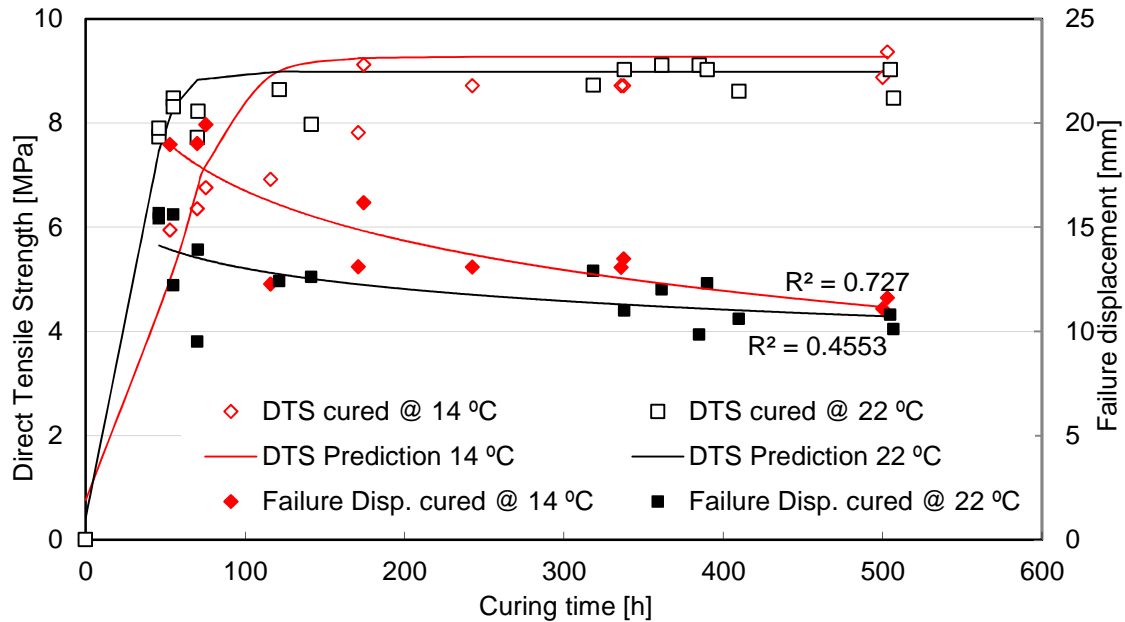


Figure 5-22 Curing curves for binder A3 tested at 10 °C and 6 mm/min

Table 5-12 Parameters for the prediction models

Binder	Curing temperature	δ	α	β	γ	R^2
A1	14 °C	-10.5	29	0.55	0.045	0.959
	22 °C	-15.5	33.5	0.09	0.083	0.863
A2	14 °C	-1.5	13.8	2	0.042	0.904
	22 °C	-5.3	18.45	0.9	0.06	0.879
A3	14 °C	-0.0293	9.3	2.38	0.048	0.924
	22 °C	-0.0147	9	3	0.1	0.958

Figure 5-23 shows the stiffness in relation to the curing time. The stiffness of A1 is developing very fast and can reach a value above 700 MPa after fully curing. The stiffness of A2 and A3 develops slower than the stiffness of the A1 binder. After 200 hours, the stiffness of A2 and A3 is still increasing. The maximum stiffness of A3 when tested at 10 °C and 6 mm/min displacement rate is about 30 MPa.

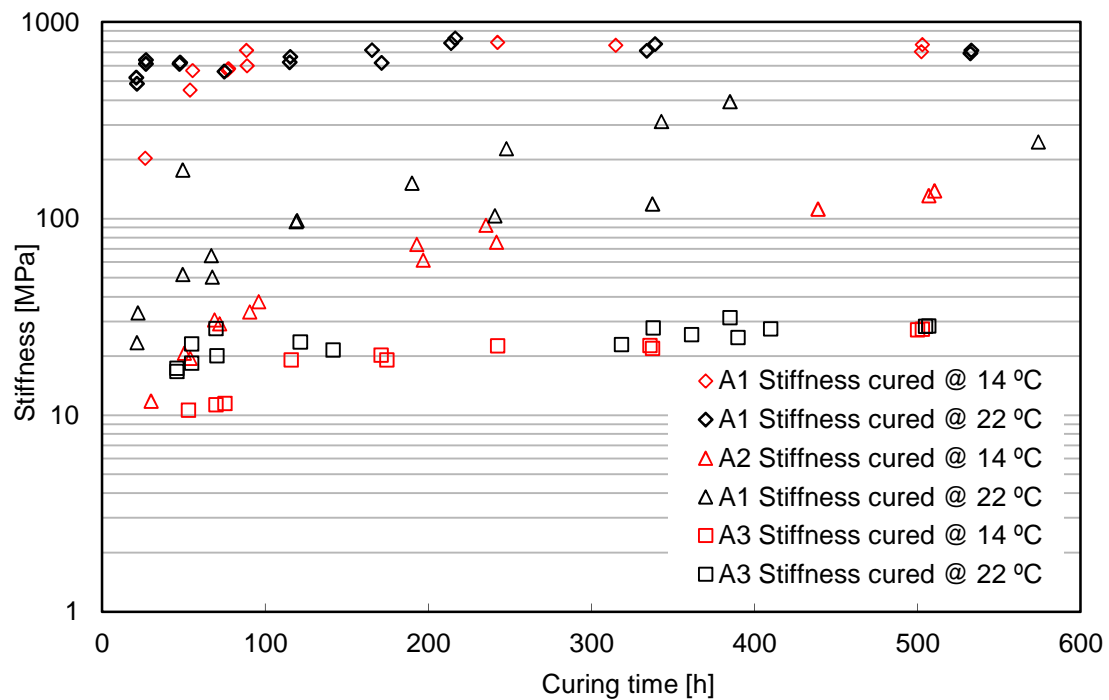


Figure 5-23 Stiffness in relation to curing time for EMB binders

5.3.1.2 Dynamic Shear Rheometer Results

First of all, strain sweep tests were conducted to determine suitable strain levels for the frequency sweep tests. Figure 5-24 and Figure 5-25 present the shear stress and complex modulus curves in relation to the applied strain for the fully cured A3 binder. The test was conducted at a frequency of 10 Hz.

Strain sweep test results obtained on the A1 and A2 binders are presented in Figure A-5 to Figure A-8 in the attached Appendix. Based on these results, certain stress levels were calculated to be applied in the frequency sweep tests. Table 5-13 presents these applied stresses for the individual tests at different temperatures. Frequency sweep tests were performed on fully cured binders and oven aged binders (oven aged binder means binder aged in the oven for 7 days at 85 °C) at temperatures of -10 °C, 0 °C, 10 °C, 20 °C, 40 °C, and 60 °C. The frequency ranges from 0.1 rad/s (approximately 0.0159 Hz) to 300 rad/s (approximately 47.73 Hz).

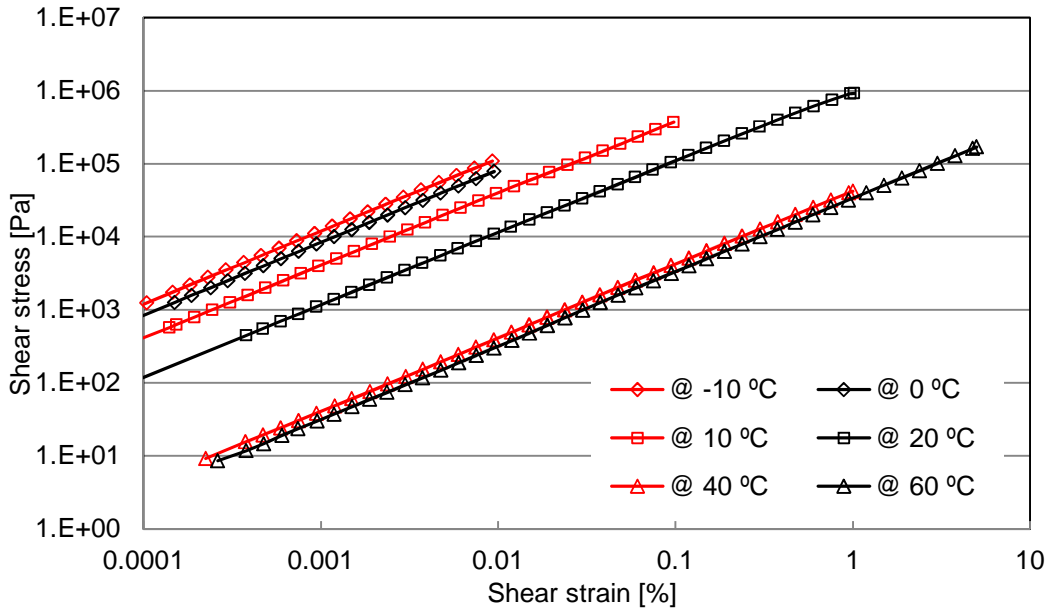


Figure 5-24 Stress-strain relationship in LVE range of fully cured A3

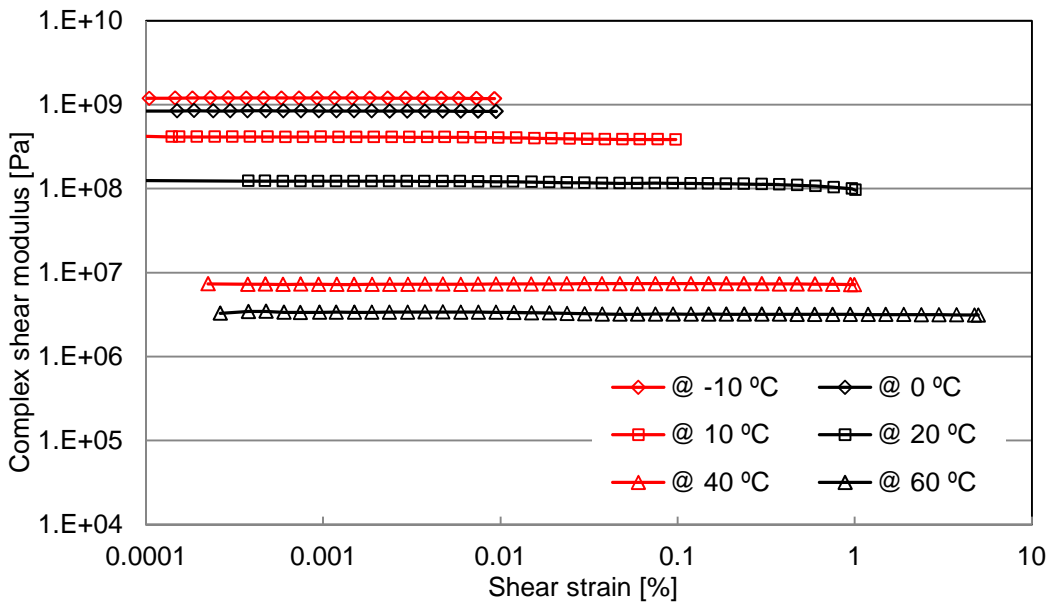


Figure 5-25 Modulus curves from strain sweep tests on fully cured A3 samples

Table 5-13 Stress [Pa] level applied on the EMB binders

Temperature [°C]		-10	0	10	20	40	60
EMB-A1	Fully cured	25930	23580	18860	7060	471.6	235.8
	7d aged	25940	23580	18860	7073	2358	235.8
EMB-A2	Fully cured	25930	23580	18860	7072	471.6	235.8
	7d aged	25940	23580	18860	7073	471.6	235.8
EMB-A3	Fully cured	25940	23580	18860	7076	2358	245.9
	7d aged	25940	23580	18860	7073	2358	235.8

Figure 5-26 shows the master curves of the complex shear modulus and phase angle for the A1, A2 and A3 binders, at the reference temperature of 20 °C. The fitting parameters are given in Table 5-14.

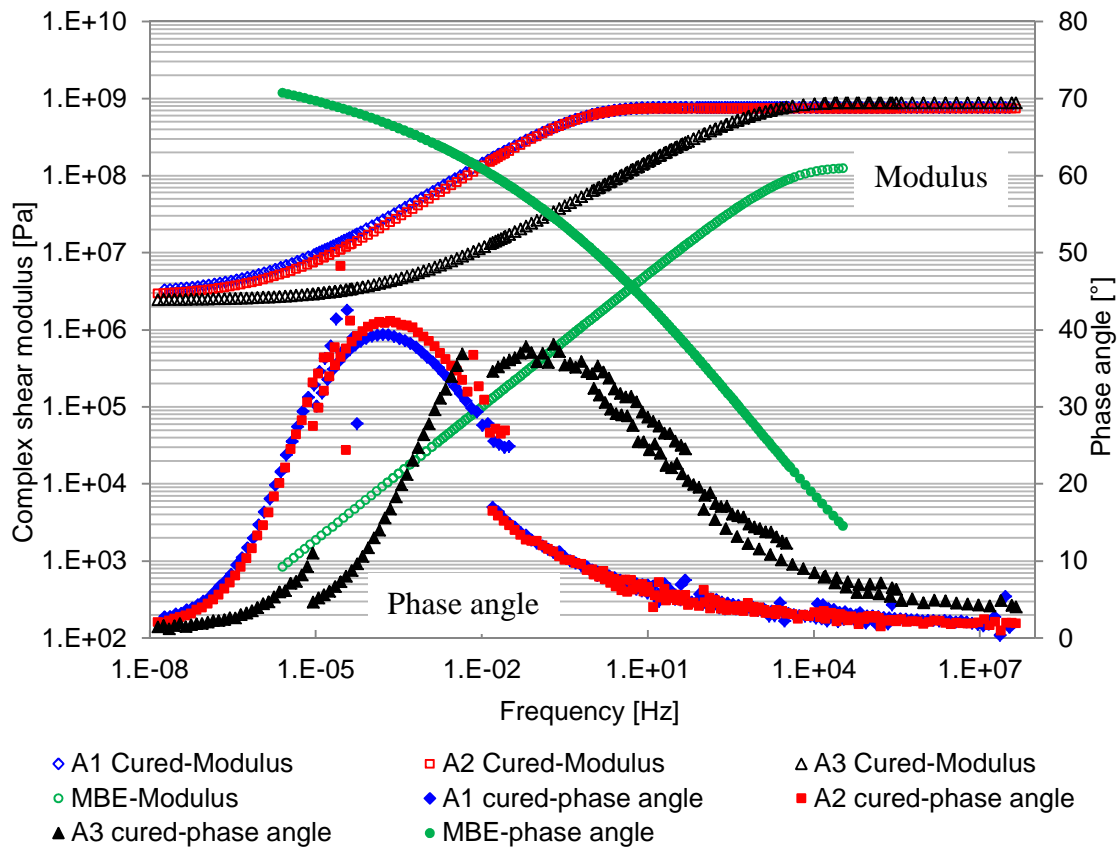


Figure 5-26 Master curves of cured A1, A2 and A3 binders at Tref=20 °C

Table 5-14 Fitting parameters for EMB binders

Fitting Parameters	A1		A2		A3	
	Original	Oven aged	Original	Oven aged	Original	Oven aged
C_1	43	7638.23	43.96	11315.55	43.96	3700
C_2	250	40959.44	250.52	65027.25	250.52	22920.96
G_{max}^*	7.68E8	9.14E8	7.4E8	8.44E8	8.78E8	9.96E8
G_{min}^*	2.91E6	3.08E5	2.73E6	7.3E5	2.43E6	3.17E6
β_G	0.34	0.0027	0.33	0.008	543.02	50.2
γ_G	0.45	0.29	0.48	0.32	0.42	0.4

The phase angle curves of A1 and A2 binders are not continuous with frequency. This is mainly caused by the test temperatures. In the lower temperature range, -10 °C, 0 °C, 10 °C and 20 °C were selected for frequency sweep tests. The temperature gap between each test was 10 °C. In the higher

temperature range, 20 °C, 40 °C, and 60 °C were selected for frequency sweep tests. The temperature gap was 20 °C. When using the Time-Temperature superposition principle, the phase angle curves at a high frequency (low temperature) range is very smooth, but a gap appeared in the low frequency (high temperature) range. So, in the future smaller temperature gaps of 10 °C, e.g. 20 °C, 30 °C, 40 °C, 50 °C and 60 °C, should be used during frequency sweep tests on EMB binders.

The green lines in Figure 5-26 represent the master curves of 3rd cured MBE residue. The figure indicates that the EMB binders have a higher modulus than the MBE residue. The slopes of the modulus master curves for EMB are smaller than the slope of MBE. This means that the EMB is less temperature susceptible. The modulus of EMB at the low frequency range, which represents a high temperature condition of around 60 °C, is higher than 2 MPa. The phase angle at the high temperature condition (lower frequency range) is around 5 degree. It means that the EMB behaves as an elastic material at low frequency and/or high temperature.

The phase angle curves of EMB binders are totally different from that of MBE residue. They have a distinct peak value at a certain frequency, in contrast to the phase angle curve of the MBE residue that keeps increasing with decreasing frequency. The phase angles of all three EMB binders are much lower than that of the MBE residue meaning that they behave more elastic.

Binder A3 has the same modulus and phase angle values as A1 and A2 at higher and lower frequency range. In the middle range, A3 has a lower complex modulus. The A1 and A2 binder have similar master curves of modulus and phase angle. Figure 5-27 shows a magnified graph of the modulus curves and clearly shows the differences at the lower frequency range.

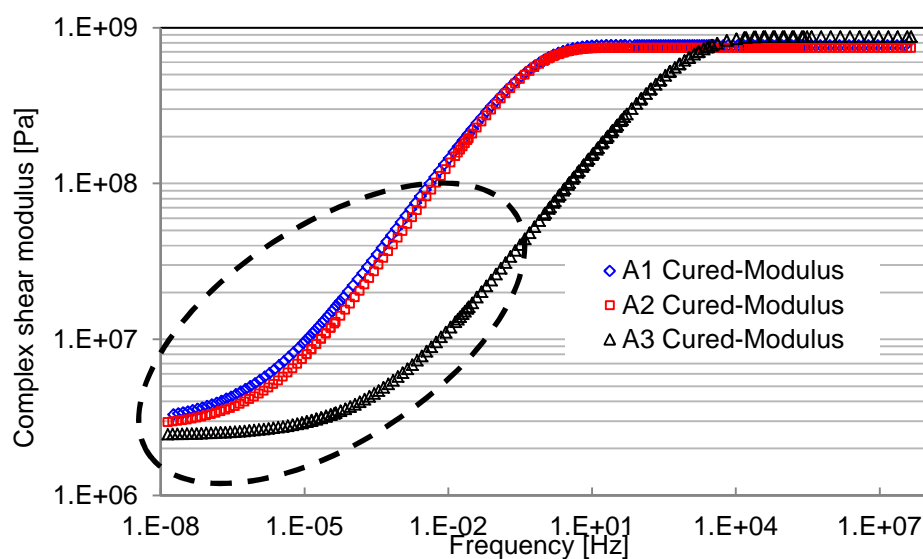


Figure 5-27 Master curves of the modulus for cured A1, A2 and A3 binders at $T_{ref}=20\text{ }^{\circ}\text{C}$

5.3.1.3 Direct Tensile Strength

The direct tensile strength of cured EMB binders (after curing for more than 10 days at ambient temperature) were studied by conducting DTT tests at 0 °C, 10 °C and 20 °C, with displacement speeds of 1 mm/min and 6 mm/min at each test temperature. Figure 5-28 and Figure 5-29 show the test results. Three tests were conducted at the same test condition and the average values were used.

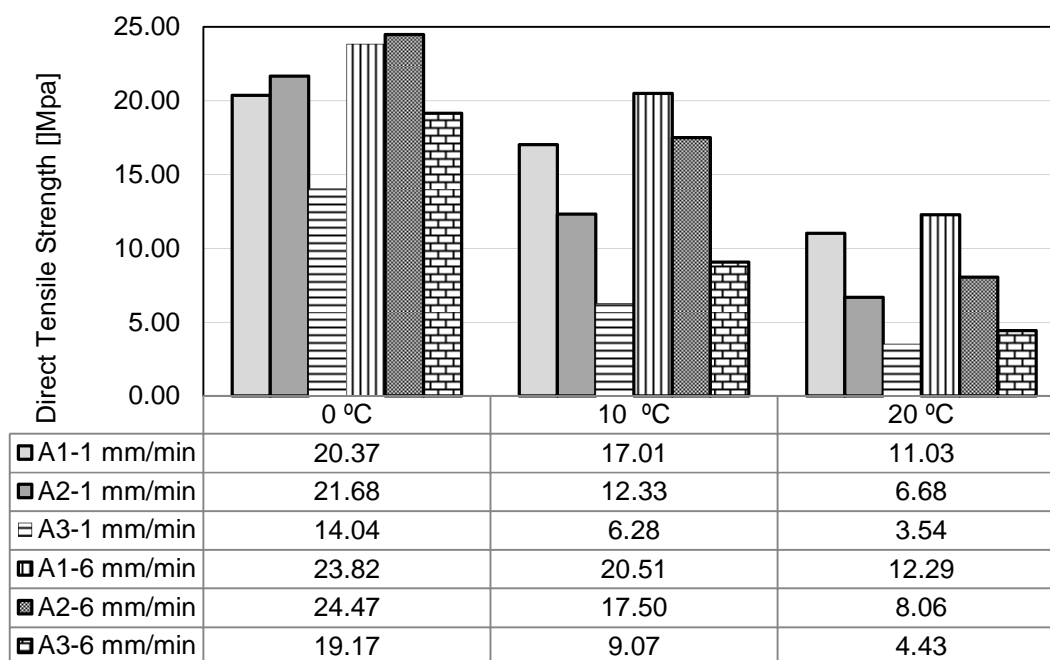


Figure 5-28 Direct tensile strength of EMB

Both at 10 °C and 20 °C, binder A1 has the highest tensile strength while A3 has the lowest tensile strength at the same loading speed. The tensile strength increased when a higher displacement speed was used. The tensile strengths of A2 and A1 at 0 °C are quite similar.

The failure strain, which is shown in Figure 5-29, indicates that EMB has a relatively small failure strain at a lower temperature of 0 °C. At 0 °C, the maximum failure strain of EMB is 9.9%. The failure strain at 0 °C of A1 and A2 is less than 2.2% of. The failure strains of A3 at 10 °C and 20 °C are more than 34%, both at 1 mm/min and 6 mm/min.

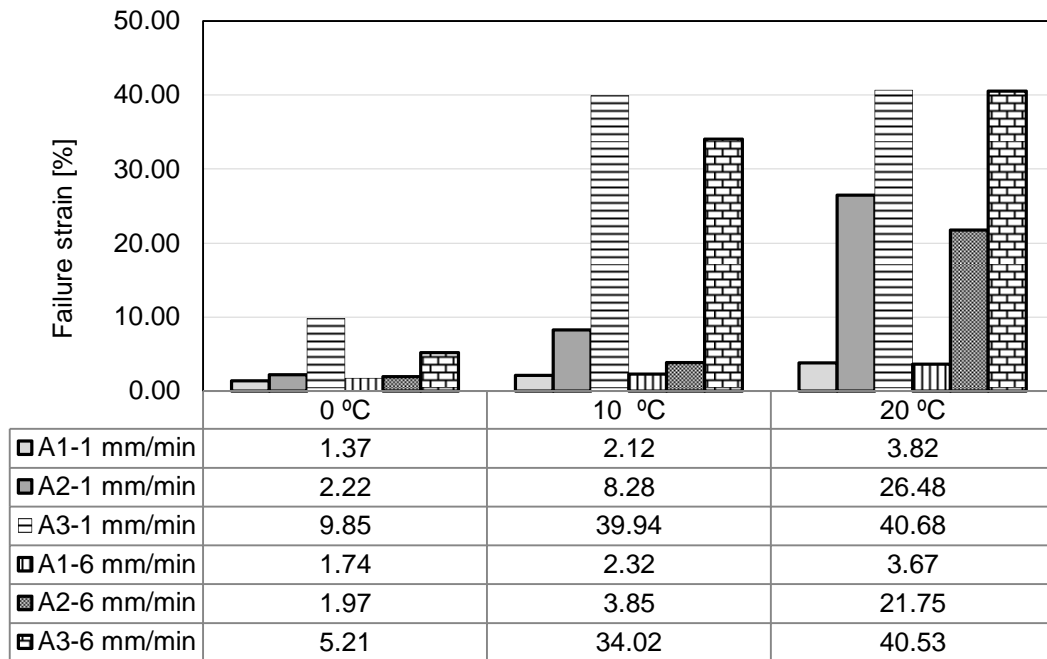


Figure 5-29 Failure strains of EMB

Figure 5-30 presents the force-displacement curves for fully cured EMB binders at 0 °C and 1 mm/min. These curves indicate that at low temperatures A1 and A2 seem to behave rather brittle, while A3 shows a real ductile behavior. A3 binder has a significantly higher failure strain than the other two binders at all three investigated temperatures. Furthermore, A3 binder provides a much higher failure strain than MER (Modified Epoxy Resin), compared to the DTT results of MER listed in Table 5-3 and Figure 5-9.

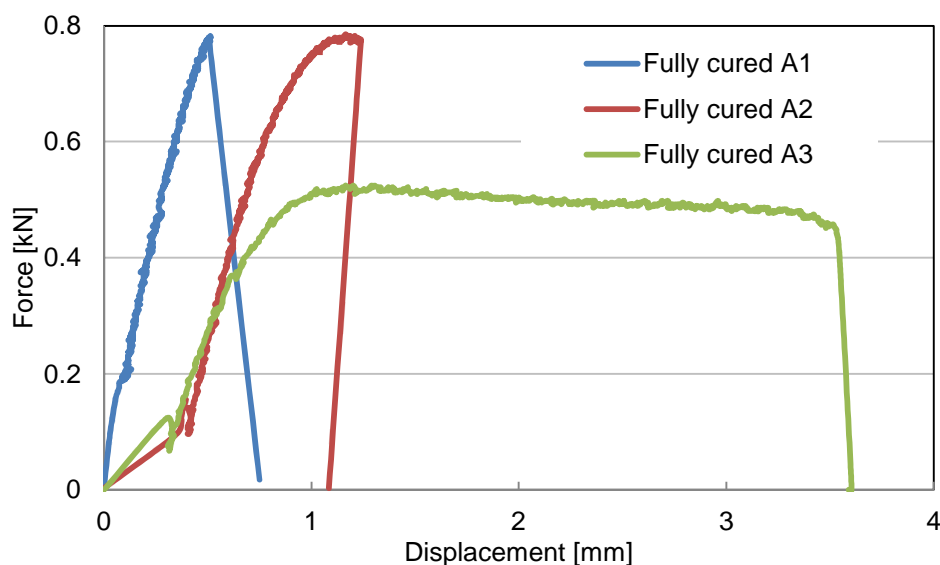


Figure 5-30 Force-displacement curves for cured EMB at 0 °C and 1 mm/min

5.3.1.4 Relaxation

Relaxation tests were conducted at 0 °C, 10 °C and 20 °C. Forty percent of the force at failure was used as the maximum applied force in the relaxation test. Three tests were conducted at every different test conditions. Figure 5-31 presents the results of binder A2 at three different temperatures. The applied forces for these three tests are different because the temperature influenced the failure force a lot, which makes that 40% of the failure force is a different value at different temperatures.

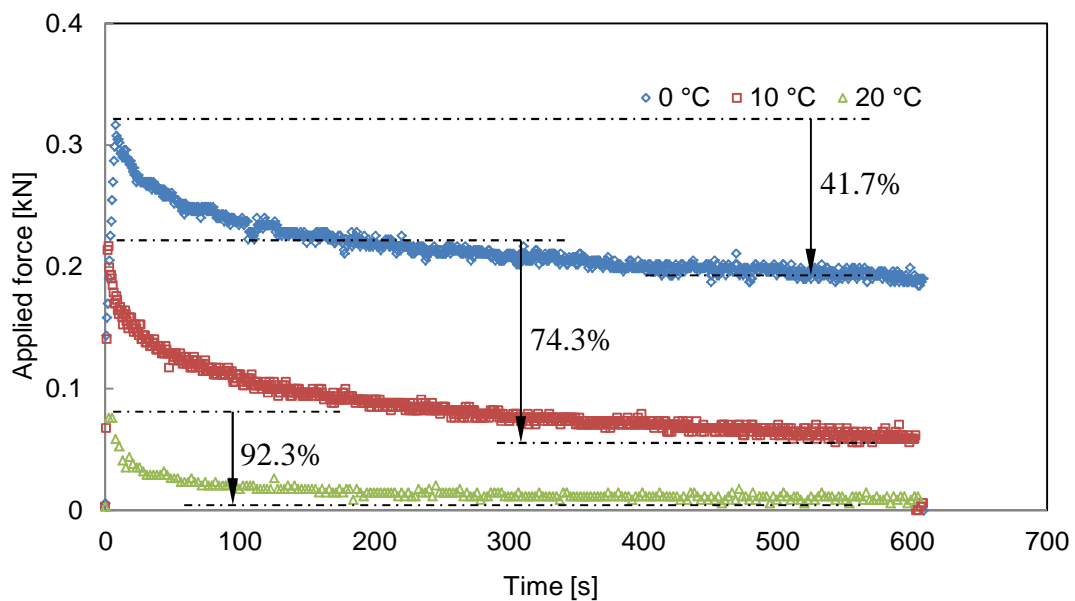


Figure 5-31 Relaxation results of A2 at different temperatures

The 40% of the maximum failure force of binder A3 at 20 °C is 0.063 kN, which is too low to be applied in the DTT test. The noise in the load signal is about 0.01 kN which is large enough to influence the interpretation of the relaxation results if 0.063 kN is applied. For this reason no data are presented for binder A3 at 20 °C in Figure 5-32.

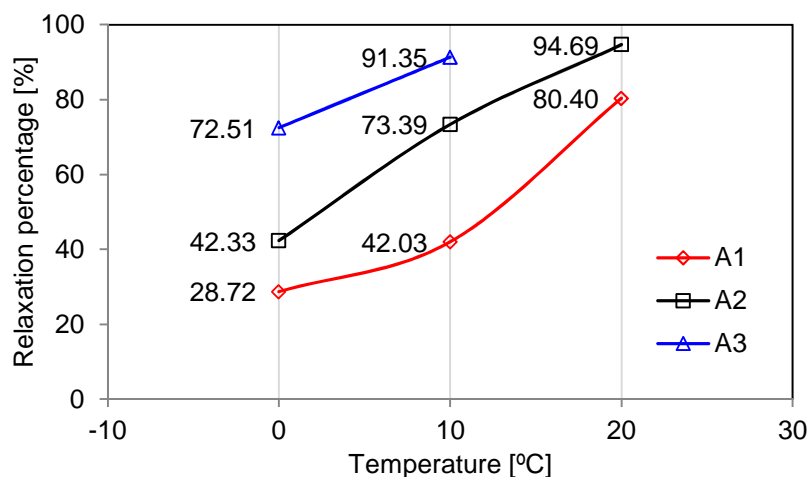


Figure 5-32 Relaxation percentage of binder A1, A2 and A3

Compared to the other binders, A3 shows the highest relaxation capacity. Binder A1 is more sensitive to temperature. When the test temperature changed from 0 °C to 10 °C and from 10 °C to 20 °C, its relaxation property increased with 46.3% (from 28.7 to 42) and 91.3% (from 42 to 80.4). Binder A3 has the best relaxation properties. At the temperatures between 0 °C and 20 °C, it has at least a 72.5% relaxation capacity. By comparing to the relaxation property of MER (Modified Epoxy Resin), which are presented in Table 5-5 and Figure 5-11, A3 binder has much better stress recovery behavior.

5.3.1.5 Ageing Resistance

Frequency sweep tests were also conducted on oven aged A1, A2 and A3 binders. Figure 5-33 compares the changes of modulus and phase angle between the original A1 binder and aged A1 binder. Figure 5-34 and Figure 5-35 present the changes in binder A2 and A3 respectively. The fitting parameters for the master curves are presented in Table 5-14. The reference temperature is 20 °C.

It is clear that the high temperature ageing in the oven has a significant influence at the lower frequency range, where the modulus has increased significantly after ageing. At high frequency levels, the modulus before and after the oven ageing is more or less the same. The high temperature in the oven probably causes the epoxy to react to a more mature degree, demonstrated by further modulus development.

The phase angle curves are shifted to the low frequency area after oven ageing. The peak point of the phase angle curves is the transition point between bituminous domain properties to epoxy domain property. Therefore, the curves illustrate that the transition temperature increased after oven ageing (lower frequency states higher temperature).

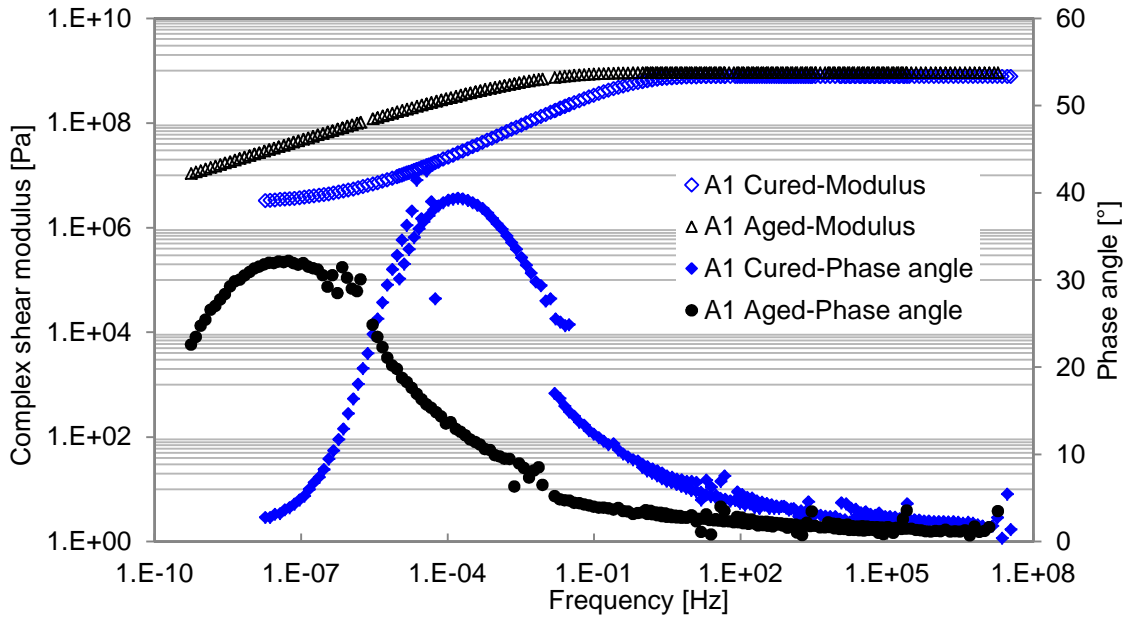


Figure 5-33 Master curves of the original and oven aged A1 binder

Figure 5-35 illustrates that the changes of modulus and phase angle of binder A3 after oven ageing were smaller than those of the other two binders. This means that the A3 binder has a better high temperature resistance. Figure 5-36 compares the master curves of all the three aged binders. A3 binder has a lower modulus at low frequency range. Because its phase angle curve of A3 is shifted to the right compared to the aged A1 and aged A2. This means that the aged A3 binder has a lower transition temperature (higher frequency states lower temperature) than the other two aged binders.

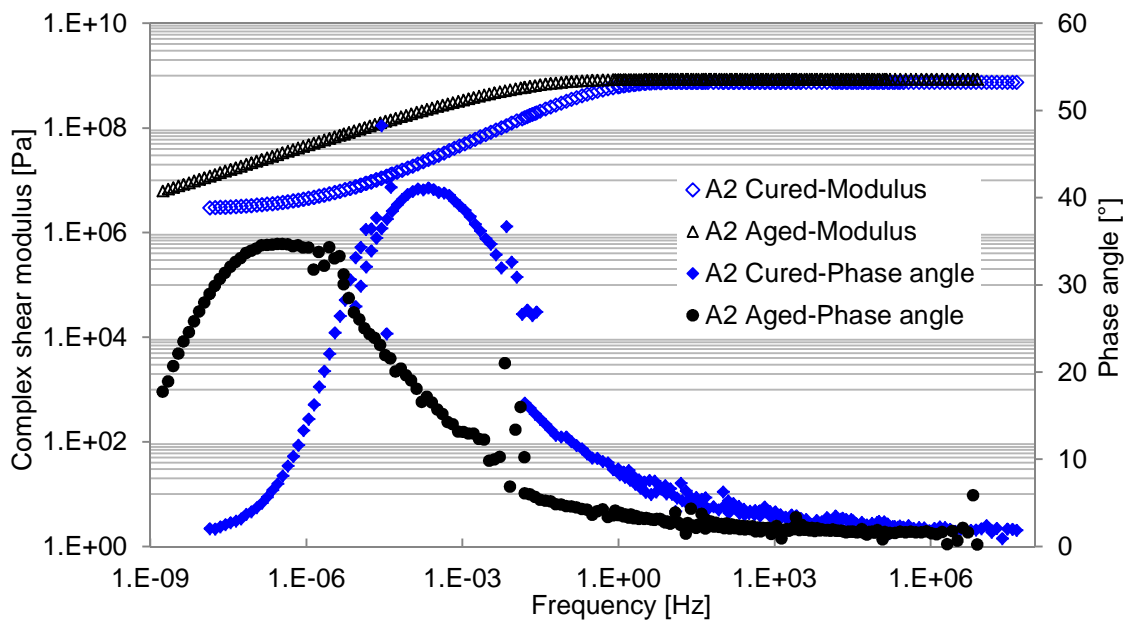


Figure 5-34 Master curves of the original and oven aged A2 binder

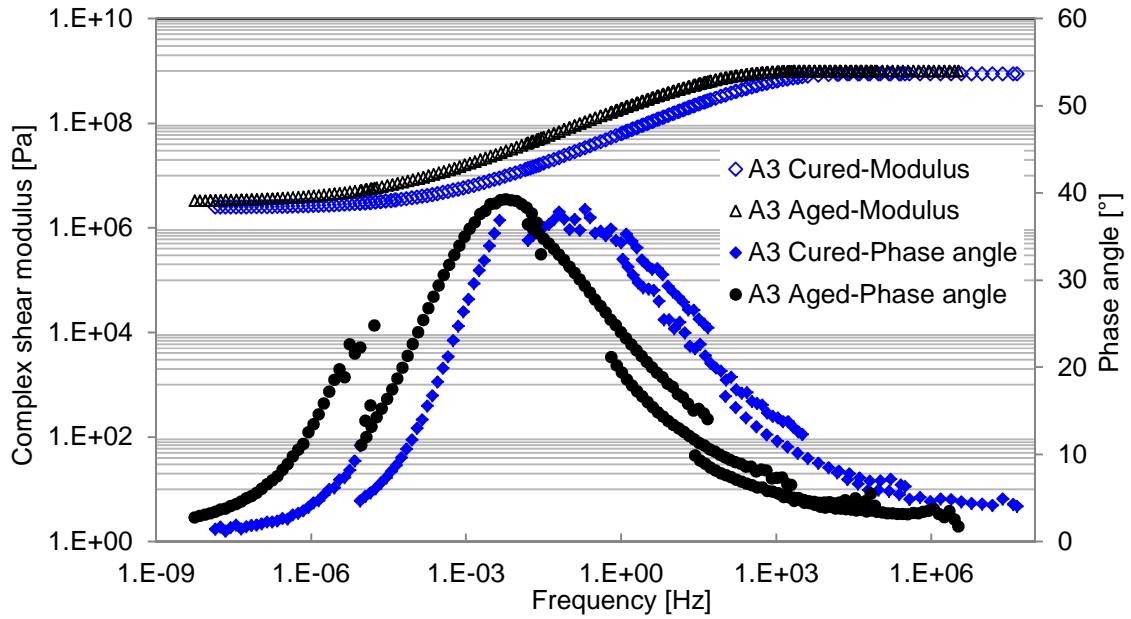


Figure 5-35 Master curves of the original and oven aged A3 binder

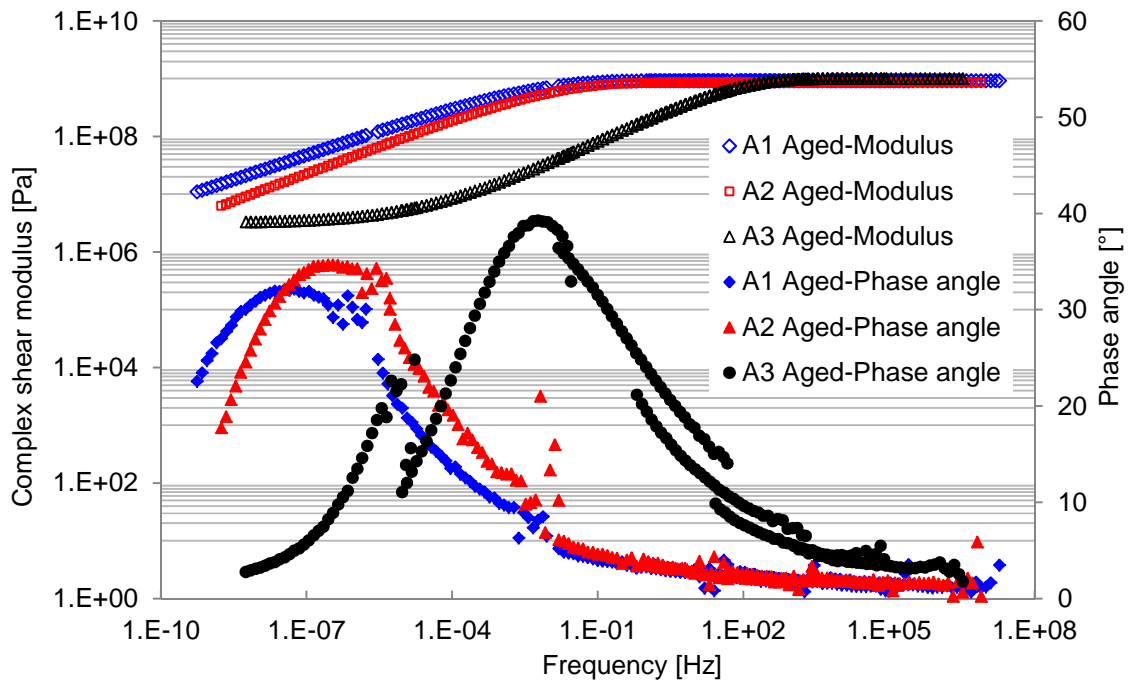


Figure 5-36 Master curves of the oven aged A1, A2 and A3 binders

Relaxation tests were also conducted at 10 °C on the oven aged EMB binders with DTT specimens. Figure 5-37 shows, as an example, the difference in relaxation behavior between the original and aged A2 binder. It clearly shows that the original binder has better relaxation properties.

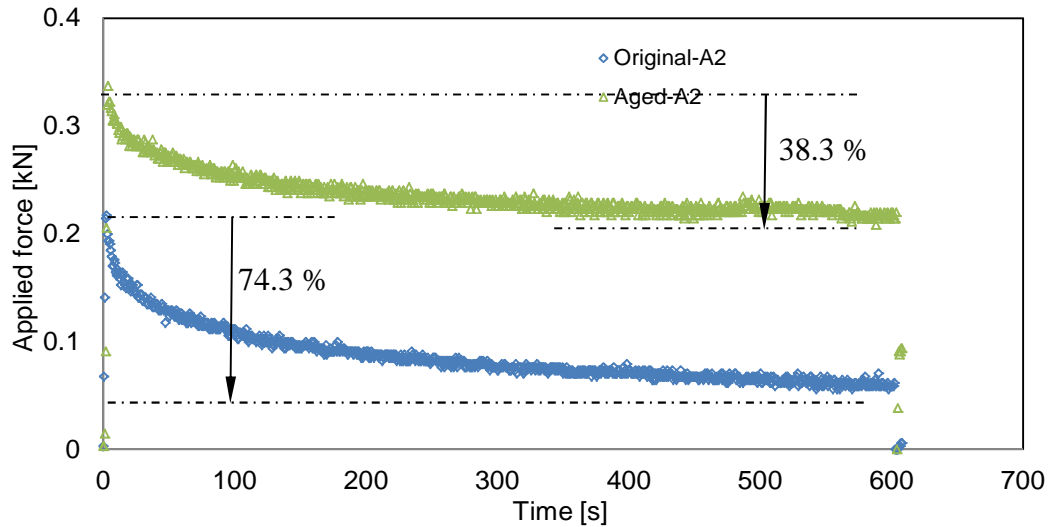


Figure 5-37 Relaxation curves of the original and oven aged A2 binder

Table 5-15 shows the results of the relaxation tests before and after ageing of the EMB binders. The relaxation capacity of binders A1 and A2 decreased with about 45%, which is much more than the decreased percentage observed for binder A3. This again shows that the A3 binder has a better resistance to ageing due to high temperatures than the A1 and A2 binders.

Table 5-15 Relaxation of EMB at 10 °C before and after oven ageing

Relaxation	A1	A2	A3
Before ageing	42.03	73.39	91.35
After ageing	24.32	39.39	80.36
Decrease [%]	45.79	46.33	12.03

5.3.2 A3-UV Binder

The preliminary tests illustrate that A3 has better relaxation property, larger tensile strength and better ageing resistance. Therefore, it may be concluded that the A3 binder has significant advantages over binder A1, A2 and MER, and was chosen for further analysis.

Antiskid surfacings are applied on the pavement (or runway) surface where they are directly exposed to the environment. They are exposed to the influence of water, moisture, oxygen and UV light. All these factors can cause ageing and damage. A good weather resistance is therefore absolutely required. In the EMB, the hardener is an amine-based chemical, which is sensitive to UV radiation. As a result, the epoxy may degrade and lose strength in time.

Therefore, 1 wt. % of UV absorber (Hindered Amine Light Stabilizer, HALS) was added to improve the resistance to weather ageing of A3 binder. HALS does not absorb UV radiation, but acts to inhibit degradation of the polymer. It slows down the photochemically initiated degradation reactions in a

similar way as antioxidants do. This binder was named A3-UV in this research. Weatherometer ageing was conducted on this binder to simulate long term weather ageing.

5.3.2.1 Weatherometer Ageing

A weatherometer was used for accelerated ageing under environmental conditions. Cylindrical specimens and small beams were placed in the weatherometer. The ageing conditions were discussed in Section 3.2.1.2 of Chapter 3. Figure 5-38 shows a picture of the original binder and the weatherometer aged binder. It can be clearly seen that after weatherometer ageing, a lot of bubbles appeared on the specimen surface. This illustrates that severe ageing occurred at the surface of the specimen during weatherometer ageing.



Figure 5-38 Specimens of the original and weatherometer aged specimens

Both DSR (from $-10\text{ }^{\circ}\text{C}$ to $80\text{ }^{\circ}\text{C}$) and DMA (from $-40\text{ }^{\circ}\text{C}$ to $100\text{ }^{\circ}\text{C}$) tests were used to characterize the viscoelastic behavior of the original and aged A3-UV in the lower and higher temperature range.

5.3.2.2 Dynamic Shear Rheometer

DSR tests were carried out using temperatures ranging from $-10\text{ }^{\circ}\text{C}$ to $80\text{ }^{\circ}\text{C}$, which is a wider range than that used in the previous section, Section 5.3.1.2. The strain sweep test results on weatherometer aged A3-UV binder are presented in Figure A-9 and Figure A-10 in the attached Appendix. Based on the strain sweep tests, strain levels were defined for the frequency sweep tests. Table 5-16 gives the information of different applied strain levels at different temperatures for the frequency sweep test.

Table 5-16 Applied strain (%) for original, oven aged and weatherometer aged A3-UV binders

Temperature [°C]	-10	0	10	20	40	60	80
Original binder	0.005	0.005	0.008	0.01	0.1	0.2	0.5
Oven aged binder	0.01	0.1	0.05	0.1	0.1	0.2	0.5
Weatherometer aged binder	0.005	0.005	0.01	0.02	0.04	0.05	0.05

Table 5-17 gives the fitting parameters for the master curves. Figure 5-39 compares the curves of modulus and phase angle between fully cured A3 (see Figure 5-35) and A3-UV. It shows that adding UV absorber hardly influenced the modulus value. The slopes of the phase angle curves are quite close, although the phase angle changed when the UV absorber was added.

Table 5-17 Fitting parameters for A3-UV binders

Fitting parameters	A3-UV		
	Original	Oven aged	Weatherometer aged
C_1	97866.31	91513.42	61513
C_2	597584.67	555931.93	555931
G_{max}^*	9.68E+8	9.69E+8	9.8E+8
G_{min}^*	1.64E+6	1.65E6	2.59E+6
β_G	1495.2	38.03	1910.29
γ_G	0.355	0.326	0.327

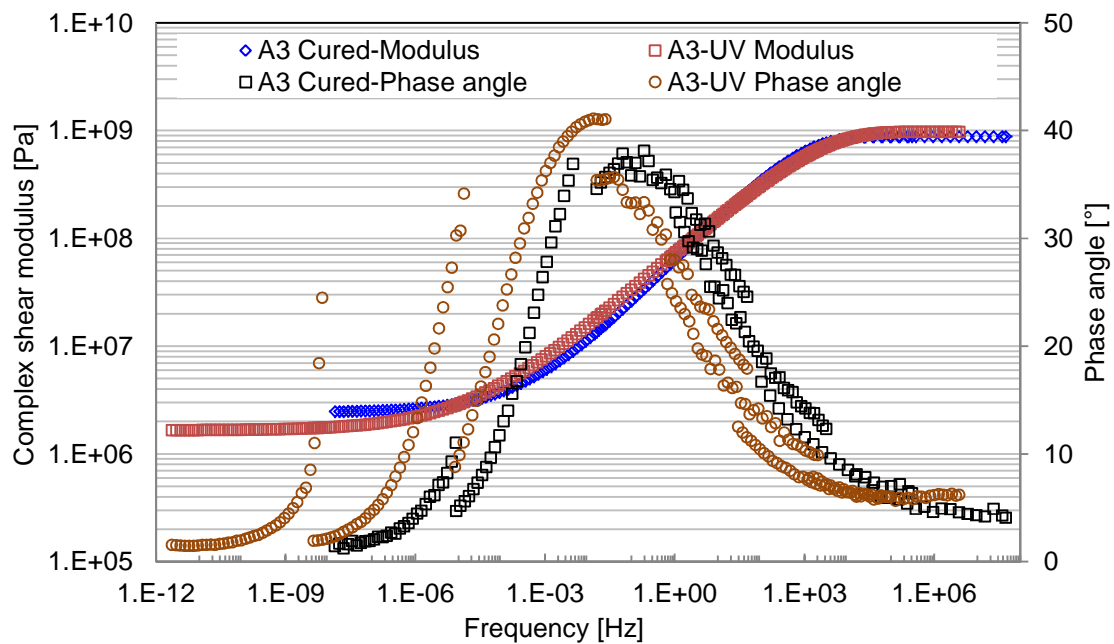


Figure 5-39 Comparison between A3 and A3-UV

Figure 5-40 compares the master curves of the modulus of the original binder, the oven aged and weatherometer aged binder. At lower frequencies, the complex modulus is higher than 2 MPa and the phase angle is around 5 degree. This means that the binder behaves elastically at higher temperatures and long loading times.

After oven ageing, the complex modulus curve shifts to a higher level. But after weatherometer ageing, which represents better the severe ageing conditions that occur in practice, there is no obvious change of the modulus at the higher frequency range. At the lower frequency range, the modulus of weatherometer aged binder is higher than the modulus for the original binder, but lower than the value of the high temperature aged binder.

At the EMB based surface, where there is direct contact to the air, rain, and solar radiation, ageing could be much more severe due to the influences of a high temperature than due to oxygen or UV radiation. UV cannot penetrate deeply into the bitumen because of the absorption from the graphite-like structures in the asphaltenes [6]. It is known that UV-light only penetrates 10 to 30 micrometers deep, giving oxidation to bitumen molecules. This can be seen by the surficial chalking in Figure 5-38. But the core of the specimen is protected and will only be aged by high temperature. The temperature during weatherometer ageing is 40 °C, which is much lower than oven ageing (85 °C). It is a well-known fact however that the surface layers can reach temperature of 65 °C on hot summer days in the tropics.

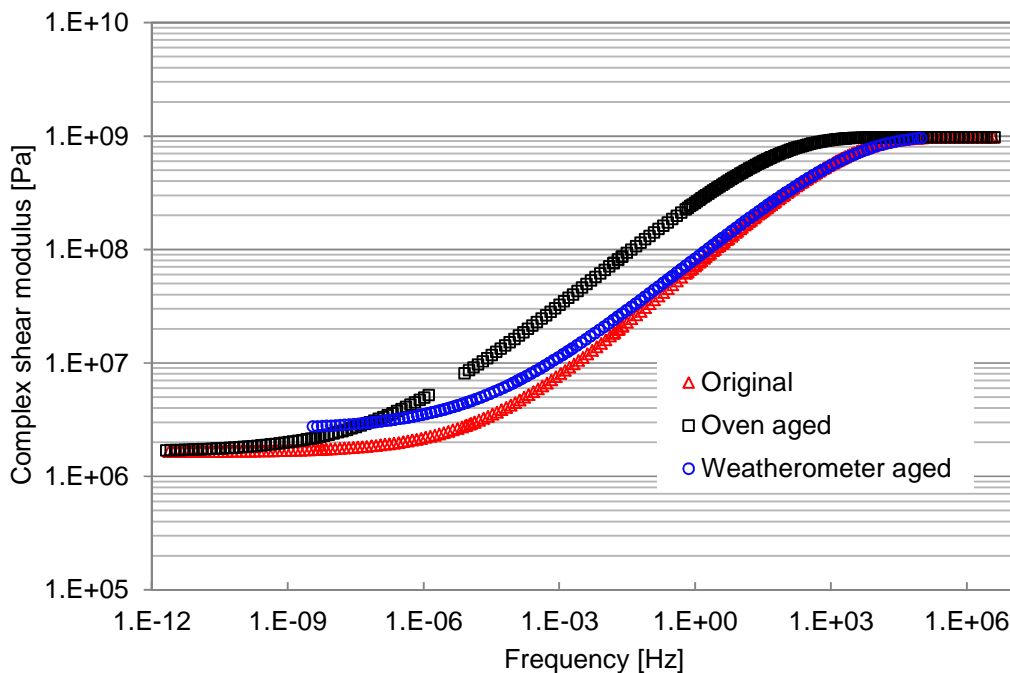


Figure 5-40 Master curve of complex modulus for original and aged A3-UV

Furthermore, the epoxy reaction will give more maturing at high temperatures. Both effects imply that EMB is subject to more serious ageing conditions in the oven than in the weatherometer.

5.3.2.3 Dynamic Mechanic Analysis

The DSR test already gave clear information on the viscoelastic properties of the tested binders. However, this research was carried on to give guidance to the producers for binder evaluations for thin surfacings. Some of the producers may prefer to do Dynamic Mechanic Analysis (DMA) tests instead of DSR. DMA tests can also be used to understand the viscoelastic behavior (stiffness and phase angle) of binders at a wider range of temperatures. Figure 5-41 shows the DMA test specimens and three points bending test setup. The beams shown in Figure 5-38 are too big for the testing. Therefore, the beams were cut and polished to small sizes: the thickness is approximately 1 mm and the width is 3.5 mm, while the distance between the two supporting points is 10 mm.

The DMA temperature sweep test was conducted at 1 Hz and 10 Hz on the original binder and aged binders. The temperature during the test increased from -40 °C to 100 °C with steps of 5 °C/min.

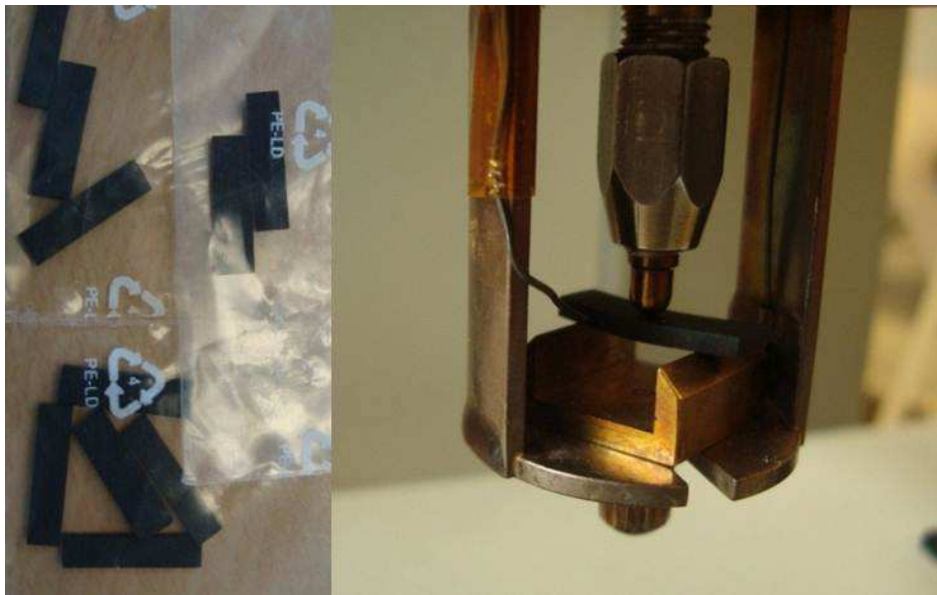


Figure 5-41 DMA test specimens and test setup

Figure 5-42 shows the stiffness and phase angle curves at 1 Hz. In the figure, O is the original binder, OA is the oven aged binder and WA is the weatherometer aged binder. It can be clearly observed that at temperatures below 20 °C, the phase angle does not change too much and the binders behave elastically. At a temperature around 100 °C, the stiffness curves seem to reach a plateau at 6 MPa.

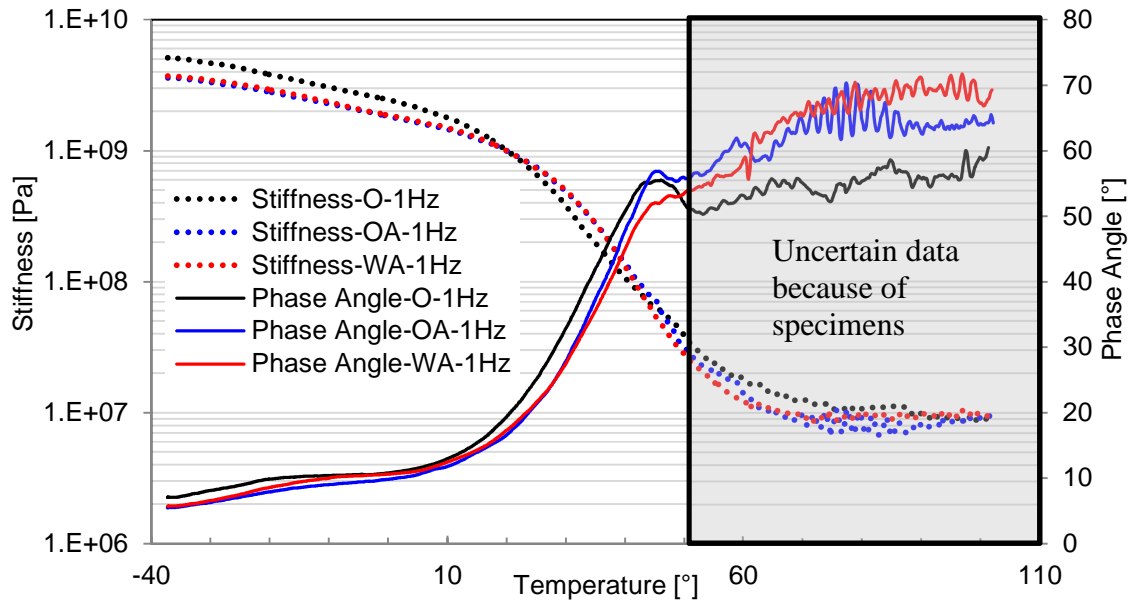


Figure 5-42 Stiffness and phase angle of A3-UV binders at 1 Hz

However, when the temperature was raised to 50 °C and higher, the binder became soft and only a very low load was needed to keep the required amplitude of 10 micrometer. When the testing temperature was further increased, the required load became so small that it was close to the resolution limits of the DMA tester. This makes the results at the higher temperature range less reliable.

There are only slight differences between the original binder and the aged binders, which mean that ageing has a limited influence on the binder properties. The blue line represents the oven aged binder, while the red line represents the weatherometer aged binder. No significant difference at lower temperature can be observed between these two specimens who were aged following two different ageing procedures. The UV light in the weatherometer ageing can just influence the surface of the binder up to 30 micrometers deep. During the sample preparation for the DMA test, approximately 0.5 mm thickness of the specimen surface was polished away and the core of the weatherometer aged samples were used for DMA tests. So, the influence of UV light was probably eliminated and the core parts were therefore subjected to long term high temperature ageing. Therefore no obvious difference can be observed.

Table 5-18 compares the test data from DSR and DMA. The stiffness (E) values from the DMA test and the complex modulus (G) value from the DSR test can be compared with the equation:

$$E = 2 \times (1 + \nu) \times G \quad (5-5)$$

Where, ν is the Poisson's ratio.

The results shows that DSR and DMA test give similar results. The shear modulus and the bending stiffness can fit each other by using equation 5-5 and assuming the Poisson's ratio is 0.3. The phase angles are also quite similar.

Table 5-18 Comparison between DSR and DMA data on A3-UV

DSR		Original		Oven aged		Weatherometer aged	
°C	Hz	Complex modulus [Pa]	Phase angle [degree]	Complex modulus [Pa]	Phase angle [degree]	Complex modulus [Pa]	Phase angle [degree]
-10	1	6.60E+08	6.041	1.89E+08	22.2	3.69E+08	21.41
	10	7.58E+08	6.097	1.97E+08	25.39	4.09E+08	24.51
0	1	5.41E+08	7.187	7.76E+08	6.942	3.96E+08	11.72
	10	6.40E+08	6.337	8.87E+08	7.037	5.22E+08	10.36
10	1	2.95E+08	14.61	5.70E+08	7.839	2.33E+08	16.43
	10	4.10E+08	11.29	6.82E+08	6.981	3.48E+08	14.13
20	1	1.01E+08	27.99	2.99E+08	15.35	0.81E+08	22.44
	10	1.87E+08	21.57	4.16E+08	11.99	1.45E+08	21.98
40	1	5.34E+06	33.18	0.27E+08	34.3	0.17E+08	21.99
	10	0.14E+08	40.28	0.64E+08	32.46	0.3E+08	25.12
60	1	2.11E+06	7.087	3.39E+06	20.38	6.33E+06	23.9
	10	2.77E+06	19.75	6.98 E+06	35.17	1.20E+07	27.71
80	1	2.02E+06	2.213	2.39E+06	4.087	2.87E+06	16.35
	10	2.15E+06	4.954	2.74E+06	11.61	4.72E+06	25.17
DMA		Original		Oven aged		Weatherometer aged	
°C	Hz	Stiffness [Pa]	Phase angle [degree]	Stiffness [Pa]	Phase angle [degree]	Stiffness [Pa]	Phase angle [degree]
-10	1	3.05E+09	10.367	2.3E+09	8.946	2.4E+09	9.978
	10	3.6E+09	5.116	3.3E+09	3.894	3.6E+09	4.858
0	1	2.4E+09	10.773	1.8E+09	9.809	1.9E+09	10.598
	10	2.9E+09	5.777	2.7E+09	5.751	2.9E+09	6.016
10	1	1.8E+09	12.945	1.5E+09	11.804	1.5E+09	12.468
	10	2.3E+09	6.914	2.2E+09	7.082	2.3E+09	7.278
20	1	1.01E+09	19.273	1E+09	16.616	1E+09	17.311
	10	1.6E+09	10.373	1.7E+09	10.564	1.6E+09	10.701
40	1	1.1E+08	50.795	1.4E+08	47.719	1.3E+08	44.983
	10	2.7E+08	32.973	3.8E+08	31.51	2.8E+08	34.903

5.3.2.4 Relaxation

A3-UV is a modified A3 binder and Figure 5-39 shows they have the same viscoelastic properties as each other. So no DTT tests were conducted on A3-UV binder anymore. Also the relaxation test cannot be performed in the same way as used for Modified Epoxy Resin (see Section 5.1.3) and the first three Epoxy Modified Bitumen binders (see Section 5.3.1.4).

The relaxation behavior of A3-UV was therefore investigated by using the DSR. A shear strain of 2% was first applied onto the specimen within two seconds. Afterwards the strain was kept constant for 5 minutes. The induced

stress was recorded in time. Relaxation at $-10\text{ }^{\circ}\text{C}$, $0\text{ }^{\circ}\text{C}$ and $10\text{ }^{\circ}\text{C}$ was measured. Figure 5-43 shows the relaxation curves of the weatherometer aged binders at $-10\text{ }^{\circ}\text{C}$, $0\text{ }^{\circ}\text{C}$ and $10\text{ }^{\circ}\text{C}$. Applying the same strain at lower temperatures implies that a higher stress is generated in the binder.

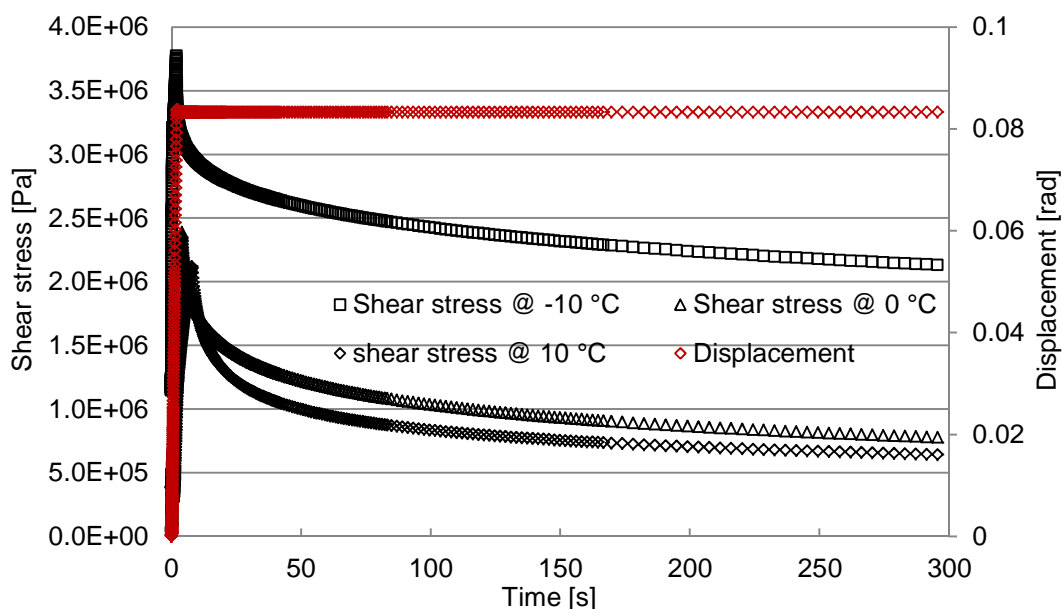


Figure 5-43 Relaxation curve of weatherometer aged A3-UV binders at -10 , 0 and $10\text{ }^{\circ}\text{C}$

Table 5-19 presents the relaxation behavior of A3-UV binders at lower temperatures. At $-10\text{ }^{\circ}\text{C}$, the relaxation percentage of the original binder is 55.5%, while for the weatherometer aged binder it is 47.6%. By neglecting the scatter in the test, it can be concluded that ageing will decrease the relaxation capacity of the binder. Weatherometer ageing will introduce a larger decrease of relaxation at lower temperatures.

Compared to the relaxation values of A3 binder that were presented in Figure 5-32, one can observe that the relaxation percentage of A3-UV is lower than that of A3 binder. This is probably because of the addition of the UV absorber. However, it may also be because different test methods were used. Nevertheless, the virgin and aged A3-UV binders show approximately 50% relaxation at $-10\text{ }^{\circ}\text{C}$. This value is much better than the investigated epoxy resin, A1 and A2 binders.

Table 5-19 Relaxation percentage at lower temperatures

Temperature	$-10\text{ }^{\circ}\text{C}$	$0\text{ }^{\circ}\text{C}$	$10\text{ }^{\circ}\text{C}$
Original binder	55.46%	52.69%	82.32%
Oven aged	49.28%	--	58.63%
Weatherometer aged	47.63%	55.71%	74.68%

5.4 Conclusions

The curing behavior, direct tensile strength and relaxation behavior of MER were investigated by means of the DTT test. Dynamic Mechanical Analysis was used to characterize the elasticity of MER. Based on the research results, the following items can be concluded with respect to MER:

1. Two-component MER needs a curing period to develop sufficient strength to be subjected to traffic loads without early failure. It can reach a DTS of 5 MPa within 1 day at a curing temperature of 14 °C. Environmental factors during application can accelerate the curing speed.
2. At high temperatures (more than 100 °C), MER behaves as a rubbery elastic material and has a stiffness value above 10 MPa while its phase angle value is close to 5 degree. So MER will behave as an elastic material at higher temperature.
3. When the temperature is below 20 °C, the frequency has only a limited influence on the binder stiffness and phase angle.
4. The tensile strength of MER is dependent on the test temperature. The applied displacement rate does not have a significant effect. The failure strain of MER is very limited and not sensitive to the temperature and displacement rate. The influence of oven ageing on the tensile strength and failure strain is not significant.
5. The relaxation of all the researched binders decreases when the temperature decreases. The original MER binder shows 39.2% relaxation at 0 °C. Aged MER has a poorer relaxation behavior.
6. Although MER has a high DTS and good high temperature resistance, its failure strain is around 10% at the three test temperatures of 0 °C, 10 °C and 20 °C. This is relatively low compared to bituminous binders.

The curing procedure and elasticity of MBE were studied via Dynamic Shear Rheometer.

7. The silicon rubber mould designed to prepare samples for DSR test is not suitable for the curing procedure of bitumen emulsion.
8. At higher temperatures like 60 °C, the MBE has a modulus of approximately 300 Pa, while its phase angle is above 60 degree. The binder has a viscous domain property and behaves like a liquid.

The curing behavior, direct tensile strength, relaxation, elasticity and ageing resistance of EMB (A1, A2, A3 and A3-UV) were first studied by testing three different 2-component EMB binders. Then one binder was selected for further evaluations.

9. The higher the curing temperature is, the faster the DTS will develop. Binder A1 has the fastest curing speed and the highest DTS, while A3 has the lowest curing speed and the smallest DTS of 9 MPa. The DTS of EMB is temperature dependent.

10. The relaxation of EMB is temperature dependent. Binder A3 has a higher relaxation value than the other two binders. At a lower temperature of 0 °C, it still has 72.5% of relaxation percentage.
11. The decreased percentage of relaxation between the original binder and the high temperature aged binder for A1, A2 and A3 is 45.79%, 46.33% and 12.03% respectively. The relaxation difference in original A3 binder and high temperature binder is the smallest. This illustrates that binder A3 has a better high temperature ageing resistance.
12. At higher temperatures like 80 °C, the complex modulus of EMB is higher than 2 MPa, while its phase angle is around 5 degree. The binder has elastic domain property at high temperature. EMB is less temperature sensitive than the residues from MBE.
13. Ageing will result in higher modulus, but A3 has the smallest changes of modulus after ageing. A3-UV has excellent ageing resistance.

These conclusions imply that the investigated MER binder needs long time for curing. The relaxation property of MER at lower temperature is much lower than EMB binders. The failure strain of MER is also very limited. The investigated MBE residue does not satisfy the high temperature resistance. So these two binders were probably not suitable enough for antiskid surfacing. The A3-UV binder has better relaxation property, nice high temperature resistance and ageing resistance. Therefore it was used for new antiskid surface design in the lab. The test results on the newly designed antiskid surface will be discussed in Chapter 6.

REFERENCES

1. Xiao, Y., et al., *Characteristics of two-component epoxy modified bitumen*. Materials and Structures, 2011. **44**(3): p. 611-622.
2. Ven, M.v.d., T. Medani, and A. Molenaar, *Open Synthetic Wearing Course*, in *83rd Annual TRB Meeting*. 2004: Washington DC, USA.
3. Muraya, P.M., *Permanent Deformation of Asphalt mixtures*, ISBN-13: 978-90-9021895-3. 2007, Delft University of Technology.
4. Cerni, G., F. Cardone, and S. Colagrande, *Low-temperature tensile behaviour of asphalt binders: Application of loading time-temperature-conditioning time superposition principle*. Construction and Building Materials, 2011. **25**(4): p. 2133-2145.
5. Petersen, J.C., et al., *Binder Characterization and Evaluation Volume 4-Test Methods (SHRP-A-370)*. 1994: Strategic Highway Research Program (SHRP), Washington, DC.
6. Wu, S., et al., *Laboratory Study on Ultraviolet Radiation Aging of Bitumen*. Journal of Materials in Civil Engineering, 2010. **22**(8): p. 767-772.

6. Tests on Newly Designed Antiskid Surfaces and Thin Surfaces

In the beginning of Chapter 3, it clearly states that the binder properties play an essential role in the performance of antiskid layers. Therefore ample attention has been given to these properties in the previous chapter.

In this Chapter, several potential alternative binders were investigated. Based on those results, a two-component Epoxy Modified Bitumen (A3-UV) was selected for the design of a new antiskid surface. The reasons for this were that compared to the other binders, the A3-UV binder has a high tensile strength, the best relaxation behavior, better high temperature ageing resistance and better UV resistance.

Slabs were produced in the laboratory on which the antiskid layer containing the A3-UV binder was applied. Details about these slabs are given in Chapter 3. Properties of the EMB-based antiskid surface were determined and the results are presented in this Chapter. Furthermore, a newly designed antiskid surface layer constructed on runways in Schiphol airport was investigated and the results are also presented in this Chapter. Tests on the slabs/cores involved texture depth measurements, pull tests and shear tests. Table 6-1 presents the requirements concluded in Chapter 4 [1].

Table 6-1 Requirements for new antiskid surfacings

	Required Values	Test conditions
Texture depth	≥ 1.3 mm	Sand patch test
Tensile adhesion strength	≥ 1.0 MPa	10 °C, 0.025 MPa/s
Shear adhesion strength	≥ 1.2 MPa	20 °C, 50 mm/min

6.1 Test results on EMB-based Antiskid

The EMB-based antiskid surface was constructed by first spraying a thin film (approximately 1.5 mm thickness) of 2-component epoxy modified bitumen binder (A3-UV) to the surface of the asphalt mixture layer. Then uniformly graded aggregates were sprinkled on top of that surface.

Before producing the asphalt slabs with the antiskid layers, a pre-investigation was conducted to determine the right application procedure to achieve a satisfactory texture depth. For this purpose five smaller tiles of size 200×200mm with antiskid layer were prepared to find the best solution. Table 6-2 presents the compositions of these experimental antiskid samples.

Table 6-2 Five types of EMB-based antiskid surfaces

Sample No.	1	2	3	4	5
Bitumen emulsion [300-400 g/m ²]		√			
Aggregate [0.8-1.7 mm]					√
Aggregate [0.3-2.4 mm]				√	
Aggregate [1-2 mm]			√		
Aggregate [1-3 mm]	√	√	√	√	√
EMB [2.5 kg/m ²]	√	√	√	√	√

Normally antiskid layers are swept (cleaned) after being placed to avoid any loose particles to be present, because these loose particles can cause FOD. As an alternative, an emulsion can be sprayed on top of the newly laid antiskid layer in order to ensure that all particles are glued together. Such an emulsion was applied on sample No. 2.

In samples No. 1 and 2 only single sized aggregates (1-3 mm) were used. In samples No. 3, No. 4 and No. 5, two fractions of mineral aggregates were used in order to achieve a better interlocking skeleton. Figure 6-1 shows the five trial antiskid surfaces. Sand patch tests were carried out on the samples and Table 6-3 presents the test results [2, 3].

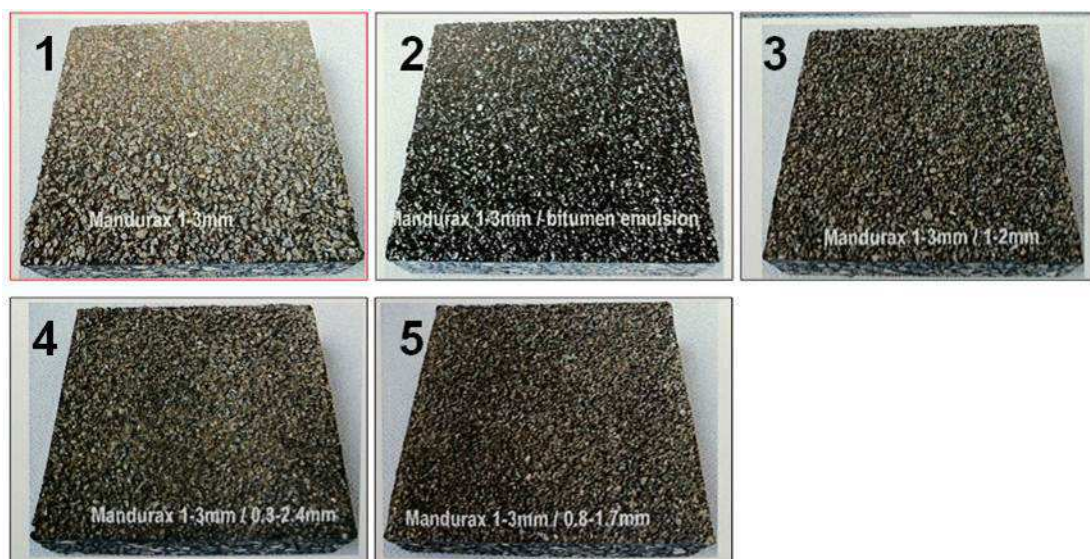


Figure 6-1 Trial on texture depth on five pieces of different antiskid surfaces

As we can see, the texture depths of samples No. 3 to 5 are much lower than the texture depth (see Table 6-1) of the tar-containing antiskid surface which was used as benchmark [1]. This means that antiskid surfaces made from a combination of coarse aggregates and fine aggregates can probably not provide enough texture depth.

Table 6-3 Results of sand patch test on trial antiskid surfaces

	Volume [ml]	Diameter [cm]					Depth [mm]
		D1	D2	D3	D4	Average D	
No. 1	25	14.2	13.9	14.1	14.2	14.10	1.60
No. 2	20	13.3	13.4	13.1	13.2	13.25	1.45
No. 3	15	14.3	14.2	14	14	14.13	0.96
No. 4	10	13.7	13.6	13.7	13.5	13.63	0.69
No. 5	10	13.5	13.2	13	13.3	13.25	0.73

The texture depths of sample No. 1 and No. 2 are both above the required values [1]. However, the application procedure used to prepare sample No. 2 implies that a thin film of bitumen emulsion is sprayed on the applied antiskid surface. The purpose of doing this is to achieve a better adhesion between the aggregates. But this thin bitumen film in combination with rubber disposal from the aircraft tires might cause clogging of the surface in the touch down area which will result in a decrease of the texture depth during the service period.

Therefore, sample No. 1 was chosen for further research. The newly designed antiskid layer was then placed on three asphalt slabs (see Figure 3-8 in Chapter 3). The details of these slabs were given in Section 3.1.3 in Chapter 3.

It should be noted that the sand patch test was performed on the slabs to determine the texture depth. After the texture depth measurements, test specimens were cored for the Pull test, Leutner shear test and CT scans.

6.1.1 Texture Depth

Figure 6-2 shows the sand patches on the slabs, and the test results are presented in Table 6-4.

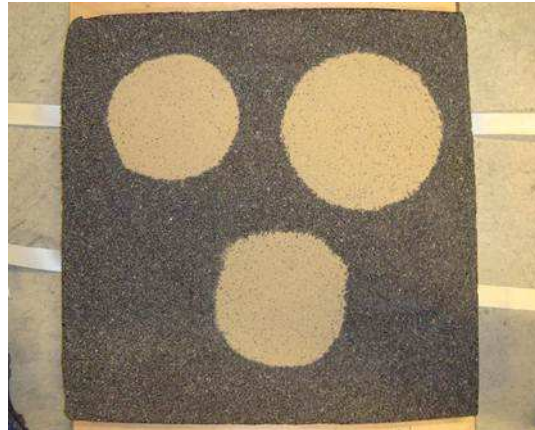


Figure 6-2 Sand patch test on EMB-based antiskid layer

Table 6-4 Sand patch test results on EMB-based antiskid layer

Volume [ml]	Diameter [mm]					Average R [mm]	Texture Depth [mm]
	D1	D2	D3	D4	D5		
50	180	183	199	187	190	93.9	1.81
50	184	191	185	189	188	93.7	1.81
80	230	228	230	227	236	115.1	1.92
80	225	220	224	221	222	111.2	2.06
80	225	221	217	224	221	110.8	2.07

The texture depth of the EMB-based antiskid surface is in the range between 1.81 mm and 2.07 mm, while its average value is 1.93 mm. This is higher than the texture depth of tar-containing antiskid layer and far above the 1.3 mm value that is required in Table 6-1 [1]. The texture depth of this antiskid surface is higher than the No. 1 trial antiskid surface in Table 6-3. This is possibly caused by the preparation procedure. The antiskid surface on the slabs was produced in the laboratory involving hand labor, instead of using an actual full size field applicator. This might have influenced the surface texture.

Although the texture depth of the EMB-based antiskid surface is higher than the required value, it is necessary to make sure that this value stays high enough during its service life. Therefore the texture depth should be checked regularly in the field. The ability of maintaining a high texture level relates to the adhesion behaviour of the antiskid surface, including the adhesion between aggregates and binder and the adhesion at the interface to the underlying layer. The adhesion at the interface is discussed in the following Sections.

The adhesion between aggregates and binder is influenced by the mineralogical composition of the aggregates (presented in Chapter 3).

6.1.2 Tensile Strength

The adhesion between the EMB-based antiskid layer and the underlying asphalt mixture layer was evaluated by means of Pull test on cores. Nine tests were conducted at three temperatures and a fixed loading speed of 0.025 MPa/s. The sample preparation and setup for the pull test are shown in Figure 3-27 [4, 5].

It should be noted however that all the failures occurred through the asphalt mixture below the interface (see Figure 6-3). This implies that the obtained tensile strength actually represents the tensile strength of the asphalt mixture, but not the tensile strength of the interface. This means that in this case the Pull test is not measuring the strength at the interface, because this is not the weakest area. Nevertheless, the test results still give indications on the tensile adhesion strength at the interface between the EMB-base antiskid layer and the underlying asphalt mixture layer.

Figure 6-4 shows typical force-displacement curves at three different test temperatures in the underlying asphalt mixture layer. Figure 6-5 shows the resulting displacement curves versus time. At 0 °C, the displacement curves are almost linear till the point of failure. At temperatures of 10 °C and lower, the asphalt mixture appears to behave brittle since sudden failure occurs.

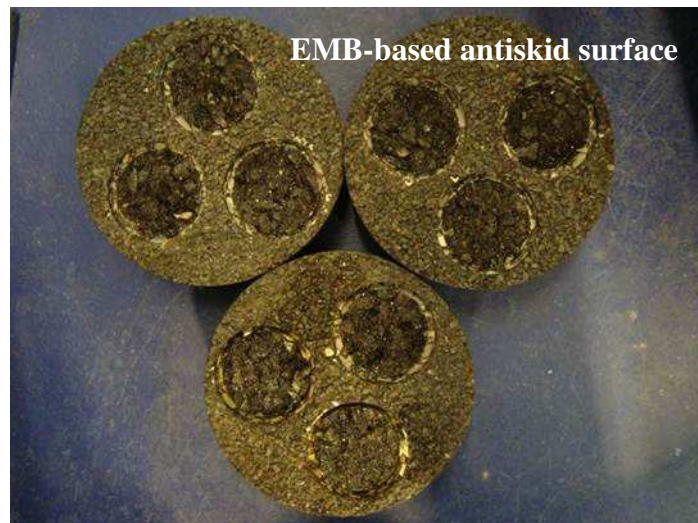


Figure 6-3 Failure in the asphalt mixture during the pull test

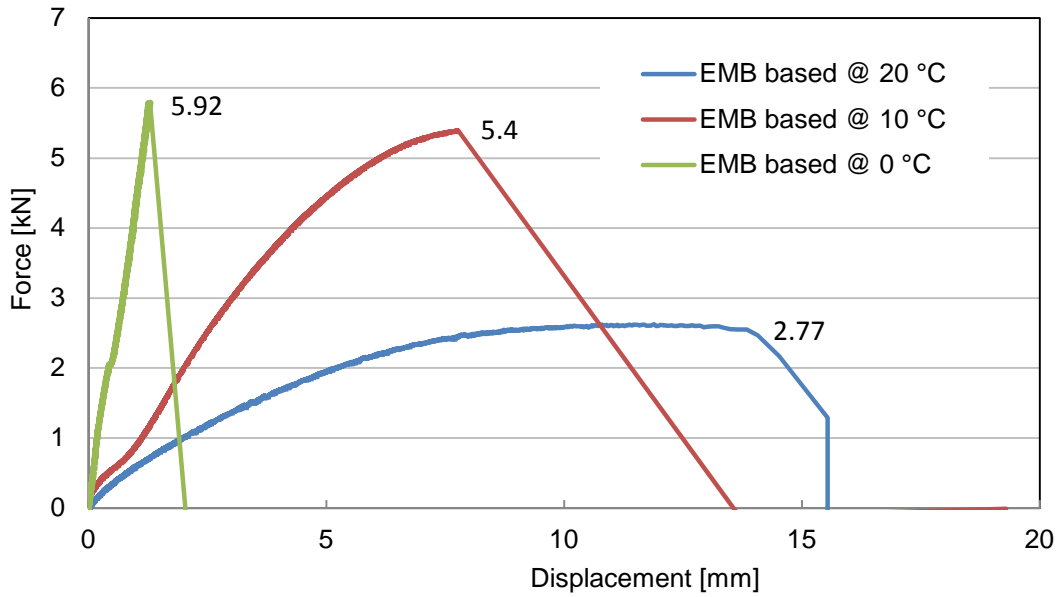


Figure 6-4 Force-displacement diagrams of the pull tests on EMB-based antiskid

The results obtained from the tensile adhesion tests are given in Table 6-5. It shows that the tensile strength of the asphalt mixture is sensitive to the test temperature. At 20 °C, it is 1.4 MPa, while at lower temperatures, the tensile strength is higher. The average value of tensile strength at 10 °C is 2.5 MPa. The failure type indicates that the tensile adhesion strength at the interface is higher than the results listed in Table 6-5 (higher than 2.5 MPa at 10 °C), and also higher than the value specified in Table 6-1 [1].

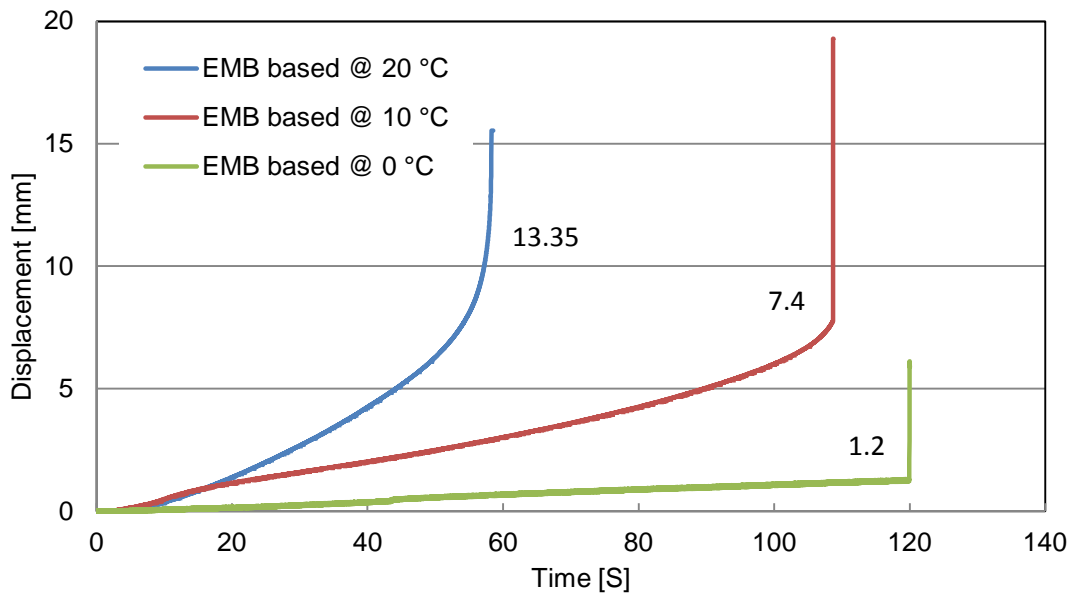


Figure 6-5 Displacement versus time during pull tests on the EMB-based antiskid

The stiffness value in Table 6-5 is defined as the failure force (maximum load) divided by the failure displacement. Tensile tests at higher temperatures resulted in lower tensile strength and higher failure displacements. Therefore the stiffness (N/m) at higher temperature is much lower than the value at lower temperatures.

Table 6-5 Tensile strength of EMB-based antiskid surfaces

T [°C]	Failure Force [kN]	Tensile strength [MPa]	Average [MPa]	Failure disp. [mm]	Stiffness [N/m]	Average [MPa]
20	2.77	1.41	1.40	13.35	2.08×10^5	2.37×10^5
	2.96	1.51		8.62	3.44×10^5	
	2.52	1.28		15.9	1.58×10^5	
10	4.4	2.24	2.50	4.3	1.02×10^6	8.77×10^5
	5.4	2.75		7.4	7.3×10^5	
0	4.46	2.27	2.51	1.4	3.18×10^6	3.63×10^6
	4.42	2.25		1.6	2.76×10^6	
	5.92	3.02		1.2	4.93×10^6	

6.1.3 Shear Strength

The shear strength through the interface between the antiskid surface layer and the asphalt mixture layer underneath was investigated by means of the Leutner shear test. The sample preparation and test setup are introduced in Figure 3-33.

The tests were performed at 0 °C, 10 °C and 20 °C, using a displacement rate of 50 mm/min. Figure 6-6 shows typical examples of the displacement-force curves obtained from these shear tests. Furthermore the “zero displacements corrections” are shown which were needed to calculate the failure displacement (at maximum load). At a lower temperature like 0 °C, the resulting force developed very fast and hence the specimen failed in a sudden and brittle way. At higher temperatures like 10 °C and 20 °C, the displacement-load curves indicated a much more ductile behavior.

Table 6-6 presents the test results. The shear strength through the interface is dependent on the test temperature. The shear strength increases when the test temperature decreases. The higher the test temperature is, the larger the displacement at failure will be. The average shear strength at 20 °C is 3.37 MPa, which is much higher than the required value mentioned in Table 6-1 [1]. The stiffness is also dependent on the test temperatures. The lower the test temperature is, the higher the stiffness is.

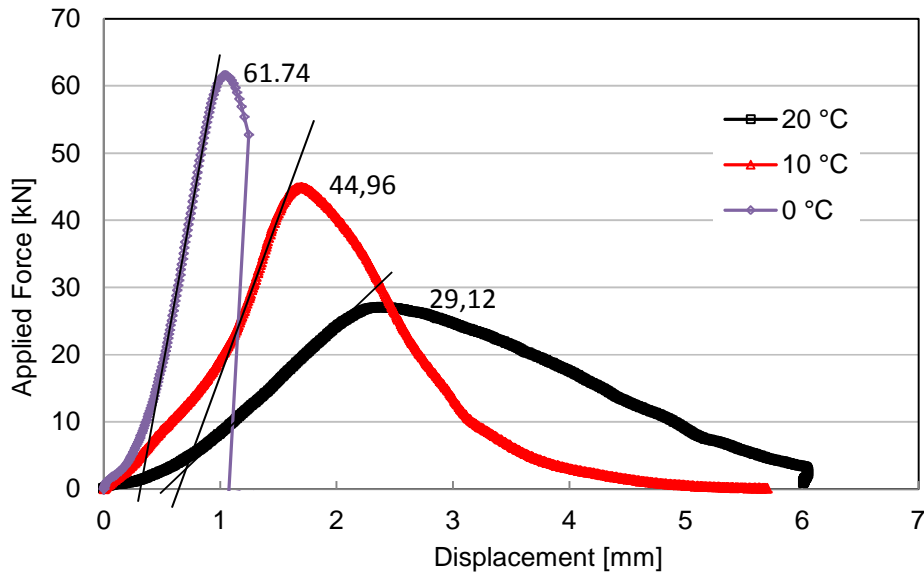


Figure 6-6 Loading curves obtained for the EMB-based antiskid surfaces by means of the Leutner shear test at three temperatures

Table 6-6 Shear results of the EMB-based antiskid surface

T	Failure Force [kN]	Shear strength [MPa]	Average	Failure Disp. [mm]	Stiffness [N/m]
20 °C	27.07	3.45	3.37 MPa	2.08	1.3×10^7
	23.29	2.97		1.59	1.46×10^7
	29.12	3.71		0.91	3.2×10^7
10 °C	47.40	6.04	5.96 MPa	1.08	4.39×10^7
	44.96	5.72		1.5	3×10^7
	47.98	6.11		0.77	6.23×10^7
0 °C	49.78	6.34	6.97 MPa	0.45	1.11×10^8
	52.79	6.72		0.45	1.17×10^8
	61.74	7.86		0.74	8.34×10^7

6.2 Test Results on Schiphol Antiskid

Cylindrical cores of 150 mm diameter with a Modified Bitumen based antiskid surface on top were obtained from Schiphol airport (Figure 3-9 shows the picture of samples). This new Schiphol antiskid layer is a non-tar-containing antiskid surface layer that was applied on Schiphol runways. It is an alternative product designed by Possehl, the company that constructed the tar-containing antiskid surfaces, with a patent protected binder also designed by Possehl. Sand patch tests, Pull tests and Leutner shear tests were conducted on these specimens.

6.2.1 Texture Depth

Also in this case, the sand patch test was used to determine the texture depth of the modified bitumen based antiskid surface [2, 3]. The sand patch tests

had to be performed on cores with the same method described in Section 4.1.3. Because of the fact that the 150 mm sample diameter was limiting the area, 25 ml of sand was used. Figure 6-7 shows the circles after spreading the sand on the cores. The test results are presented in Table 6-7.



Figure 6-7 Spreading of the sand on the 150 mm diameter cores

Table 6-7 Sand patch test results of the Schiphol antiskid surface

Volume [ml]	Diameter [cm]				Average D [cm]	Texture Depth [mm]	Average Texture Depth [mm]
	D1	D2	D3	D4			
25	13.6	13.8	14	13.8	13.80	1,67	1.86
25	12.7	12.9	13.1	13	12.93	1,91	
25	12.6	12.7	12.5	12.5	12.58	2,01	

The texture depth of the Schiphol antiskid layer varied between 1.67 mm and 2.01 mm, while its average value is 1.86 mm. This means that the texture depth fulfills the requirement of 1.3 mm mentioned in Table 6-1 [2].

6.2.2 Tensile Strength

Also the Pull test was used to determine the adhesive tensile strength of the Schiphol antiskid layer on the cores. Nine tests were conducted at three temperatures and one loading speed. The sample preparation and setup for the pull test are shown in Figure 3-27 [4, 5].

Most of the failures (see Figure 6-8 and Table 6-8) occurred in the asphalt mixture below the interface. Only two tests at 0 °C failed at the interface, the failure of all the other tests occurred in the underlying asphalt mixture. This means that the obtained tensile strength actually represents the tensile strength of the asphalt mixture, instead of the interface. The tensile strength at the interface is higher than the values obtained from the pull test.



Figure 6-8 Failure in the asphalt mixture and at the interface

Table 6-8 Failure mode during the pull test on Schiphol antiskid specimens

Temperature [°C]	Failure Mode
20	In asphalt mixture
	In asphalt mixture
	In asphalt mixture
10	In asphalt mixture
	In asphalt mixture
0	At interface (2.61 MPa)
	At interface (2.63 MPa)
	In asphalt mixture

Figure 6-9 shows the force-displacement curves and Figure 6-10 shows the resulting displacement curves versus time obtained on the Schiphol antiskid specimens. At higher temperatures like 20 °C, the displacement is increasing smoothly indicating a ductile behavior. At lower temperatures like 0 °C and 10 °C, the displacement curves are almost linear till the point of sudden failure. This indicates brittle failure at temperatures below 10°C.

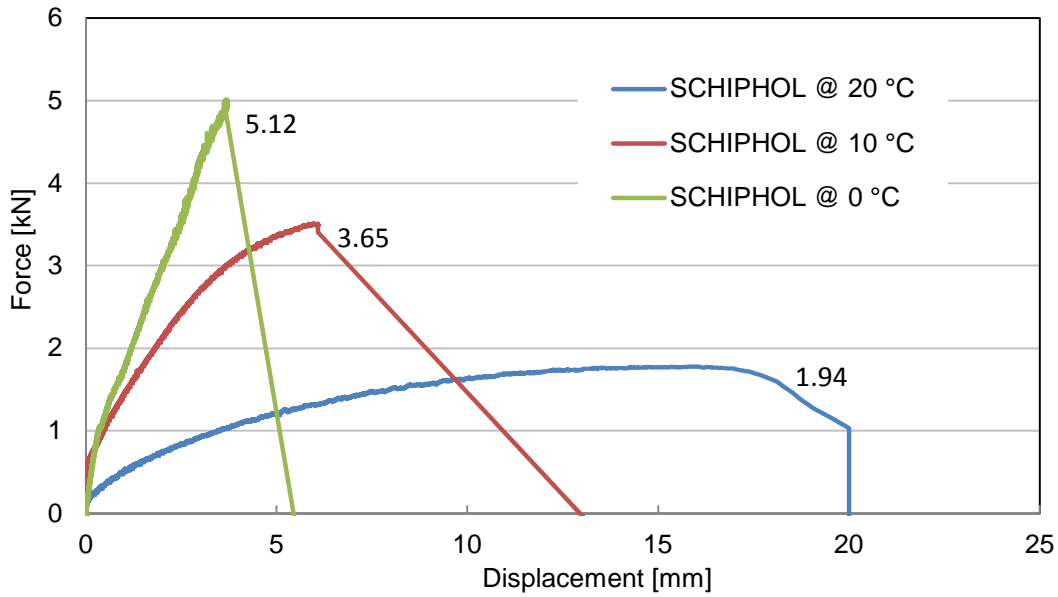


Figure 6-9 Force-displacement curves during pull tests on Schiphol antiskid layer

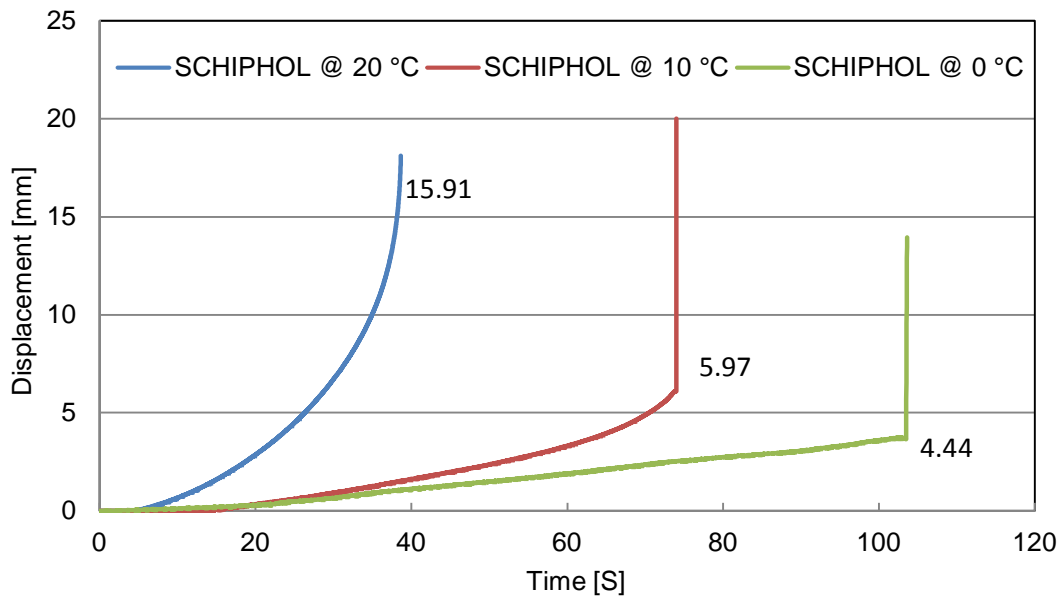


Figure 6-10 Displacement curves during pull tests on Schiphol antiskid layer

Table 6-9 presents the results. The data with gray background represent the two tests where failure occurred at the interface. The tensile strength of the asphalt mixture from Schiphol antiskid specimens is more sensitive to temperature than the asphalt mixture underneath the EMB-based antiskid specimens. The tensile strength increased substantially when the test temperature decreased from 20 °C to 10 °C and from 10 °C to 0 °C.

Table 6-9 Direct tensile strength from pull test on Schiphol antiskid layer

Temperature	20 °C			10 °C		0 °C		
Failure Force [kN]	1.88	1.94	2.01	3.65	4.07	5.16	5.12	5.4
Tensile strength [MPa]	0.96	0.99	1.03	1.86	2.07	2.63	2.61	2.75
Average [MPa]	0.99			1.97		2.62		2.75
Failure displacement [mm]	10.37	15.91	13.39	5.97	9.19	3.69	2.66	4.44
Stiffness [N/m]	1.51×10^5			5.27×10^5		1.66×10^6		1.22×10^5

The average tensile strength of the underlying asphalt mixture layer of Schiphol antiskid specimens at 10 °C is 1.97 MPa. The tensile strength at the interface is therefore higher than 1.97 MPa. Hence it is also much higher than obtained on the tar-containing antiskid layers and satisfies the required value of 1 MPa mentioned in Table 6-1 [2]. The stiffness at the interface of the Schiphol specimens was lower than the value obtained on the EMB-based specimens.

Furthermore, it shows that the interface is less sensitive to the temperature than the underlying asphalt mixture, because all of the three tests at 20 °C failed in the asphalt mixture, which means that the asphalt mixture is the weakest at that temperature. However at 0 °C, two tests out of three failed at the interface, which indicates that the interface is the weakest area at this lower temperature. So at 0 °C the interface strength should be close to 2.62 MPa. The tensile strength of the interface at 20 °C is probably much higher than 0.99 MPa and in the same range as 2.62 MPa at 0 °C.

6.2.3 Shear Strength

Again the Leutner test was used to evaluate the shear strength through the interface between the Schiphol antiskid surface layer and the underlying asphalt mixture layer. The tests were performed at 0 °C, 10 °C and 20 °C, with a displacement rate of 50 mm/min [4, 5].

Figure 6-11 shows typical displacement-force curves for the Schiphol antiskid layers. At lower temperatures like 0 °C, the load increases fast and the failure mode is quite brittle, with a sharp declining softening phase. At higher temperatures like 10 °C and 20 °C, a large softening phase can be observed after the maximum load.

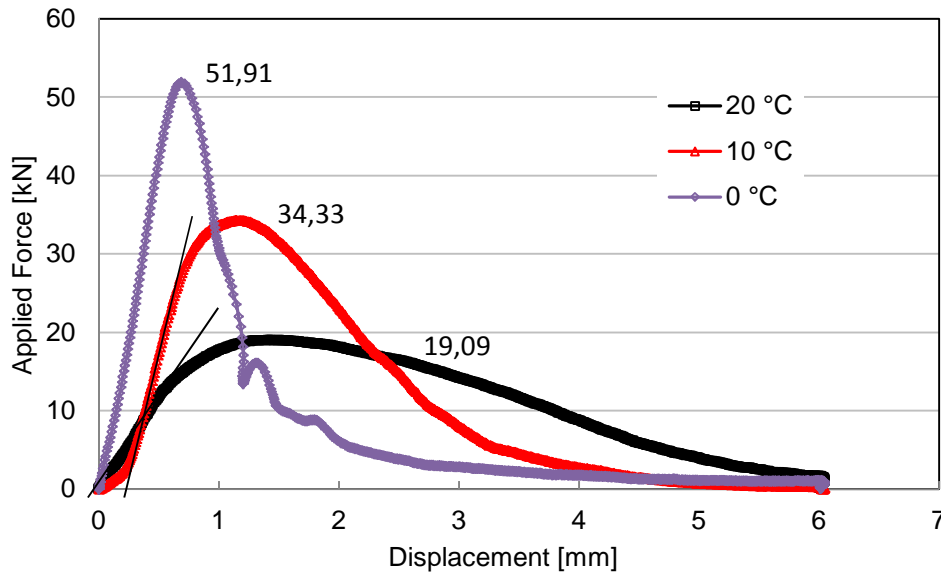


Figure 6-11 Applied curves at three test temperatures of the Schiphol antiskid

Table 6-10 presents the test results. The shear strength of the Schiphol antiskid is lower than the strength of the EMB-base antiskid at the same test temperatures. But the shear stiffness is very similar to the value of EMB-base antiskid. The average shear strength at 20 °C is 2.49 MPa, which satisfies the required value of 1 MPa mentioned in Table 6-1 [2].

Table 6-10 Shear test results of the Schiphol antiskid specimens

T	Failure Force [kN]	Shear strength [MPa]	Average	Failure Disp. [mm]	Stiffness [N/m]
20 °C	22.70	2.89	2.49 MPa	1.22	1.86×10^7
	19.09	2.43		1.44	1.33×10^7
	16.87	2.15		1.41	1.2×10^7
10 °C	37.91	4.83	4.60 MPa	0.75	5.05×10^7
	34.33	4.37		1.14	3.01×10^7
0 °C	52.32	6.66	6.64 MPa	0.45	1.16×10^8
	51.91	6.61		0.69	7.52×10^7

6.3 Failure Energy

Failure energy is the energy that is needed to get failure. It is a useful indicator of the performance of asphalt mixtures. However, during the Leutner shear test in this research, the testing area was the interface. It is hard to define a thickness for this testing interface. This means that the strain value cannot be calculated.

The load-displacement curve (see Figure 6-12) was used to define the failure energy. The area under the displacement-force curve from the corrected start point to 4 mm displacement was calculated as the failure energy during the

shear test in this research. The area under the displacement-force curve from the corrected start point to the failure point can be also defined as the failure energy. However, in this research most of the displacement-force curves have a remarkable softening phase before the failure occurs. Considering the curves presented in Figure 6-13, point at 4 mm of displacement was used to include the softer phase stage in the failure energy. The failure energy defined by a stress-strain curve is independent of the specimen size, while failure energy defined by a load-displacement curve is dependent on specimen dimensions. The calculated values obtained from tests can only be used for direct comparison when the test specimens have the same dimensions.

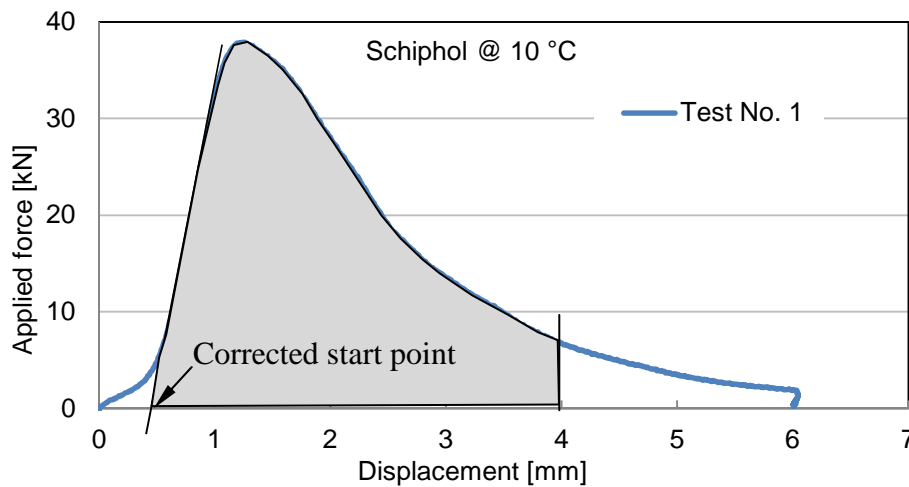


Figure 6-12 Example of the failure energy calculated from the Leutner Shear test

Table 6-11 presents the failure energy calculated from the Leutner shear tests. Figure 6-13 compares the displacement-force curves. The blue line and red line at 0 °C of EMB based antiskid show the displacement decreased a little bit at the end of the tests. This might be caused by the displacement sensors punched back when the failed specimen fell down. The results show a very large variation at the same test temperature. At low temperatures, the interface will fail with a very short failure propagation stage.

Table 6-11 Failure energy [N·m] of interfaces during shear tests

Temperature		20 °C			10 °C			0 °C		
EMB antiskid	Failure energy	66.4	52.2	57.3	85.2	78.6	55.9	41.5	55.4	113.9
	Average	58.6			73.2			70.3		
Schiphol antiskid	Failure energy	60.5	57.1	48.9	73.2	67.1	97.7	52.6		
	Average	55.5			70.2			75.2		

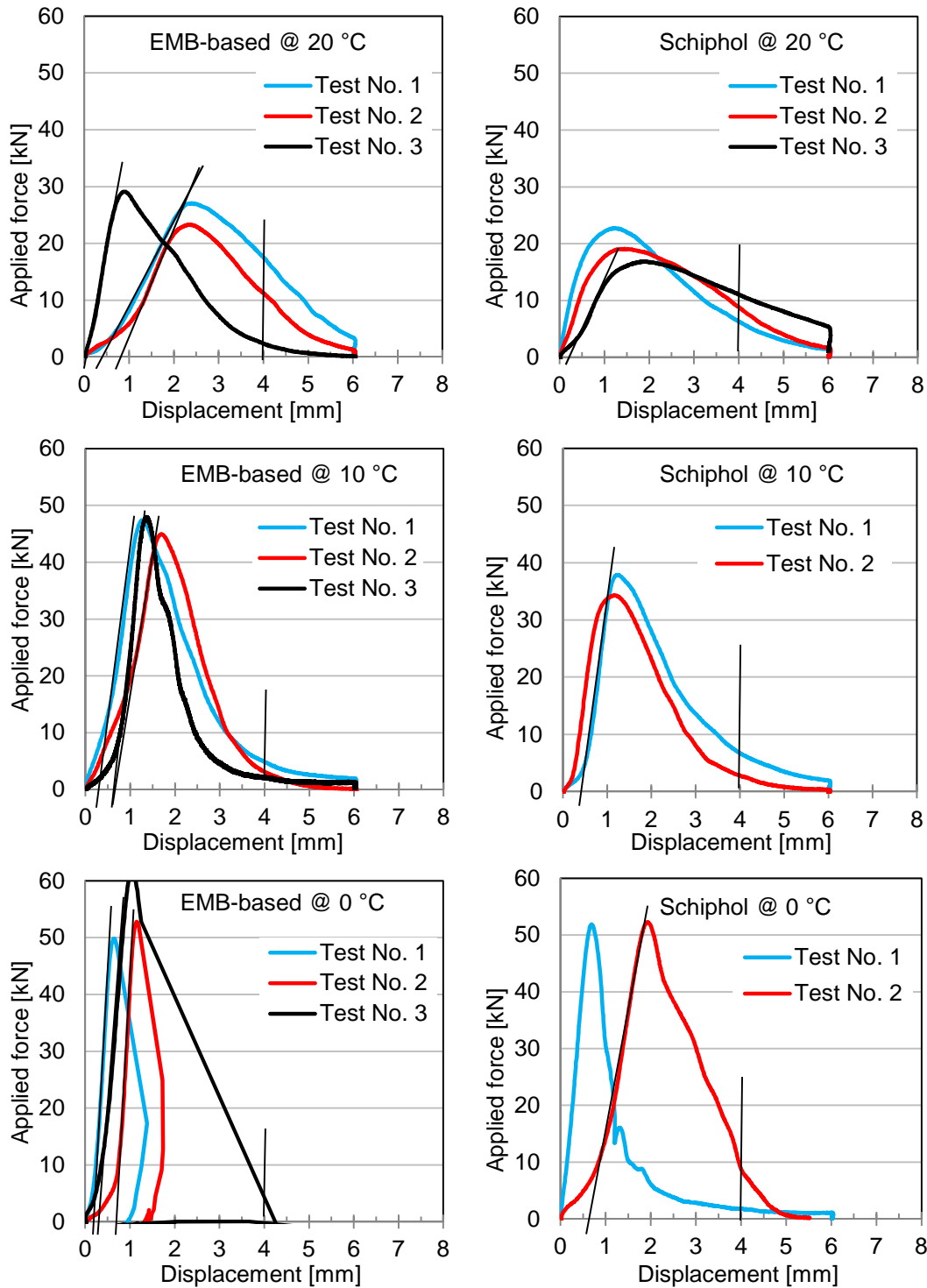


Figure 6-13 Force-displacement curves in shear test on antiskid layers

6.4 Thin Surface Layer

The adhesion properties at the interface between a Noise Reducing Thin Surface Layer (NRTSL) and underlying asphalt mixture layer were also investigated. NRTSL have a fairly high void content and are therefore vulnerable to high stresses induced by traffic and the environment. However, the adhesion

of a NRTSL to the layer below is also importance. If this adhesion is too low, pothole formation is likely to occur. Basic information about the two TSLs investigated in this research is given in Section 3.1.4, Chapter 3.

6.4.1 Tensile Strength

Six Pull Tests were performed at 20 °C and 4 tests at 10 °C. Just three out of these ten tests failed at the interface. All the other failures could be observed in the NRTSL (see Figure 6-14 and Table 6-12). Therefore, tensile tests at 0 °C were not done anymore.

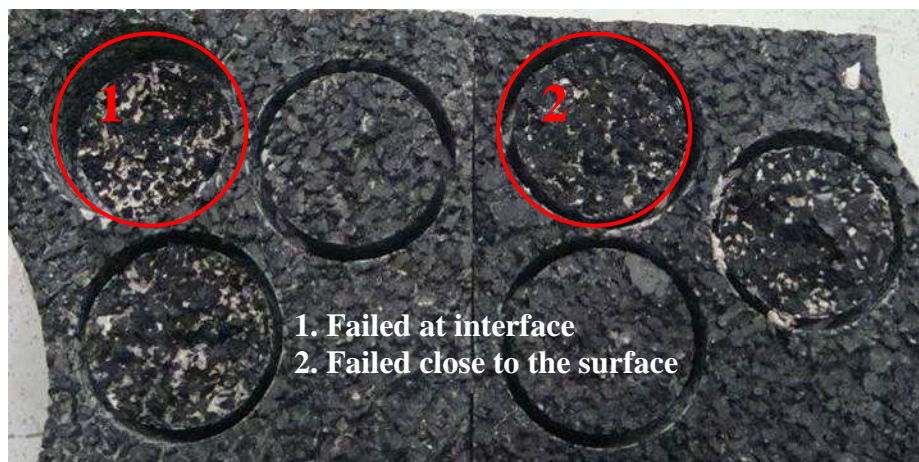


Figure 6-14 Failures in pull tests on NRTSLs

Table 6-12 Failure mode during the pull test on NRTSLs

NRTSLs	Temperature	Failure Mode	Failure Strength [MPa]
TSL-1	20 [°C]	In NRTSL mixture, close to surface	0.58
		At interface	0.66
		At interface	0.58
	10 [°C]	In NRTSL mixture, close to surface	--
		In NRTSL mixture, close to surface	--
		At interface	--
TSL-R	20 [°C]	In NRTSL mixture, close to surface	0.8
		In NRTSL mixture, close to surface	0.77
		In NRTSL mixture, close to surface	0.74

The effect of the high void content of the TNRSLS is reflected in the pull strength of the specimens. This becomes obvious when the values obtained for the TNRSLS (0.58 – 0.8 MPa at 20 °C) are compared with those obtained for the asphalt layer underneath the EMB antiskid (1.4 MPa at 20 °C, Table 6-5) and the asphalt layer underneath the Schiphol antiskid (0.99 MPa at 20 °C, Table 6-9).

6.4.2 Shear Strength

The Leutner shear test was used to determine the shear strength through the interface between the NRTSLs and the underlying asphalt mixture layer. The thickness of NRTSLs is approximately 30 mm. Therefore it was not necessary to use the steel caps to lengthen the specimens as was done for the shear tests on the antiskid surfaces. The standard Leutner shear test can be performed on these specimens. Figure 6-15 shows the NRTSL specimens after the Leutner shear tests. The failure through the interface can easily be detected.



Figure 6-15 NRTSL specimens after Leutner shear test

The tests were performed at 0 °C, 10 °C and 20 °C, with a displacement rate of 50 mm/min. Table 6-13 presents the test results. Figure 6-16 presents the displacement-force curves. From the results it can be concluded that:

- The shear strength is sensitive to the test temperature. At lower temperatures a higher shear strength is found.
- At the same test conditions, the NRTSL-R specimens had slightly lower shear strength than NRTSL-1.
- The stiffness at the interface is much lower when the test temperature is higher.
- Furthermore, the shear strength between the NRTSL and underlying layer is much lower than the shear strength between the antiskid surface layer (EMB-based antiskid and Schiphol antiskid) and underlying asphalt mixture layer.
- Table 4-14 presents the shear strength at 20 °C through the interface between asphalt mixture layers, which is between 1 and 1.12 MPa. The shear strength through the interface between the investigated NRTSLs and underlying asphalt mixture layer is higher than the shear strength between traditional asphalt mixture layers.

Table 6-13 Shear test results of NRTSL specimens

Temp.	NRTSLs	Failure force [kN]	Strength [MPa]	Average [MPa]	Displacement [mm]	Stiffness [N/m]
20 °C	NRTSL-1	13.45	1.71	1.64	1.73	7.77×10^6
		12.25	1.56		1.24	9.88×10^6
	NRTSL-R	10.33	1.32	1.46	1.60	6.46×10^6
		12.20	1.55		1.34	9.1×10^6
		11.93	1.52		1.39	8.58×10^6
10 °C	NRTSL-1	17.85	2.27	2.66	0.88	2.03×10^7
		25.03	3.19		0.93	2.69×10^7
		19.83	2.52		0.83	2.34×10^7
	NRTSL-R	22.00	2.80	2.65	1.13	1.95×10^7
		23.20	2.95		1.03	2.25×10^7
		17.29	2.20		0.83	2.08×10^7
0 °C	NRTSL-1	31.83	4.05	4.04	0.84	3.79×10^7
		30.31	3.86		1.14	2.66×10^7
		33.13	4.22		0.57	5.81×10^7
	NRTSL-R	32.64	4.16	3.72	0.62	5.27×10^7
		30.62	3.90		1.01	3.03×10^7
		24.31	3.10		0.79	3.08×10^7

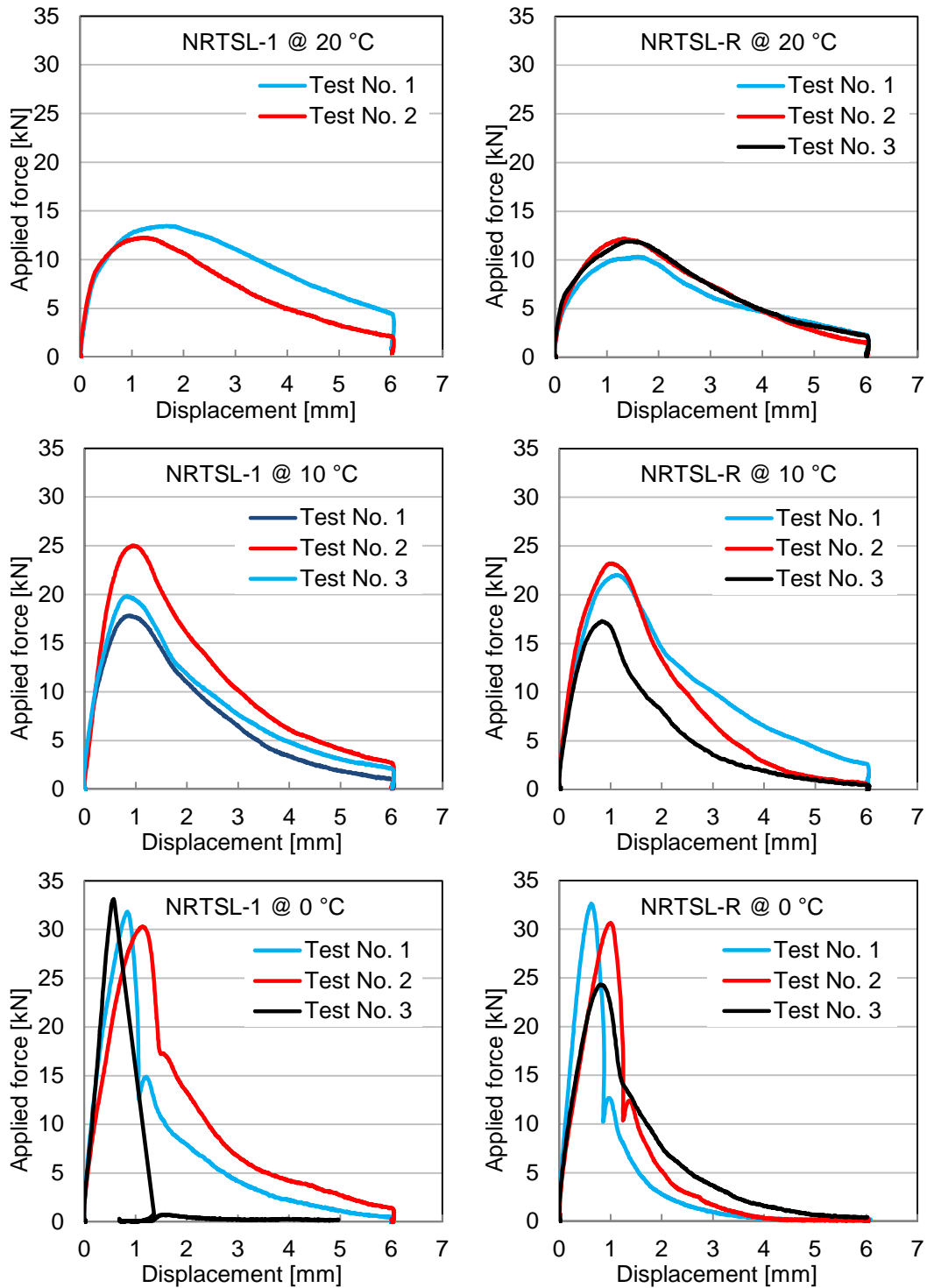


Figure 6-16 Force-displacement curves in Leutner shear test on NRTSLs

6.5 CT Scan Results

Nano CT scans were conducted on 40 mm diameter cores because of two reasons. On the one hand, cross section images were needed to develop the FEMs, which will be discussed in Chapter 7. On the other hand, the volumetric characteristics can be investigated by means of Nano CT scan. Table 6-14

presents the volume contents of air voids, binder and aggregates in EMB-based antiskid layer and Schiphol antiskid layer.

One specimen with 40 mm diameter was scanned for both antiskid layers. The two newly designed antiskid layers have a quite similar aggregate volume content, although it is sure that they have totally different structures because they were designed by two companies. The Schiphol antiskid sample shows a higher void content and lower mortar content (consisting of bitumen, filler and fine sand).

Table 3-6 in Chapter 3 present basic information for the thin surface layers. The table shows that the void contents of TSL-R and TSL-1 are 12% and 18% by volume, respectively. The results from CT scan in Table 6-14 confirm these void contents. But the mortar content and aggregate content reported in Table 6-14 differ a lot from what was reported in Table 3-6. Firstly, these differences show that there is quite some variation in the mixture composition. Secondly, the mortar content presented in Table 6-14 includes the binder, filler and fine sand. It is therefore higher than the binder content that was presented in Table 3-6.

Table 6-14 Volumetric characteristics of antiskid layers and TSLs

Volume percentage [%]		Void content	mortar content	Aggregate content
Antiskid layers	EMB-based	9.5	38.7	51.8
	Schiphol	17.1	30.8	52.1
TSLs	TSL-R	12	32	56
	TSL-1	15	26.6	58.4

Figure 6-17 shows the scan images of the Schiphol antiskid (left) and the EMB-based antiskid (right). The grey value of the aggregates in EMB-based antiskid layer is relatively higher (lighter) than the aggregates used in Schiphol antiskid. This means that the density of the aggregate used in this antiskid layer is quite high. Figure 3-10 in Chapter 3 shows that the aggregates used in the EMB-based antiskid layer is composed of Corundum (Al_2O_3), Hematite (Fe_2O_3) and Quartz (SiO_2).

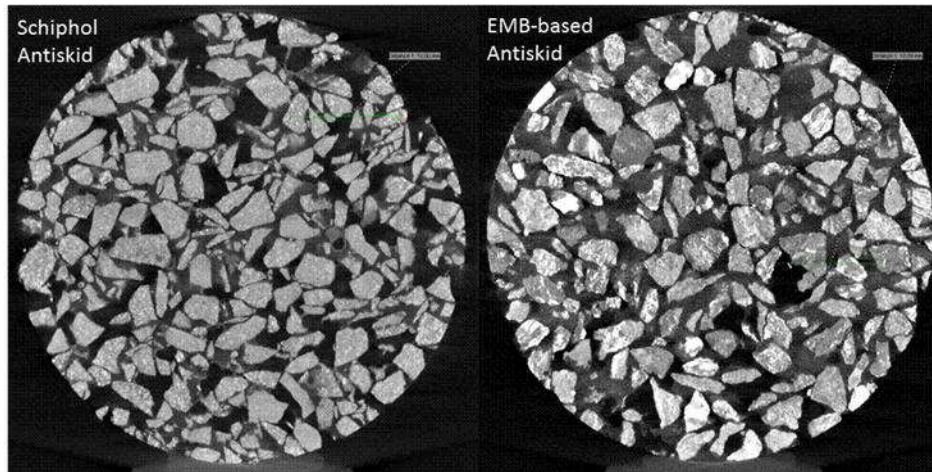


Figure 6-17 Front views of Schiphol antiskid (left) and ICOPAL antiskid (right)

6.6 Conclusions

The surface texture and interface adhesion properties of two newly designed antiskid layers were investigated in this chapter. The EMB-based antiskid layer was designed by using the binder that was selected in Chapter 5. The Schiphol antiskid layer specimens were collected from Schiphol airport. Based on the research results, the following conclusions may be drawn:

1. The texture depths of newly designed EMB-based and Schiphol antiskid layers are 1.93 mm and 1.86 mm respectively. Both are far above the 1.3 mm value which is used as benchmark.
2. All of the EMB-based specimens, and six out of eight of the Schiphol specimens failed in the underlying asphalt mixture during the pull test. These results indicate that the tensile strength at the interface is higher than the reported values.
3. From the test results, it is obvious that the tensile strength at the interface of EMB-based specimens and Schiphol specimens satisfies the requirement from the benchmark.
4. The average shear strength through the interface at 20 °C of the EMB-based and Schiphol antiskid layer are 3.37 MPa and 2.49 MPa respectively. Both values satisfy the requirement in the benchmark.
5. The shear tests illustrated that the epoxy modified bitumen can provide a better adhesion than the polymer modified bitumen which was used in the Schiphol antiskid layer.

The pull test and Leutner shear test were also used on NRTSLs to characterize the thin surface layers.

6. Three out of ten tests failed at the interface during the pull test.
7. The shear strength between the NRTSL and underlying layer is much lower than the shear strength between the antiskid surface layer (EMB-based antiskid and Schiphol antiskid) and underlying asphalt mixture layer.

REFERENCES

1. CROW, *D11-01 Specification for Runway Surface Dressings on Airfields*. 2011: the Netherlands.
2. Xiao, Y., et al., *Surface Texture of Antiskid Surface Layers Used on Runways*, in *TRB 90th Annual Meeting*. 2011: Washington DC, USA. p. 11.
3. NEN-EN, *EN 13036-1, Road and airfield surface characteristics-Test methods-Part 1: Measurement of pavement surface macro texture depth using a volumetric technique*. 2010.
4. Xiao, Y., et al. *Adhesion Properties of Tar-Containing Antiskid Surface Layers on Runways in Airfield*. in *T&DI Congress 2011: Integrated Transportation and Development for a Better Tomorrow*. 2011. USA: ASCE.
5. Xiao, Y., et al., *Assessment Protocol for Tar-containing Antiskid Layers for Runways, Report No. 7-10-185-2*. 2010, Delft University of Technology.

7. Finite Element Modeling of Surface Layers

Finite Element Models (FEMs) of antiskid surface layers were developed to analyze the effect of different binders and aggregate skeletons on the behavior of these layers. The results of these analyses are reported in this chapter. The 2D cross section images from Nano CT scans were used to develop photo FEMs of antiskid surfaces. ABAQUS was then used to run the simulations. Three antiskid structures, named Antiskid-1, Antiskid-2 and Antiskid-3, were simulated in this research. The Antiskid-1 represents the antiskid layer from Woensdrecht airport, the Antiskid-2 represents the antiskid layer applied on the slabs, and the Antiskid-3 represents the new antiskid layer applied on Schiphol. The viscoelastic properties of residues from Modified Bitumen Emulsion (MBE) and Epoxy Modified Bitumen binder (EMB) were modelled by means of Prony Series.

7.1 FEM Methodology

Basically, an antiskid layer is a complex and non-homogeneous material. It consists of aggregate, binder, air voids and adhesive zones. The properties of these different components vary significantly, from high stiff aggregates to soft binder. Furthermore, the aggregate skeleton is also important. This implies that all these factors should be taken into account in a FEM simulation.

To model such a layer as a homogeneous material is very simple, as indicated in the left graph in Figure 7-1. When the layer is considered as a composite material consisting of aggregates bound together by binder (the right graph in Figure 7-1), then modeling of this layer becomes much more complicated. Since modeling of the individual components and the skeleton is required, the size, shape and position of each aggregate particle should be taken into account.



Figure 7-1 Spatial definition of antiskid layer, homogeneous (left) and individual composites (right) [1]

Given the limitations of the available computational capacity, 2D FEM models were derived from 2D photo models. The background of this approach is described in Section 2.6, Chapter 2.

7.1.1 2D Images for FEM Model

A two-Dimensional (2D) FEM model for an antiskid layer was developed by transforming cross section images into a 2D element mesh. Figure 7-2 shows the obtained mesh in relation to the original image of the antiskid layer. The different materials are separated based on the contrast of gray values in the CT scan images. The gray value varies as the material density changes, black is air, and white is very high density like steel. Figure 7-3 shows the definition of the gray values used to separate the individual materials. The gray values between the two red lines can be changed manually to define composition of aggregates, binder and air voids.

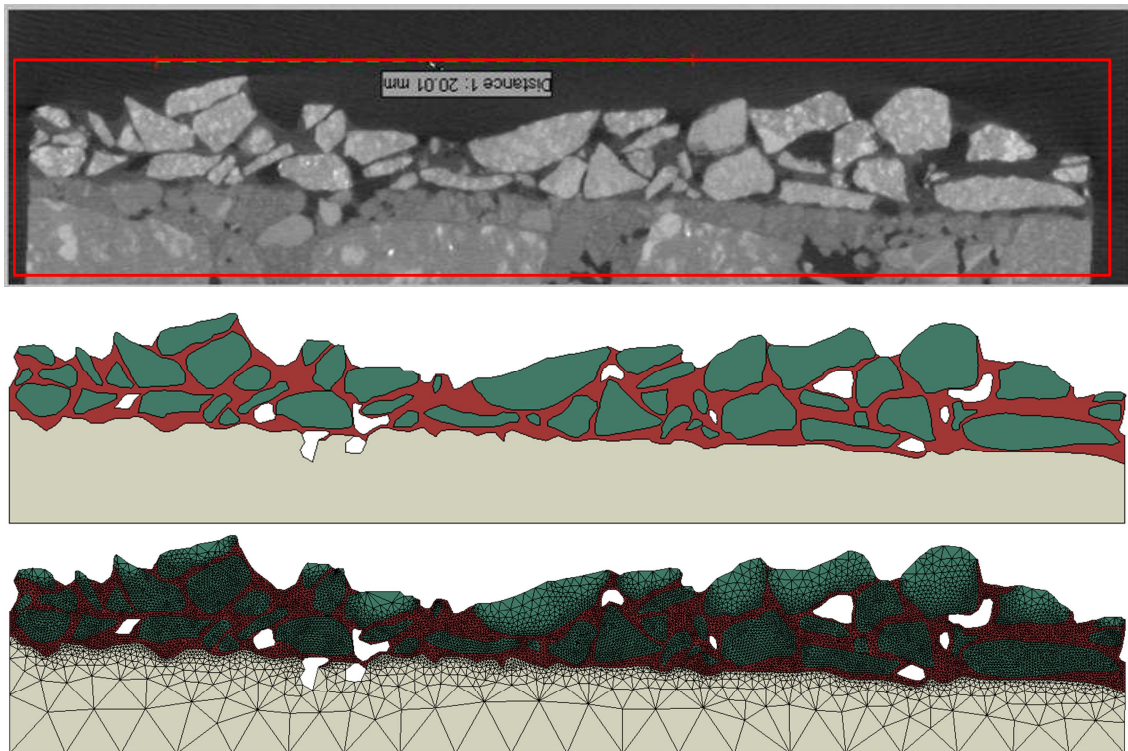


Figure 7-2 2D cross section image of Antiskid-1 layer obtained by means of CT scan (top), three phases model (middle) and finite element mesh (bottom)

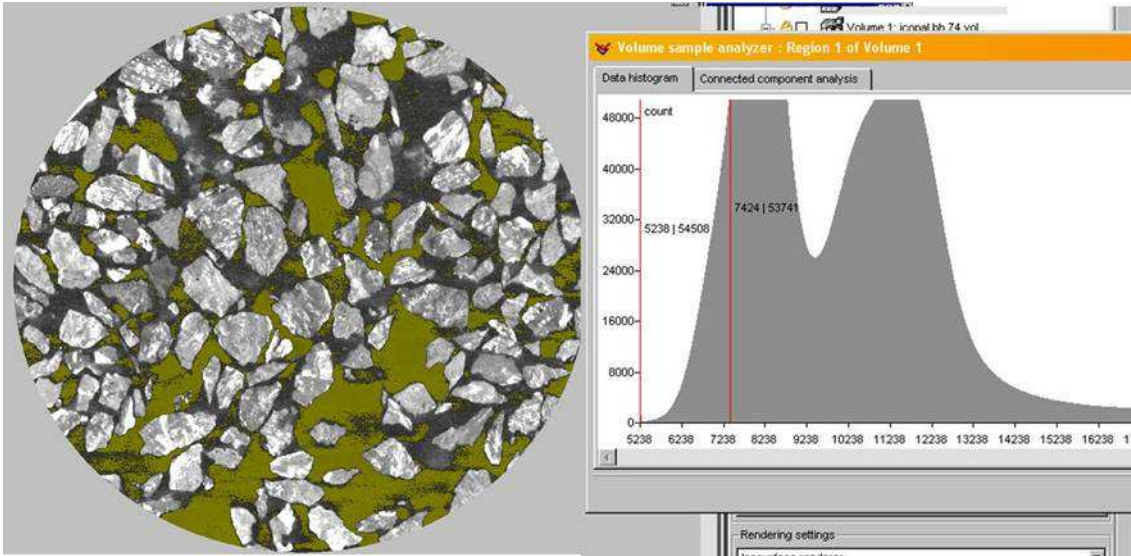


Figure 7-3 Compositions based on the contrast of gray values

Figure 7-4 shows that the choice of gray values can influence the final model. Although the first settings for aggregate particles, binder and voids, is done automatically, several unclear locations need to be corrected manually. This requires expertise and experience and is dependent on the image resolution. A higher resolution of the images will result in a better antiskid model and a more experienced person is better qualified to make the manual corrections.

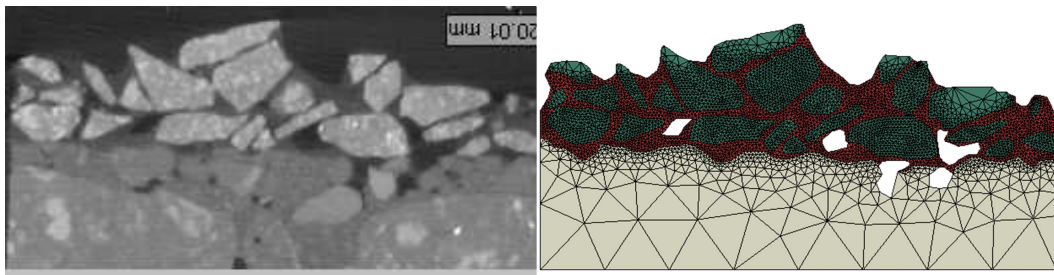


Figure 7-4 Influence of gray value judgment during the model transition

As was explained in Section 3.4.4 in Chapter 3, the resolution of a medical CT scanner, which was extensively used in previous research for analyzing big specimens, was too low to separate the aggregates and binder (see the left graph in Figure 7-5). Therefore a Nano CT scanner with a much higher resolution was used in order to clearly define the small aggregate particles. The disadvantage of the Nano scanner is that only small sized objects can be scanned. The maximum size of the specimen for the required accuracy is 40 mm and the photo models discussed in this chapter are therefore all based on 40 mm diameter specimens.

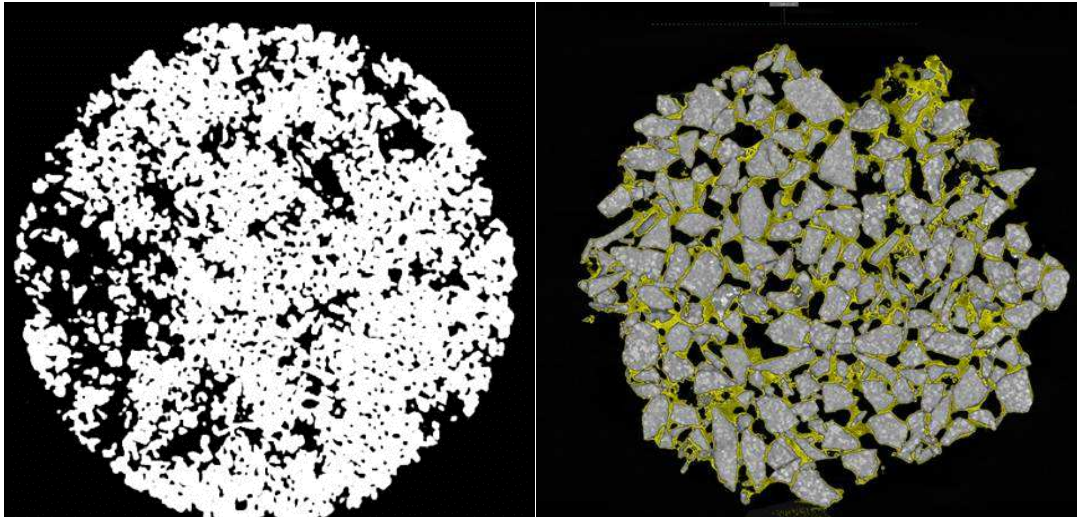


Figure 7-5 Difference between the image resolutions of the medical scanner and Nano scanner (on Eindhoven antiskid)

7.1.2 Antiskid Models

Three antiskid models were developed in this research. The Antiskid-1 model was already shown in Figure 7-2. The Antiskid-2 and Antiskid-3 models are illustrated in Figure 7-6 and Figure 7-7. A 6-node modified quadratic plane strain triangle mesh type was used. The models were fully fixed at the bottom, and fixed in x-direction (horizontal) at the two sides.

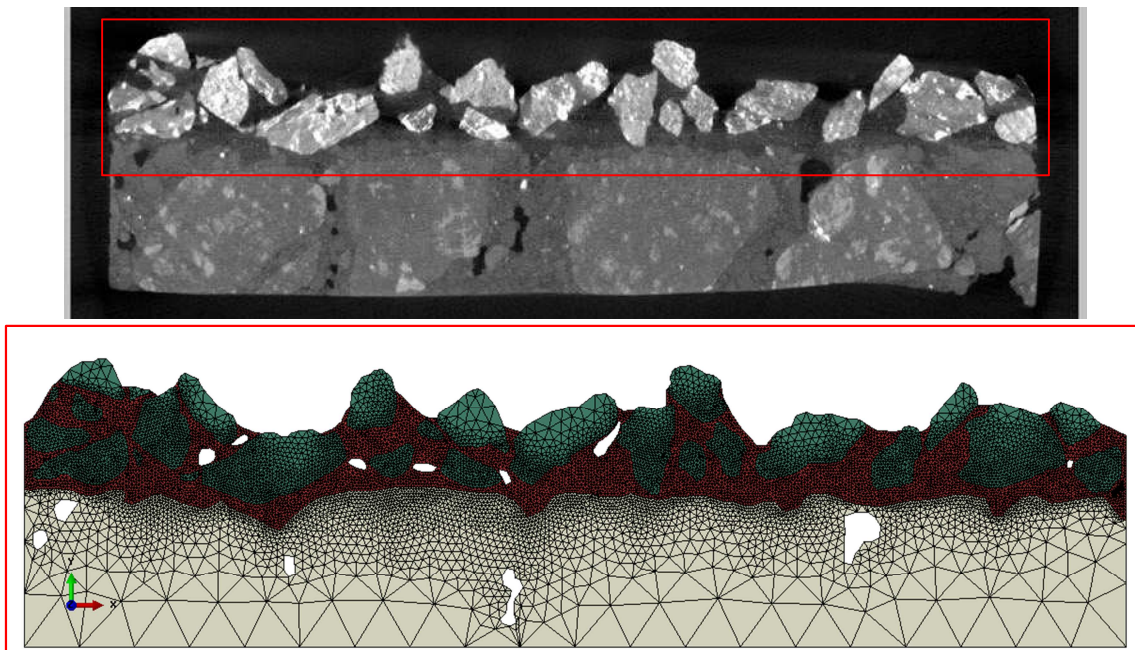


Figure 7-6 FEM structure of Antiskid-2

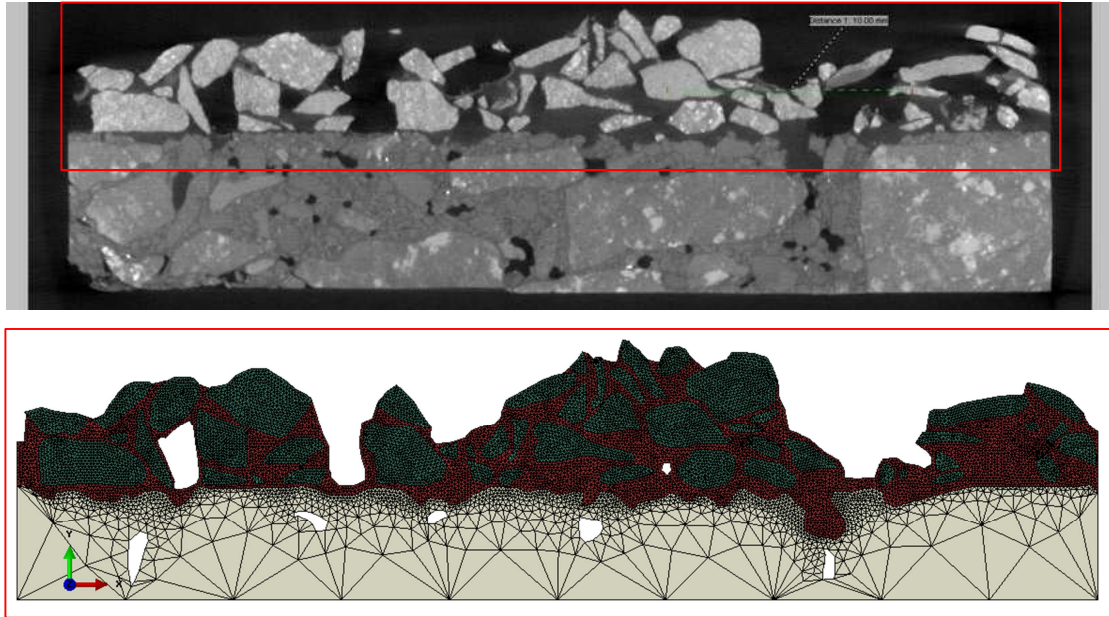


Figure 7-7 FEM structure of Antiskid-3

The described antiskid models have a length of 40 mm and are approximately 10 mm high, including the underlying asphalt mixture layer. They are too small to predict the real situation in the field. In the field, bending occurs when the tire loading is applied. This already implies that the boundary conditions used are not the same as in the field. Nevertheless, these antiskid models are believed to be good enough for comparison purposes. The behavior of different binders was investigated by models at meso-scale level. The boundary conditions and finite element types are the same in the three models.

It is interesting to note the differences between Antiskid-1 (Figure 7-2) and Antiskid-3 (Figure 7-7) on one hand and Antiskid-2 (Figure 7-6) on the other. The figures indicate that Antiskid-2 is much like a layer with a thickness of a single aggregate layer while the thicknesses of Antiskid-1 and Antiskid-3 layers seem to be composed of more than one aggregate. Antiskid-1 and Antiskid-3 are produced in the field by the same contractor while Antiskid-2 is made in the laboratory by another producer.

7.2 Loading Signals

Several basic parameters are needed for the FEM simulations, which include the wheel load, tire pressure, the speed of the aircraft, and the friction between rolling/breaking tire and antiskid surface.

Figure 7-8 shows the tire pressure trends of aircrafts. The A350-900 aircraft, which is scheduled to enter service in the second half of 2014¹, will have a tire pressure of 1.65 MPa [2, 3].

¹http://en.wikipedia.org/wiki/Airbus_A350#A350-900

As mentioned before, the friction between the aircraft tire and the pavement surface is of great importance to ensure safe take-off and landing operations. Once the friction goes below 0.40, the Federal Aviation Administration advises airports to begin advising pilots of potentially hazardous conditions. Any friction value below 0.25 is generally considered to give "poor" runway braking conditions [4]. Technically, an incoming airplane uses flaps and reverses power to slow down. The wheel brakes are normally only used at a taxi speed. Full braking occurs very rarely, only in emergency situations.

In this research, a maximum tire pressure of 1.5 MPa and a friction coefficient of 0.4 were chosen for the simulations. The speed of aircraft will decrease to a much lower speed after landing, and a speed of 75 km/h was selected for the simulations in this research.

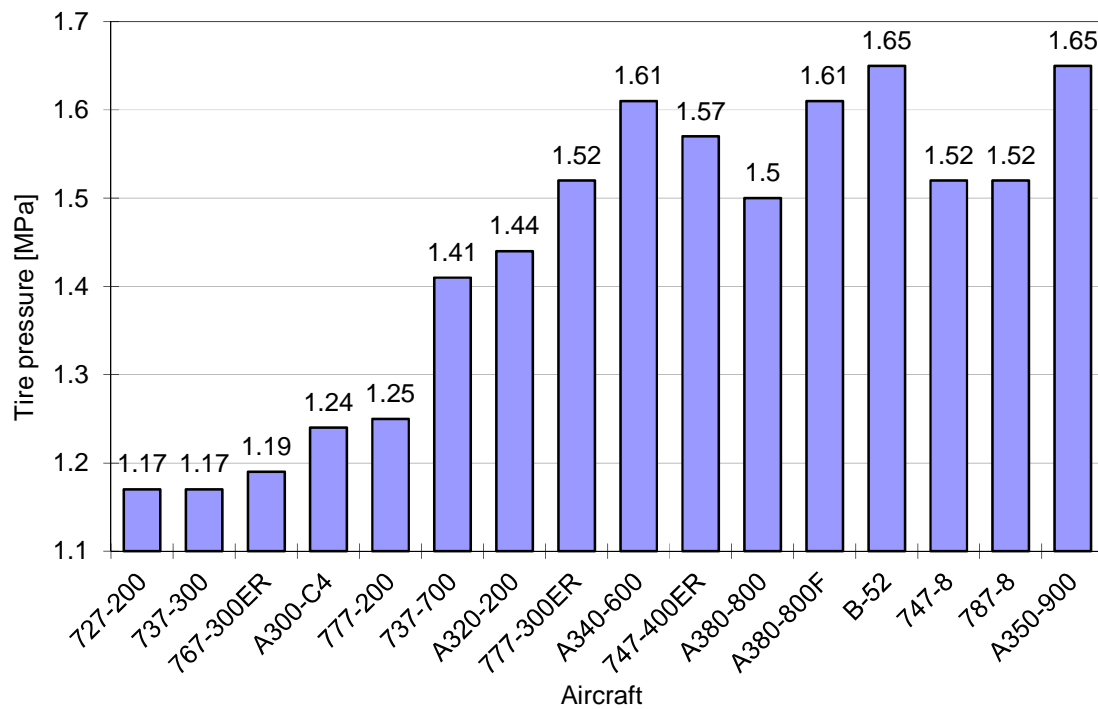


Figure 7-8 Tire pressure trends of aircrafts [3]

An aircraft tire signal as provided by the computer program TyreStress [5, 6] was used in this research. TyreStress is developed by the CSIR (the Council for Scientific and Industrial Research in South Africa) for SANRAL (the South African National Roads Agency Limited) to provide estimations of the tire contact stress distributions in the longitudinal, lateral and vertical directions across the tire contact area. The program is based on actual tire-road pavement contact stresses from slow moving tires. A tire pressure of 1.5 MPa and load of 100 kN per tire (more or less representative for B737 with higher tire pressure) were used as input to generate the loading signals. Figure 7-9 shows the distribution of the vertical and longitudinal stress under an aircraft tire.

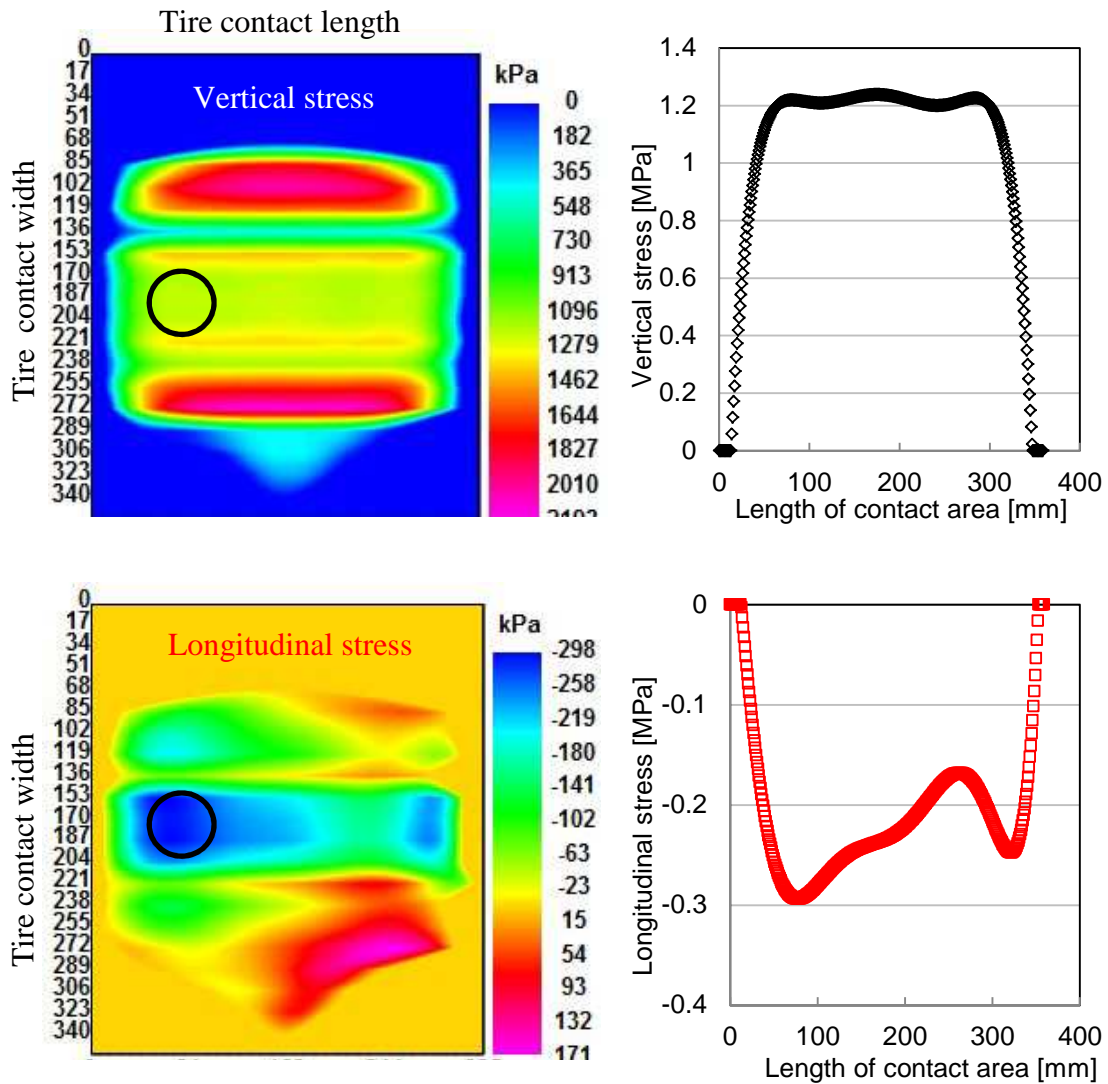


Figure 7-9 Vertical and longitudinal stresses under the aircraft tire at 100 kN and 1.5 MPa [5, 6]

Moisescu [7] investigated the distributions of longitudinal stresses in the contact area under a truck tire in case of braking and traction conditions, with a 3D tyre model. Figure 7-10 shows the results. The vertical stress distributions are quite similar in braking condition and traction condition, and also similar to the up-left figure presented in Figure 7-9. Therefore the signal of vertical stresses presented in the up-right graph in Figure 7-9, which was obtained from the location marked on the up-left figure, was used as the input vertical stress for the FEMs.

The bottom-right graph in Figure 7-9 indicates the longitudinal stress at the middle of a slow moving aircraft tire. When considering braking, this longitudinal stress distribution cannot be used as input. The two bottom pictures in Figure 7-10 indicate that the longitudinal stress is strongly influenced by the rolling conditions. In the braking condition the longitudinal stress is oriented

mainly in the rolling condition, with a very small stress value in the opposite direction. In the traction condition, the longitudinal stress distribution is totally different. In the traction conditions, the longitudinal stress is opposite to the rolling direction. Moisescu unfortunately did not report the braking effort and the friction that was used in the simulation.

Similar information as provided by Moisescu for truck tires is not available for aircraft tires. Anyway Moisescu's results show that the longitudinal stress distribution due to braking is complex.

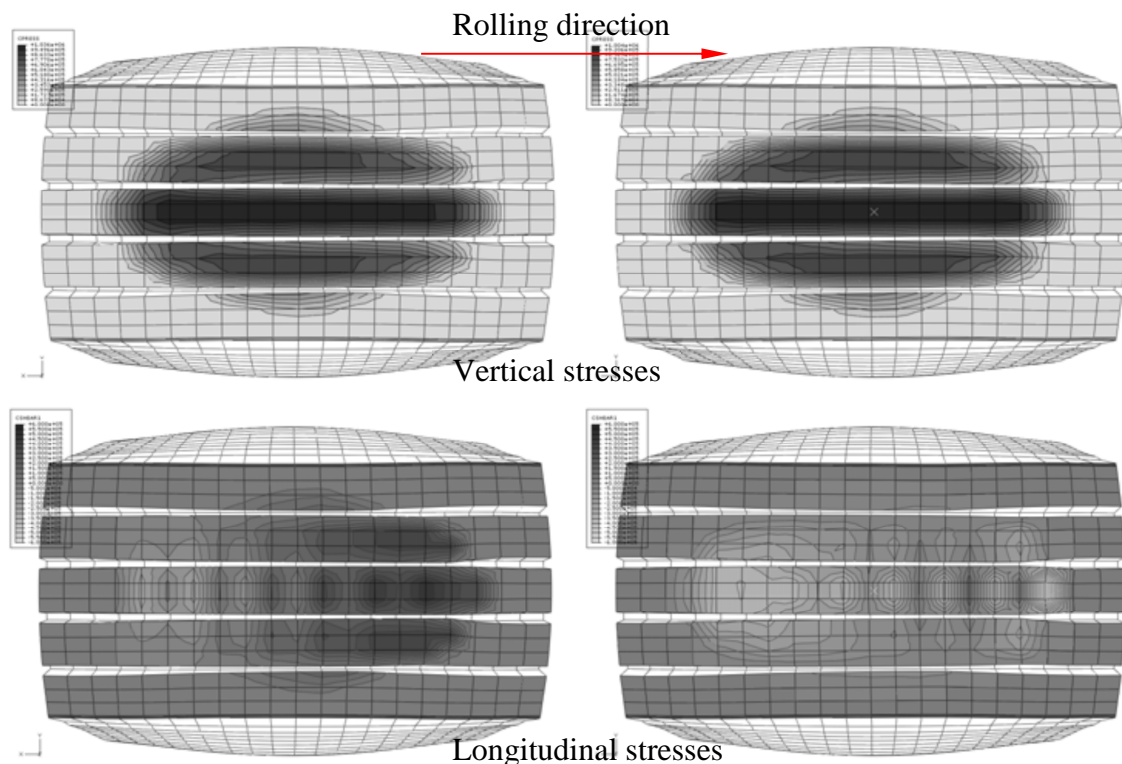


Figure 7-10 Stresses in case of braking (left) and traction (right) conditions [7]

Because of the uncertainties in how to model the longitudinal stress distribution due to braking and because the goal of using FEM in this research was to compare different antiskid surfaces in terms of type of binder and aggregate skeleton, and not to predict the lifetimes, a simple longitudinal stress distribution was used in the FEM simulations.

Figure 7-11 shows the friction coefficient as a function of tire slip (it should be noted that these data are obtained by means of friction measurement using a certain device [8]). The figure shows that a friction coefficient of 0.4 is a reasonable assumption. It was further assumed that high slip percentages would occur which implied that the longitudinal stress due to rolling as presented in Figure 7-9 could be ignored.

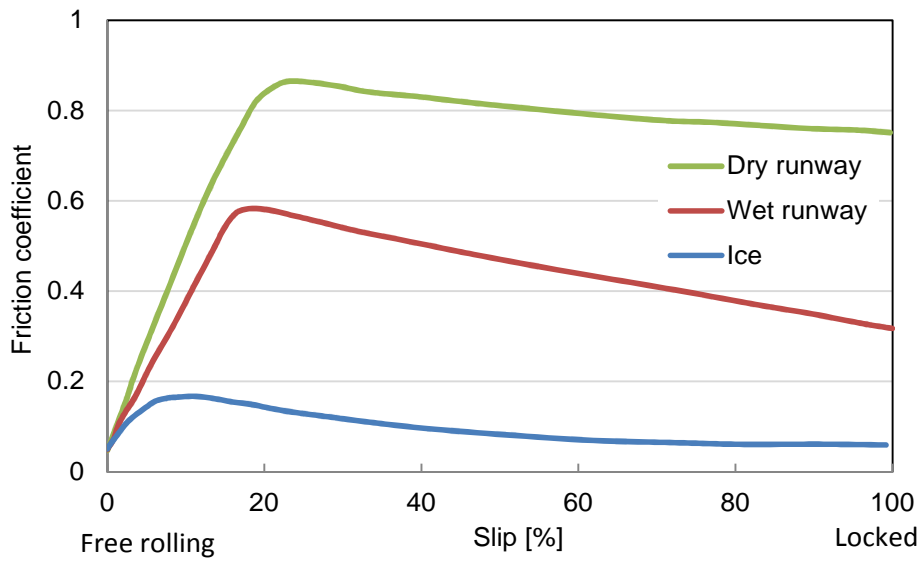


Figure 7-11 Relationship between tire slip and friction coefficient [8]

Friction coefficients are measured between slipping or blocked tires and the pavement surface. So it is logical to assume that the overall longitudinal stress can be defined as in equation:

$$\sigma_{Longitudinal} = \mu \times \sigma_{Vertical} \quad (7-1)$$

Where,

$\sigma_{Longitudinal}$ = longitudinal stress resulted from braking, [MPa];

μ = friction coefficient, 0.4 was used in this research;

Figure 7-12 presents the vertical and longitudinal stresses used for the antiskid models at an aircraft speed of 75 km/h. The loading time is approximated by the length of the contact area (see Figure 7-9) divided by the aircraft speed. The longitudinal stress is the vertical stress multiplied by the friction coefficient according to equation 7-1. As mentioned before, any horizontal stresses due to rolling were ignored.

Once again it is mentioned that the assumed longitudinal stress distribution is a very crude simulation of reality. Nevertheless these assumptions were considered to be acceptable since the main goal of the simulations was to make comparisons and not to make predictions of the lifetime of the antiskid layers.

Since all the FEMs developed in this research were 2D models, lateral stress distributions were not included.

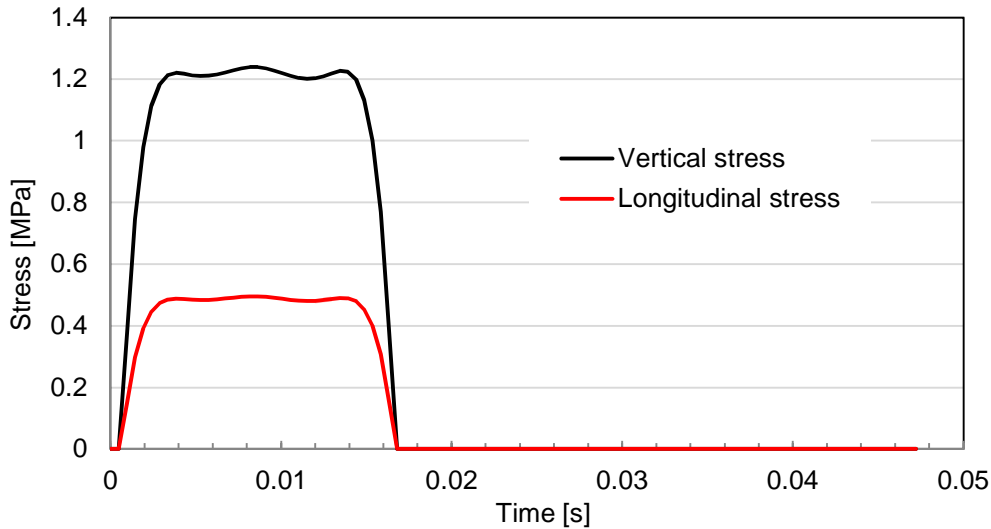


Figure 7-12 Load signals for an antiskid layer at an aircraft speed of 75 km/h

As discussed in Chapter 4 and Chapter 6, the antiskid layers have a high texture depth. The texture depth has a large effect on the generation of vertical and longitudinal stresses, because the applied tire load is transferred to the pavement through the individual aggregates. In the antiskid models, the stresses were transformed into forces applying on individual aggregates by assuming that each aggregate is subjected to a force that equals the stress multiplied by the area in which the aggregate is sitting [9]. Figure 7-13 shows how the forces are applied on individual aggregates via a certain number of nodes on the rigid bodies representing the aggregates.

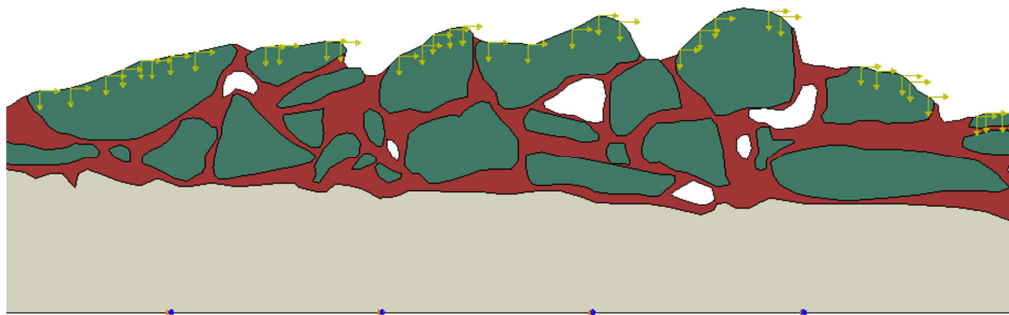


Figure 7-13 Force applied on individual aggregates

7.3 Material Inputs

7.3.1 Binder inputs

The two-component epoxy modified binder (A3-UV) and 3rd stage cured residue of modified bitumen emulsion (MBE), investigated in Chapter 5 were used as binders in the models. The tar-containing binder was not included in this research. As explained in Chapter 4, it was not possible to recover the tar-

containing binder from the cores obtained from the six airfields. As a consequence properties of the tar-containing binder needed for the simulation could not be obtained.

The generalized Maxwell model and its parameter determination method introduced by Woldekidan [10] was used in this research to define the visco-elastic properties.

7.3.1.1 Generalized Maxwell Model

A visco-elastic model is used to represent the binder behavior in the FEM analysis. Many models, comprising of springs and dashpots are available for describing visco-elastic behavior [10, 11]. One of the common rheological models that is used for pavement analysis purposes is the Generalized Maxwell model, also known as Prony series, in which a number of Maxwell elements are placed in parallel (Figure 7-14). The number of terms required for accurately modeling a given material response is based on the quality of fitting of measured response data [10].

Figure 7-14 describes the Generalized Maxwell model and the material model as used in the ABAQUS simulation. The presence of the parallel spring in the right hand figure implies that the model is intended for visco-elastic solid materials. The parallel spring represents the rubbery modulus of the material.

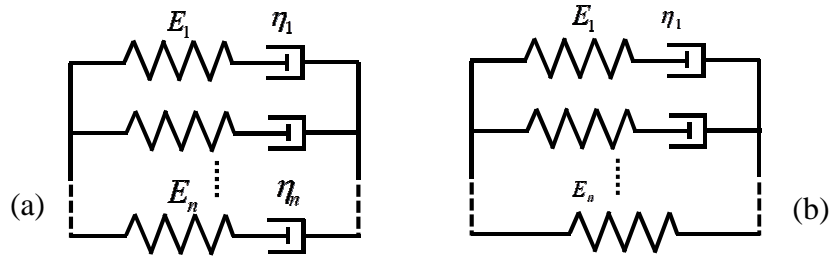


Figure 7-14 Generalized Maxwell model (a) and the form used in Abaqus (b)

The relaxation function for the model in the right part of Figure 7-14 with n Prony terms can be obtained as a summation of the functions for the individual terms as:

$$E(t) = \frac{\sigma(t)}{\epsilon_0} = E_0 + \sum_{i=1}^n E_i \exp(-t / \tau_i) \tag{7-2}$$

The corresponding expressions in the frequency domain are:

$$E'(\omega) = E_0 \times \sum_{i=1}^n \frac{\frac{E_i}{E_0} \omega^2 \tau_i^2}{1 + \omega^2 \tau_i^2} \tag{7-3}$$

$$E''(\omega) = E_0 \times \sum_{i=1}^n \frac{\frac{E_i}{E_0} \omega \tau_i}{1 + \omega^2 \tau_i^2} \quad (7-4)$$

$$g_{-i} = \frac{E_i}{E_0} \quad (7-5)$$

$$|E^*(\omega)| = \sqrt{(E'(\omega))^2 + (E''(\omega))^2} \quad (7-6)$$

Where, E_0 , g_{-i} and τ_i are material parameters, here they are named as Prony series parameters.

7.3.1.2 Model Parameter Determination

Data obtained from the DSR frequency sweep tests on the binders was used to determine the Prony series parameters by means of Matlab.

Pre-Smoothing the Experimental Data

Model parameter determination is sensitive to the scatter in the experimental data. Literature showed that better results are obtained when pre-smoothing of the experimental data is performed before the regression analysis is started [10, 12, 13]. In this research the Williams-Landel-Ferry (WLF) model and S-curve model introduced in Section 3.2.4.3 in Chapter 3 were chosen to perform pre-smoothing of the experimental data. This is because of the excellent ability of the S-curve model to describe the experimental data over a wide range of frequencies.

The pre-smoothing results (master curves) of MBE and A3-UV are shown in Figure 5-17 and Figure 5-39 respectively. After a good fit is obtained for the complex shear modulus and the phase angle, Matlab is used to optimize the Prony parameters. This optimization is discussed hereafter.

Optimization Procedure

The parameter determination procedure is incorporated in a user friendly graphical user interface program in Matlab (See Figure 7-15 and Figure 7-16). The program was designed by Woldekidan and is briefly introduced in his PhD thesis [10]. With this tool, by changing the number of Prony terms, optimization can be performed until a satisfactory fit is obtained.

Twelve Prony terms were used for EMB, while 10 Prony terms were used for the MBE binder. Figure 7-15 and Figure 7-16 present the fitting curves of the shear modulus of the original A3-UV binder and 3rd stage cured MBE binder. The blue curve is the pre-smoothed data, and the red curve is the fitting data from Prony series model. The two figures illustrate that the modeled data fit the pre-smoothed data quite well.

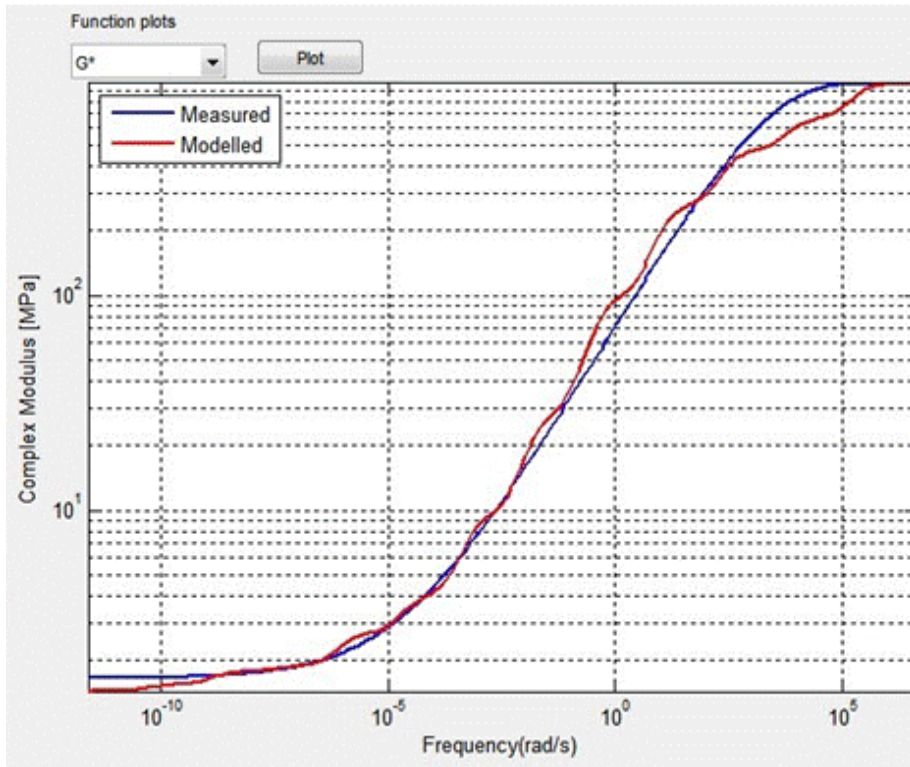


Figure 7-15 Pre-smoothed data and modeled data for original A3-UV binder, $T_{ref}=20\text{ }^{\circ}\text{C}$

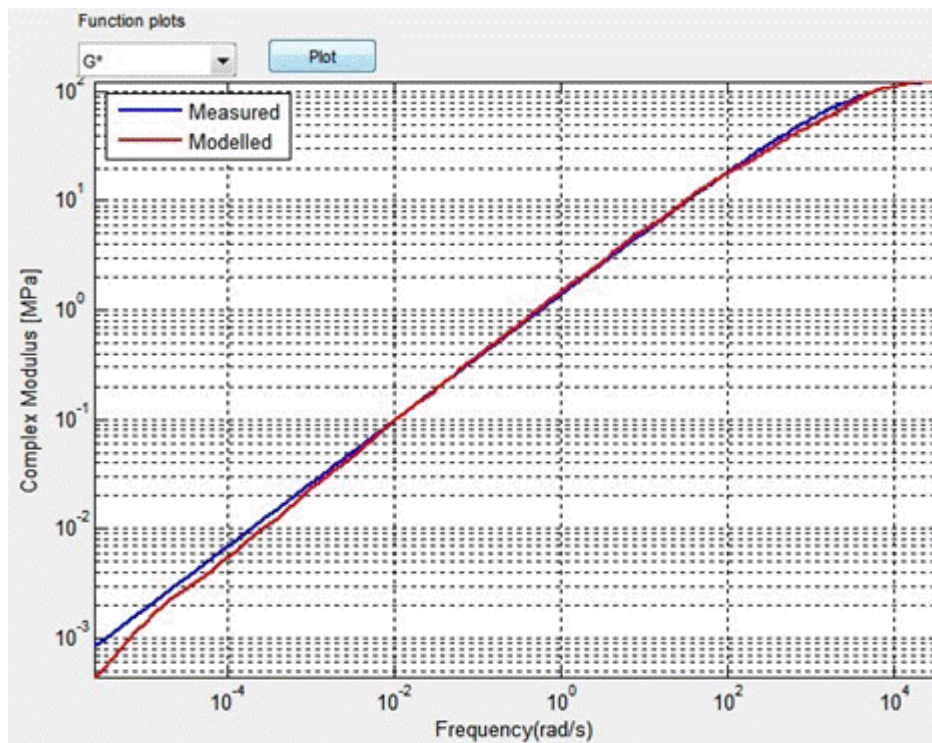


Figure 7-16 Pre-smoothed data and modeled data for 3rd stage cured MBE binder, $T_{ref}=20\text{ }^{\circ}\text{C}$

Table 7-1 presents the Prony series parameters for the A3-UV and MBE binder. They are used as input parameters to define the visco-elastic properties of binder for the simulations. The reference temperature is 20 °C.

Table 7-1 Prony series parameters for binders, Tref=20 °C

N	EMB binder		Modified Bitumen Emulsion (MBE)	
	τ_i [s]	g_{-i} [-]	τ_i [s]	g_{-i} [-]
1	5.52E-06	3.19E-01	2.11E-04	6.53E-01
2	1.43E-04	1.95E-01	1.81E-03	2.18E-01
3	3.70E-03	2.21E-01	1.56E-02	9.22E-02
4	9.60E-02	1.68E-01	1.34E-01	2.65E-02
5	2.49E+00	6.95E-02	1.16E+00	7.60E-03
6	6.44E+01	1.78E-02	9.97E+00	2.04E-03
7	1.67E+03	5.30E-03	8.58E+01	5.72E-04
8	4.32E+04	1.27E-03	7.39E+02	1.48E-04
9	1.12E+06	8.01E-04	6.36E+03	3.27E-05
10	2.90E+07	1.12E-04	5.48E+04	1.42E-05
11	7.51E+08	2.37E-04		
12	1.95E+10	1.12E-04		
G_0 [MPa]	968		123.5	
E_0 [MPa]	2613.6		333.45	

The Young’s modulus, E_0 , and Poisson’s ratio of binder are also required to define the visco-elastic properties of the binder for the models. Young’s modulus is estimated from the shear modulus (G_0), using the following relation:

$$E_0 = 2 \times G_0 (1 + \nu) \tag{7-7}$$

Where, ν is the Poisson’s ratio; 0.35 was assumed in this research.

7.3.2 Other Inputs

Aggregates have a much higher stiffness than the binder. So in the antiskid FEMs, aggregates are simulated as rigid bodies. The asphalt mixture layers under the antiskid layers were simulated as homogeneous elastic materials with an estimated Young’s modulus of 6000 MPa and an estimated Poisson’s ratio of 0.35.

7.4 Results and Analyses

The responses of antiskid models are given in Figure 7-17. The figures present an indication of the maximum principal stresses in the EMB-based antiskid layers. These figures show that there are some locations in the 2D image

models where stresses in the binder are higher (elements with red color) than in other areas. At these locations failure may start. Therefore further analyses of the stress and strain development at these locations are of interest. In each 2D photo-model 3 locations have been identified to plot results.

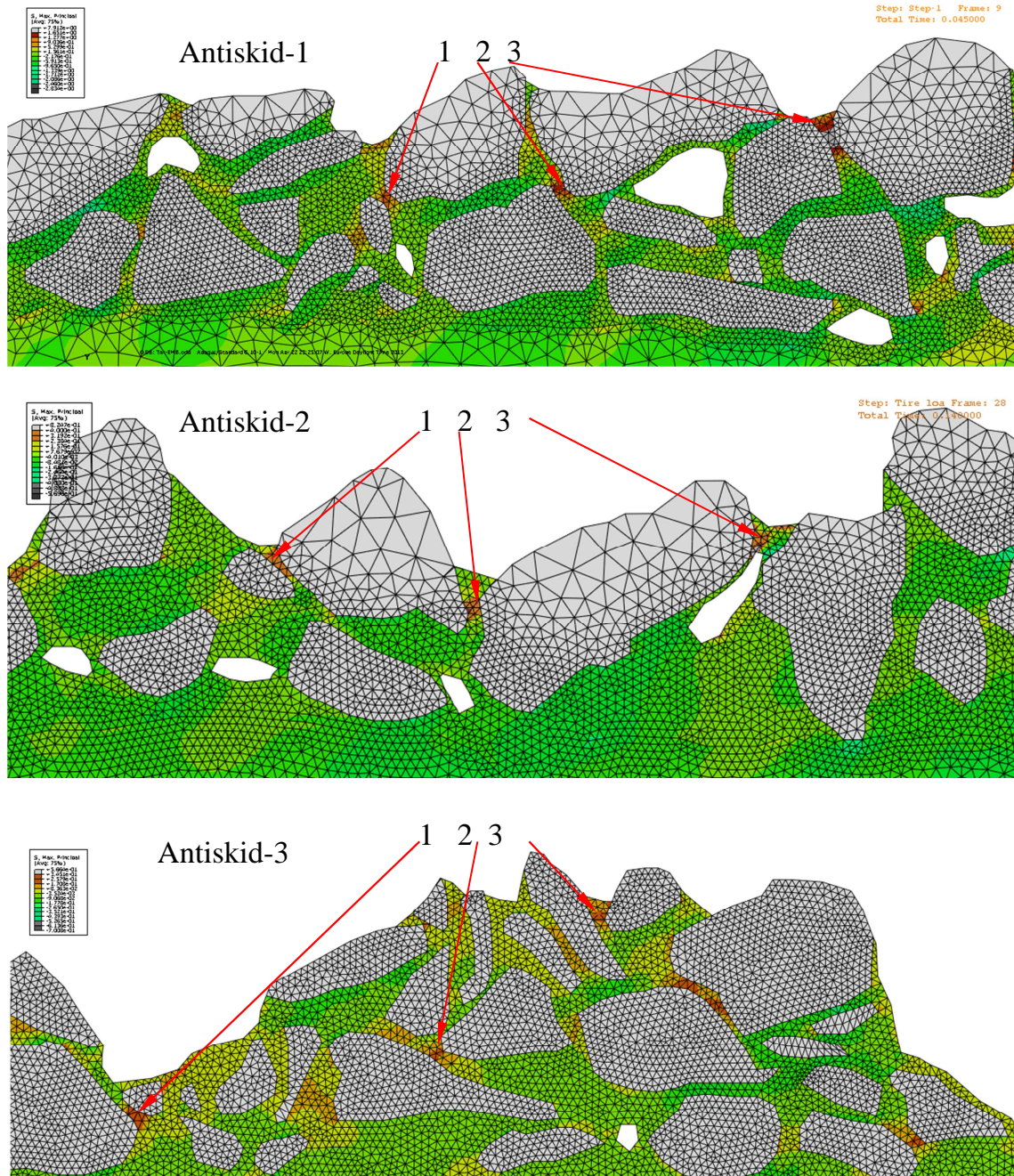


Figure 7-17 Response of EMB based antiskid models, indication of maximum principal stress

Figure 7-18 shows the stresses occurring at location 3 in the EMB based Antiskid-2 model. A shear stress of 0.76 MPa can be observed.

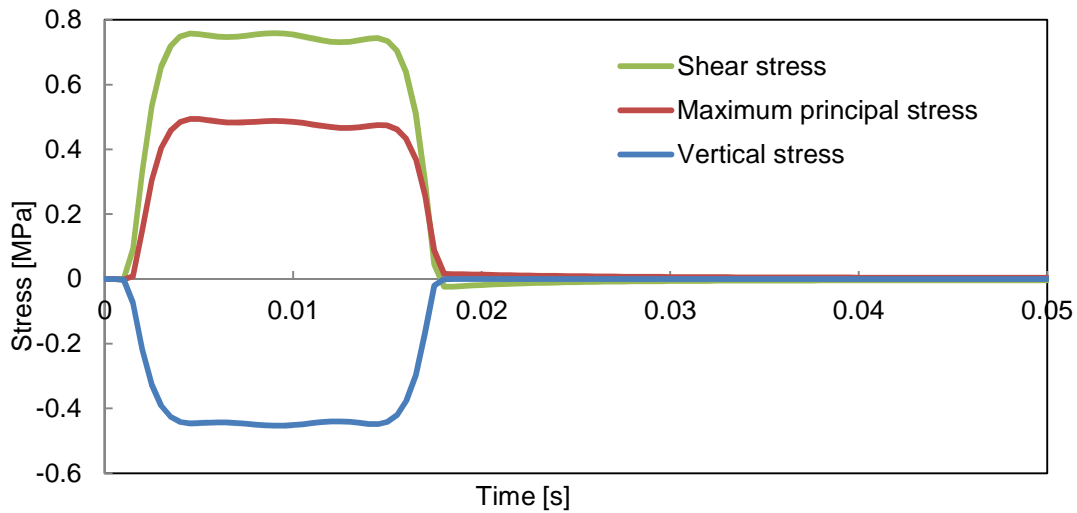


Figure 7-18 Stresses at location 3 in EMB based Antiskid-2 model

7.4.1 Influence of the Antiskid Structures

As an example, the stress and strain responses that developed in the binder in EMB based Antiskid-1 model during loading are displayed in Figure 7-19. The maximum principal stress in EMB based Antiskid-1 model varies from 1.01 MPa to 1.79 MPa. The shear stress can be as low as 0.03 MPa and as high as 0.5 MPa. This illustrates that different locations in a single antiskid model may result in large differences in the binder behavior and damage development. It is clear however from the calculations that failure will start very locally.

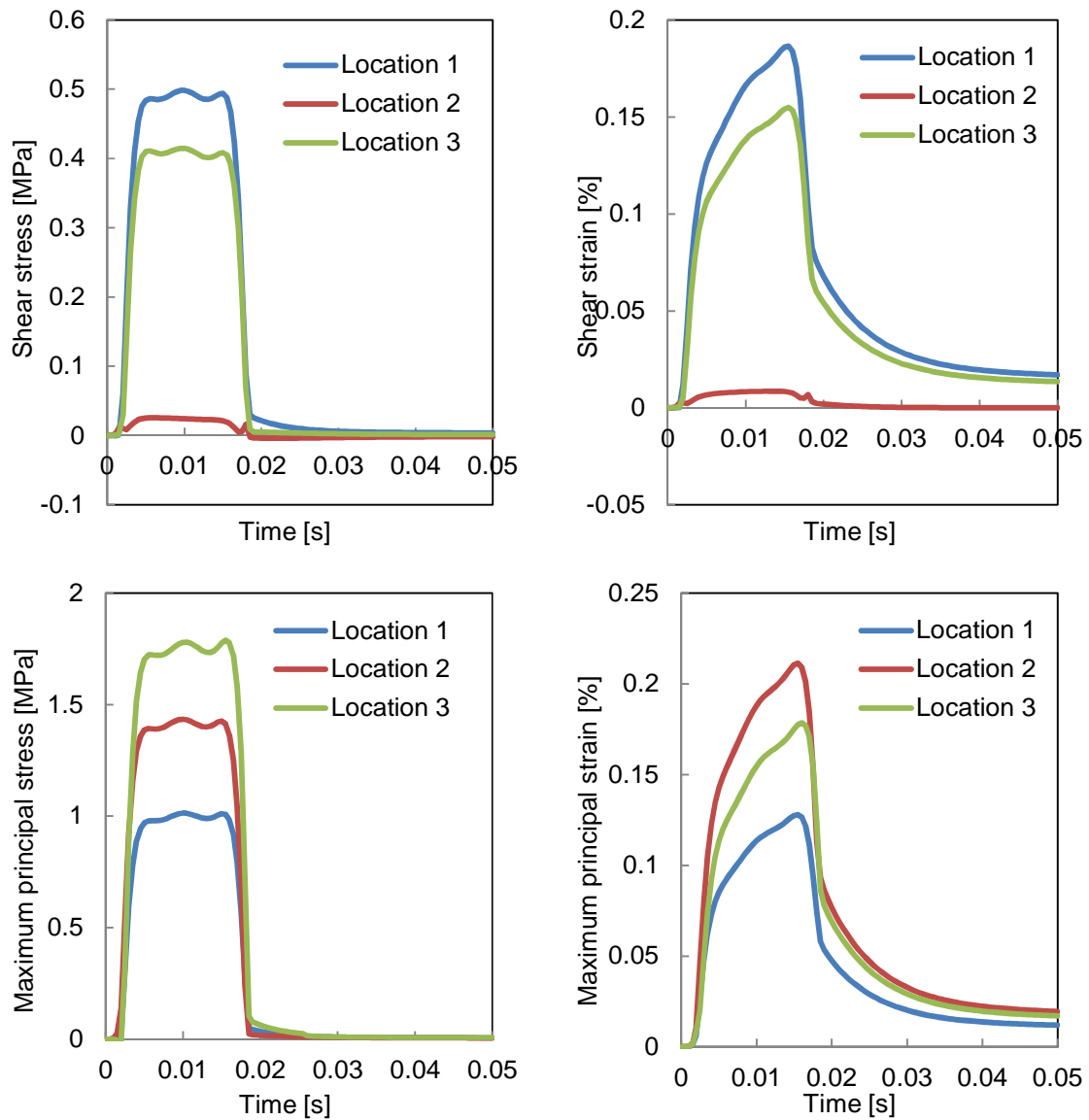


Figure 7-19 Stress-strain responses in EMB based Antiskid-1 model

The maximum principal stresses and strains, shear stresses and shear strains, in the EMB based antiskid models are presented in Table 7-2. The results show that the antiskid structures (the aggregate skeletons) have a significant influence on the stress responses in the binder. It clearly shows that the highest maximum principal stresses and strains are generated in Antiskid-1. The maximum principal stress in Antiskid-1 is 1.79 MPa. In Antiskid-2 the maximum principal stress is 0.5 MPa while it is about 0.2 MPa in Antiskid-3. The maximum principal strains in Antiskid-1 model are also larger than that in the Antiskid-2 and Antiskid-3 models. The shear stresses in the three models are more or less in the same range. Antiskid-1 model has a shear stress value between 0.03 and 0.5 MPa, and in Antiskid-2 model it varies from 0.06 to 0.76 MPa. The shear stress values in Antiskid-3 model are in the range of 0.01 MPa to 0.13 MPa.

Table 7-2 Outputs from EMB based antiskid models

Antiskid types	Locations	Antiskid-1	Antiskid-2	Antiskid-3
Maximum principal stress [MPa]	1	1.012	0.205	0.223
	2	1.434	0.295	0.212
	3	1.788	0.494	0.179
Maximum principal strain [%]	1	0.128	0.022	0.031
	2	0.211	0.048	0.032
	3	0.178	0.129	0.02
Maximum shear stress [MPa]	1	0.498	0.055	0.128
	2	0.026	0.234	0.111
	3	0.415	0.759	0.014
Maximum shear strain [%]	1	0.187	0.021	0.047
	2	0.009	0.088	0.041
	3	0.155	0.282	0.005

7.4.2 Influence of the Binders

Figure 7-20 and Figure 7-21 illustrate the differences in stresses when using EMB and MBE residues as a binder in Antiskid-2 model. The differences of using the two investigated binders in Antiskid-1 and Antiskid-3 models are presented from Figure A-11 to Figure A-14 in the Appendix. The figures show that when a softer binder (MBE residues) is used, a higher vertical displacement and higher strain levels and consequently lower stresses are generated than when using the stiffer EMB binder. Figure 7-21 shows that the MBE binder has a shear strain of more than 5%, which is much higher than the value generated in EMB binder. The shear strain in EMB binder, at the same location under the same loadings, is less than 0.3%.

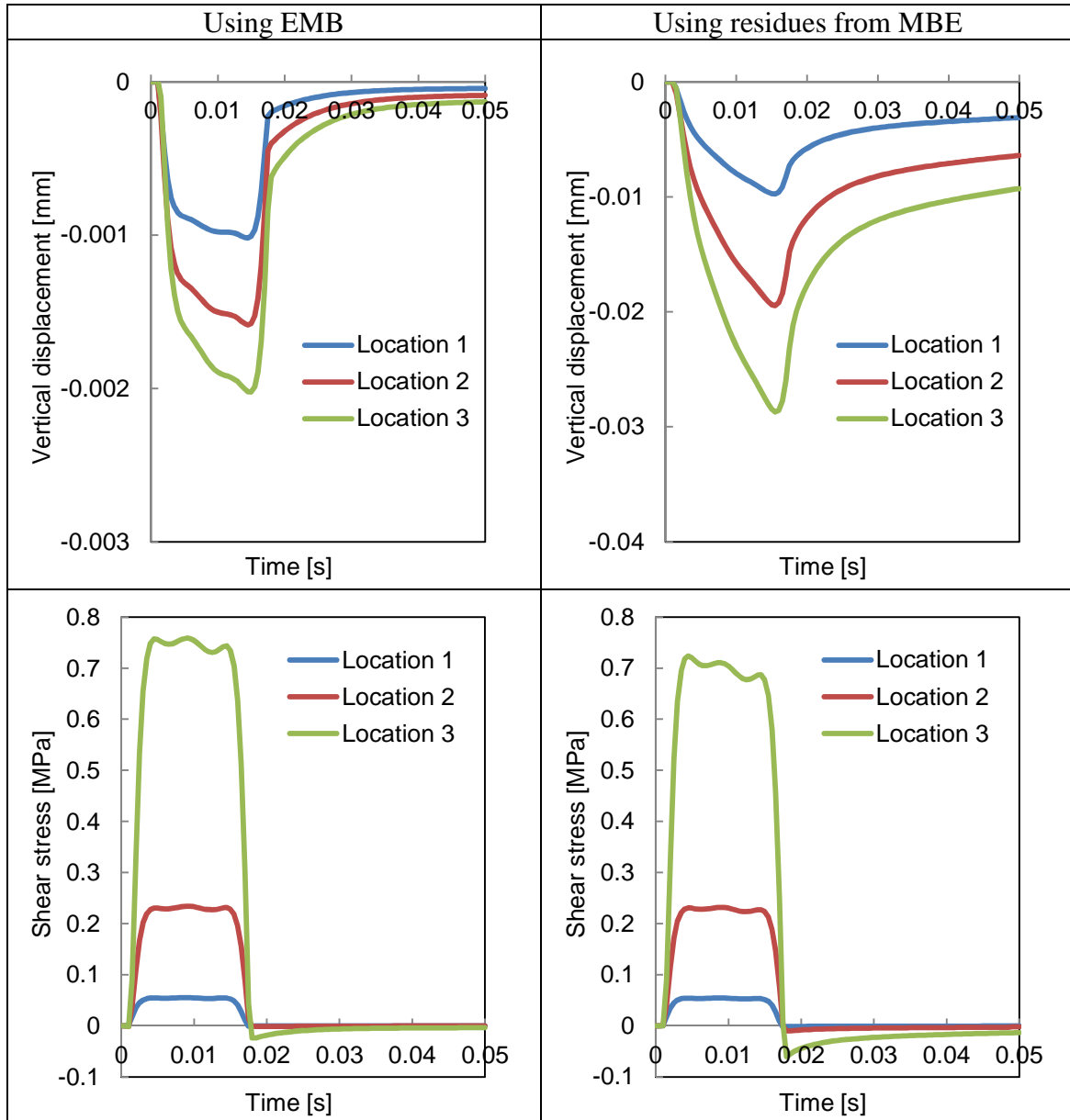


Figure 7-20 Stress and strain responses in Antiskid-2 model (a)

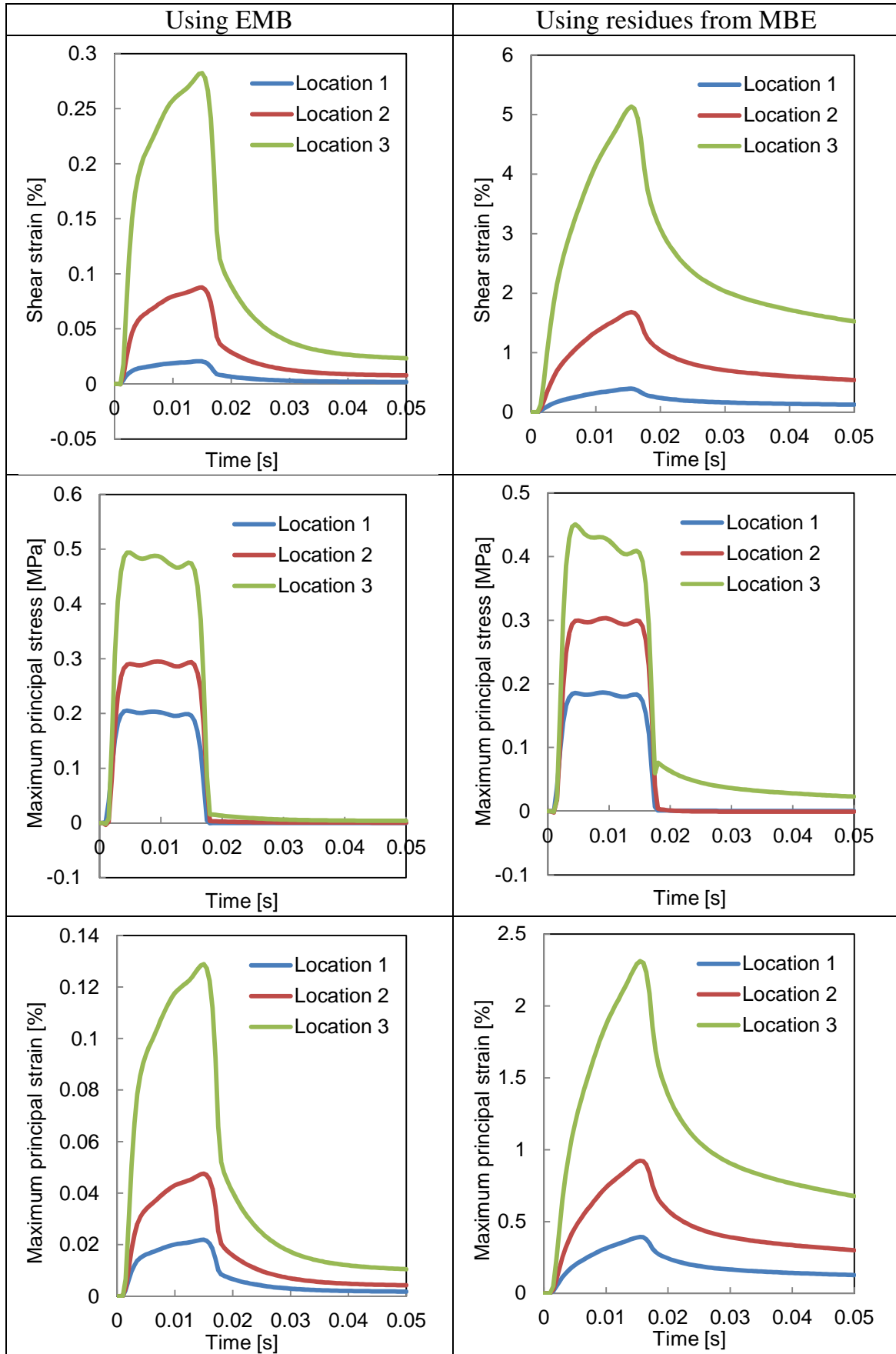


Figure 7-21 Stress and strain responses in Antiskid-2 model (b)

Table 7-3 shows the maximum principal stresses and strains, shear stresses and shear strains in the three MBE based antiskid models. By comparing the results presented in Table 7-2 and Table 7-3 with each other, it is clear that the shear strain levels in MBE binder are much higher than those in the EMB based models, while the resulted maximum principal stresses and shear stresses are slightly lower. The simulations showed that the stresses in the EMB binder are slightly higher than the stresses in the MBE binder. Previous research in Chapter 5 showed that at the same loading conditions, the EMB binder will result in a higher modulus and tensile strength than for the MBE binder. This means that the EMB binder has better ability than MBE for antiskid surface layer to carry this heavy loading.

Table 7-3 Outputs from MBE based antiskid models

Antiskid types	Locations	Antiskid-1	Antiskid-2	Antiskid-3
Maximum principal stress [MPa]	1	1.082	0.186	0.191
	2	1.512	0.303	0.2
	3	1.904	0.45	0.181
Maximum principal strain [%]	1	2.58	0.392	0.52
	2	4.209	0.923	0.595
	3	3.68	2.311	0.391
Maximum shear stress [MPa]	1	0.51	0.054	0.109
	2	0.046	0.232	0.103
	3	0.402	0.724	0.013
Maximum shear strain [%]	1	3.679	0.395	0.794
	2	0.18	1.683	0.734
	3	2.916	5.133	0.096

After the load pulse is applied, the stress curves in EMB based models decreased very fast to zero. And the strains reduced to a very low percentage of the maximum strain value. But in the MBE based models, still very high strain exists in the binder after the same unloading period. This is of importance when the load does not consist of a single load pulse as simulated here but of multiple pulses that do occur under 4 and 6 wheel landing gears. In the case of MBE a much higher built up of residual stresses would occur then in EMB antiskid layers. These higher accumulated strains might lead to earlier failure.

7.4.3 Principal Stresses and Strains

The principal stresses and strains are summarized in Table 7-4. Clear differences can be observed in this table between the three analyzed models. These results also prove that the different geometries of antiskid layers have significant influence on the stresses in the binder. These stresses are also dependent on the locations of interest. As a result, although the same binders were used, the stress and strain behaviors in the binder differ from one location to another location. One should however take into account that it is very well

possible that the arrangement of the aggregate particles observed for the Antiskid-1 layer might also occur in the Antiskid-2 and the Antiskid-3 layer. Therefore the results shown in Table 7-4 can be considered as an indication of the stresses and strains that can occur in one antiskid layer.

Comparing the results at the same locations with different binders, in general one can state that the maximum principal stresses are the highest in Antiskid-1 model. Antiskid-2 and Antiskid-3 have more or less the same maximum principal stresses. One can also observe that the maximum principal stresses in the EMB based antiskid layers are slightly higher than that in the MBE based antiskid layers. The maximum principal strains in the EMB based antiskid are much lower than in the MBE based antiskid layers. These results clearly indicate that higher strains will develop when a softer binder (lower modulus) is used compared to using an EMB binder. The maximum principal strain can reach to more values than 4% higher than when a MBE binder was used.

Table 7-4 Maximum principal stresses and strains in antiskid models

Antiskid models		Principal stress [MPa]			Principal strain [%]		
		σ_1	σ_2	σ_3	ϵ_1	ϵ_2	ϵ_3
EMB based Antiskid-1	Location 1	1.012	0.336	-0.159	0.128	0	-0.07
	Location 2	1.434	0.307	-0.559	0.211	0	-0.162
	Location 3	1.788	0.842	0.616	0.178	0	-0.042
MBE base Antiskid-1	Location 1	1.082	0.369	-0.112	2.58	0	-1.43
	Location 2	1.512	0.351	-0.527	4.209	0	-3.11
	Location 3	1.904	0.896	0.657	3.68	0	-0.88
EMB based Antiskid-2	Location 1	0.205	0.086	0.041	0.022	0	-0.008
	Location 2	0.295	0.057	-0.178	0.048	0	-0.04
	Location 3	0.494	-0.205	-1.074	0.129	0	-0.162
MBE base Antiskid-2	Location 1	0.186	0.079	0.038	0.392	0	-0.147
	Location 2	0.303	0.056	-0.168	0.923	0	-0.77
	Location 3	0.45	-0.211	-1.038	2.311	0	-2.97
EMB based Antiskid-3	Location 1	0.223	0.057	-0.06	0.031	0	-0.022
	Location 2	0.212	0.039	-0.101	0.032	0	-0.026
	Location 3	0.179	0.072	0.027	0.02	0	-0.008
MBE base Antiskid-3	Location 1	0.191	0.048	-0.054	0.52	0	-0.368
	Location 2	0.2	0.036	-0.098	0.595	0	-0.484
	Location 3	0.181	0.074	0.03	0.391	0	-0.161

σ_1 , ϵ_1 are the maximum principal stress and strain;
 σ_2 , ϵ_2 are the middle principal stress and strain;
 σ_3 , ϵ_3 are the minimum principal stress and strain.

Furthermore, Table 7-4 shows that the effect of aggregate skeletons on the maximum principal strains in the binder is the highest for the layer with an MBE

binder (0.39-4.2%). For the layers with an EMB binder this range is from 0.02 to 0.21%. This indicates that the aggregate skeletons will have a significant influence on the binder behaviors when a softer binder is used for antiskid layer.

7.5 Conclusions

By developing three photo FEMs of antiskid layers from the Nano CT scan images, the stress-strain responses in EMB binder and MBE binder were investigated separately. The Prony series parameters of binders were defined as input for models to represent their visco-elastic properties. The following conclusions can be drawn from the FEM simulations:

1. The stresses and strains responses in the antiskid thin surfaces can be well analysed by FEM at meso-level. Antiskid layers use fine aggregates and therefore high resolution images are required to get a clear separation of aggregates and binder during the model development. Nano CT scan images can be used for this purpose.
2. The antiskid aggregate skeletons have a huge influence on the stresses in the binder. The calculation results from 2D photo model vary with the geometries of the photo models, as well as with different locations of interest.
3. The FEM results indicate that the stresses generated in the EMB binder are slightly higher than in the MBE binder, while the MBE will be subjected to much higher maximum principal strain and shear strain levels. Furthermore, the EMB binder recovers faster after the loading has been removed.
4. The aggregate skeletons have a greater influence on the stresses in the binder when a softer binder is used.
5. Above all, it can be concluded that for an antiskid surface the EMB binder is to be preferred above the MBE binder based on this preliminary analysis. No study has been conducted on the influence of low temperatures on the internal stresses.

REFERENCES

1. Huurman, M., *Lifetime Optimisation Tool, LOT, Main Report, Report No. 7-07-170-1*. 2007, Delft University of Technology.
2. Transport-Canada, *Aircraft Load Ratings in Transport Canada Technical Programs*. 2004, <http://www.tc.gc.ca/eng/air-menu.htm>.
3. Orest, S., *Boeing and Airbus Tire Pressure Test Programs*, in *ALACPA Airport Pavement Seminar and FAA Workshop*. 2009: Brazil.
4. IFALPA, *Runway Safety Manual*. 2009, IFALPA (International Federation of Airline Pilots' Associations) Aerodrome & Ground Environment Committee.
5. M. De Beer. *Measurement of tyre/pavement interface stresses under moving wheel loads*, in the *Vehicle-Road and Vehicle-Bridge Interaction Conference*. 1996: Noordwijkerhout, The Netherlands.
6. M. De Beer, C. Fisher, and F.J. Jooste. *Determination of pneumatic tyre/pavement interface contact stresses under moving loads and some effects on*

- pavements with thin asphalt surfacing layers.*, in *Proceedings of the Eight International Conference on Asphalt Pavements*. 1997: Seattle, Washington.
7. MOISESCU, R. and G. FRĂȚILĂ, *Finite element model of Radial Truck Tyre for Analysis of Tyre-Road Contact Stress*. UPB Scientific Bulletin, Series D: Mechanical Engineering, 2011. **73**(3).
 8. *Avoiding overrun accidents on contaminated runways*. Available from: Professional Pilot: http://www.propilotmag.com/archives/2009/Dec%2009/A4_runway_p1.html.
 9. Huurman, M., *Developments in 3D surfacing seals FE modelling*. International Journal of Pavement Engineering, 2010. **11**(1): p. 1-12.
 10. Woldekidan, M.F., *Response modelling of bitumen, bituminous mastic and mortar*. 2011, Delft University of Technology: Delft.
 11. Christensen, D.W. and D.A. Anderson, *Interpretation of Dynamic Mechanical Test Data for Paving Grade Asphalt Cements* Journal of the Association of Asphalt Paving Technologists, 1992. **61**: p. 67-116.
 12. Park, S.W. and Y.R. Kim, *Fitting Prony-Series Viscoelastic Models with Power-Law Presmoothing*. Journal of Materials in Civil Engineering, 2001. **13**(1): p. 26-32.
 13. de AL Babadopulos, L.F., et al., *Prony series fitting method to creep experimental data with different numbers of elements*.

8. Conclusions and Recommendations

This research was started to finding alternatives for tar containing binders to be used in antiskid surfacings for airfield runways. The conclusions can be divided in five groups based on the flow of the research.

1. First of all a benchmark was developed for the macrotexture, shear strength and pull-of strength that could be used in a specification to be developed for anti-skid surfacing for airfields. Specimens from six military airfields were investigated to develop a benchmark based on the well performing tar-containing antiskid layers.
2. In the second phase alternative binders were investigated. Several potential binders, such as Modified Bitumen Emulsion (MBE), 2-component Modified Epoxy Resin and 2-component Epoxy Modified Bitumen (EMB) were studied. Special attention was also given to the curing time, because of the relatively short time slots available for maintenance.
3. After selection of some promising alternative binders, antiskid layers produced with these MBE and EMB were designed and slabs were produced in the laboratory to find out if they could satisfy the benchmark
4. Finite Element Models were developed for anti-skid surfacings based on Nano CT scans. In this way loading of the anti-skid system could be simulated to study stresses and strains that can develop in these layers.
5. Diverse: some research was also performed on Noise Reducing Thin Surface Layers as extension of the anti-skid surfacings.

In this chapter, the important conclusions from the five research items described above are presented. Furthermore recommendations for future research are given.

8.1 Conclusions

8.1.1 Benchmark Development

Tar-containing antiskid layer samples were collected from six military airfields. Surface characteristics, ageing and adhesion properties were investigated.

1. A tar-containing antiskid layer is a thin layer with a thickness between 3 to 5 mm. They have a high macrotexture. The texture depth of tar-containing antiskid layers varies between 1.26 to 1.46 mm. It appeared that these high

texture levels remain more or less constant for a long period of time (20 years). Using these data as a benchmark implies that alternatives to tar containing antiskid layers should have a texture depth of at least 1.25 mm during the whole service life.

2. The tested six tar-containing antiskid samples appeared to have more or less the same ageing index, which is much lower than the ageing index of long term aged bitumen binder. This means that the ageing resistance of tar-containing binder is much better than that of traditional bitumen binder.
3. The test methods used for evaluating the adhesion properties between the thin antiskid layers and the underlying asphalt mixture layer did work well. With these test methods, the shear strength and tensile strength at the interface between the antiskid surface layer and the underlying layer could be evaluated.
4. The minimum shear strength at the interface between the tar-containing antiskid layer and the asphalt mixture layer was 1.16 MPa and the average was 1.5 MPa (at a temperature of 20 °C and vertical displacement speed of 50 mm/min). The age of the samples did not affect the shear strength. This means that the influence of climate and traffic on the shear strength is not significant. Based on these results, a minimum shear strength of 1.2 MPa is proposed as a benchmark to which other antiskid systems should comply.
5. The average tensile strength at the interface between the tar-containing antiskid layer and asphalt mixture layer is 1.03 MPa at 10 °C with a loading speed of 0.025 MPa/s. The minimum tensile strength is about 1 MPa. It is therefore recommended that the tensile strength of the interface of newly designed antiskid surfaces and the substratum should be at least 1 MPa.

8.1.2 Research into Alternative Binders

The curing behavior, direct tensile strength and relaxation behavior of MER were investigated by means of the direct tension test (DTT). Dynamic Mechanical Analysis was used to characterize the elastic behavior of Modified Epoxy Resin (MER).

6. Two-component MER needs a certain curing period to develop sufficient strength to be subjected to traffic loads without failure prematurely. It can reach a DTS of 5 MPa within 1 day at a curing temperature of 14 °C. Environmental factors during application can accelerate the curing speed. A curing time of one day might be too long for airfield applications given the relatively short time slots available for maintenance.
7. At high temperatures (more than 100 °C), MER behaves as a rubbery elastic material and has a stiffness value above 10 MPa while its phase angle value is close to 0 degree. The failure strain of MER is very small (about 10%) and not sensitive to temperature and displacement rate. The influence of oven ageing on the tensile strength and failure strain is not significant.
8. The relaxation of MER decreases when the temperature decreases. The original MER binder shows about 40% relaxation at 0 °C. Aged MER has a

poorer relaxation behavior. These rather low relaxation properties might cause problems when a MER based antiskid layer is subjected to high traffic induced and low temperature induced stresses during winter time. Since the temperature stresses will not relax completely, the summation of traffic and temperature induced stresses might result in failure.

9. Although MER has a high DTS, its failure strain is around 10% at the three test temperatures of 0 °C, 10 °C and 20 °C. This is relatively low compared to bituminous binders. A good flexibility of the antiskid layer is required in order to be able to cope with the fairly large temperature induced displacements which can occur during cold winter days. This implies that the investigated MER binder is probably not suitable for use in antiskid surfacings.

The elasticity of Modified Bitumen Emulsion (MBE) was studied by means of the Dynamic Shear Rheometer.

10. At a high temperature, like 60 °C, the MBE has a modulus value of approximately 300 Pa, while its phase angle is above 60 degrees. The binder has viscous domain properties. This behavior is not suitable for applications where a high temperature resistance is required, such as antiskid surfacings on airfields. Jet engines can heat up the temperature at runway surfaces to more 100 °C for a short time.

The curing property, direct tensile strength, relaxation, elasticity and ageing resistance of Epoxy Modified Bitumen (EMB) were first studied by testing three different 2-component EMB binders. Then one binder was selected for further evaluations.

11. The higher the curing temperature is, the faster the DTS will develop. Binder A1 has the fastest curing speed and the highest DTS, while A3 has the lowest curing speed and the lowest DTS (9 MPa). The DTS of EMB is temperature dependent.
12. The relaxation of EMB is temperature dependent. Binder A3 showed a better relaxation performance than the other two binders. At lower temperatures (e.g. 0 °C) it still has a relaxation percentage of 72.5%.
13. The decreased percentage of relaxation between the original binder and the high temperature aged binder for A1, A2 and A3 is 45.79%, 46.33% and 12.03% respectively. The relaxation difference in original A3 binder and high temperature binder is the smallest. This illustrates that the binder A3 has a better high temperature ageing resistance. Furthermore, ageing will result in a higher modulus, and A3 has the smallest changes of modulus after ageing.
14. At higher temperatures (e.g. 80 °C, the military runways require high temperature resistance on the runway surfaces), the complex modulus of EMB is higher than 2 MPa, while its phase angle is around 5 degree. The

binder shows rubber elastic properties at high temperature. EMB is less temperature sensitive than the residues from MBE.

8.1.3 Properties of Newly Designed Antiskid Layers

The surface texture and interface adhesion properties of two newly designed antiskid layers were investigated. The EMB-based antiskid layer was designed by using the 2-component A3-UV EMB as binder. The Schiphol antiskid layer were produced using a polymer modified bituminous binder.

15. The texture depths of newly designed EMB-based and the Schiphol antiskid layers are 1.93 mm and 1.86 mm respectively. Both are far above 1.3 mm which is concluded as a benchmark for new antiskid surfacings.
16. All of the EMB-based specimens, and six out of eight of the Schiphol specimens failed in the underlying asphalt mixture during the pull test. These results indicate that the tensile strength at the interface is higher than the reported values. From the test results, it is obvious that the tensile strength at the interface of EMB-based specimens and Schiphol specimens satisfy the benchmark. The tensile strength of the EMB-based specimens is higher than that of the Schiphol specimens.
17. The average shear strength of the interface at 20 °C of the EMB-based and Schiphol antiskid layer are 3.37 MPa and 2.49 MPa respectively. Both values satisfy the requirement set in the benchmark. The shear strength of the EMB-based specimens is higher than that of Schiphol specimens. It means that the epoxy modified bitumen did provide better adhesion properties than the Schiphol specimens.

8.1.4 FEM Analysis

FEMs of three antiskid layers were developed from Nano CT scan images. In the FEM analyses the stress-strain responses in EMB binder and BE binder were analyzed and the effect of binder type and grain skeleton on the response was evaluated.

18. Fine aggregates are used in antiskid layers and therefore high resolution images are required to get a good separation of aggregates and binder during the model development. Nano CT scan images should therefore be used for this purpose.
19. The antiskid structures have a huge influence on the stresses and strains in the binder.
20. FEM results indicate that the stresses generated in the EMB binder are slightly higher than in the MBE binder, while the MBE is subjected to much higher maximum principal strain and shear strain levels. Furthermore, the EMB binder has a better ability to recover after loading. The aggregate skeleton has a higher influence on the stresses and strains in the soft MBE binder than on the stresses and strains in the EMB binder.

8.1.5 Noise Reducing Thin Surface Layers

The pull test and Leutner shear test were also conducted on Noise Reducing Thin Surface Layers (NRTSLs).

21. Just three out of ten tests failed at the interface during the pull test, which means that this test is not suitable for testing the adhesion characteristics between a NRTSL and the substrate.
22. The shear strength between NRTSL and asphalt mixture layer is higher than the shear strength at the interface between normal asphalt mixture layers. At the same test conditions, the NRTSL-R specimen has a lower value of shear strength.

8.2 Recommendations

Based on the conclusions of this study, the following recommendations are made with respect to sustainable thin surfacings (especially antiskid surfacings).

1. **Trial section in the field:** The properties of investigated materials in the laboratory presented in this research can be used as useful guidance for field applications. But in order to make sure they can behave as well as in the lab, field tests on new antiskid surfacings are recommended.
2. **Fuel resistance:** Fuel resistance and resistance to de-icing chemicals are essential properties for antiskid surfacings. Unfortunately these important functionalities could not be evaluated because of the limited number of specimens that could be made available. Therefore research on the fuel resistance and the resistance to de-icing chemicals of new antiskid layers is highly recommended.
3. **Antiskid modeling:** The FEM models in this research simulate the stress and strain behaviors of binder in the antiskid surfacings. But damage mechanism was not included. Losing aggregates from surface layer, which is so defined as raveling, is mainly caused by the effects of repeated traffic loading. This means that the raveling is fatigue related damage. In the future, fatigue property and failure mechanics can be studied to investigate the damage mechanisms with FEM model. Furthermore, the temperature aspects can be also taken into account to give an indication of what tensile stresses can be expected due to a strong drop in temperatures at the surface in relation to the relaxation behavior of the binder.

Appendix

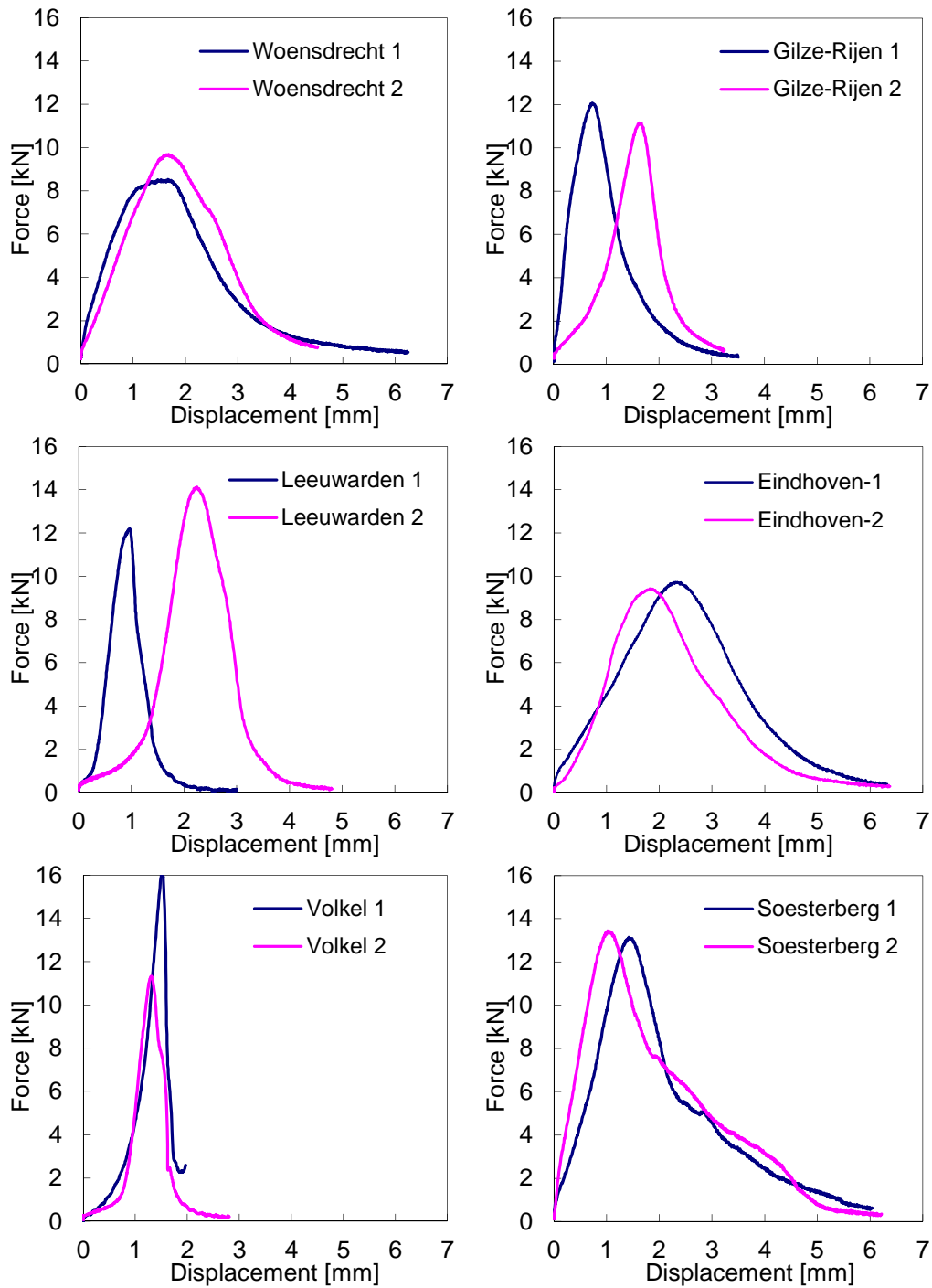


Figure A- 1 Displacement-force curves in shear test on tar-containing antiskid

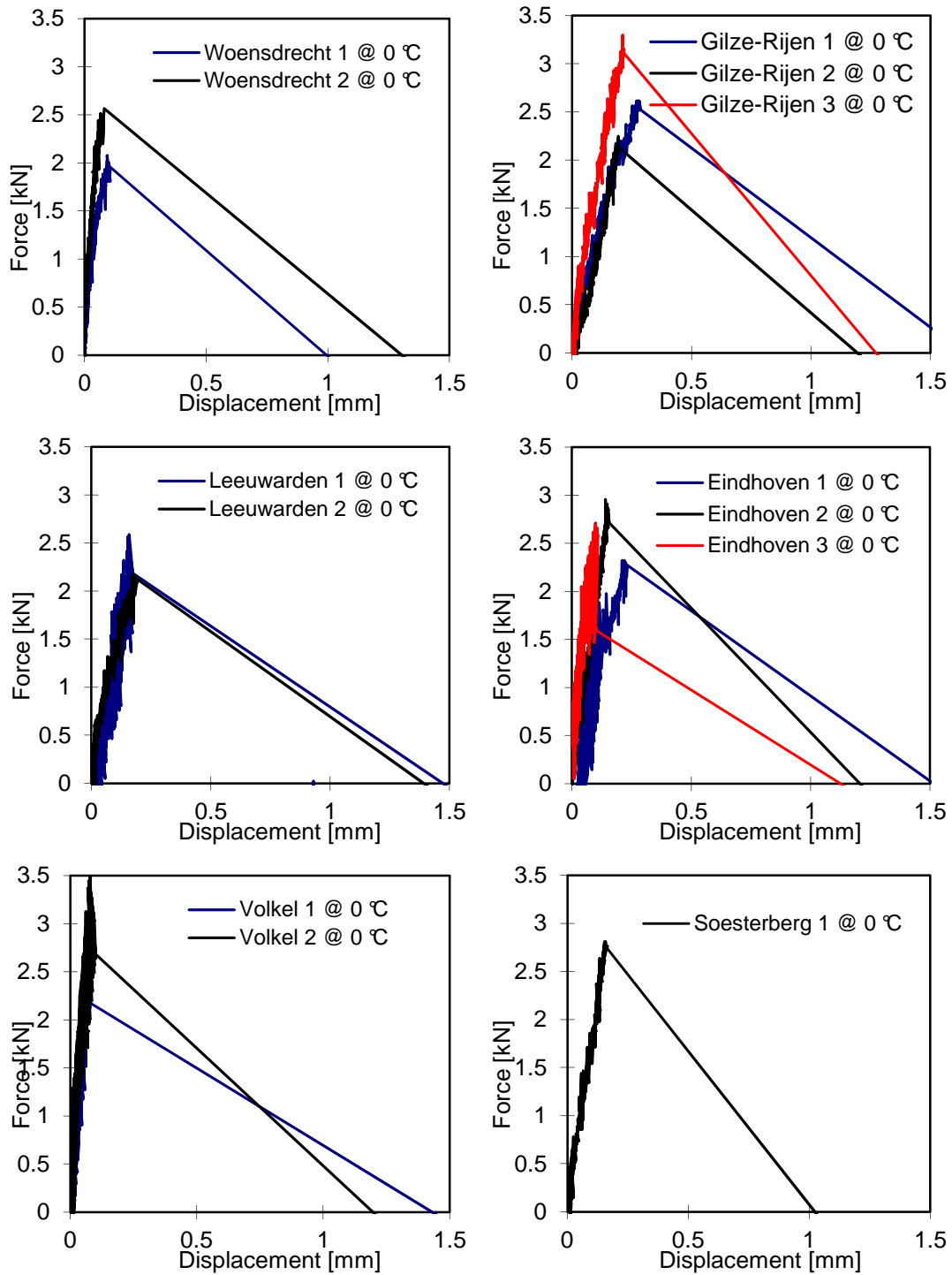


Figure A- 2 Displacement-force curves in pull test on tar-containing antiskid at 0 °C

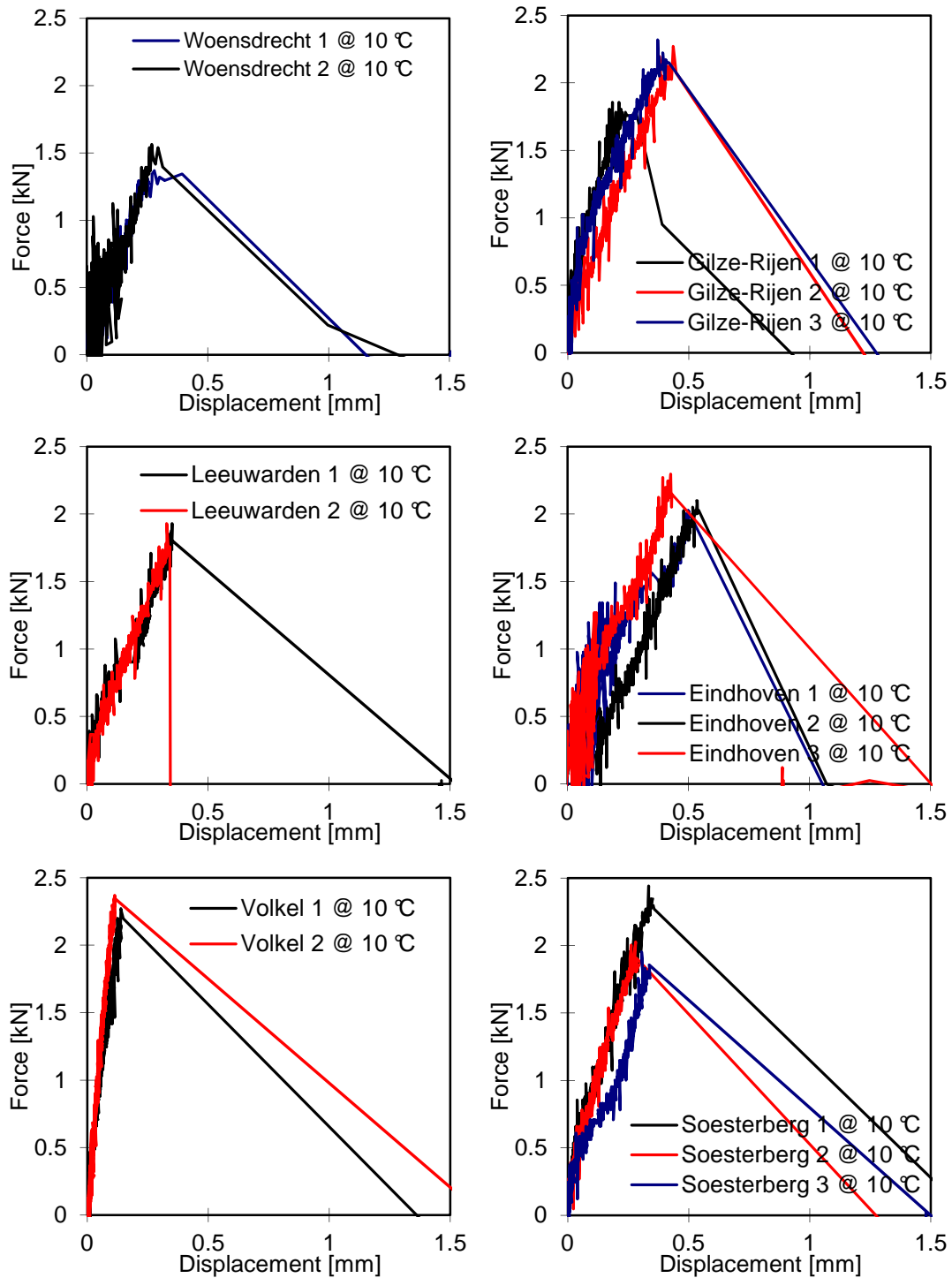


Figure A- 3 Displacement-force curves in pull test on tar-containing antiskid at 10 °C

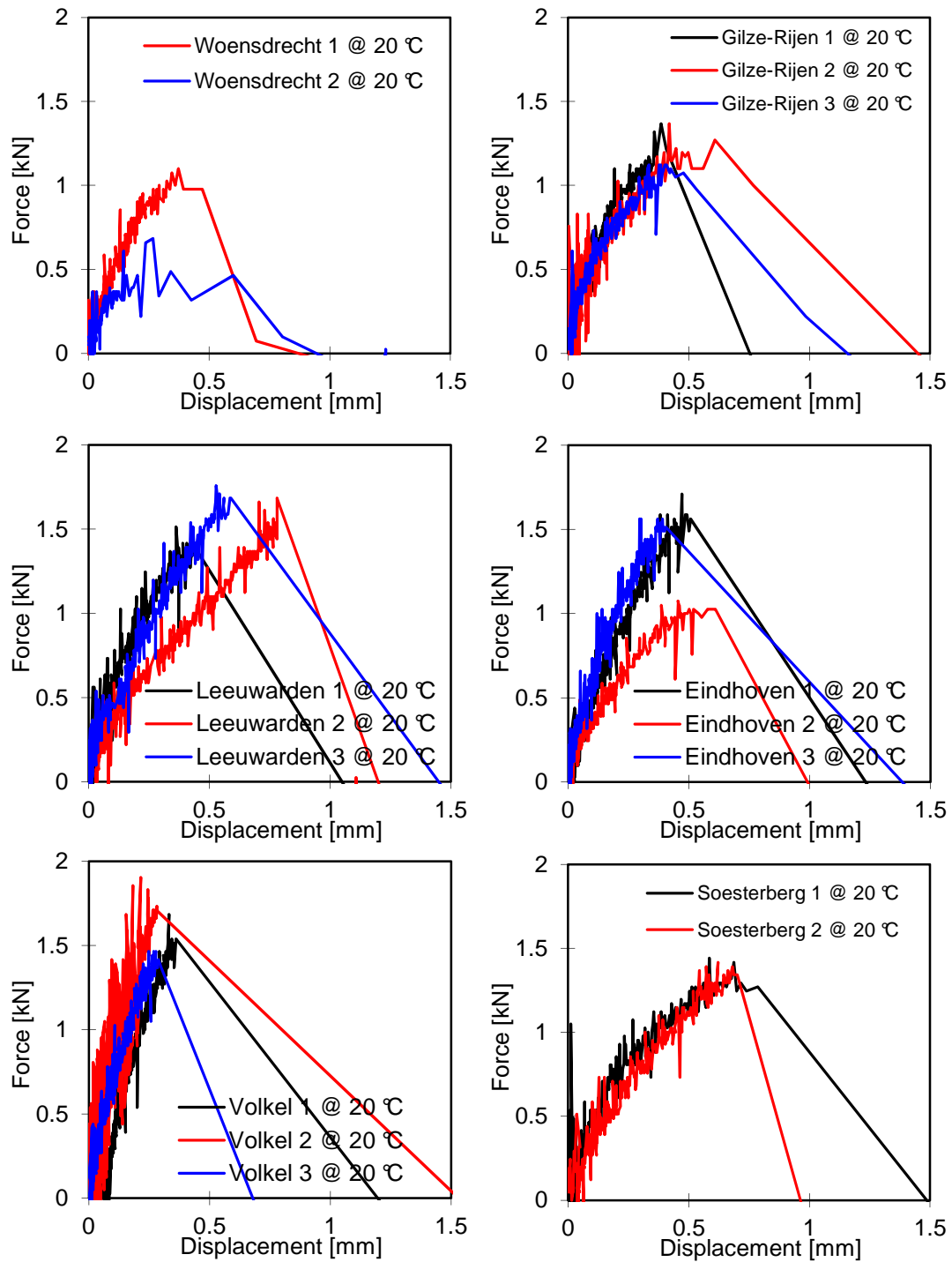


Figure A- 4 Displacement-force curves in pull test on tar-containing antiskid at 20 °C

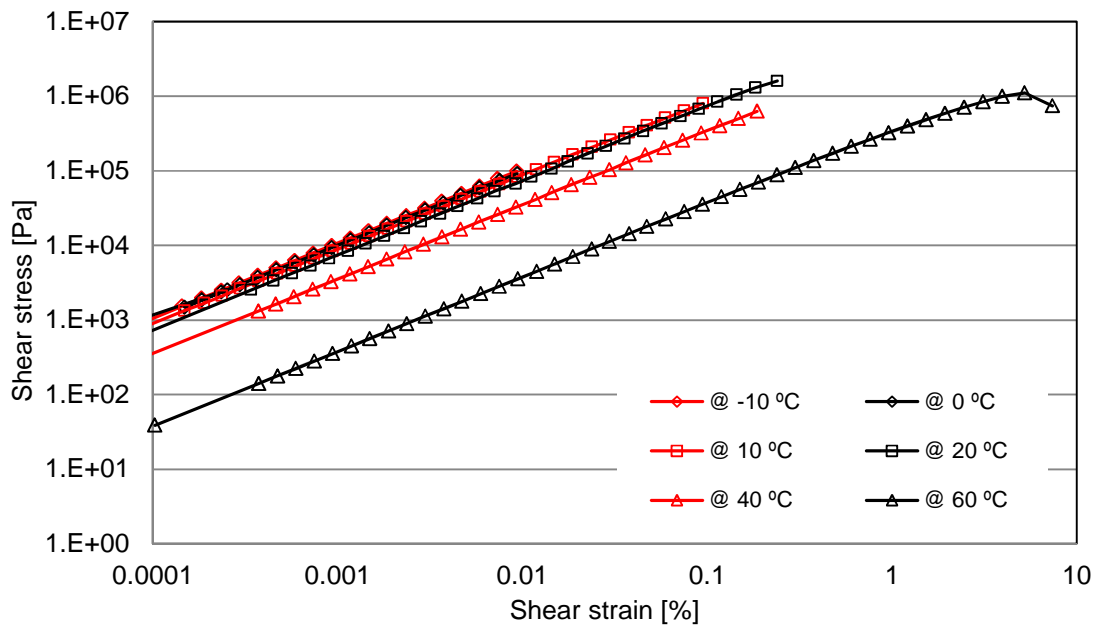


Figure A- 5 Stress-strain relationship in LVE range of oven aged A1 binder

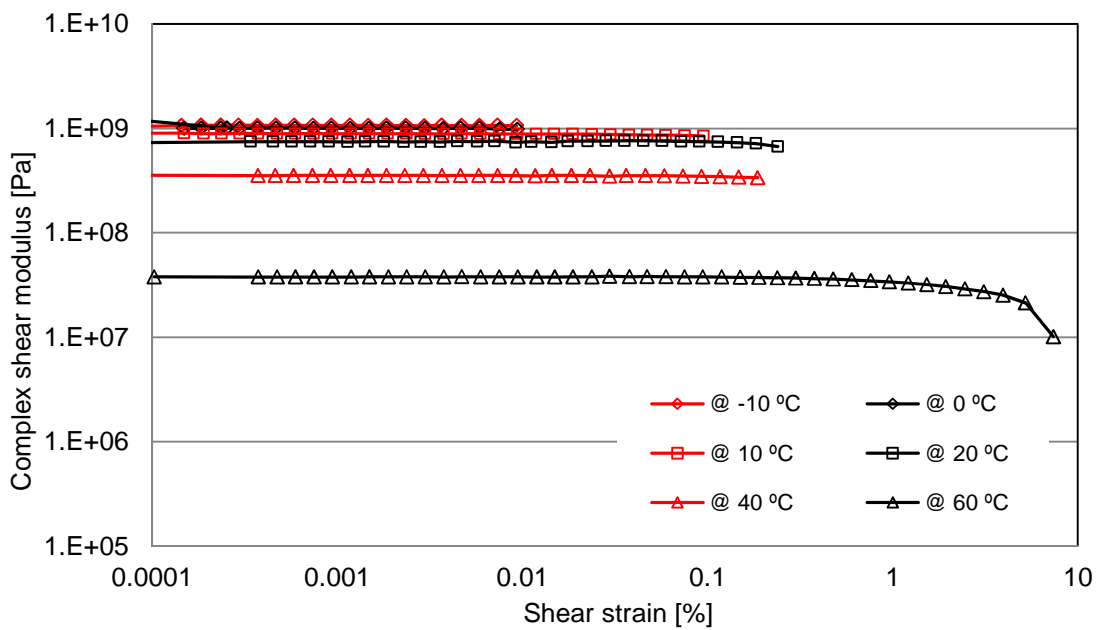


Figure A- 6 Modulus curves from strain sweep test on oven aged A1 binder

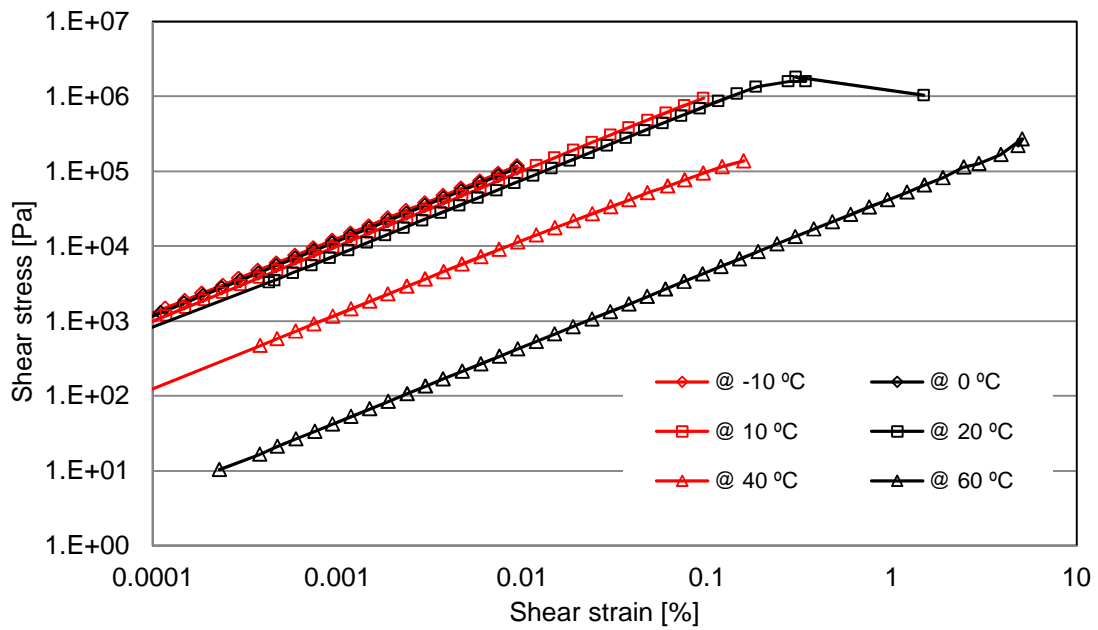


Figure A- 7 Stress-strain relationship in LVE range of fully cured A2 binder

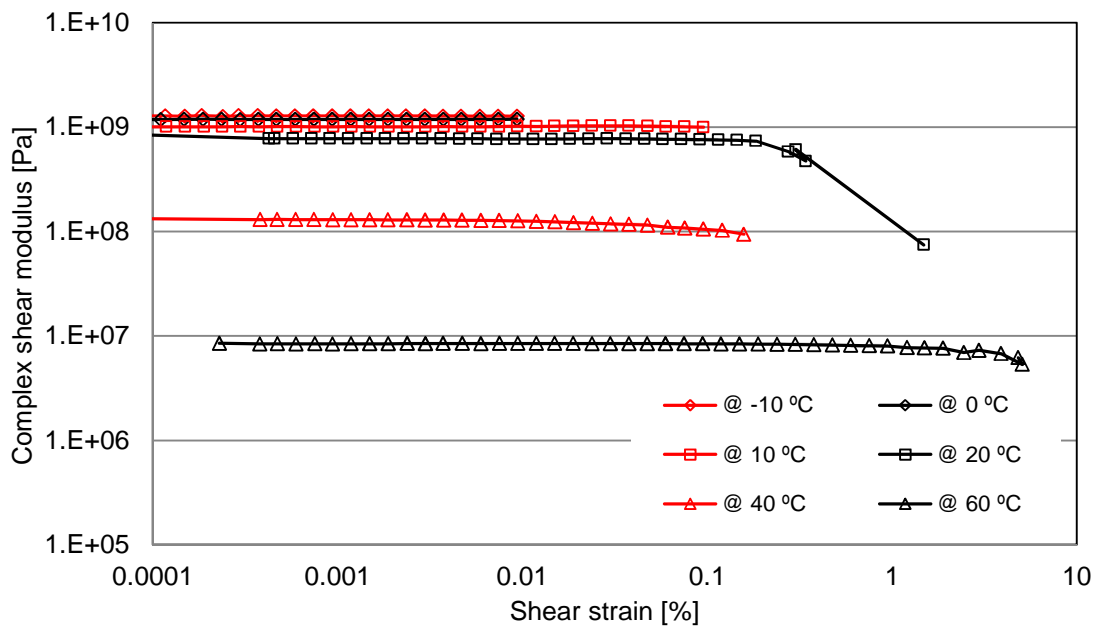


Figure A- 8 Modulus curves from strain sweep test on fully cured A2 binder

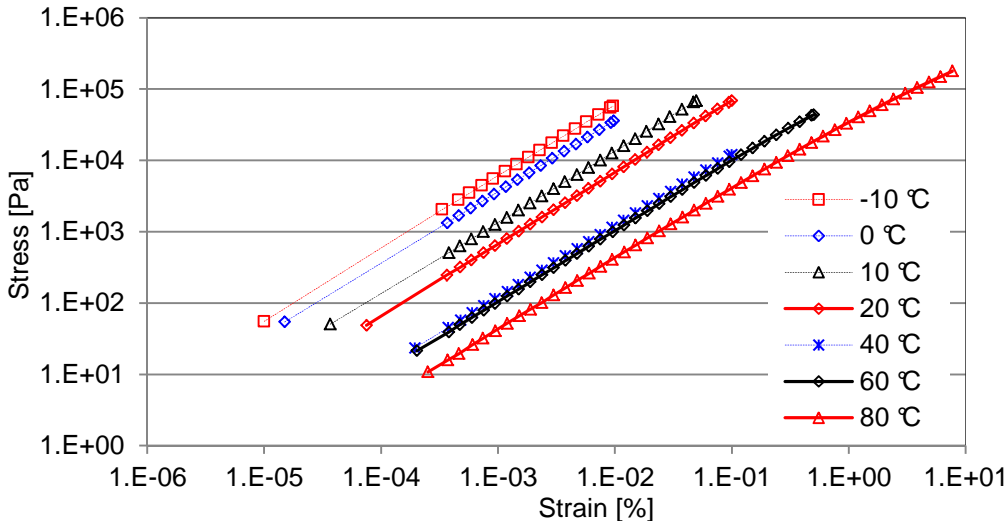


Figure A- 9 Stress-strain relationship in LVE range of weatherometer aged A3-UV binder

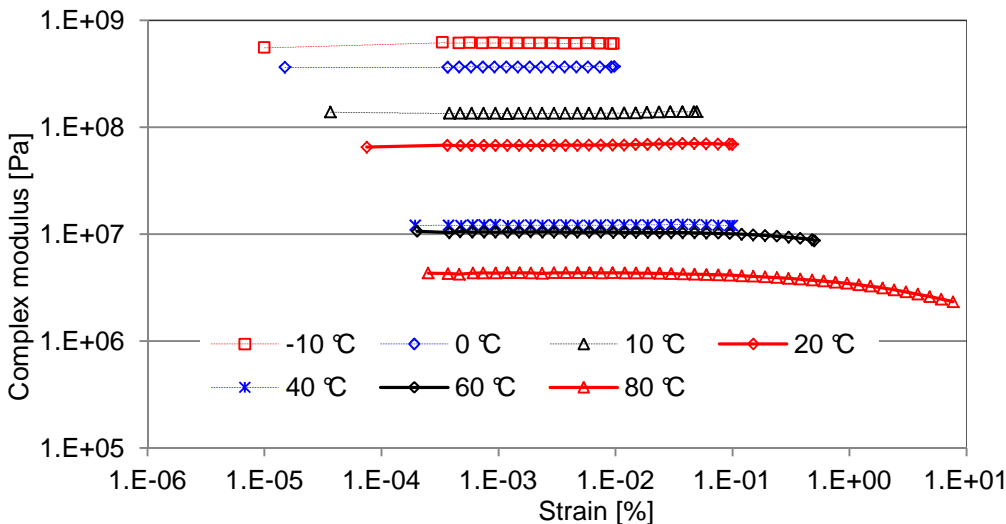


Figure A- 10 Modulus curves from strain sweep test on weatherometer aged A3-UV binder

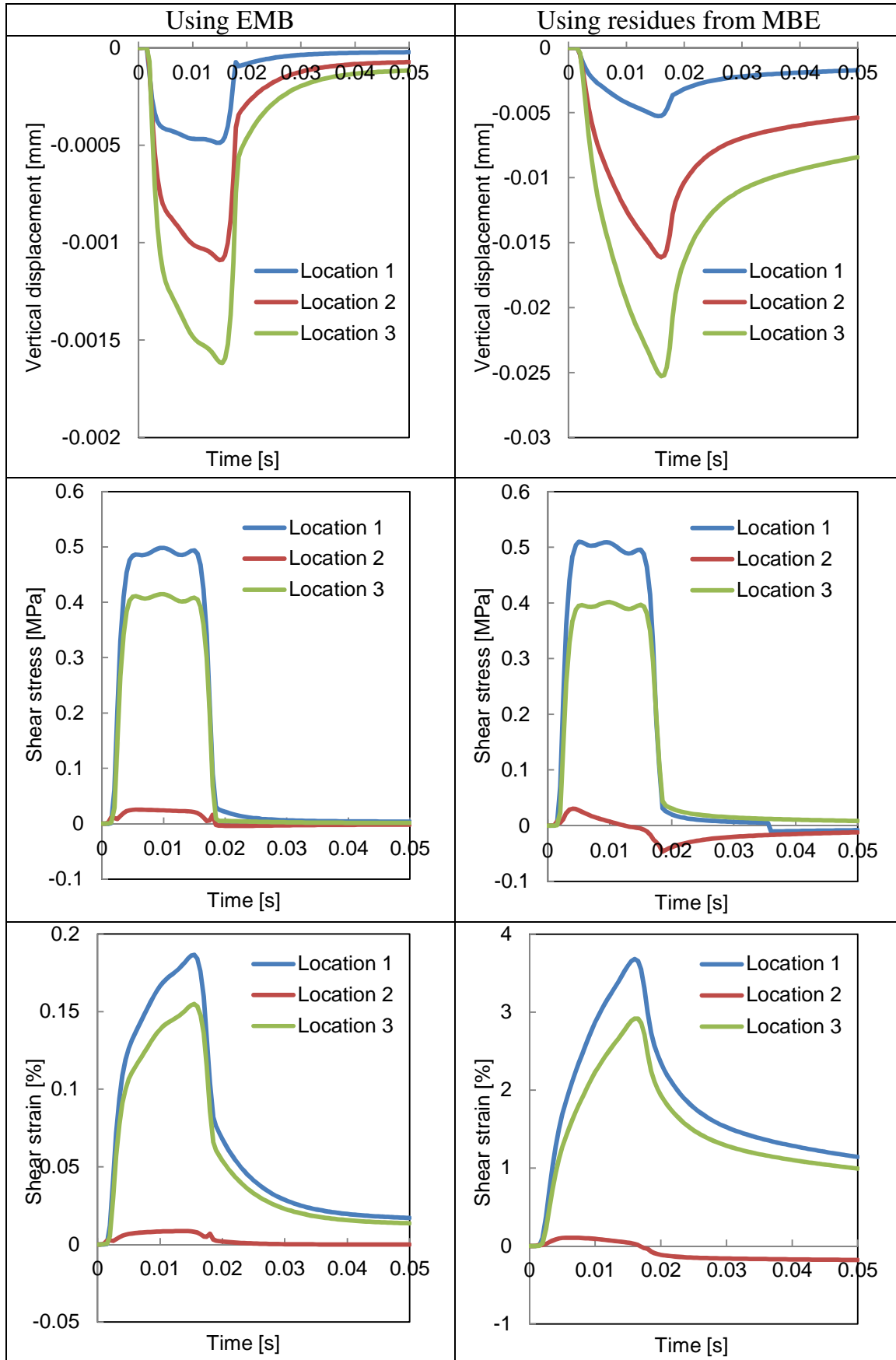


Figure A- 11 Differences of stress and strain responses in Antiskid-1 model (a)

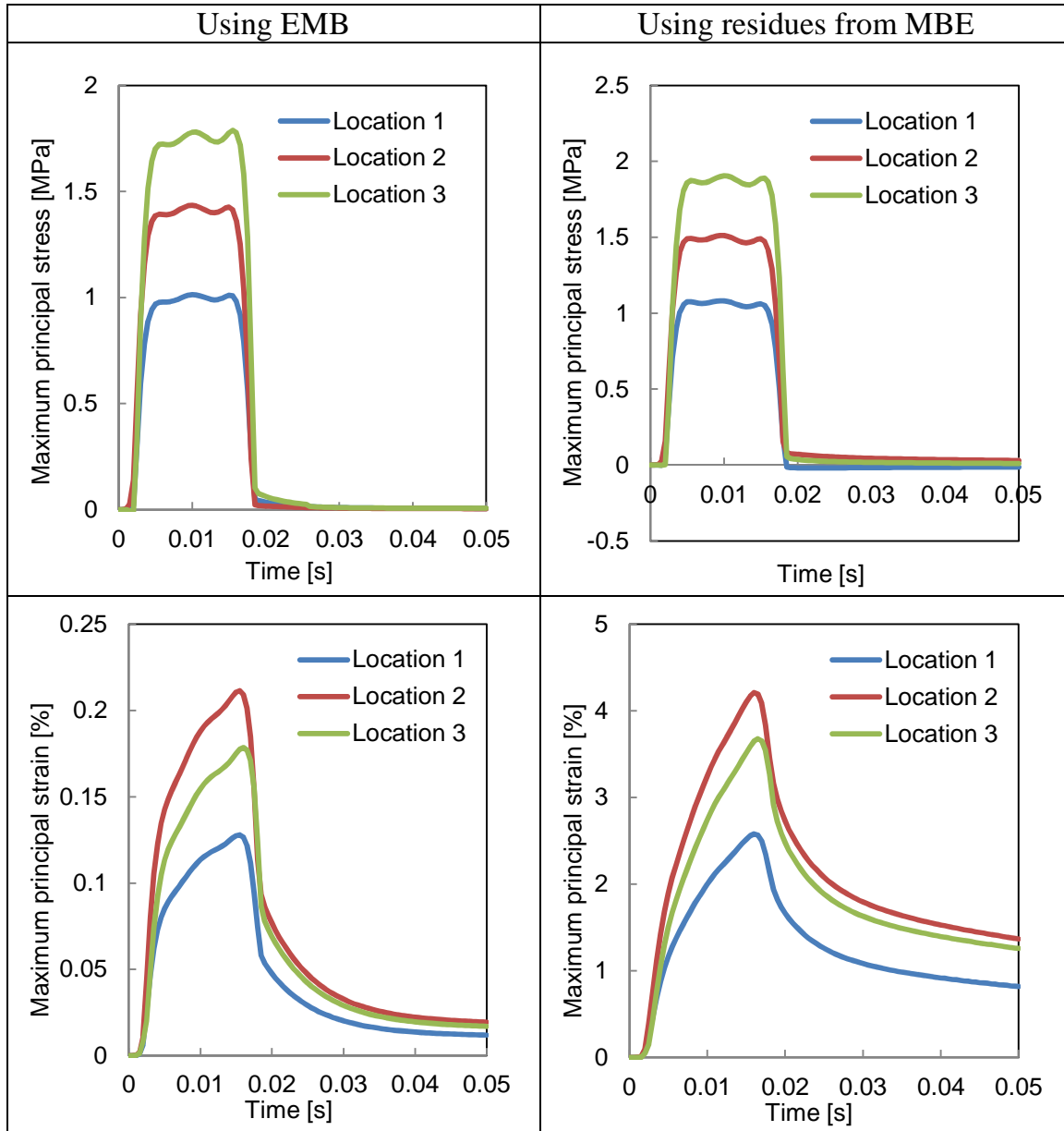


Figure A- 12 Differences of stress and strain responses in Antiskid-1 model (b)

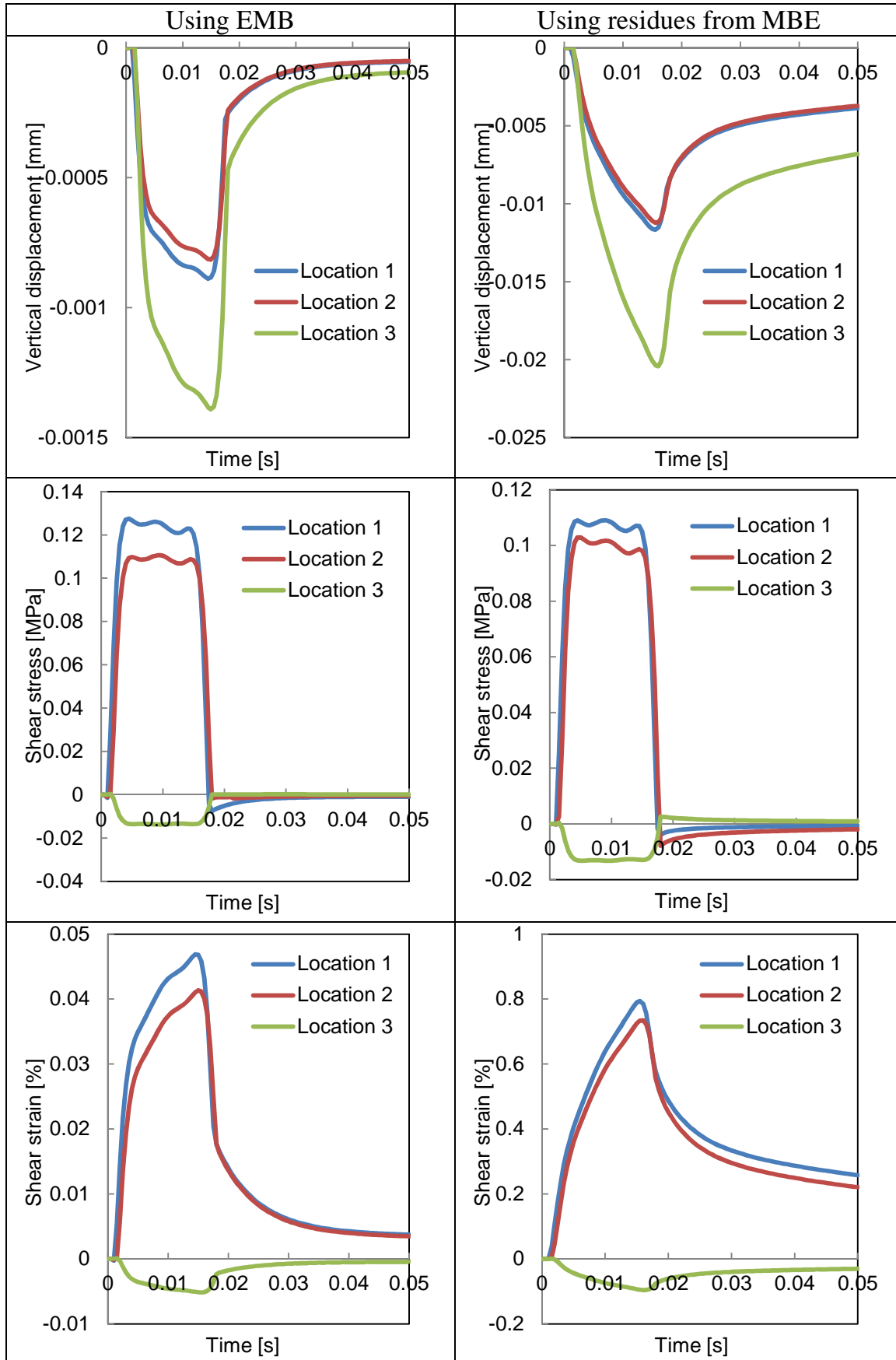


Figure A- 13 Differences of stress and strain responses in Antiskid-3 model (a)

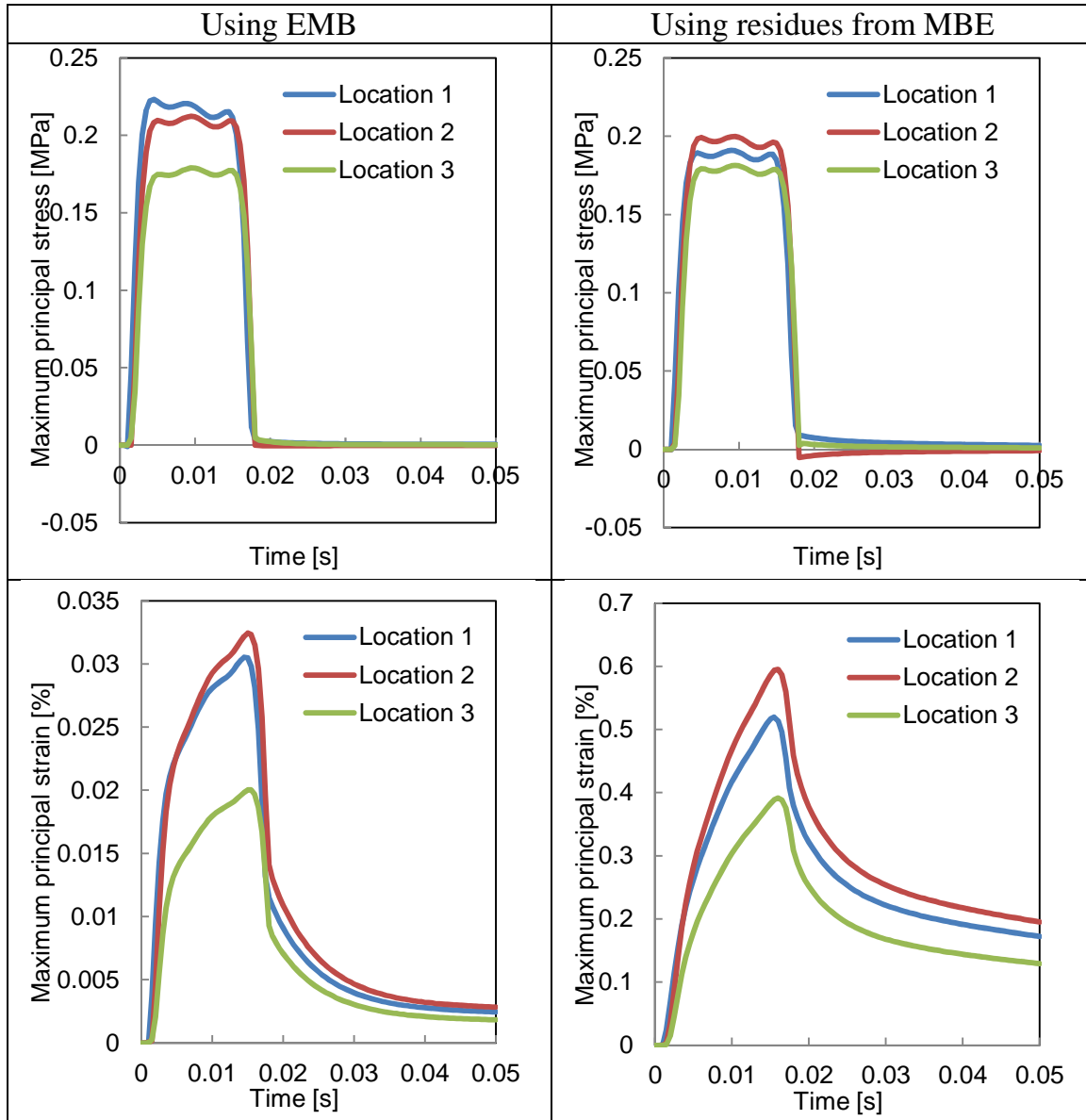


Figure A- 14 Differences of stress and strain responses in Antiskid-3 model (b)

Curriculum Vitae

Basic Information

Name: Yue Xiao (肖月)

Date of Birth: October, 1986

Place of Birth: Ji'an, Jiangxi Province, P.R. China

Email: yuedelft@gmail.com, xiaoy@whut.edu.com

About me: <http://www.yue366.com> (中文), <http://road.yue366.com> (in English)

Education Background

Oct. 2008 – Aug. 2013 PhD student in Road and Railway, Faculty of Civil Engineering and Geosciences, Delft University of Technology, Delft, the Netherlands

Sep. 2006 – Jun. 2008 Master student in Construction Materials and Engineering, Faculty of Material Science and Engineering, Wuhan University of Technology, Wuhan, P.R. China

Sep. 2002 – Jun. 2006 Bachelor student in Material Physics, Faculty of Material Science and Engineering, Wuhan University of Technology, Wuhan, P.R. China



Scan this QR code and directly go to
my CV page



扫描前往我的简历页面

Relevant Publications

Publications:

1. **Y. Xiao**, M.F.C. van de Ven, A.A.A. Molenaar, S.P. Wu. Possibility of Using Epoxy Modified Bitumen to Replace Tar-containing Binder for Pavement Antiskid Surfaces. *Construction and Building Materials*, Volume 48, (2013), P: 59-66.
2. **Y. Xiao**, M.F.C. van de Ven, A.A.A. Molenaar, Z. Su and K. Chang. Design Approach for Epoxy Modified Bitumen to be used in Antiskid Surfaces on Asphalt Pavement. *Construction and Building Materials*, Volume 41, (2013), P: 516-525.
3. J. Xie, **Y. Xiao**, S.P. Wu, J.F. Huang. Research on fracture characteristic of gneiss prepared asphalt mixture with direct tensile test. *Construction and Building Materials*, Volume 28, Issue 1, (2012), P: 476-481.
4. **Y. Xiao**, M.F.C. van de Ven, A.A.A. Molenaar, S.P. Wu. Stress and strain analysis in tar-containing antiskid runways using finite element models. *Construction and Building Materials*, Volume 27, Issue 1, (2012), P: 24-31.
5. **Y. Xiao**, M.F.C. van de Ven, A.A.A. Molenaar, Z. Su and F. Zandvoort. Characteristics of two-component epoxy modified bitumen. *Materials and Structures*, Volume 44, Number 3, (2011), P: 611-622.
6. **Y. Xiao**, M.F.C. van de Ven, A.A.A. Molenaar, M.L. Li. Test methods on Binder Selection for Antiskid Surface Applications. The 2nd International Conference on Sustainable Construction Materials: Design, Performance and Application (SusCoM2012), Wuhan, China.
7. **Y. Xiao**, M.F.C. van de Ven, S.P. Wu, M.F. Woldekidan. Advanced Pull Test to Determine Adhesion. Properties of Thin Surfaces for Pavement. ISAP 2012 international Symposium on Heavy Duty Asphalt Pavements and Bridge Deck Pavements, Nanjing, China.
8. **Y. Xiao**, M.F.C. van de Ven, A.A.A. Molenaar, S.P. Wu. Stress and strain distributions in tar-containing antiskid layers of runways. the 7th International Conference on Road and Airfield Pavement Technology (ICPT2011), Bangkok, Thailand.
9. **Y. Xiao**, M.F.C. van de Ven, A.A.A. Molenaar, S.P. Wu, M.R. Poot. Adhesion Properties of Tar-Containing Antiskid Surface Layers on Runways in Airfield. First T&DI Congress 2011: Integrated Transportation and Development for a Better Tomorrow, Chicago IL, USA.

10. **Y. Xiao**, M.F.C. van de Ven, A.A.A. Molenaar, S.P. Wu, W. Verwaal. **Surface Texture of Antiskid Surface Layers Used on Runways**. Transportation Research Board 90th Annual Meeting, (2011), Washington DC, USA.
11. **Y. Xiao**, M.F.C. van de Ven, A.A.A. Molenaar, S.P. Wu. **Environmental Concern of Using Coal Tar in Road Engineering and Its Possible Alternatives**. Journal of Wuhan University of Technology, Volume 32, Issue 17, (2010), P:1-7. The 1st International Conference on Sustainable Construction Materials: Design, Performance and Application (SusCoM2010), Wuhan, China.

Involved in Specification:

12. D11-01. CROW-Specifications for runway surface dressings on airfields. 2011, the Netherlands. Via link:
<http://www.crow.nl/nl/Publicaties/publicatiedetail?code=D11-01>

Project Reports:

13. **Y. Xiao**. Investigation on Resin Based Antiskid Surface Layer from ICOPAL. Delft University of Technology (TU Delft) Report, No. 7-10-185-6, (2013).
14. **Y. Xiao**, L.J.M. Houben. Onderzoek aan ELA-krete Antiskid Laag van Coldmix. Delft University of Technology (TU Delft) Report, No. 7-10-185-5N, (2013).
15. **Y. Xiao**. Investigation on ELA-krete Antiskid Surface Layer from Coldmix. Delft University of Technology (TU Delft) Report, No. 7-10-185-5, (2013).
16. **Y. Xiao**, M.F.C. van de Ven, A.A.A. Molenaar. Investigation on Schiphol Antiskid Surface Layer-Alternative for Tar-containing Antiskid. Delft University of Technology (TU Delft) Report, No. 7-10-185-4, (2012).
17. **Y. Xiao**, M.F.C. van de Ven, A.A.A. Molenaar. Investigation on ICOPAL Antiskid Surface Layer-type 1, Alternative for Tar-containing Antiskid. Delft University of Technology (TU Delft) Report, No. 7-10-185-3, (2012).
18. **Y. Xiao**, M.F.C. van de Ven, A.A.A. Molenaar, J.P. Verbeek. Report on an Assessment Protocol for Tar-containing Antiskid Layers for Runways. Delft University of Technology (TU Delft) Report, No. 7-10-185-2, (2010).
19. **Y. Xiao**. Literature Review on Possible Alternatives to Tar for Antiskid Layers. Delft University of Technology (TU Delft) Report, No. 7-10-185-1, (2010).